Università degli Studi dell'Insubria

Corso di Dottorato di Ricerca in Fisica e Astrofisica - XXX ciclo

PhD thesis

Post-Newtonian evolution of massive black hole triplets in galactic nuclei

Candidate:
Matteo Bonetti
Matricola 726034

Supervisor:
Prof. Francesco Haardt

Co-supervisors:
Dr. Alberto Sesana, Dr. Enrico Barausse

Anno Accademico 2016–2017

Considerate la vostra semenza:
fatti non foste a viver come bruti,
ma per seguir virtute e canoscenza.

— Inferno, Canto XXVI
Dante Alighieri

Contents

List of Figures

List of Tables

Introduction

Massive black holes (MBHs), i.e., black holes with masses exceeding $\gtrsim 10^5$ $M_\odot$, are ubiquitous in the nuclei of nearby galaxies (see Kormendy and Ho, 2013, and references therein), and are believed to represent a crucial, still poorly understood, ingredient in the process of galaxy formation and evolution. Indeed, the presence of MBHs as the powerhouse of distant QSOs can be traced back to early times, when the Universe was less than 1 Gyr old (Mortlock et al., 2011). The interplay between the central MBH and its host galaxy along the $\gtrsim 10$ Gyr of evolution of the cosmic structures is regarded as one of the main topics of research in physical cosmology (see, e.g., Volonteri, 2012).

In the standard Λ-CDM cosmology (see, e.g., Planck Collaboration et al., 2016, for the most recent values of the cosmological parameters) the large scale structure of the Universe evolves in a bottom-up assembling hierarchy, and as a consequence galaxies formed in dark matter over-densities at early times undergo several merger events along their cosmic evolution. This fact, connected to the notion that MBHs were common in galaxy nuclei at all epochs, leads to the inevitable conclusion that a large number of massive black hole binaries (MBHBs) did form during the evolution of the Universe (Begelman, Blandford, and Rees, 1980).

MBHBs are recognized as the loudest source of gravitational waves (GWs) in the low-frequency domain corresponding to the nHZ-mHZ range surveyed by ongoing and forthcoming Pulsar Timing Array (PTA) campaigns (Haehnelt, 1994; Jaffe and Backer, 2003; Wyithe and Loeb, 2003; Enoki et al., 2004; Sesana et al., 2004; Sesana et al., 2005; Jenet et al., 2005; Rhook and Wyithe, 2005; Barausse, 2012; Klein et al., 2016) and, in the future, by the laser interferometer space antenna (LISA) (Amaro-Seoane et al., 2017) recently approved by ESA. Together, the two experiments span the relevant frequency band in which MBHBs can emit a detectable GW signal during their path to the coalescence.

Nevertheless, a crucial and long lasting issue that poses a clear and present threat to the detection of the MBHBs as source of GWs is the possibility that the coalescence timescale of MBHBs typically exceeds the Hubble time, thus preventing the emission of any detectable GW signal. Indeed, the efficiency of GW emission essentially depends on two physical parameters, the mass of the system ($\dot{E} \propto (m_1 m_2)^2 (m_1 + m_2)$) and the separation of the orbiting bodies

($\dot{E} \propto r^{-5}$).

Although the high mass of MBHs identifies MBHBs as the most powerful source of GWs, because of the strong dependence on the separation, an efficient emission of GWs requires that the two bodies lie on a very close orbit, which is not straightforward to reach when the initial separation of two MBHs is of the order of several kpc. To reach separations close enough for efficient GW losses, a binary system has to rely on many different environmental effects determined by the stellar and/or gaseous components of the host galaxies. If conditions are not favourable, there is then the possibility that a MBHB stops its orbital shrinking at separations typically around the parsec scale.[1] Therefore, if a MBHB effectively stalls, it will never coalesces within the current age of the Universe, a situation referred in the literature as "the final parsec problem" (Milosavljević and Merritt, 2003; Vasiliev, Antonini, and Merritt, 2014; Vasiliev, Antonini, and Merritt, 2015).

It is well understood that whenever two galaxies merge, the MBHs hosted in their centre migrate towards the innermost region of the merger remnant, as a result of the cumulative effect of two-body encounters between a single MBH and background stars, a process known as dynamical friction (Chandrasekhar, 1943). During every encounter, fractions of momentum and kinetic energy are exchanged between the MBH and the star. Depending on the ratio between the MBH velocity in the galactic potential and the stellar velocity dispersion, the interaction can have different outcomes. If such ratio is $\ll 1$, i.e., stars move, on average, faster than the MBH, the net effect on the MBH is practically negligible as stars approach the MBH almost isotropically. On the contrary, if the MBH on average moves moderately faster than the stars, then its net motion in the galactic potential determines a symmetry breaking and during the interactions, stars gain velocity against the MBH, which in turn experiences a slow down. Therefore, the cumulative effect of a series of encounters generates a net drag force (the dynamical friction force) that acts as a brake for the motion of the MBH, determining its migration toward the centre of the global gravitational potential. Finally, if the MBH moves much faster than background stars, then the interaction time becomes so small such that the effect of dynamical friction is again negligible.

Because of dynamical friction, two MBHs can get close enough that their self gravity dominates their dynamics over external factors, effectively binding the two objects in a quasi-Keplerian binary. Once the binary is formed, the effect of dynamical friction becomes more and more negligible as the orbital velocity grows. At this stage, only single three-body encounters among the MBHB and close background stars can further shrink the orbit by transferring a fraction of orbital energy and angular momentum to nearby interacting objects, a process known as stellar hardening. During the complex three-body interaction, because of the huge mass differences, stars are likely ejected from the surroundings of the MBHB (Quinlan, 1996; Sesana, Haardt, and Madau, 2006), gradually decreasing the reservoir of objects that can sustain the process itself. This translates in

[1] The specific details of the stalling scale depends on various parameters, both of the binary and the host galaxy.

a gradual depletion of stars with orbital parameters suited to intersect the orbit of the MBHB, the so-called "loss-cone" in the energy-angular momentum parameter space. Hence, after an early efficient phase, also this mechanism, can become highly inefficient as fewer and fewer stars can interact with the MBHB. This is especially true in spherical potentials, where the dynamical mechanisms that can induce the replenishment of the binary loss-cone (e.g., two-body stellar relaxation) have timescales typically of the order of several Gyrs (Yu, 2002; Milosavljević and Merritt, 2003). Therefore, when the stellar hardening effectively halts, the MBHB stalls at separations at which GW emission alone could lead to coalescence in a time exceeding an Hubble time.[2]

In the last years, many extensive efforts have been directed towards a consistent solution of the final parsec problem. In particular, it has been advocated that galactic rotation (Holley-Bockelmann and Khan, 2015) or a certain degree of triaxiality of the galactic potential due to, e.g., a recent galaxy merger (Yu, 2002; Berczik et al., 2006; Preto et al., 2011; Khan, Just, and Merritt, 2011; Gualandris and Merritt, 2012; Vasiliev, 2014; Vasiliev, Antonini, and Merritt, 2014; Vasiliev, Antonini, and Merritt, 2015; Khan et al., 2016; Gualandris et al., 2017), can increase the replenishment rate of the loss-cone. Deviation from spherical symmetry, indeed, generates potentials characterised by families of centrophillic orbits, i.e., peculiar orbits crossing the centre of the matter distribution, forcing in this way new stars to populate the loss cone. Although triaxiality can keep the stellar hardening activate, still the binary orbital decay may anyway last several Gyr if the stellar density in the galaxy core is not particularly large (especially true for very massive systems hosted in elliptical galaxies, see e.g., Sesana and Khan, 2015).

In the presence of a galactic gas-rich environment, instead, it is known that either because of the interaction of a MBHB with a gaseous circumbinary disk or with a series of gas clouds incoherently accreted (Dotti et al., 2007; Haiman, Kocsis, and Menou, 2009; Cuadra et al., 2009; Nixon et al., 2011; Colpi, 2014; Goicovic et al., 2017), the shrinking timescale of the binary can be reduced because of the efficient torque exerted by the gas, a mechanism which is effective in removing angular momentum from the MBHB. Although the interaction with gas represents a promising answer to the final parsec problem, the actual efficiency of gas-MBHB interaction in realistic physical conditions is poorly known, and stalling of the binary could still be a realistic possibility (see, e.g., Lodato et al., 2009), in particular in dry mergers involving gas-poor elliptical galaxies.

Among other possible (and in principle not mutually exclusive) solutions of the final parsec problem, an intriguing viable process consist in the interaction of a MBHB with a third MBH. This situation can be quite common in the framework of the hierarchical clustering, since if MBHBs commonly stall and do not merge, then it is inevitable that sooner or later an other galaxy merger brings a third MBH to interact with the pre-existing binary, then forming a MBH triplet.

[2]This is strictly true only for the most massive systems, see, e.g., Merritt, Mikkola, and Szell (2007).

It is well known that the three-body problem, unlike binary systems, does not allow for a general analytic solution, rather it is intrinsically chaotic. i.e., the long-term predictability about the evolution of the system is lost. Indeed, the chaotic dynamics implies that choosing a pair of three-body systems with arbitrary close initial conditions, their evolution can not be a priori predicted and (after a sufficiently long time) it follows a completely different path. This represents one of the most striking characteristic of the three-body (or in general N-body) gravitational dynamics and also one of the major difficulties that we have to face in order to tackle phenomena that involves more than two gravitating bodies.

Analytical approximations can be employed whenever a three-body system owns a particular configuration such that the equations of motion can be expanded as a power series of some small quantity. Such approach, when possible, gives a deep physical insight on the analysed dynamics. However, it can be self-consistently applied in a limited range of configurations, e.g., when one of the bodies is much less massive than the other two (the so-called restricted three-body problem), or when one of the bodies lies much farther apart. This latter case turns out to have remarkable importance in various field, in particular, as we will see, in our study of MBH triplets. Triplets in this peculiar configuration are called hierarchical, because the system can be formally treated as formed by two separate binaries, an inner closer one and an outer, much wider system defined by the third body and the centre of mass of the inner binary. The importance of the hierarchical configuration stems from the fact that various secular processes, i.e., phenomena that proceed on a timescale much longer than the orbital periods of the two binaries, are manifest and can be formally treated.

One of the most important and extensively studied secular process in hierarchical triplets is the so called Kozai-Lidov (K-L) mechanism (or resonance) (Kozai, 1962; Lidov, 1962). In the standard lore, the K-L mechanism operates when the relative inclination of the orbital plane of the two binaries forming the triplet is high enough. In this case, because of secular exchanges of angular momentum between the inner and outer binaries, large amplitude oscillations of the relative inclination and the eccentricity of the inner binary are triggered. The closer to 90° is the initial relative inclination, the larger is the maximum eccentricity that the inner binary can attain.

The standard method to investigating the K-L mechanism leverages on a perturbative approach in which the equations are first expanded as power series in terms of ratio of the inner ($a_{\rm in}$) to outer ($a_{\rm out}$) semi-major axis (the small quantity mentioned before), and then averaged over the orbital periods of the two binaries. In the original works by Kozai and Lidov only the first term in the expansion was taken into account, i.e., the quadrupole term proportional to $(a_{\rm in}/a_{\rm out})^2$. In addition, the secondary mass of the inner binary was assumed to be a test particle. Remarkably, the problem recast in this fashion has a complete analytical solution. Introducing higher order terms and/or allowing all three body to have non-negligible masses, new and sometimes more extreme phenomenologies arise (orbital flips, modulation of eccentricity etc., see e.g., Ford, Kozinsky, and Rasio, 2000; Naoz, 2016, and references therein).

Because of its peculiar characteristics, the K-L mechanism has been invoked to explain various phenomena in many astrophysical contexts, including planetary dynamics (Holman, Touma, and Tremaine, 1997; Katz, Dong, and Malhotra, 2011; Naoz, Farr, and Rasio, 2012; Naoz et al., 2013), interactions of stellar size objects in globular clusters (Antonini et al., 2016) and around a MBH (Antognini and Thompson, 2016). For the case of MBH triplets considered in this thesis, it is clear that if a MBHB stalls and its host galaxy undergoes a further merger, then the triplet that forms naturally presents an hierarchical configuration. Therefore, these systems can be prone to the K-L mechanism[3] as first investigated by Blaes, Lee, and Socrates (2002). Those authors, by employing the secular analysis at the next to leading order (i.e., at octupole order) combined with the general relativistic corrections to account for GW back-reaction and apsidal precession, found that the merger time-scale of a MBHB can be reduced by up to an order of magnitude by the action of the K-L mechanism.

In spite of the low-to-modest computational cost, a major drawback of the secular formalism consists in its inability to solve for the dynamics of high eccentric binaries, particularly when the triplet can not be treated as hierarchical. Such situation is commonly met when MBH triplets form and evolve in galactic nuclei, as environmental processes, such as the stellar hardening, cause the shrinking of the outer binary. It turns out that the K-L mechanism in such evolving triplets is characterized by a dynamics much more complex than the standard, hierarchical case. Qualitatively, as the outer semi-major axis shrinks, the K-L timescale changes accordingly, until the three bodies attain relative separations so small that the dynamics becomes chaotic. Once this happens, the triplet can not be analysed with perturbation techniques any longer, and direct numerical integration is then necessary.

A great advantage of numerical methods consists in their applicability to systems of arbitrary configuration, such as an unstable, chaotic triplet, allowing us to circumvent the limitations typical of the analytical technique. On the other hand, the computational cost of numerical methods can be an issue, along with the necessity of controlling the discretisation and roundoff errors. In particular, the monitoring of discretisation errors is crucial, since, if underestimated, they can lead to spurious results. However, despite the particular care that the numerical integration of orbits requires, such methods are powerful in investigating the dynamics of triple systems. Iwasawa, Funato, and Makino (2006) and Iwasawa, Funato, and Makino (2008) performed fully numerical N-body simulations of a galactic spheroid containing three MBHs, and found that K-L oscillations accompanied by strong resonant interactions can greatly increase the eccentricity of the innermost binary. However, the method employed is computationally demanding, and the survey of the parameter space was necessarily limited.

A hybrid approach, first proposed by Hoffman and Loeb (2007), consists in staging the orbit integration of the three-body system in an analytical, external potential, allowing for dissipative effects due to the environment. Hoffman and Loeb (2007), starting from triplets initialised according to cosmologically

[3]Note that, if an isotropic distribution for the angular momentum directions of the two binaries is assumed, then high relative inclinations are favoured.

motivated initial conditions, found that three-body interactions can enhance the rate of MBHB coalescences, hence easing the final parsec problem. The authors suggested the production of burst-like GW signals due to the high eccentricities reached by the simulated systems. Similar conclusions were also reached by Kulkarni and Loeb (2012), starting from cosmological simulations of the large scale structure.

However, contrary to Blaes, Lee, and Socrates (2002) (which nevertheless follow a secular perturbative approach), such works do not include any GR effect except the back-reaction of the GWs, with the possible result of an overestimation of the merger rate generated by triple interactions. As a matter of fact, any kind of precession acting on a time-scale shorter than the K-L timescale can dump the K-L oscillations, hence making such mechanism ineffective. Precession can hamper the coherent piling up of the perturbation induced by the third body on the inner binary, i.e., it can effectively destroy the resonance on which the K-L mechanism relies on. In the case of MBHs, the most relevant form of precession is of course given by the relativistic precession of the pericentre.

GR dynamics can produce important effects, and its inclusion represents one of the major novelty of the present thesis. We implemented, in a hybrid scheme, a direct three-body PN integrator that includes relativistic correction terms up to 2.5PN order, consistently derived from a three-body PN Hamiltonian. In addition, we considered the effects of an external spherical potential mimicking the host galaxy and the connected dissipative effects, i.e., the hardening of the outer binary generated by scattering off background stars, and the action of the dynamical friction. Our approach allowed us to perform a detailed survey of the parameter space in terms of MBH masses, mass ratios, eccentricities and inclinations.

One of the main reasons leading us to consider a more complex physics lies in the remarkable high eccentricity that a binary system can acquire when involved in a triple interaction, both secular or chaotic. Eccentricity is intimately connected to the efficiency of GWs. A highly eccentric binary has a coalescence timescale that can be orders of magnitude shorter than a circular system, because of the dependence of the GW power on the relative separation of the orbiting bodies. If triple interactions can produce a sizeable population of highly eccentric merging binaries, then a characteristic signature can be left on the GW signal, which could be detected by ongoing and forthcoming experiments, like PTA and the future space-borne LISA mission.

A non-zero eccentricity has the effect of broaden the GW frequency spectrum emitted by a MBHB, and to push the typical frequencies to high values (Peters and Mathews, 1963). If a circular binary effectively represents a monochromatic source that emits GWs at twice the orbital frequency, an eccentric binary distributes the power of the GWs among higher harmonics. Moreover, the more eccentric the binary, the larger the frequency at which most of the power is emitted, simply because GWs are efficiently emitted at the closest approach, i.e., at the pericentre. In case of high eccentricity, the time of the pericentre passage and therefore the time at which most part of the energy is radiated is only a small fraction of the whole orbital period. For an eccentric binary the whole GW emission is therefore essentially concentrated in relatively high

frequency, high luminosity, short-lasting bursts. The above considerations have two fundamental effects.

A first effect can be understand by considering that GW losses always tend to circularise the orbit of a binary system. This fact, combined to the blueshift due to the eccentricity, leads to the conclusion that the stochastic GW background from a cosmic population of MBHBs is suppressed at low frequencies ($10^{-10} - 10^{-9}$ Hz) because of the power shifting, while at higher frequencies the signal should follow the power law form (proportional to $f^{-2/3}$) proper of circular binaries (see e.g., Sesana, 2013). Hence, the broadband GW spectrum is expected to feature a turnover, whose exact position in the frequency domain depends on the eccentricity distribution of the binaries across the Universe. As already stated, triple interactions can produce highly eccentric binaries, pushing the turnover to comparatively high frequencies. Therefore, in order to concretely assess the detection figures by PTA experiments (see e.g., Siemens et al., 2013; Rosado, Sesana, and Gair, 2015), it is necessary to estimate the eccentricity distribution of cosmic MBHBs. This is precisely one of the main results we have obtained. In particular, demonstrating the viability of the triplet-induced mergers, we are in the position to perform for the first time robust predictions about the minimum level of the expected PTA signal. This represents a very relevant point for PTA.

Secondly, always in the PTA band, the very existence of a population of eccentric MBHBs enhances the probability of resolving single sources (opposed to the detection of a stochastic background), because of the high luminosity of the burst-like signal, corresponding to the pericentre passage. Eccentric MBHBs in wide orbits can therefore give rise to burst-like events in the PTA band (Amaro-Seoane et al., 2010). The very same effect can also be quite relevant in the LISA band, but for low mass MBHB. Indeed, because of its designed sensitivity, the planned space interferometer will mainly detect GW radiation from relatively low mass MBHBs, i.e., up to a chirp mass of 10^7 $M_\odot$. Some of these low mass and highly eccentric binaries may not merge during the nominal duration of the LISA mission because of a wide orbital separation. However, because of the very high eccentricity, they may be detected as burst-like sources, representing therefore a new class of resolvable objects, which may be of particular importance when assessing the expected detection rate by LISA, as we will explore in a future analysis.

The thesis is organised as follows: in chapter 1 I analyse the main features of the relativistic three-body dynamics. I derive the equations of motions and present a detailed analysis of the GW emission formalism when triple systems are involved, highlighting some peculiar subtle issues that we have encountered. In chapter 2 I describe the theoretical and numerical setup employed to perform simulations of MBH triplets that may form in galactic nuclei. I test the numerical code and present some representative examples. In chapter 3 I report the results of the analysis of a large set of simulations (~ 15000) spanning a wide parameter space in terms of MBH masses, mass ratios, eccentricity and inclinations. In chapter 4 I briefly describe a state-of-the-art semi-analytical code of galaxy formation and our original method to include the effect of MBH

triple interactions in a cosmological framework. In chapter 5, by employing the whole setup worked out in the previous chapters, I discuss how to draw robust predictions about the nHz stochastic background of GWs. In chapter 6 I briefly depict the implications of triple MBH interactions in the framework of LISA and I argument some of the work-in-progress developments. Finally, in the last chapter, I sketch the main conclusions of the work presented here.

Chapter 1

Relativistic three-body dynamics

The Newtonian theory of gravity has represented for centuries a perfect description of all gravitational phenomena, from everyday human scales to the dynamics of planets. However, with the development of always more precise instruments and the achievement of a deeper comprehension of gravitational phenomena, it became clear that Newton's theory could not represent the ultimate theory of gravity.[1] The nowadays universally accepted theory that describes the gravitational interaction is indeed represented by the General Relativity (GR), a geometric theory of gravity, which to date has provided a remarkable number of predictions, each of them verified by observations (the latest being the direct detection of GWs, Abbott et al., 2016).

Despite the general and elegant setup of GR, the intrinsic non-linearity of its field equations poses an overwhelming challenge in obtaining exact analytical solutions in the vast majority of realistic physical situations. While the two-body problem is completely solvable in Newtonian theory, no general exact solution to it is known in GR. As a result, the dynamics of a binary system in GR can only be obtained by solving perturbatively the field equations, or through numerical techniques on a computer ("numerical relativity" Pretorius, 2005; Campanelli et al., 2006; Baker et al., 2006; Alcubierre, 2008; Lehner and Pretorius, 2014).

It turns out that in many astrophysical situations the effects of GR can be treated as small perturbations of the leading Newtonian order. Therefore, the relativistic dynamics, through the employment of perturbation analysis, can be treated in a Newtonian-like fashion, i.e., by adding correction terms to the standard non-relativistic equations of motions. Among perturbative schemes valid in different regimes, the more commonly used are the so-called post-Newtonian (PN) approximation (Einstein, Infeld, and Hoffmann, 1938; Will, 1993; Blanchet, 2014), which consists in expanding the dynamics in powers of

[1] An early hint towards the failure of the Newtonian theory was, for instance, the anomalous advance of the pericentre of Mercury, which could not be explained in the framework of Newtonian dynamics, while it can be naturally explained employing a general relativistic approach.

$v/c \ll 1$[2] (v being the relative velocity of the binary, c the speed of light in vacuum), and the self-force formalism, which instead relies upon an expansion in the mass ratio of the binary, assumed to be small (Poisson, 2004).

Not surprisingly, the three-body problem, which already in Newtonian theory does not admit any general closed form solution and, moreover, gives rise to chaotic dynamics, becomes considerably harder to tackle in GR. However, the three-body general-relativistic dynamics can be obtained within the PN approximation scheme, just like in the two-body case. Indeed, one can write a PN-expanded, time-dependent Hamiltonian (Schäfer, 1987; Königsdörffer, Faye, and Schäfer, 2003; Lousto and Nakano, 2008; Galaviz and Brügmann, 2011) that describes the conservative dynamics of a system of three non-spinning bodies up to the 2PN order (i.e., through order $(v/c)^4$ beyond the leading Newtonian dynamics), as well as its dissipative dynamics (i.e., the back-reaction due to GW emission) to leading order in v/c, which corresponds to a contribution of 2.5PN order, or $\mathcal{O}(v/c)^5$, in the equations of motion.[3] In this thesis we treat the relativistic dynamics in the framework on the PN approximation.

This first chapter is fully devoted to describe some of the features of the relativistic three-body dynamics. We begin by summarising the post-Newtonian approach to the GR dynamics and we report the relevant expressions needed to obtain the PN equations of motion of a general three-body system. These equations represent one of the key element of our work on triple interactions. Then, we proceed by focusing on the dissipative aspects of the relativistic gravitational interaction, i.e., we concentrate on the gravitational radiation that triple (and also binary) systems generate. We briefly summarise the standard formalism for the computation of the GW emission from binaries and we extend to the triplet case. Next, we remark and explain some peculiar subtle issues that affect naive implementations of gravitational waveforms from numerically-integrated trajectories of two- and three-body systems.

1.1 PN equations of motion

The Hamiltonian for a triple system of non-spinning bodies is given, in schematic form and through 2.5PN order, by

$$H = H_0 + \frac{1}{c^2}H_1 + \frac{1}{c^4}H_2 + \frac{1}{c^5}H_{2.5} + \mathcal{O}\left(\frac{1}{c^6}\right). \tag{1.1}$$

Each PN order, through its corresponding Hamiltonian, introduces different relativistic corrections to the standard Newtonian laws of motion, and therefore a qualitatively different dynamics. Even powers of c^{-1} represent conservative

[2] Actually, the PN formalism relies on two small parameters, i.e., v/c and $GM/(c^2r)$, where G is the Newton's constant, while v, M and r represent the typical velocity, mass and size of the considered system. However, the PN framework further assumes that the system is self-gravitating, therefore $v^2/c^2 \sim GM/(c^2r)$. This fact allows to recast the approximation in terms of v/c only.

[3] In the standard PN book-keeping a term suppressed by a factor $(v/c)^{2n}$ with respect to the leading (i.e., Newtonian) order is said to be of nPN order.

terms, while odd powers are dissipative terms. In particular, H_0, H_1 and H_2 are functions of the positions and conjugate momenta of the three bodies, i.e., $\boldsymbol{x}_A$ and $\boldsymbol{p}_A$ (with $A = 1, 2, 3$). Explicit expressions for the Hamiltonian are given by Schäfer (1987), Lousto and Nakano (2008) and Galaviz and Brügmann (2011) (see also Königsdörffer, Faye, and Schäfer, 2003, for higher-order terms), and reads[4]

$$H_0 = \frac{1}{2}\sum_A \frac{|\boldsymbol{p}_A|^2}{m_A} - \frac{G}{2}\sum_A \sum_{B\neq A} \frac{m_A m_B}{r_{AB}}, \tag{1.2}$$

$$\begin{aligned} H_1 = &-\frac{1}{8}\sum_A m_A \left(\frac{|\boldsymbol{p}_A|^2}{m_A^2}\right)^2 \\ &- \frac{G}{4}\sum_A \sum_{B\neq A} \frac{1}{r_{AB}}\left[6\frac{m_B}{m_A}|\boldsymbol{p}_A|^2 - 7\boldsymbol{p}_A\cdot\boldsymbol{p}_B - (\boldsymbol{n}_{AB}\cdot\boldsymbol{p}_A)(\boldsymbol{n}_{AB}\cdot\boldsymbol{p}_B)\right] \\ &+ \frac{G^2}{2}\sum_A \sum_{B\neq A}\sum_{C\neq A} \frac{m_A m_B m_C}{r_{AB} r_{AC}}, \end{aligned} \tag{1.3}$$

$$\begin{aligned} H_2 = &\frac{1}{16}\sum_A m_A \left(\frac{|\boldsymbol{p}_A|^2}{m_A^2}\right)^3 \\ &+ \frac{G}{16}\sum_A \sum_{B\neq A} \frac{(m_A m_B)^{-1}}{r_{AB}}\left[10\left(\frac{m_B}{m_A}|\boldsymbol{p}_A|^2\right)^2 - 11|\boldsymbol{p}_A|^2|\boldsymbol{p}_B|^2 - 2(\boldsymbol{p}_A\cdot\boldsymbol{p}_B)^2\right. \\ &+ 10|\boldsymbol{p}_A|^2(\boldsymbol{n}_{AB}\cdot\boldsymbol{p}_B)^2 - 12(\boldsymbol{p}_A\cdot\boldsymbol{p}_B)(\boldsymbol{n}_{AB}\cdot\boldsymbol{p}_A)(\boldsymbol{n}_{AB}\cdot\boldsymbol{p}_B) \\ &\left.- 3(\boldsymbol{n}_{AB}\cdot\boldsymbol{p}_A)^2(\boldsymbol{n}_{AB}\cdot\boldsymbol{p}_B)^2\right] \\ &+ \frac{G^2}{8}\sum_A \sum_{B\neq A}\sum_{C\neq A} \frac{1}{r_{AB} r_{AC}}\left[18\frac{m_B m_C}{m_A}|\boldsymbol{p}_A|^2 + 14\frac{m_A m_C}{m_B}|\boldsymbol{p}_B|^2\right. \\ &- 2\frac{m_A m_C}{m_B}(\boldsymbol{n}_{AB}\cdot\boldsymbol{p}_B)^2 - 50 m_C(\boldsymbol{p}_A\cdot\boldsymbol{p}_B) + 17 m_A(\boldsymbol{p}_B\cdot\boldsymbol{p}_C) \\ &- 14 m_C(\boldsymbol{n}_{AB}\cdot\boldsymbol{p}_A)(\boldsymbol{n}_{AB}\cdot\boldsymbol{p}_B) + 14 m_A(\boldsymbol{n}_{AB}\cdot\boldsymbol{p}_B)(\boldsymbol{n}_{AB}\cdot\boldsymbol{p}_C) \\ &\left.+ m_A(\boldsymbol{n}_{AB}\cdot\boldsymbol{n}_{AC})(\boldsymbol{n}_{AB}\cdot\boldsymbol{p}_B)(\boldsymbol{n}_{AC}\cdot\boldsymbol{p}_C)\right] \\ &+ \frac{G^2}{8}\sum_A \sum_{B\neq A}\sum_{C\neq A} \frac{1}{r_{AB}^2}\left[2 m_B(\boldsymbol{n}_{AB}\cdot\boldsymbol{p}_A)(\boldsymbol{n}_{AC}\cdot\boldsymbol{p}_C)\right. \\ &\left.+ 2 m_B(\boldsymbol{n}_{AB}\cdot\boldsymbol{p}_B)(\boldsymbol{n}_{AC}\cdot\boldsymbol{p}_C) + \frac{m_A m_B}{m_C}\big(5(\boldsymbol{n}_{AB}\cdot\boldsymbol{n}_{AC})|\boldsymbol{p}_C|^2\right. \end{aligned}$$

[4]The Hamiltonians closely follow those reported by Galaviz and Brügmann (2011), in which we corrected a typo in the fourth to last line of the H_2 term reported below ($r_{AB}^2 \to r_{AB}$).

$$
\begin{aligned}
&- (\boldsymbol{n}_{AB}\cdot\boldsymbol{n}_{AC})(\boldsymbol{n}_{AC}\cdot\boldsymbol{p}_C)^2 - 14(\boldsymbol{n}_{AB}\cdot\boldsymbol{p}_C)(\boldsymbol{n}_{AC}\cdot\boldsymbol{p}_C)\Big)\Big] \\
&+ \frac{G^2}{4}\sum_A\sum_{B\neq A}\frac{m_A}{r_{AB}^2}\left[\frac{m_B}{m_A}|\boldsymbol{p}_A|^2 + \frac{m_A}{m_B}|\boldsymbol{p}_B|^2 - 2(\boldsymbol{p}_A\cdot\boldsymbol{p}_B)\right] \\
&+ \frac{G^2}{2}\sum_A\sum_{B\neq A}\sum_{C\neq A,B}\frac{(n^i_{AB}+n^i_{AC})(n^j_{AB}+n^j_{CB})}{(r_{AB}+r_{BC}+r_{CA})^2}\Big[8m_B(p_{Ai}p_{Cj}) \\
&- 16m_B(p_{Aj}p_{Ci}) + 3m_C(p_{Ai}p_{Bj}) + 4\frac{m_Am_B}{m_C}(p_{Ci}p_{Cj}) + \frac{m_Bm_C}{m_A}(p_{Ai}p_{Aj})\Big] \\
&+ \frac{G^2}{2}\sum_A\sum_{B\neq A}\sum_{C\neq A,B}\frac{m_Am_Bm_C}{(r_{AB}+r_{BC}+r_{CA})r_{AB}}\Bigg[\\
&\quad 8\frac{\boldsymbol{p}_A\cdot\boldsymbol{p}_C - (\boldsymbol{n}_{AB}\cdot\boldsymbol{p}_A)(\boldsymbol{n}_{AB}\cdot\boldsymbol{p}_C)}{m_Am_C} - 3\frac{\boldsymbol{p}_A\cdot\boldsymbol{p}_B - (\boldsymbol{n}_{AB}\cdot\boldsymbol{p}_A)(\boldsymbol{n}_{AB}\cdot\boldsymbol{p}_B)}{m_Am_B} \\
&- 4\frac{|\boldsymbol{p}_C|^2 - (\boldsymbol{n}_{AB}\cdot\boldsymbol{p}_C)^2}{m_C^2} - \frac{|\boldsymbol{p}_A|^2 - (\boldsymbol{n}_{AB}\cdot\boldsymbol{p}_A)^2}{m_A^2}\Bigg] \\
&- \frac{G^3}{2}\sum_A\sum_{B\neq A}\left(\sum_{C\neq A,B}\frac{m_A^2m_Bm_C}{r_{AB}^2r_{BC}} + \frac{1}{2}\sum_{C\neq B}\frac{m_A^2m_Bm_C}{r_{AB}^2r_{BC}}\right) \\
&- \frac{3G^3}{8}\sum_A\sum_{B\neq A}\left(\sum_{C\neq A}\frac{m_A^2m_Bm_C}{r_{AB}^2r_{AC}} + \sum_{C\neq A,B}\frac{m_A^2m_Bm_C}{r_{AB}^2r_{BC}}\right) \\
&- \frac{3G^3}{8}\sum_A\sum_{B\neq A}\sum_{C\neq A,B}\frac{m_A^2m_Bm_C}{r_{AB}r_{AC}r_{BC}} \\
&- \frac{G^3}{64}\sum_A\sum_{B\neq A}\sum_{C\neq A,B}\frac{m_A^2m_Bm_C}{r_{AB}r_{AC}^3r_{BC}}\Bigg[18r_{AC}^2 - 60r_{BC}^2 - 24r_{AC}(r_{AB}+r_{BC}) \\
&+ 60\frac{r_{AC}r_{BC}^2}{r_{AB}} + 56r_{AB}r_{BC} - 72\frac{r_{BC}^3}{r_{AB}} + 35\frac{r_{BC}^4}{r_{AB}^2} + 6r_{AB}^2\Bigg] \\
&- \frac{G^3}{4}\sum_A\sum_{B\neq A}\frac{m_A^2m_B^2}{r_{AB}^3}.
\end{aligned}
\tag{1.4}
$$

where, Latin indices label 3-dimensional vector components (e.g., x_{Ai} indicates the i-th position coordinate of the A-th body), and we have defined

$$
\begin{aligned}
\boldsymbol{r}_{AB} &= \boldsymbol{x}_A - \boldsymbol{x}_B, \\
r_{AB} &= |\boldsymbol{r}_{AB}|, \\
\boldsymbol{n}_{AB} &= \frac{\boldsymbol{r}_{AB}}{r_{AB}}.
\end{aligned}
\tag{1.5}
$$

On the contrary, the dissipative 2.5PN Hamiltonian $H_{2.5}$ must also depend explicitly on time to account for the leading-order back-reaction of GW emission onto the triplet dynamics (this is because otherwise $dH/dt = \partial H/\partial t = 0$,

which would imply energy conservation) and for this reason is slightly trickier to tackle. The dissipative Hamiltonian can be written in the following concise form:

$$H_{2.5} = \frac{G}{45}\chi^{ij}(\boldsymbol{x}_A, \boldsymbol{p}_A)\,\dot{\chi}_{ij}(\boldsymbol{x}_{A'}, \boldsymbol{p}_{A'}), \tag{1.6}$$

where

$$\begin{aligned}\chi_{ij}(\boldsymbol{x}_A, \boldsymbol{p}_A) = &\sum_A \frac{2}{m_A}\left(|\boldsymbol{p}_A|^2\delta_{ij} - 3p_{A,i}p_{A,j}\right)\\ &+ \sum_A \sum_{B\neq A} \frac{Gm_Am_B}{r_{AB}}\left(3n_{AB,i}n_{AB,j} - \delta_{ij}\right),\end{aligned} \tag{1.7}$$

and

$$\begin{aligned}\dot{\chi}_{ij}(\boldsymbol{x}_{A'},&\boldsymbol{p}_{A'}) =\\ &\sum_{A'} \frac{2}{m_{A'}}\Big[2(\dot{\boldsymbol{p}}_{A'}\cdot\boldsymbol{p}_{A'})\delta_{ij} - 3(\dot{p}_{A'i}p_{A'j} + p_{A'i}\dot{p}_{A'j})\Big]\\ &+ \sum_{A'}\sum_{B'\neq A'} \frac{Gm_{A'}m_{B'}}{r_{A'B'}^2}\Big[3(\dot{r}_{A'B'i}n_{A'B'j} + n_{A'B'i}\dot{r}_{A'B'j})\\ &+ (\boldsymbol{n}_{A'B'}\cdot\dot{\boldsymbol{r}}_{A'B'})(\delta_{ij} - 9n_{A'B'i}n_{A'B'j})\Big].\end{aligned} \tag{1.8}$$

Here δ_{ij} is the usual Kronecker delta, while primed quantities denote retarded variables that are not subject to the derivative operators $\partial/\partial\boldsymbol{x}_A$ and $\partial/\partial\boldsymbol{p}_A$ employed in the standard Hamiltonian equations. Primed and unprimed variables are then identified once the derivatives in the equations of motion (eqs. 1.11 and 1.12 below) have been calculated. This implicitly makes $H_{2.5}$ time-dependent, as expected. In more detail, the 2.5PN contribution to the equations of motion reads

$$\begin{aligned}(\dot{\boldsymbol{x}}_A)_{2.5} &= \frac{1}{c^5}\frac{\partial H_{2.5}}{\partial \boldsymbol{p}_A}\\ &= \frac{G}{45c^5}\dot{\chi}_{ij}(\boldsymbol{x}_A, \boldsymbol{p}_A)\frac{\partial}{\partial \boldsymbol{p}_A}\chi^{ij}(\boldsymbol{x}_A, \boldsymbol{p}_A)\end{aligned} \tag{1.9}$$

$$\begin{aligned}(\dot{\boldsymbol{p}}_A)_{2.5} &= -\frac{1}{c^5}\frac{\partial H_{2.5}}{\partial \boldsymbol{x}_A}\\ &= -\frac{G}{45c^5}\dot{\chi}_{ij}(\boldsymbol{x}_A, \boldsymbol{p}_A)\frac{\partial}{\partial \boldsymbol{x}_A}\chi^{ij}(\boldsymbol{x}_A, \boldsymbol{p}_A).\end{aligned} \tag{1.10}$$

Note that in order to have terms not higher than 2.5PN, the time derivatives of the positions and conjugate momenta that appear in the function $\dot{\chi}_{ij}$ should be replaced by their Newtonian limits, i.e., $\dot{\boldsymbol{x}}_A \to \partial H_0/\partial \boldsymbol{p}_A$ and $\dot{\boldsymbol{p}}_A \to -\partial H_0/\partial \boldsymbol{x}_A$.

Finally, the full equations of motion for the A-th body take the usual canonical form,

$$\dot{\boldsymbol{x}}_A = \sum_n \frac{1}{c^{2n}} \frac{\partial H_n}{\partial \boldsymbol{p}_A}, \tag{1.11}$$

$$\dot{\boldsymbol{p}}_A = -\sum_n \frac{1}{c^{2n}} \frac{\partial H_n}{\partial \boldsymbol{x}_A}, \tag{1.12}$$

which, given the rather cumbersome form, we avoid to explicitly report the complete expressions maintaining an implicit notation only. These equations represent one of the key ingredient of our main code appositely design to evolve realistic MBH triplets and that we will present in much more detail in the next chapter.

1.2 Gravitational-wave generation by binary and triple systems

The GW emission from binary systems with relative velocities $v \ll c$ can be modelled, at leading order, through the Einstein quadrupole formula (Einstein, 1918; Landau and Lifshitz, 1975; Blanchet, 2014). Next-to-leading order corrections are given by the mass-octupole and current-quadrupole contributions (Thorne, 1980; Blanchet, 2014). A key requirement implicit in the derivation of the corresponding formulae is that the binary must be contained in its "Near Coordinate Zone" (NCZ), i.e., a region (centred on the origin of the coordinates) of radius comparable to (but smaller than) the GW wavelength λ. This requirement comes about because the PN formalism for GW generation, which can only be legitimately applied as long as the source is much smaller than λ, is based on a systematic multipole expansion of the gravitational field outside the source. In order to ensure an overlap between the domain of validity of this expansion (say $|\boldsymbol{x}| \gtrsim r_{\min}$) and the near zone (where the dynamics of the source is computed neglecting retardation effects), one must clearly have $r_{\min} \sim$ [size of the near zone] $\sim \lambda$, so the coordinate origin and the source cannot be more than one wavelength apart.[5] Indeed, these formulae are usually applied in the reference frame of the binary centre of mass (CoM). In that frame, in the PN regime, the existence of a NCZ containing the binary is guaranteed, since the size of the system — its separation a — is negligible relative to the wavelength $\lambda \sim a/(v/c)$.

For a triple system with relative velocities $v \ll c$, it would seem natural to apply the very same formulae in the reference frame of the CoM of the three-body system. However, by doing so, one obtains unphysical results such as

[5] Nevertheless, the exact choice of where the NCZ is centred is a matter of definition. The important point is that it must contain both the whole source and the origin of the coordinates. In fact, one may alternatively think in terms of the binary near zone, which is defined to be (roughly) centred on the CoM of the binary. In that case, a proper derivation of the quadrupole formula would require choosing the origin within the near zone. The adoption of this point of view would not alter any of the discussions of this chapter.

those reported in fig. 18 of Galaviz and Brügmann (2011), as we will now explain. Indeed, we have reproduced the same behaviour by applying the quadrupole and "quadrupole-octupole" formulae in the CoM reference frame of a series of triple systems with mass ratios $m_2/m_1 = 0.5$ and $m_3/(m_1+m_2) = 0.05$, whose trajectories are computed with the 1PN and 2PN conservative triple dynamics, and the leading order dissipative dynamics as described in section 1.1. The "inner binary" (comprised of m_1 and m_2) of these hierarchical triplets has zero initial eccentricity and an initial separation $a_{\rm in} = 150Gm_t/c^2$, with m_t the total mass of the triplet (throughout this chapter we instead reserve the symbol m to indicate the total mass of binary systems, i.e., $m = m_1+m_2$). The "outer binary" (comprised of m_3 and the CoM of the inner binary) has instead initial separation varying in the range $a_{\rm out} \in [625, 10000]Gm_t/c^2$, and zero initial eccentricity. The results are displayed in fig. 1.1, where one can observe, paradoxically, that the effect induced by the third body grows as it gets farther away from the inner binary. In this chapter, we will analyse this situation in detail and show that the problem is connected to the fact that a NCZ region centred on the CoM of the triplet and having size comparable to the minimum gravitational wavelength excited by the system does *not* include the whole triplet, unlike what happens for a binary system.

This, however, is just one example of the subtleties one should be aware of when computing GW emission from binary or triple systems in a too naive fashion. Another interesting apparent paradox arises, e.g., if one tries to compute the gravitational waveforms of a binary (or triple) system by directly integrating the equations for the linear perturbations $h_{\mu\nu}$ over a background Minkowski space-time (endowed with a flat metric $\eta_{\mu\nu} = \text{diag}(-1, 1, 1, 1)$ and coordinates $\{x^\mu\}_{\mu=0,1,2,3}$).

In the harmonic gauge, which is defined by the condition $\partial_\mu \bar{h}^{\mu\nu} = 0$, where ∂_μ is the flat four-dimensional derivative and $\bar{h}^{\mu\nu} = h^{\mu\nu} - 1/2\, \eta^{\mu\nu} h^\alpha{}_\alpha$ represents the trace-reversed metric perturbation,[6] the linearised Einstein equations read (see, e.g., Maggiore, 2007; Misner, Thorne, and Wheeler, 1973)

$$\Box_{\rm flat} \bar{h}^{\mu\nu} = -\frac{16\pi G}{c^4} T^{\mu\nu} \,, \tag{1.13}$$

where the d'Alembert operator $\Box_{\rm flat} = \eta^{\mu\nu}\partial_\mu\partial_\nu$ is computed with the background Minkowski metric and $T^{\mu\nu}$ is the source stress-energy tensor. These equations can be integrated exactly by using the (retarded) Green function of $\Box_{\rm flat}$. The resulting waveforms (obtained from the transverse trace-free part of the spatial components) may then be compared to those predicted by the quadrupole formula (and its higher-order corrections that we have mentioned above).

[6] In our conventions, space-time Greek indices are raised or lowered with the metric $\eta_{\mu\nu}$ or its inverse $\eta^{\mu\nu}$, whereas space Latin indices are raised or lowered with the Euclidean metric δ_{ij} or its inverse δ^{ij}. In particular: $h^{\mu\nu} = \eta^{\mu\alpha}\eta^{\nu\beta}h_{\alpha\beta}$ and $h^\alpha{}_\alpha = \eta^{\alpha\beta}h_{\alpha\beta}$.

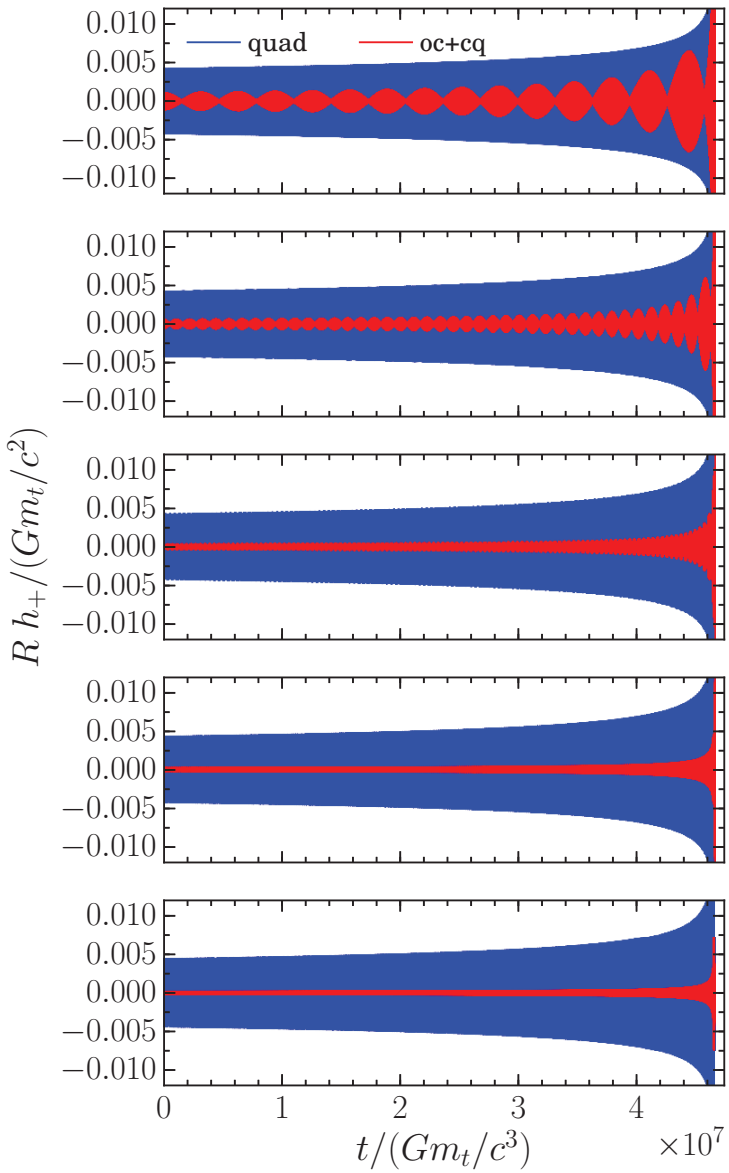

Figure 1.1: Waveforms from five triple systems with relative inclination $i = 0$, inner separation $a_{\rm in} = 150Gm_t/c^2$, inner eccentricity $e_{\rm in} = 0$, outer eccentricity $e_{\rm out} = 0$, and mass ratios $m_2/m_1 = 0.5$ and $m_3/(m_1 + m_2) = 0.05$. From top to bottom $a_{\rm out} = [10000, 5000, 2500, 1250, 625]Gm_t/c^2$. The observer is located in the xz plane of a fixed spatial frame (x, y, z), with spherical coordinates $\theta = \pi/4$, $\phi = 0$. To be compared with Galaviz and Brügmann (2011), fig. 18. As in Galaviz and Brügmann (2011), the orbits are obtained by integrating numerically the Hamilton equations for the triple systems, through the 2PN order in the conservative dynamics and at the leading (Newtonian) order in the dissipative one.

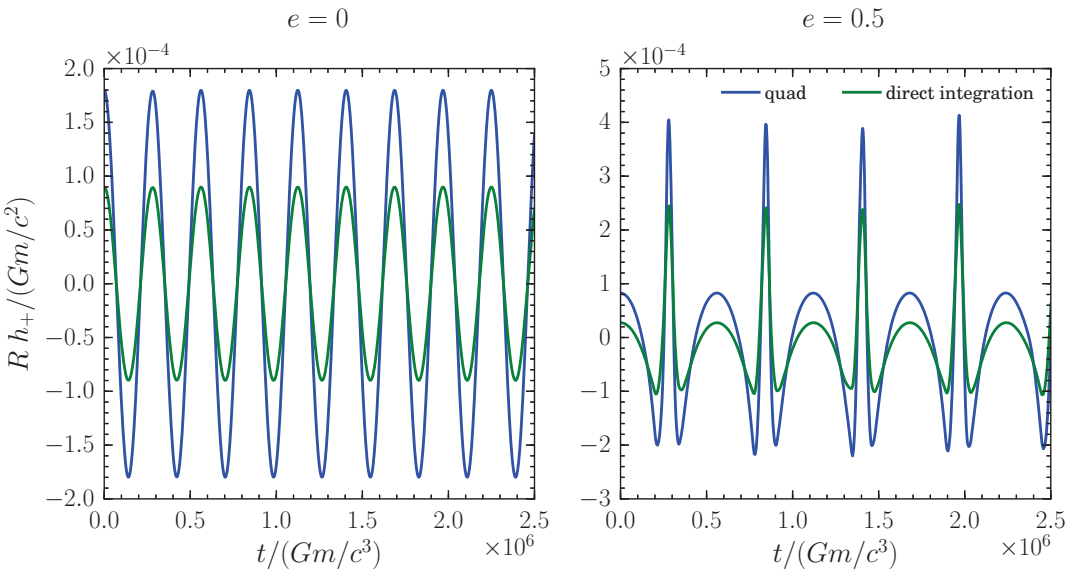

Figure 1.2: Quadrupole waveforms from two simulations of circular binaries with masses $m_1 = 0.9m$, $m_2 = 0.1m$. Blue lines are obtained with the quadrupole formula (see eq. 1.14); green lines are computed by direct integration of eq. 1.13. *Left panel*: circular case. *Right panel*: $e = 0.5$.

The comparison between the GW amplitudes obtained with the two procedures for various binaries is shown in fig. 1.2. As can be seen, there appears to be a factor ~ 2 discrepancy (this factor becomes exactly 2 for binary in circular orbits). Similar discrepancies arise when integrating eq. 1.13 for triple systems. This puzzling difference will be discussed in more details. It is related to the fact, often mentioned but rarely illustrated in introductory GR textbooks (see however Maggiore, 2007; Misner, Thorne, and Wheeler, 1973), that a naive derivation of the quadrupole formula based on eq. 1.13 is wrong. It is because that equation (via the harmonic gauge condition) implies that $\partial_\mu T^{\mu\nu} = 0$, which is clearly not verified for a binary system since it entails that bodies move along straight lines.

In the following sections, we will discuss the two problems mentioned above as well as other subtleties that we have encountered when computing gravitational waveforms from numerically-integrated orbits of binary and triple systems.

1.2.1 Emission of gravitational waves in hierarchical triplets

The leading-order contribution to the GW signal observed at space position $\boldsymbol{x}$ and time t is given, in an appropriate "radiative" gauge, by the quadrupole formula (see, e.g., Misner, Thorne, and Wheeler, 1973; Maggiore, 2007; Blanchet, 2014)

$$h_{ij}^{\mathrm{TT}}(t, \boldsymbol{x}) = \frac{2G}{Rc^4} \Lambda_{ijkl}(\boldsymbol{n}) \, \frac{\mathrm{d}^2 M^{kl}(t_{\mathrm{ret}})}{\mathrm{d}t^2} + \mathcal{O}\Big(\frac{1}{c^5}\Big) \,, \tag{1.14}$$

where $R = |\boldsymbol{x}| \equiv \sqrt{x^i x_i}$ is the distance of the observer (assumed to be very far from the source compared with the wavelength λ of the emitted GWs), $t_{\rm ret} = t - R/c$ is the retarded time of the background space-time,[7] $\Lambda_{ijkl}(\boldsymbol{n})$ denotes the projector on the transverse-traceless (TT) gauge (see Appendix A for the explicit definition), while

$$M^{ij}(t) = \int \mathrm{d}^3\boldsymbol{x}'\, c^{-2} T^{00}(t, \boldsymbol{x}') \left(x'^i x'^j - \frac{1}{3}\delta^{ij} x'^k x'_k \right) \tag{1.15}$$

represents the mass quadrupole moment of the source. As mentioned in the introduction, implicit in the derivation of the quadrupole formula (eq. 1.14) is the assumption that the source be contained in its NCZ (see, e.g., Misner, Thorne, and Wheeler, 1973; Press, 1977; Maggiore, 2007), i.e., the reference frame in which the quadrupole moment (eq. 1.15) is evaluated must be such that the source be contained within a region of size $\sim \lambda$ centred on the origin of the coordinates. Finding a frame satisfying this property is always possible for slowly moving binary systems, since λ is related to the system typical (relative) velocity v and its typical separation a by $\lambda \sim a/(v/c)$.

The most natural reference frame to describe the dynamics of an N-body system is that of the CoM, where the equations of motion take their simplest form. (Note that the usual Newtonian expression of the CoM position in terms of the body locations $\boldsymbol{x}_1$, $\boldsymbol{x}_2$ for a binary, namely $\boldsymbol{r}_0 = (m_1\boldsymbol{x}_1 + m_2\boldsymbol{x}_2)/m$, is modified beyond the leading order.[8]) In the case under consideration here (i.e., a three-body system), a particularly interesting configuration is that of the so-called hierarchical triplet. The latter is comprised of an inner close binary (m_1, m_2), supplemented by a third body m_3 at larger distance. From the point of view of the dynamics, the choice of the reference frame is of course irrelevant. Indeed, the Hamiltonian (both at the Newtonian order and when including the PN corrections) depends only upon the relative separations of the three bodies, hence the dynamics of the system is frame-independent (see e.g., Goldstein, 1950). However, caution must be exercised when applying the quadrupole formula (eq. 1.14) (and its higher-order generalizations including octupolar corrections, etc.) to the orbits resulting from numerical integrations of the equations of motion (see fig. 1.1 and related discussion).

[7] Note that t as appearing in eq. 1.14 should rigorously be replaced by the radiative time $T = t - 2GM/c^3 \ln[R/(cb)]$, with M being the total Arnowitt-Deser-Misner energy-mass (Arnowitt, Deser, and Misner, 1959) and b representing an additive constant that defines a reference time (i.e., how the "zero" of the time axis has been chosen). It is crucial to do so at future radiative infinity. However, since $2GM/c^3 \ln[R/(cb)] \ll R/c$, we may write $T \approx t$ for sufficiently large R if t remains bounded. See Blanchet (2002) for more details, in particular on how the logarithmic term is connected to the tail contribution to the waveform.

[8] The fact that the time derivative of the CoM position must be constant implies that the latter variable must be constructed in relation to a Noetherian current. In special relativity, this current, $\boldsymbol{r}_0 - t\dot{\boldsymbol{r}}_0$, is nothing but the conserved quantity associated with the invariance of the dynamics under Lorentz boosts. Thus, the usual Newtonian definition has to be modified, the masses being replaced, notably, by the total energies of the bodies (see, e.g., Landau and Lifshitz, 1975). A similar extension of the Newtonian concept of CoM applies in GR (see, e.g., Landau and Lifshitz, 1975). We refer to Damour and Schäfer (1985) and Georg and Schäfer (2015) for an explicit construction in the case of binary systems.

To illustrate this point, let us consider a circular binary located "far" from the origin of the coordinates. In triple systems, this happens for the inner binary when $m_3 a_{\rm out} \gg (m_1+m_2+m_3)a_{\rm in}$ since, in this case, the inner binary is located far away from the CoM *of the triplet* chosen as the origin of the coordinates. Setting the GW source in the xy plane and the observer along the z axis, eq. 1.14 takes the simplest possible form, i.e.,

$$h_{ij}^{\rm TT}(t,\boldsymbol{x}) = \frac{2G}{Rc^4}\begin{pmatrix} \frac{1}{2}[\ddot{M}_{11}(t_{\rm ret}) - \ddot{M}_{22}(t_{\rm ret})] & \ddot{M}_{12}(t_{\rm ret}) & 0 \\ \ddot{M}_{12}(t_{\rm ret}) & -\frac{1}{2}[\ddot{M}_{11}(t_{\rm ret}) - \ddot{M}_{22}(t_{\rm ret})] & 0 \\ 0 & 0 & 0 \end{pmatrix}, \tag{1.16}$$

where the dots placed over the quadrupole components M_{ij} represent time derivatives. The two independent polarizations of a propagating GW, referred to as the "plus" and "cross" polarizations, are (in the situation considered here) simply the diagonal and off-diagonal part of eq. 1.16:

$$\begin{aligned}(h_+)_{\rm quad} &= \frac{G}{Rc^4}(\ddot{M}_{11} - \ddot{M}_{22}),\\ (h_\times)_{\rm quad} &= \frac{2G}{Rc^4}\ddot{M}_{12}\,,\end{aligned} \tag{1.17}$$

where all M_{ij} components are evaluated at retarded time. Explicitly, for a binary these expressions become (see, e.g., Problem 3.2 of Maggiore, 2007)

$$\begin{aligned}(h_+)_{\rm quad} &= \frac{4G^2 m_1 m_2}{aRc^4}\cos(2\omega t_{\rm ret}),\\ (h_\times)_{\rm quad} &= \frac{4G^2 m_1 m_2}{aRc^4}\sin(2\omega t_{\rm ret})\,,\end{aligned} \tag{1.18}$$

a denoting the separation of the binary and ω its orbital frequency.

Let us now consider two different circular binaries, both with $m_1 = 0.9m$ and $m_2 = 0.1m$ but representative of two different regimes: a rather relativistic binary with separation $a = 20Gm/c^2$, which corresponds to a relative orbital velocity $v/c \simeq 0.2$, and a mildly-relativistic one, with $a = 2000Gm/c^2$ (corresponding to $v/c \simeq 0.02$). For these two systems, eq. 1.18 gives $Rc^2/(Gm)(h_+)_{\rm quad} \simeq 1.8\times10^{-2}$ and $Rc^2/(Gm)(h_+)_{\rm quad} \simeq 1.8\times10^{-4}$, respectively. We then evolve them numerically in two different frames: (1) one with the origin coinciding with the CoM, and (2) one with the origin shifted by 10^5 gravitational radii (i.e., $10^5 \times Gm/c^2$) from the CoM. Next, we compute the waveforms directly via eq. 1.17 from the numerical trajectories. Results are reported in fig. 1.3 as dashed lines. The mildly-relativistic case is consistent with the analytic predictions of eq. 1.18. Instead, for the relativistic binary, $(h_+)_{\rm quad}$ given by eq. 1.17 is more than one order of magnitude higher than the prediction from eq. 1.18 *when the origin of coordinates is far away from the CoM*. Indeed, we have checked that applying eq. 1.17 directly to numerically-integrated trajectories yields results that are coordinate-dependent. The discrepancy with eq. 1.18 grows with the binary relative velocity.

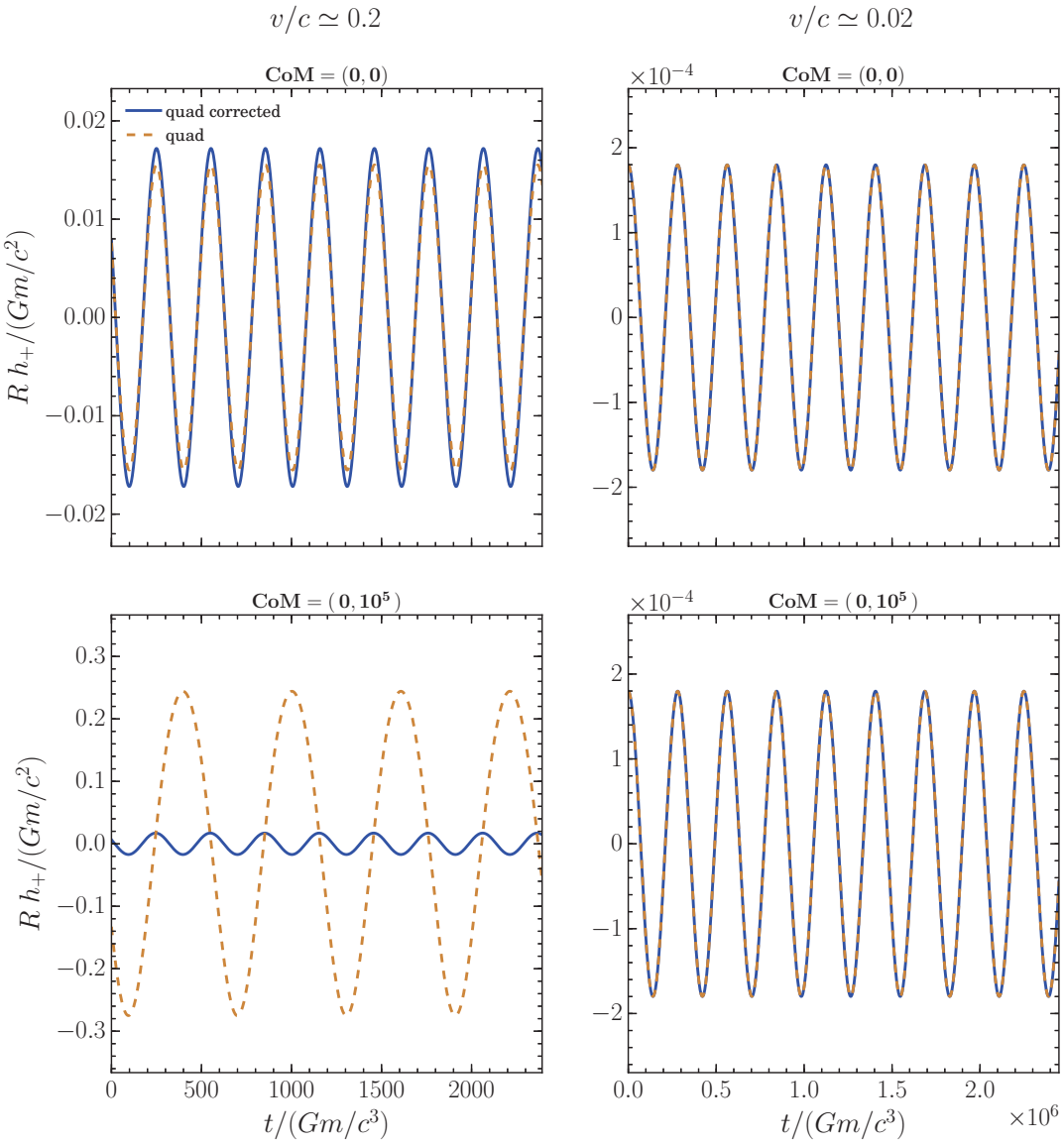

Figure 1.3: Quadrupole waveforms from four simulations of circular binaries with masses $m_1 = 0.9m$, $m_2 = 0.1m$ evolving according to the 1PN dynamics. *Left panels*: highly relativistic regime $v/c \simeq 0.2$. *Right panels*: mildly relativistic regime $v/c \simeq 0.02$. *Upper panels*: The binary CoM is placed in the origin of coordinates. *Lower panels*: The binary CoM is located at distance $10^5 \times Gm/c^2$ from the origin. The dashed lines represent quadrupole waveforms computed by simply inserting the trajectories of our simulations in eq. 1.14, while the solid blue lines are waveforms obtained from an "amended" quadrupole formula (see text for details). The "standard" quadrupole formula fails in the most relativistic and shifted binary case, whereas the amended one provides the correct result in all cases (note the different y-axis scales in the two left panels).

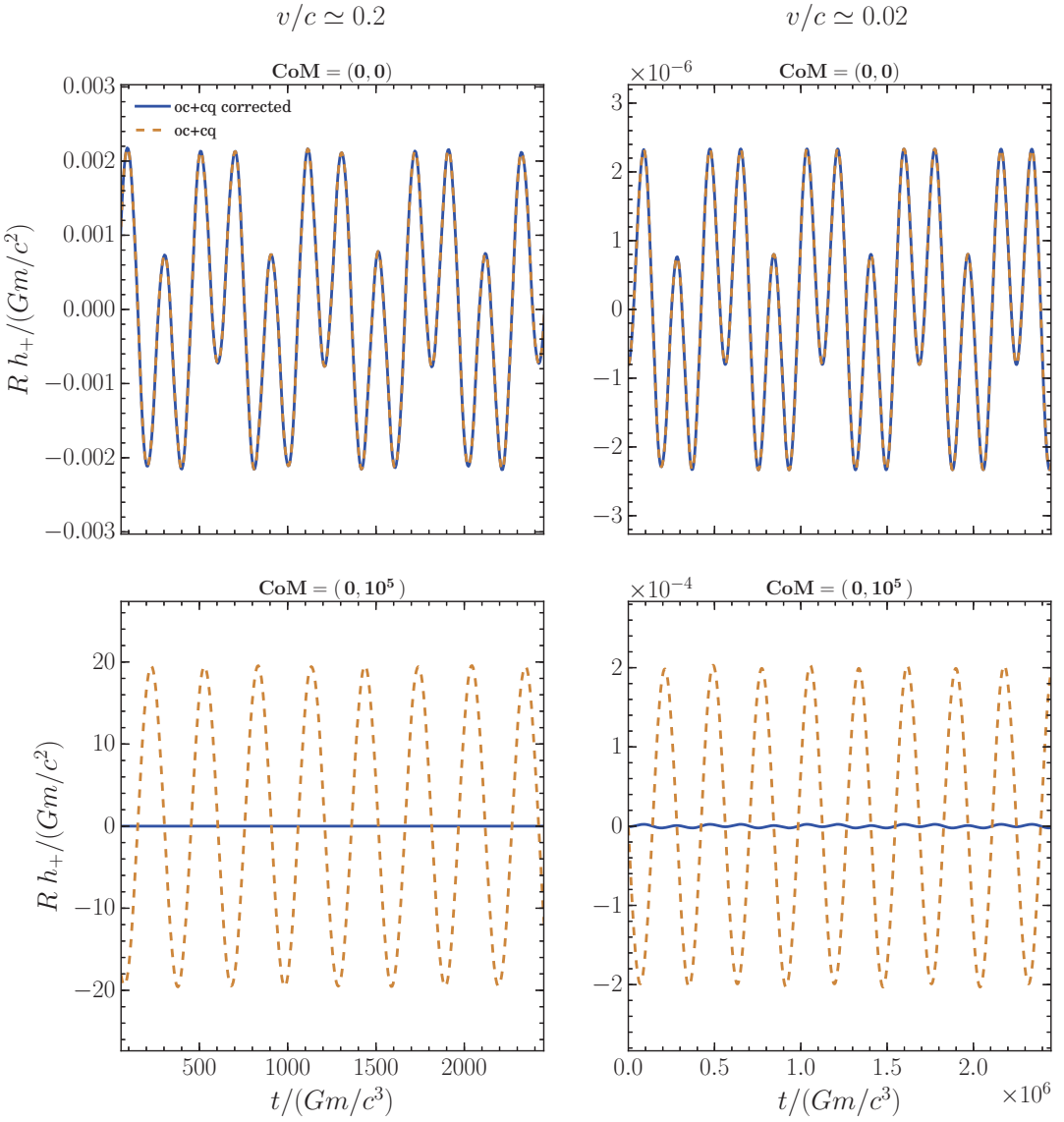

Figure 1.4: Same as in fig. 1.3, except that we report the waveforms computed with the mass octupole and current quadrupole corrections (at the 0.5PN order) whereas the observer is located on the y axis. Again, note the different y-axis scales between the upper and lower panels for each value of v/c.

Let us consider now the next-to-leading order contributions to the waveform, comprised of a mass octupole and a current quadrupole term. When these terms are taken into account, eq. 1.14 becomes (see Maggiore, 2007)

$$h_{ij}^{\mathrm{TT}}(t,\boldsymbol{x}) = \frac{2G}{Rc^4}\Lambda_{ijkl}(\boldsymbol{n})\left[\frac{\mathrm{d}^2 M^{kl}}{\mathrm{d}t^2} + \frac{n_m}{3c}\left(\frac{\mathrm{d}^3 M^{klm}}{\mathrm{d}t^3} + 2\frac{\mathrm{d}^2 S^{klm}}{\mathrm{d}t^2}\right)\right] + \mathcal{O}\left(\frac{1}{c^6}\right), \tag{1.19}$$

where $\boldsymbol{n} = \boldsymbol{x}/R$, and M^{klm}, S^{klm} are respectively the Newtonian octupole and current quadrupole moments (evaluated at $t_{\rm ret}$ [see Appendix A]). Again, for a binary in the xy plane and an observer in the same plane,[9] the above equation implies (see Problem 3.3 of Maggiore, 2007, and the corresponding erratum)

$$(h_+)_{\rm oc+cq} = \frac{1}{R}\frac{G^{5/2} m_1 m_2 \delta m}{4(ma^3)^{1/2}c^5}\left[5\cos(\omega t_{\rm ret}) - 9\cos(3\omega t_{\rm ret})\right],$$
$$(h_\times)_{\rm oc+cq} = 0\,, \tag{1.20}$$

with $\delta m = m_1 - m_2$. For the two binaries considered above, we obtain $Rc^2/(Gm)(h_+)_{\rm oc+cq} \simeq 2.2\times10^{-3}$ in the relativistic case, and $Rc^2/(Gm)(h_+)_{\rm oc+cq} \simeq 2.2\times10^{-6}$ in the mildly relativistic one. From fig. 1.4 (dashed lines), we can see that if the origin of the coordinates coincides with the CoM, then $(h_+)_{\rm oc+cq}$ as given by eq. 1.19 applied to the numerically-integrated orbits agrees well with the analytic result of eq. 1.20. Conversely, if one shifts significantly the origin of the coordinates, $(h_+)_{\rm oc+cq}$ computed from the numerical trajectories no longer agrees with eq. 1.20, even for the mildly-relativistic binary.

In the next two sections, we will analyse the reasons behind these discrepancies and explain how they can be avoided, first for the Newtonian quadrupole formula and next for the 0.5PN quadrupole formula with octupolar corrections.

Quadrupole waveform

If we explicitly compute the second-order time derivatives in eq. 1.14, for a binary system, we obtain

$$h_{ij}^{\rm TT}(t,\boldsymbol{x}) = \frac{2G}{Rc^4}\Lambda_{ijkl}(\boldsymbol{n})\Big(2m_1\dot{x}_1^k\dot{x}_1^l + 2m_2\dot{x}_2^k\dot{x}_2^l + m_1(\ddot{x}_1^k x_1^l + x_1^k\ddot{x}_1^l) + m_2(\ddot{x}_2^k x_2^l + x_2^k\ddot{x}_2^l)\Big) + \mathcal{O}\Big(\frac{1}{c^5}\Big)\,. \tag{1.21}$$

Now, the position vectors of the two masses can be expressed in terms of the CoM position $\boldsymbol{r}_0$ and the relative separation vector $\boldsymbol{r} = \boldsymbol{x}_1 - \boldsymbol{x}_2$ as

$$\boldsymbol{x}_1 = \boldsymbol{r}_0 + \frac{m_2}{m}\boldsymbol{r}\,, \qquad \boldsymbol{x}_2 = \boldsymbol{r}_0 - \frac{m_1}{m}\boldsymbol{r}\,. \tag{1.22}$$

so that eq. 1.21 takes the form

$$h_{ij}^{\rm TT}(t,\boldsymbol{x}) = \frac{2G}{Rc^4}\Lambda_{ijkl}(\boldsymbol{n})\Big[\frac{2}{m}(m_1\dot{x}_1^k + m_2\dot{x}_2^k)(m_1\dot{x}_1^l + m_2\dot{x}_2^l) + \frac{2m_1m_2}{m}(\dot{x}_1^k - \dot{x}_2^k)(\dot{x}_1^l - \dot{x}_2^l) + r_0^k(m_1\ddot{x}_1^l + m_2\ddot{x}_2^l) + r_0^l(m_1\ddot{x}_1^k + m_2\ddot{x}_2^k) + \frac{m_1m_2}{m}\Big(r^k(\ddot{x}_1^l - \ddot{x}_2^l) + r^l(\ddot{x}_1^k - \ddot{x}_2^k)\Big)\Big] + \mathcal{O}\Big(\frac{1}{c^5}\Big)\,. \tag{1.23}$$

[9] We choose the observer in the xy plane rather than in the z direction because the mass octupole and current quadrupole corrections vanish with the latter choice.

Since the CoM absolute coordinates $\boldsymbol{r}_0$ explicitly appears in this expression, it would seem that the GW amplitude should depend on the choice of the origin of the coordinate system. However, because eq. 1.23 is only correct at leading order in PN theory, it is actually sufficient to compute the accelerations $\ddot{\boldsymbol{x}}_1$ and $\ddot{\boldsymbol{x}}_2$ at leading (i.e., Newtonian) order. If one does so, the identity $m_1\ddot{\boldsymbol{x}}_1 + m_2\ddot{\boldsymbol{x}}_2 = 0$ holds for an isolated system, hence the dependence on the position of the centre of mass (and thus on the location of the origin) disappears from eq. 1.23. Similarly, $m_1\dot{x}_1^k + m_2\dot{x}_2^k$ is constant and independent of the location of the origin.

One may want, however, to integrate the binary equations of motion to higher PN order, either analytically or numerically. Now, when one includes these PN corrections, $m_1\ddot{\boldsymbol{x}}_1 + m_2\ddot{\boldsymbol{x}}_2 \neq 0$ already at 1PN order, so that the dependence on the location of the origin does *not* disappear. This is the reason of the unphysical behaviour visible in fig. 1.3 (and partly in fig. 1.1, see also the next section).

A first solution can be therefore to avoid the use of the numerical trajectories to compute the accelerations in eq. 1.23, but instead evaluate them directly from the positions of the two bodies by using the Newtonian dynamics (i.e., Newton's second law, which ensures $m_1\ddot{\boldsymbol{x}}_1 + m_2\ddot{\boldsymbol{x}}_2 = 0$). Alternatively, one can note that the combination $m_1\ddot{\boldsymbol{x}}_1 + m_2\ddot{\boldsymbol{x}}_2$ is simply (at Newtonian order) the time derivative of the total linear momentum $\boldsymbol{P}_{\rm N} = m_1\dot{\boldsymbol{x}}_1 + m_2\dot{\boldsymbol{x}}_2$. Thus, the identity $m_1\ddot{\boldsymbol{x}}_1 + m_2\ddot{\boldsymbol{x}}_2 = 0$ just reflects the conservation of $\boldsymbol{P}_{\rm N}$, which is an automatic consequence of the Newtonian dynamics. Beyond it, when PN corrections are included, $m_1\ddot{\boldsymbol{x}}_1 + m_2\ddot{\boldsymbol{x}}_2$ does not vanish, because the Newtonian linear momentum $\boldsymbol{P}_{\rm N} = m_1\dot{\boldsymbol{x}}_1 + m_2\dot{\boldsymbol{x}}_2$ is no longer a conserved quantity. This is what causes the dependence on the choice of $\boldsymbol{r}_0$ observed in fig. 1.3. However, one can exploit the fact that there exists a conserved PN linear momentum $\boldsymbol{P}_{n\rm PN}$ generalizing $\boldsymbol{P}_{\rm N}$ at the nPN order. In practice, replacing $\boldsymbol{P}_{\rm N}$ with $\boldsymbol{P}_{n\rm PN}$ is equivalent to computing the accelerations appearing in eq. 1.23 as $\ddot{\boldsymbol{x}}_i = \boldsymbol{\pi}_i/m_i$, with $i = 1, 2$ and $\boldsymbol{\pi}_i$ denoting the conjugate momentum of each body entering the Hamilton equations. Then, the combination $m_1\ddot{\boldsymbol{x}}_1 + m_2\ddot{\boldsymbol{x}}_2$ always vanishes, even if PN corrections are included in the Hamiltonian dynamics.

In conclusion, either of these two workarounds (which give rise to the "amended" waveforms represented by blue solid lines in fig. 1.3) is sufficient to eliminate the unphysical dependence on the origin of the coordinates.

Octupole and Current Quadrupole waveforms

Let us now examine what happens to the contribution of the mass octupole and current quadrupole moments to the waveform under a change of reference frame of the form of eq. 1.22. After expanding the time derivatives appearing in the term $n_m/(3c)\,(\dddot{M}^{klm} + 2\ddot{S}^{klm})$ of eq. 1.19 by means of the Leibniz rule, the dependence on the CoM location does not cancel out in the waveform, but gives instead a contribution[10]

[10]Note that we have neglected terms $\propto \delta^{ij}$ in the sum as they disappear when they are TT-projected since $\Lambda_{ijkl}(\boldsymbol{n})\delta^{kl} = 0$ (see Appendix A).

$$\delta_{r_0} h_{ij}^{\rm TT} = \Lambda_{ijkl}(\boldsymbol{n}) \frac{n_m r_0^m}{3c} \sum_A m_A \left(3 \dddot{x}_A^k x_A^l + 3 x_A^k \dddot{x}_A^l + 9 \ddot{x}_A^k \dot{x}_A^l + 9 \dot{x}_A^k \ddot{x}_A^l \right) . \tag{1.24}$$

This may be rewritten as

$$\delta_{r_0} h_{ij}^{\rm TT} = \Lambda_{ijkl}(\boldsymbol{n}) \frac{{\rm d}^3 M^{kl}}{{\rm d}t^3} \frac{\delta R}{c} , \tag{1.25}$$

with $\delta R = \boldsymbol{n} \cdot \boldsymbol{r}_0 = n_m r_0^m$. Hence, the terms proportional to $\boldsymbol{r}_0$ produced by the mass octupole and current quadrupole moments can be reabsorbed in a shift $\delta R/c$ of the retarded time at which the (quadrupole) waveform is evaluated:

$$\begin{aligned} &\Lambda_{ijkl}(\boldsymbol{n}) \left[\frac{{\rm d}^2 M^{kl}(t - R/c)}{{\rm d}t^2} + \frac{{\rm d}^3 M^{kl}(t - R/c)}{{\rm d}t^3} \frac{\delta R}{c} \right] \\ &\qquad = \Lambda_{ijkl}(\boldsymbol{n}) \left[\frac{{\rm d}^2 M^{kl}(t - R/c + \delta R/c)}{{\rm d}t^2} \right] + \mathcal{O}\left(\frac{[\delta R]^2}{c} \right) . \end{aligned} \tag{1.26}$$

This time shift simply enforces the invariance of the waveform under translations of the reference frame in which it is computed. Indeed, the retarded time is always, by definition, $t_{\rm ret} = t - |\mathbf{x}|/c$ in the generic frame $(t, \boldsymbol{x})$ (assuming radiative coordinates), where $R = |\boldsymbol{x}|$ is the distance between the observer at position $\boldsymbol{x}$ and the origin. This implies in particular that $t_{\rm ret} - t_{\rm ret}^{\rm CoM} = |\boldsymbol{x}^{\rm CoM}|/c - |\boldsymbol{x}|/c = -\delta R/c + \mathcal{O}([\delta R]^2/c)$, where the quantities labelled with the superscript CoM are referring to the CoM frame. On the other hand, the expressions of the multipole moments when $\boldsymbol{r}_0 \neq \boldsymbol{0}$ differ from their standard forms in CoM coordinates. Obviously, the modifications of $t_{\rm ret}$ and those of the multipole moments must (and do!) compensate each other so that the GW signal remains invariant, irrespective of the choice of the origin of the coordinates. This main conclusion remains true for linearly propagating waves when other multipole moments are taken into account:[11]

$$\begin{aligned} &h_{ij}^{\rm TT}[\{M_{ab}, M_{abc}, ..., S_{abc}, ...\}, t, \boldsymbol{x}] = \\ &\qquad\qquad h_{ij}^{\rm TT}[\{M_{ab}^{\rm CoM}, M_{abc}^{\rm CoM}, ..., S_{abc}^{\rm CoM}, ...\}, t, \boldsymbol{x}^{\rm CoM}] . \end{aligned} \tag{1.27}$$

However, the analytic "resummations" needed for the above argument to work, such as the one in eq. 1.26, are based on a Taylor expansion. Therefore, one has to implicitly assume that terms like those in eq. 1.24 are "small" or, more precisely, that the displacement $|\boldsymbol{r}_0|$ of the CoM from the origin of the coordinates is much smaller than the wavelength of the quadrupole waveform,

[11] Beyond linear order, one must replace the source moments M_{ab}, M_{abc}, ..., S_{abc} in eq. 1.27 by the so-called "radiative moments" which parametrize the gravitational waveform.

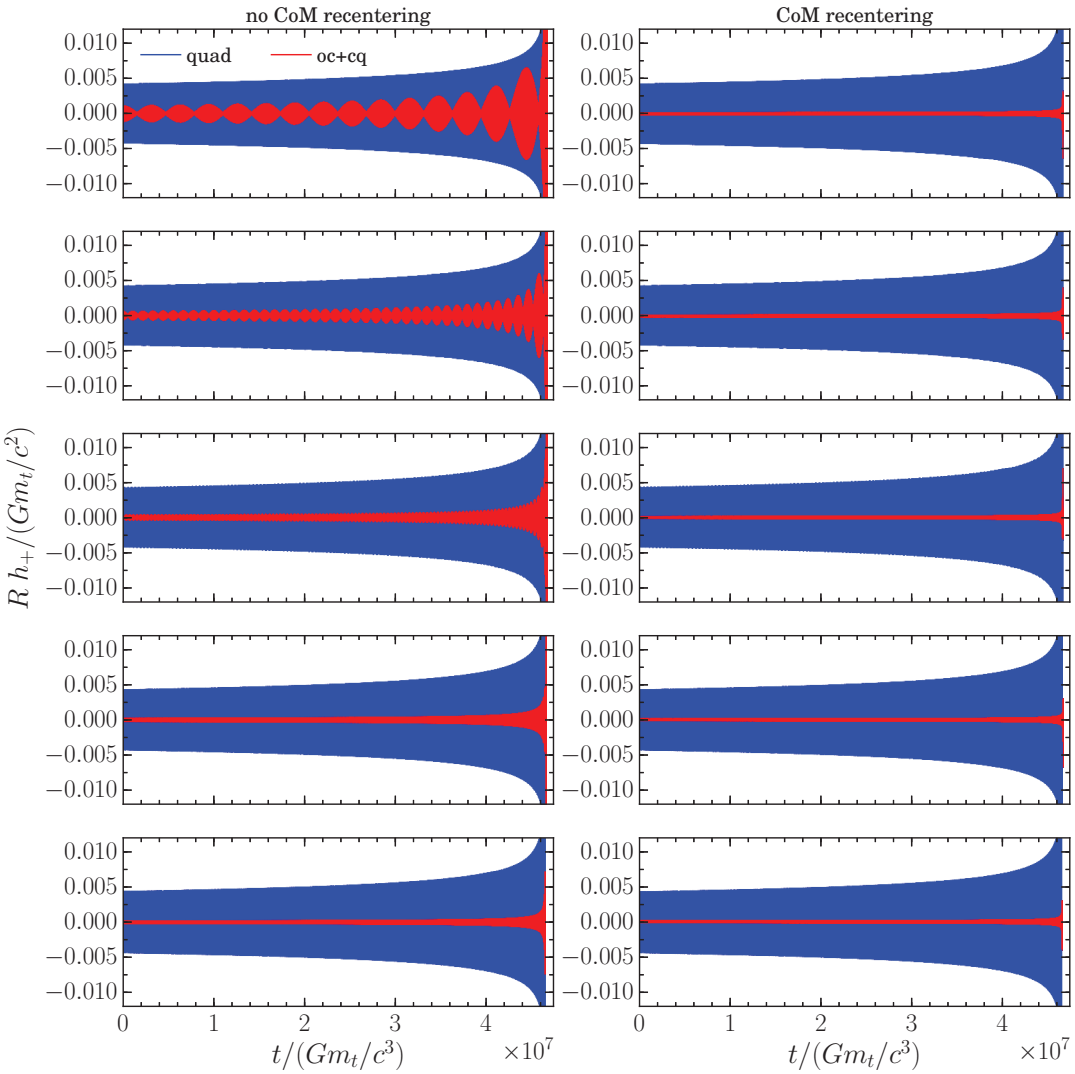

Figure 1.5: Same triplets as in fig. 1.1. *Left*: Waveform computed in the frame of the triplet CoM. *Right*: Waveform computed after shifting the origin to the CoM of the inner binary. Again to be compared to Galaviz and Brügmann (2011), fig. 18.

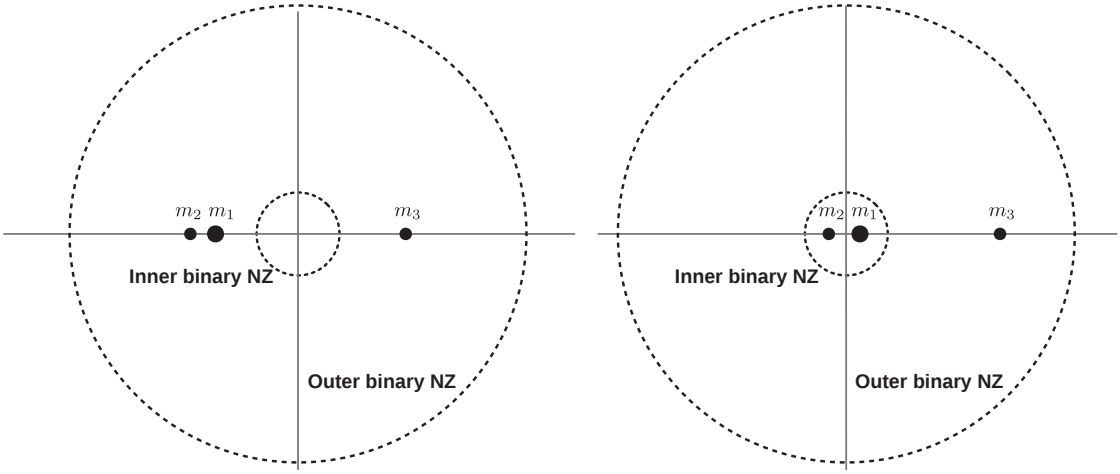

Figure 1.6: Cartoon representation of the change of reference frame needed to fix the unphysical spurious behaviour shown in fig. 1.1. *Left panel*: the origin of the reference frame coincides with the CoM of the triple system. *Right panel*: the origin instantaneously coincides with the inner binary CoM. The latter choice allows both the inner and outer binaries to lie well within their respective NCZs.

$\lambda = \pi c/\omega$. This is in fact very natural because, as already mentioned, one of the assumptions implicit in the derivation of the quadrupole/octupole formulae is that the source be well contained in a NCZ of size $\sim \lambda$ centred on the origin of the coordinates, where retardation effects are negligible. If the generalized quadrupole formula is applied to systems for which the source is *not* well contained in its NCZ, one will *not* be able to resum the terms of eq. 1.24 into a time shift. This is the origin of the discrepancy shown in fig. 1.4 for binary systems.

This observation also highlights the reason of the unphysical behaviour shown in fig. 1.5 (left panels) for *triple* systems. In fact, for a weakly/mildly relativistic binary ($v \lesssim c$) with separation a, one has $\lambda \sim a/(v/c) \gtrsim a$, i.e., if one chooses the origin of the coordinates to coincide with the binary CoM, the NCZ will always contain the binary. For a hierarchical triple system, instead, if one sets the origin at the location of the triplet CoM, the inner binary will be *outside* its NCZ provided that the separation of the outer binary is sufficiently large. This may be understood by noting that there are actually two NCZs for a hierarchical triplet, i.e., an inner-binary NCZ with size $\lambda_{\rm in} \sim a_{\rm in}/(v_{\rm in}/c)$, and an outer-binary NCZ with size $\lambda_{\rm out} \sim a_{\rm out}/(v_{\rm out}/c)$, as illustrated in fig. 1.6. Clearly, while the outer binary will always be contained in its NCZ if $v_{\rm out}/c \lesssim 1$, the inner binary will eventually be outside its NCZ if $a_{\rm out}$ is sufficiently large. Indeed, as $a_{\rm out}$ increases, the inner binary CoM ends up leaving its own NCZ (which is centred on the origin of the coordinates, i.e. on the triplet CoM).

A simple fix to this issue, as shown in fig. 1.6, is thus to evaluate the multipole moments in an *inertial* reference frame with origin instantaneously coinciding with the CoM of the *inner binary*[12], which allows both the inner

[12]Clearly, this reference frame cannot be co-moving with the CoM of the inner binary (which

and outer binaries to lie within their respective NCZs. In the right panels of fig. 1.5, we show that this eliminates the unphysical behaviour of fig. 1.1 and left panels of fig. 1.5. Therefore, the problem exhibited by those figures (and the corresponding results of fig. 18 in Galaviz and Brügmann (2011)) was simply that the waveforms were evaluated in the reference frame of the CoM of the triple system. The very same solution applies to the simpler binary cases reported in fig. 1.4. Here, since the CoM does not move, only a single transformation is needed. Once that transformation has been performed, the waveforms are given by the solid blue lines and reproduce the correct predicted result.

1.2.2 Green's solution in linearised theory

Another often overlooked problem arises when gravitational waveforms are computed by direct integration of eq. 1.13 with the help of the retarded Green function. To understand it, let us go back to the textbook derivation of the quadrupole formula for GW generation. We start from the Einstein equations relaxed by the condition of harmonic coordinates (see, e.g., Misner, Thorne, and Wheeler, 1973; Blanchet, 2014; Pati and Will, 2000, for the complete derivation):

$$\Box_{\text{flat}} H^{\alpha\beta} = -\frac{16\pi G}{c^4}\tau^{\alpha\beta}\,, \tag{1.28}$$

where the pseudo-tensor $H^{\alpha\beta}$ is defined in terms of the Minkowski metric $\eta^{\alpha\beta}$ and the space-time (inverse) metric $g^{\alpha\beta}$ as

$$H^{\alpha\beta} \equiv \eta^{\alpha\beta} - (-g)^{1/2} g^{\alpha\beta}\,, \tag{1.29}$$

and satisfies the harmonic gauge condition, i.e., $\partial_\beta H^{\alpha\beta} = 0$. Moreover, the "effective" stress-energy pseudo-tensor $\tau^{\alpha\beta}$ is comprised of a contribution from the stress-energy tensor of matter, and a contribution $\Lambda^{\alpha\beta}$ from the non-linearities of the gravitational field, i.e.,

$$\tau^{\alpha\beta} = (-g)T^{\alpha\beta} + \frac{c^4}{16\pi G}\Lambda^{\alpha\beta}\,, \tag{1.30}$$

where

$$\Lambda^{\alpha\beta} = \frac{16\pi G}{c^4}(-g)t_{\text{LL}}^{\alpha\beta} + \left(\partial_\nu H^{\alpha\mu}\partial_\mu H^{\beta\nu} - \partial_\mu\partial_\nu H^{\alpha\beta}H^{\mu\nu}\right), \tag{1.31}$$

with $t_{\text{LL}}^{\alpha\beta}$ denoting here the Landau-Lifshitz pseudo-tensor (Landau and Lifshitz, 1975). As a consequence of the harmonic gauge condition, $\tau^{\alpha\beta}$ is also flat-space conserved, i.e., $\partial_\beta\tau^{\alpha\beta} = 0$.

By using the retarded Green function, we can now integrate eq. 1.28 and obtain its formal solution:

$$H^{\alpha\beta}(t,\boldsymbol{x}) = \frac{4G}{c^4}\int \frac{\mathrm{d}^3\boldsymbol{x}'}{|\boldsymbol{x}-\boldsymbol{x}'|}\tau^{\alpha\beta}\left(t - |\boldsymbol{x}-\boldsymbol{x}'|/c, \boldsymbol{x}'\right)\,. \tag{1.32}$$

has a non-zero acceleration) and one has to consider a different inertial frame at each step of the system evolution.

If the field point $\boldsymbol{x}$ lies very far from the source, $|\boldsymbol{x}-\boldsymbol{x}'| \approx |\boldsymbol{x}| \equiv R$, and one can neglect the differences in retarded time among the source components by considering a single global retardation $t_{\rm ret} = t - R/c$. This yields[13]

$$H^{\alpha\beta}(t,\boldsymbol{x}) \approx \frac{4G}{Rc^4}\int \mathrm{d}^3\boldsymbol{x}'\tau^{\alpha\beta}\left(t_{\rm ret},\boldsymbol{x}'\right) . \tag{1.33}$$

Let us now expand the metric up to $1/c^2$ corrections,

$$\begin{aligned} g_{00} &= -1 - 2\frac{\phi}{c^2} + \mathcal{O}\Big(\frac{1}{c^4}\Big), \\ g_{0i} &= \mathcal{O}\Big(\frac{1}{c^3}\Big), \\ g_{ij} &= \Big(1 - 2\frac{\phi}{c^2}\Big)\delta_{ij} + \mathcal{O}\Big(\frac{1}{c^4}\Big) , \end{aligned} \tag{1.34}$$

so that the ij components are given at the 1PN order while the 00 and $0i$ components are Newtonian. The gravitational potential ϕ in eq. 1.34 must satisfy the Poisson equation $\nabla^2\phi = 4\pi G\rho$, with ρ being the mass density, in order for ϕ to be a solution of the relaxed Einstein equations. We can see that, at this accuracy level, the metric is linear in the source, which implies

$$H^{\mu\nu} = \bar{h}^{\mu\nu} + \mathcal{O}\Big(\frac{1}{c^4},\frac{1}{c^3},\frac{1}{c^4}\Big) , \tag{1.35}$$

where the three remainders in the arguments of the Landau symbol refer to the 00, $0i$ and ij components, respectively. From the flat-space conservation of $\tau^{\mu\nu}$, it then follows that (see Misner, Thorne, and Wheeler, 1973)[14]

$$\partial_0\partial_0(\tau^{00}x^jx^k) = \partial_l\partial_m(\tau^{lm}x^jx^k) - 2\partial_l(\tau^{jl}x^k + \tau^{kl}x^j) + 2\tau^{jk} , \tag{1.36}$$

which allows one to recast the spatial part of eq. 1.33 as (see Misner, Thorne, and Wheeler, 1973)

$$\bar{h}^{ij}(t,\boldsymbol{x}) \approx \frac{2G}{Rc^4}\frac{\mathrm{d}^2}{\mathrm{d}t^2}\int \mathrm{d}^3\boldsymbol{x}'c^{-2}\tau^{00}\left(t_{\rm ret},\boldsymbol{x}'\right)x'^ix'^j + \mathcal{O}\Big(\frac{1}{c^5}\Big) . \tag{1.37}$$

A priori, the PN expansion of the stress-energy pseudo-tensor $\tau^{\alpha\beta}$ defined by eq. 1.30 still involves both the matter term $T^{\alpha\beta}$ and the purely gravitational

[13] When neglecting the $\boldsymbol{x}'$ term in the temporal dependency of the integral in eq. 1.32 and replacing the source $\tau^{\alpha\beta}$ by its PN expansion, the integral on the right-hand side of eq. 1.33 becomes formally divergent. This is one of the main problems that GW generation formalisms have to address. In the Blanchet-Damour-Iyer formalism (Blanchet, Damour, and Iyer, 1995; Blanchet et al., 1995), this particular problem is solved by resorting to a combination of asymptotic matching techniques and a specific regularization procedure that cures those divergences (Blanchet and Damour, 1986; Blanchet and Damour, 1989; Blanchet, 1998; Poujade and Blanchet, 2002).

[14] The very same identity holds for $T^{\mu\nu}$ in linearised theory, since $\partial_\mu T^{\mu\nu} = 0$.

non-linear source term $\Lambda^{\alpha\beta}$. Modelling the matter system by point particles, i.e., taking (see Weinberg, 1972; Maggiore, 2007)

$$T^{\alpha\beta}(t,\boldsymbol{x}) = \sum_A \frac{m_A u_A^\alpha u_A^\beta}{(u_A^0/c)\sqrt{-g}} \delta^3(\boldsymbol{x} - \boldsymbol{x}_A(t)) \,, \tag{1.38}$$

where m_A is the mass of particle A and u_A^α is its four-velocity, one finds

$$\tau^{00}(t,\boldsymbol{x}) = \sum_A m_A c^2 \delta^3 \left(\boldsymbol{x} - \boldsymbol{x}_A(t)\right) + \mathcal{O}\Big(\frac{1}{c^0}\Big) \,, \tag{1.39}$$

$$\tau^{0i}(t,\boldsymbol{x}) = \sum_A m_A c\, \dot{x}_A^i \delta^3 \left(\boldsymbol{x} - \boldsymbol{x}_A(t)\right) + \mathcal{O}\Big(\frac{1}{c}\Big) \,, \tag{1.40}$$

$$\begin{aligned}\tau^{ij}(t,\boldsymbol{x}) = &\sum_A m_A \dot{x}_A^i \dot{x}_A^j \delta^3 \left(\boldsymbol{x} - \boldsymbol{x}_A(t)\right) \\ &+ \frac{1}{4\pi G}\Big(\partial^i\phi\,\partial^j\phi - \frac{1}{2}\delta^{ij}\partial_k\phi\,\partial^k\phi\Big) + \mathcal{O}\Big(\frac{1}{c^2}\Big) \,,\end{aligned} \tag{1.41}$$

where δ^3 is the three-dimensional Dirac delta function and $\dot{x}_A^i$ represents the components of the three-dimensional velocity. We observe that $\tau^{00} \approx T^{00}$ at leading PN order, hence eq. 1.37 coincides with the "usual" quadrupole formula,

$$\bar{h}^{ij}(t,\boldsymbol{x}) \approx \frac{2G}{Rc^4}\frac{\mathrm{d}^2 M^{ij}}{\mathrm{d}t^2}(t_{\mathrm{ret}}) + \mathcal{O}\Big(\frac{1}{c^5}\Big) \,. \tag{1.42}$$

By contrast, τ^{ij} contains a direct contribution from the gravitational field at Newtonian order, i.e., a term arising at the same order as T^{ij}. Therefore, the direct integration of eq. 1.13 will give an *incorrect* result, because the right-hand side is wrong already at the leading PN order.

To be more explicit, let us evaluate eq. 1.37 in the special case of a binary system ($A, B = 1, 2$) by using eq. 1.39 and the Newtonian equations of motion

$$\ddot{x}_A^i = -\sum_{B\neq A} \frac{G m_B}{r_{AB}^2} n_{AB}^i \,, \tag{1.43}$$

where $\boldsymbol{r}_{AB} = \boldsymbol{x}_A - \boldsymbol{x}_B$, $r_{AB} = |\boldsymbol{x}_A - \boldsymbol{x}_B|$, and $\boldsymbol{n}_{AB} = \boldsymbol{r}_{AB}/r_{AB}$. Straightforward algebra yields

$$\bar{h}^{ij}(t,\boldsymbol{x}) \approx \frac{4G}{Rc^4}\Big(m_1 \dot{x}_1^i \dot{x}_1^j + m_2 \dot{x}_2^i \dot{x}_2^j - \frac{G m_1 m_2 n_{12}^i n_{12}^j}{r_{12}}\Big) + \mathcal{O}\Big(\frac{1}{c^5}\Big) \,, \tag{1.44}$$

while direct integration of eq. 1.13 would lead to the different expression

$$\bar{h}^{ij}(t,\boldsymbol{x}) \approx \frac{4G}{Rc^4}\Big(m_1 \dot{x}_1^i \dot{x}_1^j + m_2 \dot{x}_2^i \dot{x}_2^j\Big) + \mathcal{O}\Big(\frac{1}{c^5}\Big) \,. \tag{1.45}$$

The extra term in eq. 1.44 that is missing in eq. 1.45 is related to the purely gravitational part of the right-hand side of eq. 1.41 (i.e., the part involving the

Newtonian potential ϕ), which is prematurely neglected in the source T^{ij} of eq. 1.13. This is the origin of the factor ~ 2 discrepancy shown in fig. 1.2.

Nonetheless, one can still obtain the correct expression without resorting to the identity 1.36. In fact, by substituting eq. 1.41 into the spatial components of eq. 1.33, one gets

$$\bar{h}^{ij}(t,\boldsymbol{x}) \approx \frac{4G}{c^4}\int \frac{\mathrm{d}^3\boldsymbol{x}'}{|\boldsymbol{x}-\boldsymbol{x}'|}\left[T^{ij}+\frac{1}{4\pi G}\left(\partial^i\phi\,\partial^j\phi-\frac{1}{2}\delta^{ij}\partial_k\phi\,\partial^k\phi\right)\right]+\mathcal{O}\left(\frac{1}{c^5}\right), \tag{1.46}$$

which may be rewritten as (see Appendix B for details)

$$\bar{h}^{ij}(t,\boldsymbol{x}) \approx \frac{4G}{Rc^4}\int \mathrm{d}^3\boldsymbol{x}'\,T^{ij}-\frac{2G^2}{Rc^4}\int \mathrm{d}^3\boldsymbol{y}'\mathrm{d}^3\boldsymbol{y}''\rho(\boldsymbol{y}')\rho(\boldsymbol{y}'')\frac{\hat{n}^i\hat{n}^j}{|\boldsymbol{y}'-\boldsymbol{y}''|}+\mathcal{O}\left(\frac{1}{c^5}\right), \tag{1.47}$$

where $\hat{n}^k = (y'^k - y''^k)/|\boldsymbol{y}'-\boldsymbol{y}''|$. Focusing again on the case of two point particles, eq. 1.47 gives

$$\bar{h}^{ij}(t,\boldsymbol{x}) \approx \frac{4G}{Rc^4}\left(m_1\dot{x}_1^i\dot{x}_1^j+m_2\dot{x}_2^i\dot{x}_2^j-\frac{Gm_1m_2n_{12}^in_{12}^j}{r_{12}}\right)+\mathcal{O}\left(\frac{1}{c^5}\right). \tag{1.48}$$

This expression agrees with eq. 1.44. In conclusion, the discrepancy shown in fig. 1.2 was simply due to neglecting the purely gravitational part of the source in the relaxed Einstein equations, which would be equivalent to assuming motion along straight lines for the binary components. In other words, the last term in eq. 1.44 accounts for the fact that motion does not take place on rectilinear trajectories, but instead along curved-spacetime geodesics.

1.3 Summary

In this chapter, we have reviewed some aspects of the PN approximation and we have consistently derived, from a three-body 2.5PN Hamiltonian, the equations of motion for a general triple system, i.e., for any combination of MBH masses.

We have then analysed the problem of the GW emission from three-body systems. We have highlighted several subtleties that occur when applying the standard formulae for the quadrupole and quadrupole-octupole waveforms to numerically-integrated orbits of binary and triple systems. We have shown that applying these formulae to a binary in a reference frame whose origin is displaced from the CoM of the system leads to unphysical results, if the displacement exceeds the wavelength λ of the emitted GWs. This simply occurs because implicit in the derivation of the (generalized) quadrupole formula is the assumption that the multipoles are defined in the NCZ (Blanchet, 2014), i.e., a region of size $\sim \lambda$ centred on the origin in which the binary is supposed to be. The same problem arises in hierarchical triple systems, when the quadrupole

and quadrupole-octupole formulae are applied in a reference frame centred on the triplet CoM. The resulting unphysical behaviour, which to the best of our knowledge was not mentioned in the literature (Galaviz and Brügmann, 2011) so far, can be understood by bearing in mind that a hierarchical triplet may be decomposed in an inner binary and an outer one. Indeed, as the separation of the outer binary grows, the CoM of the inner binary will eventually move out of its NCZ, thus violating the assumptions on which the derivation of the quadrupole and quadrupole-octupole formulae relies on.

We have described two solutions to this problem, each one valid at the quadrupole and octupole order respectively. Remarkably, neither of these two recipes seems to work for a system of *four* bodies,[15] for which a different approach has to be developed.

Finally, we have shown that a computation of the GW emission from a binary or triple system by integrating directly the equations for the linear metric perturbations over flat space leads to GW amplitudes that are off by a factor ~ 2. We have shown that this miscalculation is related to the fact that the derivation of the quadrupole formula itself is quite subtle, and actually requires the use of the *non-linear* Einstein equations.

[15] For a system of two relativistic binaries at sufficiently large mutual separations, even if we set the origin in the CoM of one binary, the NCZ corresponding to the second binary will *not* contain the CoM of that binary, hence the "standard" PN formalism is not applicable.

Appendix A

Useful definitions

In this appendix we summarize the explicit leading order expressions for the quadrupole and octupole mass radiation, as well as for the current quadrupole radiation.

The second and third mass moments are defined from the time-time component of the matter stress-energy tensor as

$$\begin{aligned} M^{ij}(t) &= \int \mathrm{d}^3\boldsymbol{x}\; c^{-2}T^{00}(t,\boldsymbol{x})x^{\langle i}x^{j\rangle}, \\ M^{ijk}(t) &= \int \mathrm{d}^3\boldsymbol{x}\; c^{-2}T^{00}(t,\boldsymbol{x})x^{\langle i}x^{j}x^{k\rangle}\,, \end{aligned} \tag{A.1}$$

where $\langle\rangle$ represents the symmetric trace-free (STF) operator, i.e., (see Maggiore, 2007)

$$x^{\langle i}x^{j\rangle} = x^ix^j - \frac{1}{3}\delta^{ij}r^2\,,\; x^{\langle i}x^jx^{k\rangle} = x^ix^jx^k - \frac{1}{5}\left(\delta^{ij}r^2x^k + \delta^{ik}r^2x^j + \delta^{jk}r^2x^i\right)\,. \tag{A.2}$$

The current quadrupole moment is defined by

$$S^{ijk} = \int \mathrm{d}^3\boldsymbol{x}\;\left[x^ij^{kj} + x^jj^{ki}\right], \tag{A.3}$$

where

$$j^{ij} = \frac{1}{c}\left(x^iT^{0j} - x^jT^{0i}\right) \tag{A.4}$$

is the angular momentum density tensor, which is connected to the angular momentum density vector by $j^{ij} = \varepsilon^{ij}{}_kj^k$. Alternatively, one may define the STF quadrupole tensor

$$J^{ij} = \operatorname*{STF}_{ij}\varepsilon_{abi}\int \mathrm{d}^3\boldsymbol{x}\; x^{\langle j}x^{a\rangle}T^{0b}\,, \tag{A.5}$$

and replace S^{abk} by $-2\varepsilon^{k}_{\ l\ a}J^{bl}$ in the waveform, using the fact that $S^{abk}n_k$ and $-2\varepsilon^{k}_{\ l\ a}J^{bl}n_k$ have the same transverse trace-free part (with respect to $\boldsymbol{n}$). The advantage of working with J_{ij} is that it belongs to an irreducible representation of SO(3).

The expression of the GW waveform up to the next-to-leading order in the TT gauge is finally given by

$$h_{ij}^{\mathrm{TT}}(t,\boldsymbol{x}) \approx \frac{2G}{Rc^4}\Lambda_{ijkl}(\boldsymbol{n})\left[\frac{\mathrm{d}^2 M^{kl}(t_{\mathrm{ret}})}{\mathrm{d}t^2} + \frac{n_m}{3c}\frac{\mathrm{d}^3 M^{klm}(t_{\mathrm{ret}})}{\mathrm{d}t^3} + \frac{2n_m}{3c}\frac{\mathrm{d}^2 S^{klm}(t_{\mathrm{ret}})}{dt^2}\right] + \mathcal{O}\Big(\frac{1}{c^6}\Big)\,, \tag{A.6}$$

where the projector tensor $\Lambda_{ijkl}(\boldsymbol{n})$ is defined in terms of the GW propagation direction $\boldsymbol{n}$ (see Misner, Thorne, and Wheeler, 1973):

$$\Lambda_{ijkl}(\boldsymbol{n}) = \mathcal{P}_{ik}\mathcal{P}_{jl} - \frac{1}{2}\mathcal{P}_{ij}\mathcal{P}_{kl}, \quad \mathcal{P}_{ij} = \delta_{ij} - n_i n_j\,. \tag{A.7}$$

Appendix B

Technical calculations

In this appendix, we perform the explicit calculation of

$$\bar{h}^{ij}(t,\boldsymbol{x}) = \frac{4G}{c^4}\int \frac{\mathrm{d}^3\boldsymbol{x}'}{|\boldsymbol{x}-\boldsymbol{x}'|}\left[T^{ij} + \frac{1}{4\pi G}\left(\partial^i\phi\,\partial^j\phi - \frac{1}{2}\delta^{ij}\partial_k\phi\,\partial^k\phi\right)\right] + \mathcal{O}\Big(\frac{1}{c^5}\Big)\,. \tag{B.1}$$

Since the first term of eq. B.1 is trivial to evaluate because it has a compact support, we focus on the second one, where one is not a priori allowed to approximate $|\boldsymbol{x}-\boldsymbol{x}'|$ by R under the integral, since the integration extends up to spatial infinity. We perform the calculation by considering only the term $\partial^i\phi\,\partial^j\phi$. Indeed, $\delta^{ij}\partial_k\phi\,\partial^k\phi$, which is simply the trace of $\partial^i\phi\,\partial^j\phi$ multiplied by a Kronecker delta, disappears when taking the TT projection.

Inserting the expression for the Newtonian gravitational potential, we find

$$\begin{aligned}\frac{1}{4\pi G}\int \frac{\mathrm{d}^3\boldsymbol{x}'}{|\boldsymbol{x}-\boldsymbol{x}'|}\partial^i\phi\,\partial^j\phi = \frac{G}{4\pi}\int \frac{\mathrm{d}^3\boldsymbol{x}'\mathrm{d}^3\boldsymbol{y}'\mathrm{d}^3\boldsymbol{y}''}{|\boldsymbol{x}-\boldsymbol{x}'|}\rho(\boldsymbol{y}')\rho(\boldsymbol{y}'')\times \\ \times\frac{\partial}{\partial x'^i}\left(\frac{1}{|\boldsymbol{x}'-\boldsymbol{y}'|}\right)\frac{\partial}{\partial x'^j}\left(\frac{1}{|\boldsymbol{x}'-\boldsymbol{y}''|}\right)\,.\end{aligned} \tag{B.2}$$

After transforming the derivative $\partial/\partial x'^i$ that acts on $|\boldsymbol{x}'-\boldsymbol{y}'|^{-1}$ into $-\partial/\partial y'^i$ by virtue of the translation invariance of $\boldsymbol{x}'-\boldsymbol{y}'$, and similarly for $\partial/\partial x'^j$, we may change the order of integration, so that $\partial^2/(\partial y'^i\partial y''^j)$ can be put outside the integral with respect to $\boldsymbol{x}'$. With this trick, eq. B.2 becomes

$$\frac{1}{4\pi G}\int \frac{\mathrm{d}^3\boldsymbol{x}'}{|\boldsymbol{x}-\boldsymbol{x}'|}\partial^i\phi\,\partial^j\phi = G\int \mathrm{d}^3\boldsymbol{y}'\mathrm{d}^3\boldsymbol{y}''\rho(\boldsymbol{y}')\rho(\boldsymbol{y}'')\frac{\partial^2}{\partial y'^i\partial y''^j}g(\boldsymbol{x}',\boldsymbol{y}',\boldsymbol{y}'')\,, \tag{B.3}$$

where g satisfies the Poisson equation $\Delta g(\boldsymbol{x},\boldsymbol{y}',\boldsymbol{y}'') = |\boldsymbol{x}-\boldsymbol{y}'|^{-1}|\boldsymbol{x}-\boldsymbol{y}''|^{-1}$ in the sense of distributions. It is straightforward to check that the relevant solution is $g = \ln(|\boldsymbol{x}-\boldsymbol{y}'|+|\boldsymbol{x}-\boldsymbol{y}''|+|\boldsymbol{y}'-\boldsymbol{y}''|) + \text{constant}$ (see, e.g., p.355

in Poisson and Will, 2014), from which one infers the asymptotic behaviour

$$\frac{\partial^2}{\partial y'^i \partial y''^j} K = -\frac{\hat{n}^i \hat{n}^j - \delta^{ij}}{2R|\boldsymbol{y}' - \boldsymbol{y}''|} + \mathcal{O}\Big(\frac{1}{R^2}\Big) . \tag{B.4}$$

At large distance R from the origin, eq. B.1 then reduces to

$$\bar{h}^{ij} = \frac{4G}{c^4 R} \int \mathrm{d}^3\boldsymbol{x}' T^{ij} - \frac{2G^2}{Rc^4} \int \mathrm{d}^3\boldsymbol{y}' \mathrm{d}^3\boldsymbol{y}'' \rho(\boldsymbol{y}')\rho(\boldsymbol{y}'') \frac{\hat{n}^i \hat{n}^j}{|\boldsymbol{y}' - \boldsymbol{y}''|} + \mathcal{O}\Big(\frac{1}{R^2 c^5}\Big) . \tag{B.5}$$

Chapter 2

MBH triplets in a stellar background

In this chapter we describe the theoretical framework and the numerical implementation aimed at simulating MBH triplets bound to form in galactic nuclei. We first depict the relevant physics considered and how it is implemented. Then, we proceed by presenting a number of standard tests aimed at validating our code in terms of numerical precision and reproducibility of results of previous works. Finally, by simulating some representative cases, we perform an analysis of the relevant dynamics that characterise MBH triplets, analysing the situations that can potentially lead a MBHB to coalescence.

2.1 Theoretical framework

The relativistic three-body systems we model are embedded in a stellar environment. Therefore, in order to simulate and study a configuration as realistic as possible, we include the effects of the stellar background on the MBHB dynamics. In the present chapter we present in detail our new method able to capture the complex dynamics of a hierarchical MBH triplet in a stellar potentials.

2.1.1 Hardening in a fixed stellar background

One of the key ingredients in the dynamical evolution of a hierarchical MBH triplet in a realistic post-merger situation is the hardening of the outer binary. Ambient stars, unbound to the outer binary, are expelled by the gravitational slingshot, carrying away the MBHB energy and angular momentum. As a result, the MBHB orbit gets tighter and, in some cases, slightly more eccentric.

The theory of the stellar scattering has been extensively analysed in the last 30 years by different groups (Hills, 1983; Quinlan, 1996; Sesana, Haardt, and

Madau, 2006). A comprehensive analysis is far beyond the goal of this thesis, however, since various results are employed in our work, we provide here a concise summary of the fundamental points.

Let consider a MBHB of total mass $M = m_1 + m_2$ ($m_2 \leq m_1$), reduced mass $\mu = m_1 m_2/M$, and semimajor axis a, orbiting in a background formed by stars of mass $m_\star$. During complex three-body interactions, energy and angular momentum are exchanged among the binary and the stars. Following Hills (1983), it is convenient to define approximate dimensionless energy and angular momentum exchange per single interaction, denoted as C and B respectively, as

$$C = \frac{M}{2m_*}\frac{\Delta E}{E} = \frac{a\Delta E_*}{G\mu}, \tag{2.1}$$

and

$$B = -\frac{M}{m_*}\frac{\Delta h}{h} = \frac{M}{\mu}\frac{\Delta h_\star}{h}. \tag{2.2}$$

The quantity $\Delta E/E$ is the fractional increase (decrease if negative) in the orbital specific binding energy $E = -GM/(2a)$, while $\Delta h/h$ is the fractional change in orbital specific angular momentum $h = \sqrt{GMa(1-e^2)}$. On the contrary, $\Delta E_\star$ and $\Delta h_\star$ are the corresponding changes suffered by the interacting star. The quantities B and C are of order unity and can be derived by performing detailed three-body scattering experiments (Hut and Bahcall, 1983; Quinlan, 1996; Sesana, Haardt, and Madau, 2006).

In these kind of experiments, for each encounter one solves nine coupled, second-order, differential equations supplied by 21 initial conditions (i.e., the masses, positions and velocities of the involved three bodies). These initial conditions reduce to 15 once the centre of mass is chosen to lie at rest in the origin of the coordinate system. Moreover, without loss of generality, fixing m_1 and a, placing the MBHB in the $x-y$ plane and considering that the incoming stars always approach the binary from infinity, further allows reducing the number of free varying parameters to 9. Thus, each simulation has to select a point in a nine-dimensional parameter space represented by the mass ratio $q = m_2/m_1$ of the binary, its eccentricity e, the mass of the incoming field star, its asymptotic initial speed $v_\star$, its impact parameter at infinity b, and four angles, one representing the initial orbital phase of the binary and the other three describing how a star approaches the MBHB.

Significant star-binary energy exchanges (i.e., characterised by a dimensionless energy change $C > 1$) occurs only for $v_\star < v\sqrt{\mu/M}$, where v is the orbital velocity of the binary (see e.g., Saslaw, Valtonen, and Aarseth, 1974; Mikkola and Valtonen, 1992).[1]

As described in Quinlan (1996), the binary global evolution in an isotropic fixed background of stars of density ρ and one-dimensional velocity dispersion

[1] This derives by requiring that the energy per unit mass of the star is lower than that of the binary.

σ at infinity is determined by three dimensionless quantities: the hardening rate

$$H = \frac{\sigma}{G\rho}\frac{\mathrm{d}}{\mathrm{d}t}\left(\frac{1}{a}\right), \tag{2.3}$$

the mass ejection rate ($M_{\rm ej}$ is the stellar mass ejected by the binary)

$$J = \frac{1}{M}\frac{\mathrm{d}M_{\rm ej}}{\mathrm{d}\ln(1/a)}, \tag{2.4}$$

and the eccentricity growth rate

$$K = \frac{\mathrm{d}e}{\mathrm{d}\ln(1/a)}. \tag{2.5}$$

In our brief description of the hardening process we do not consider the mass ejection rate J, but we choose to focus only on the hardening and the eccentricity growth rates.

Considering a Maxwellian stellar velocity distribution,[2] $f(v_\star,\sigma) = (2\pi\sigma^2)^{-3/2}\exp(-v_\star^2/2\sigma^2)$, the average hardening rate can be written as

$$H(\sigma) \equiv \int_0^\infty f(v_\star,\sigma)\frac{\sigma}{v_\star}H_1(v_\star)\,4\pi v_\star^2\,\mathrm{d}v_\star, \tag{2.6}$$

where

$$H_1(v_\star) \equiv 8\pi\int_0^\infty \langle C\rangle x\,\mathrm{d}x, \tag{2.7}$$

represents the dimensionless hardening rate in the case all stars have the same velocity $v_\star$, with x denoting the dimensionless impact parameter, defined as $x = bv_\star/(2GMa)$. An analogous expression relates the thermally-averaged eccentricity growth rate $K(\sigma)$ to $K_1(v_\star)$, where

$$K_1(v_\star) \equiv \frac{(1-e^2)}{2e}\frac{\int_0^\infty\langle B-C\rangle x\,\mathrm{d}x}{\int_0^\infty\langle C\rangle x\,\mathrm{d}x}. \tag{2.8}$$

Both H_1 and K_1 do not depend on M nor $m_\star$.

The hardening rate H, as can be inferred from fig 2.1, results to be a sharp function of the quantity a/a_h, where a_h is the so-called hardening radius, defined as (see, e.g., Quinlan, 1996; Sesana, Haardt, and Madau, 2006)

$$a_h = \frac{Gm_2}{4\sigma^2}. \tag{2.9}$$

[2]The employment of the formalism of stellar hardening is strictly self-consistent only when the stellar density profile is described by a singular isothermal sphere (SIS). However, as demonstrated by Sesana and Khan (2015), once the density and the velocity dispersion at the binary influence radius are correctly evaluated, the analytical framework of stellar hardening closely reproduces the evolution of a MBHB in general stellar profiles (and different from SIS). This conjecture has been proved by employing a set of full N-body simulations, where the stellar bulge is initialised according to an Hernquist profile, as assumed in the present work (see section 2.1.3).

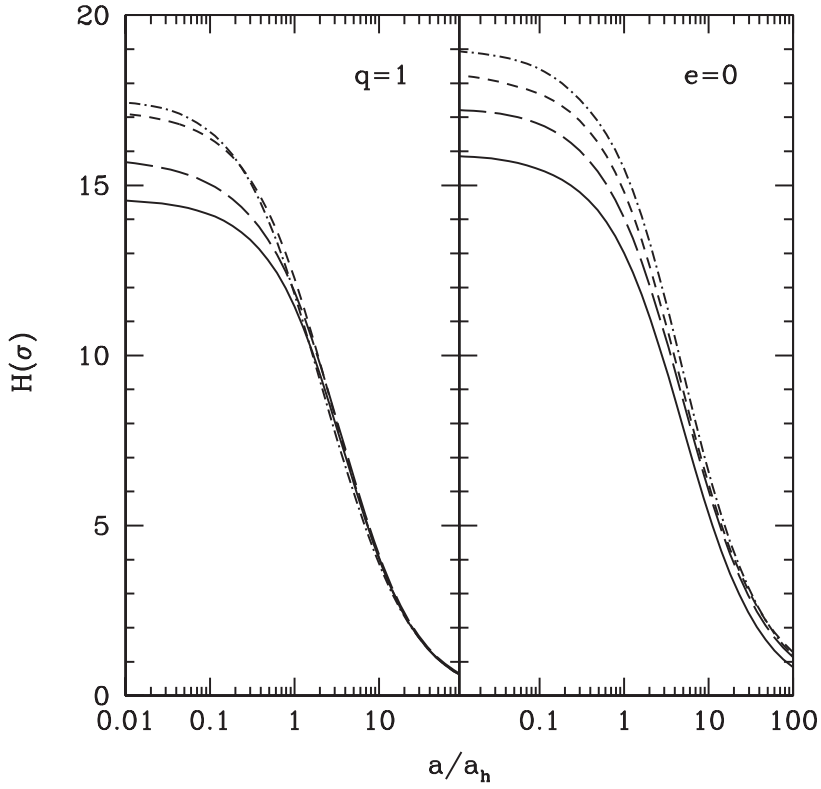

Figure 2.1: Binary hardening rate H (averaged over a Maxwellian velocity distribution) versus a/a_h. *Left:* $e = 0$ (solid line), 0.3 (long-dashed line), 0.6 (short-dashed line), and 0.9 (dot-dashed line) for $q = 1$. *Right:* $q = 1/3$ (solid line), $1/9$ (long-dashed line), $1/27$ (short-dashed line), and $1/81$ (dot-dashed line) for $e = 0$. *Credit:* Sesana, Haardt, and Madau (2006).

When $a < a_h$ the hardening rate is approximatively constant (see fig 2.1), i.e., binaries with a separation $\lesssim a_h$ harden at a constant rate.[3]

Different mass ratios and a non-zero eccentricity can influence the hardening rate. Although the global trend is maintained, H is found to be a decreasing function of the binary mass ratio, while it slightly grows as the eccentricity increases. The latter trend can be understood considering that for an eccentric binary the orbital velocity at pericentre is higher, therefore stars with small impact parameters can be accelerated at higher velocity allowing a significative enhancement of the energy exchanged. Note also that H drops to zero for $a \gtrsim 100\, a_h$, a separation at which the hardening process becomes, practically, irrelevant. On the contrary, the binary eccentricity growth K, plotted in fig.2.2 as a function of a/a_h, is close to zero for $a \sim a_h$, while grows monotonically in the case of eccentric orbits as the binary shrinks. Smaller values of q lead to larger growth rates. In the circular case K is negligible at every separation, i.e., circular binaries stay circular.

The Maxwellian averaged rates H and K derived from scattering exper-

[3]Binaries with separation $\lesssim a_h$ are denoted as "hard binaries".

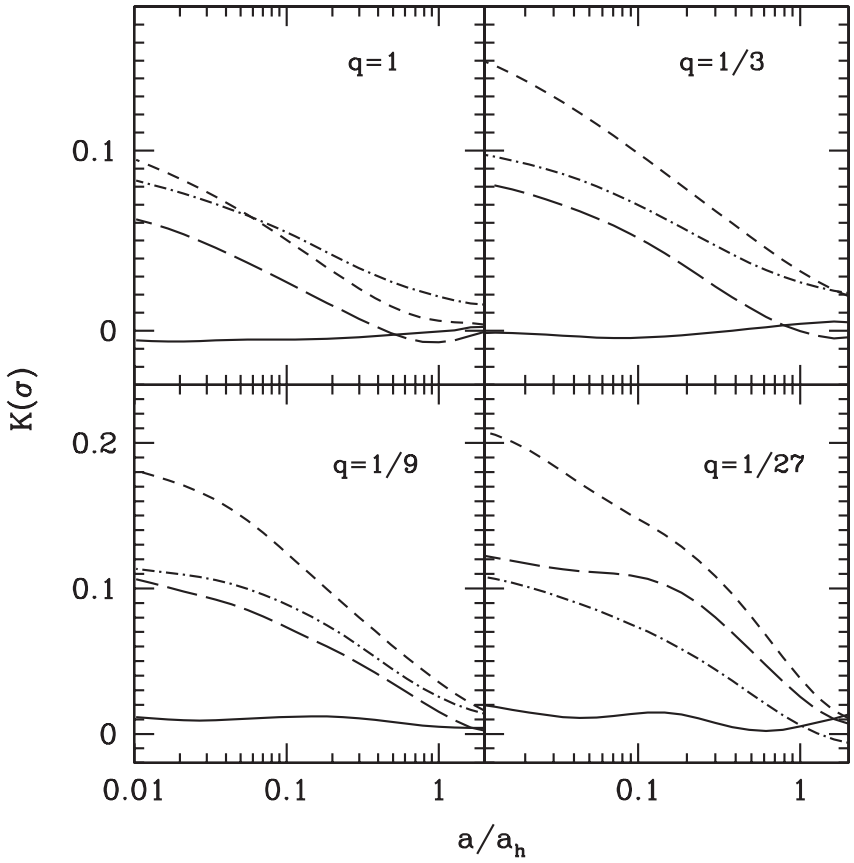

Figure 2.2: Binary eccentricity growth rate as a function of binary separation for different mass ratios. Different line styles are for $e = 0, 0.3, 0.6, 0.9$, as in the left panel of fig. 2.1. *Credit:* Sesana, Haardt, and Madau (2006).

iments can be fitted to within few percent with two analytic functions (see, Sesana, Haardt, and Madau, 2006):

$$H = A(1 + a/a_0)^{\gamma}, \tag{2.10}$$

and

$$K = A(1 + a/a_0)^{\gamma} + B, \tag{2.11}$$

where the values of the fitting parameters can be found in Sesana, Haardt, and Madau (2006).

The equations defining the hardening and the eccentricity growth rates (eq. 2.3 and eq. 2.5) can be recast to explicitly show the time evolution of the binary orbital elements, i.e., the semi-major axis and the eccentricity, as follows:

$$\dot{a} = -a^2 \frac{G\rho H}{\sigma}, \tag{2.12}$$

$$\dot{e} = a \frac{G\rho H K}{\sigma}. \tag{2.13}$$

Sesana and Khan (2015) demonstrated that the above equations are appropriate to describe the hardening in a galaxy merger remnant, provided that ρ and σ

are defined at the binary influence radius, i.e., at the the radius containing twice the binary mass in stars.

Our aim here is to include the hardening of the outer binary in the three-body dynamics previously described. The methodology we employ relies on a velocity-dependent (hence dissipative) fictitious force, which is tuned to provide an orbital averaged decay and an eccentricity growth consistent with eqs. 2.12 and 2.13. It is worth stressing that it is exactly the hierarchical nature of the triplets we consider that allows us to treat the hardening of the outer binary following Quinlan (1996) and Sesana, Haardt, and Madau (2006). The hardening binary is, in our case, formed by the intruder and by the centre of mass of the inner binary.

Under the assumption of a small dissipative force, the rates of change of the orbital elements can be derived by standard perturbation theory in the framework of celestial mechanics. We start by considering the perturbed two-body problem, i.e.,

$$\frac{\mathrm{d}^2\boldsymbol{r}}{\mathrm{d}t^2} = -\frac{GM}{r^3}\boldsymbol{r} + \boldsymbol{\delta}, \tag{2.14}$$

where M is the binary total mass, $\boldsymbol{r}$ the relative separation, and in the most general case the extra-acceleration $\boldsymbol{\delta}$ is a generic function of position, velocity and time. Given the planar geometry of the Keplerian problem, $\boldsymbol{\delta}$ can be projected along three directions, i.e., on the orbital plane along the radial direction (S) and normal to it (T), and along the direction orthogonal to the orbital plane (W):

$$S = \frac{\boldsymbol{\delta}\cdot\boldsymbol{r}}{r}, \quad T = \frac{\boldsymbol{\delta}\cdot(\boldsymbol{h}\times\boldsymbol{r})}{hr}, \quad W = \frac{\boldsymbol{\delta}\cdot\boldsymbol{h}}{h}, \tag{2.15}$$

where $\boldsymbol{h}$ is the binary angular momentum per unit mass. The specific shape of the perturbing force, i.e., the form of S, T, W, depends on the particular physical phenomena to which a binary is subjected.

In spherically symmetric bulges, during the hardening phase, the orientation of the orbital plane of a MBHB can undergo a random walk (see, Merritt, 2002), while in the presence of a net rotation of the stellar distribution the MBHB orbit tends instead to align with the global angular momentum of the stars (see, Gualandris, Dotti, and Sesana, 2012). In triaxial or axisymmetric potentials, the effect of the re-orientation is more difficult to determine and strongly depends on the specific shape of the density profile (see, Cui and Yu, 2014). In any case, considering a non-rotating spherically symmetric stellar distribution as the one we consider here (see section 2.1.2 and section 2.1.3), the magnitude of the random re-orientation of the orbital plane is $\lesssim 10^\circ$. We therefore neglect the re-orientation effect during the hardening phase, i.e., we set $W = 0$.

While the energy per unit mass in the unperturbed Keplerian problem is a constant of motion, the dissipative force is responsible for its variation in time, i.e., $\dot{E} = \boldsymbol{\delta}\cdot\boldsymbol{v} = Sv_r + Tv_t$, where v_r and v_t are the radial and tangential velocity, respectively. In terms of eccentricity e and orbital true anomaly ν, the velocity components are written as

$$v_r = \frac{GM}{h} e \sin\nu,$$

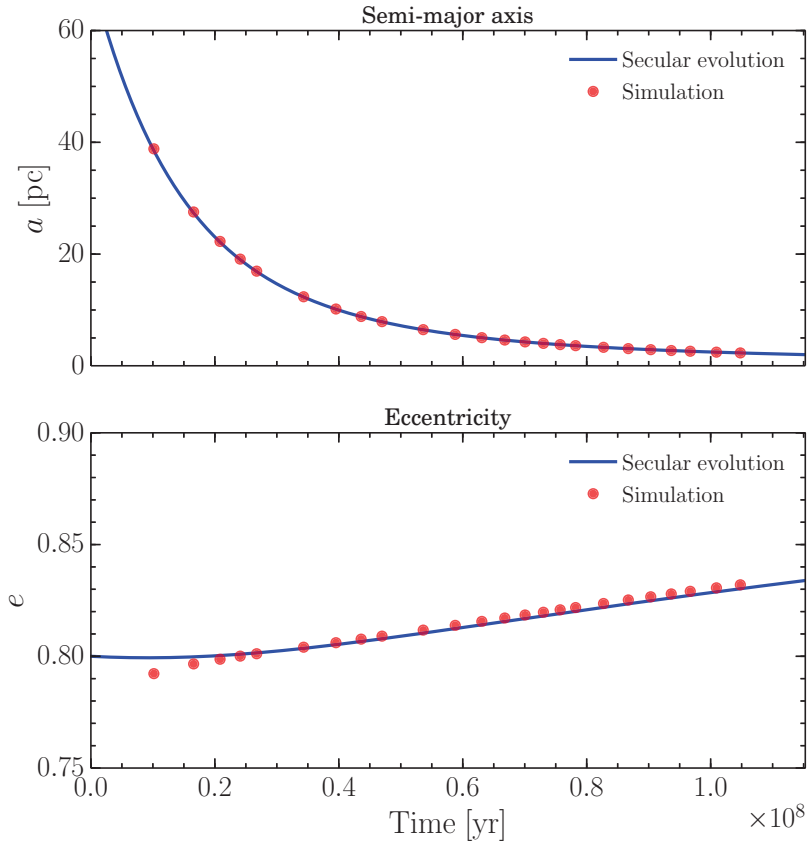

Figure 2.3: Semi-major axis (*upper panel*) and eccentricity (*lower panel*) evolution of a MBH binary scattering off background stars. Our implementation of the hardening process (shown as filled dots) is compared to the results of the scattering experiments of Sesana, Haardt, and Madau (2006), shown as solid lines.

$$v_t = \frac{GM}{h}(1 + e\cos\nu), \tag{2.16}$$

so that the energy variation becomes

$$\dot{E} = [Se\sin\nu + T(1 + e\cos\nu)]\,\frac{GM}{h}. \tag{2.17}$$

Finally, from $h = \sqrt{GMa(1-e^2)}$, eq. 2.17 gives the variation rate of the semi-major axis a:

$$\dot{a} = \frac{2a^2}{GM}\dot{E} = 2\sqrt{\frac{a^3}{GM(1-e^2)}}\,[Se\sin\nu + T(1 + e\cos\nu)]\,. \tag{2.18}$$

The perturbing force changes also the angular momentum according to the torque exerted. In our specific case (i.e., $W = 0$), the angular momentum varies

only in magnitude according to

$$\dot{h} = \frac{GM}{2h}\left[(1-e^2)\dot{a} - 2ae\dot{e}\right] = rT. \tag{2.19}$$

By substituting $\dot{a}$ from eq. 2.18 and expressing r in terms of a, e and ν, i.e.,

$$r = \frac{a(1-e^2)}{1+e\cos\nu}, \tag{2.20}$$

we finally obtain the variation rate of the eccentricity,

$$\dot{e} = \sqrt{\frac{(1-e^2)a}{GM}}\left[S\sin\nu + T\frac{2\cos\nu + e(1+\cos^2\nu)}{1+e\cos\nu}\right]. \tag{2.21}$$

Eqs. 2.18 and 2.21 represent instantaneous variation rates, that need to be compared to the orbit averaged rates derived from scattering-experiment results (eqs. 2.12 and 2.13). We then need to perform an orbit average of eqs. 2.18 and 2.21, i.e.,

$$<\dot{a}> = \frac{1}{P_{\rm orb}}\int_0^{P_{\rm orb}} {\rm d}t\,\dot{a}, \tag{2.22}$$

$$<\dot{e}> = \frac{1}{P_{\rm orb}}\int_0^{P_{\rm orb}} {\rm d}t\,\dot{e}. \tag{2.23}$$

Note that, in order to numerically compute the above integrals, the integration over time must be substituted with an integration over the true anomaly. Starting from Kelper's equation, straightforward but rather long calculations give

$${\rm d}t = \sqrt{\frac{a^3}{GM}}\frac{(1-e^2)^{3/2}}{1+e\,\cos^2\nu}{\rm d}\nu, \tag{2.24}$$

where we assumed negligible variations of both a and e along a single orbit.

Next, we need an appropriate form for $\boldsymbol{\delta}$ (i.e., appropriate S and T), such that its orbit-averaged action produces orbital variations matching eqs. 2.12 and 2.13. We assume that $\boldsymbol{\delta}$ is the sum of two terms, one orthogonal to $\boldsymbol{v}$ and one parallel to $\boldsymbol{v}$:

$$\boldsymbol{\delta} = A\frac{\boldsymbol{v}\cdot\boldsymbol{r}}{r}\left[\frac{\boldsymbol{r} - (\boldsymbol{r}\cdot\boldsymbol{v})\boldsymbol{v}/v^2}{\sqrt{r^2 - (\boldsymbol{r}\cdot\boldsymbol{v})^2/v^2}}\right] - B\,vr\boldsymbol{v}, \tag{2.25}$$

which can be decomposed into radial and tangential components (cf. eq. 2.15) as

$$S = Av_r\left(\frac{v}{v_t} - \frac{v_r^2}{vv_t}\right) - B\,vrv_r, \tag{2.26}$$

$$T = -A\frac{v_r^2}{v} - Bvrv_t, \tag{2.27}$$

where A and B are functions of (a, e). Finally, we substitute S and T in eqs. 2.18 and 2.21, and we tune the fitting functions A and B so that the orbit averages (eqs. 2.22 and 2.23) match the results obtained by scattering experiments (eqs. 2.12 and 2.13). If we choose the form

$$A(a,e) = \frac{G\rho HK}{\sigma}\frac{2a}{e(1-e^2)^{\beta_1}(1-e^5)^{\beta_2}}, \tag{2.28}$$

$$B(a,e) = \frac{G\rho H}{2\sigma}\sqrt{\frac{a}{GM}}\left[\frac{(1-e^{\beta_3})^{\beta_4}}{(1-e^{\beta_5})^{\beta_6}}\right], \tag{2.29}$$

where $\beta_1 = 0.38$, $\beta_2 = 0.055$, $\beta_3 = 8.036$, $\beta_4 = 0.148$, $\beta_5 = 1.90$, and $\beta_6 = 0.22$, we obtain a fairly good agreement with the results of three-body scattering experiments presented in Sesana, Haardt, and Madau (2006) (see fig. 2.3).

2.1.2 Scaling relations

The hardening process described in the previous section depends upon the density profile and the velocity dispersion of the stellar spheroids hosting the MBHs. Remarkably, the large scale properties of a galaxy, by means of some scaling relations, can be connected to the hosted MBH. Indeed, even if the true origin of these relations is still under debate, it is today well established that several properties of galaxies (mass, velocity dispersion, central concentration) tightly correlate with the mass of the compact object hosted in their centre (see e.g., fig. 2.4. See further Magorrian et al., 1998; Ferrarese and Merritt, 2000; Gültekin et al., 2009; Kormendy and Ho, 2013, for detailed studies and comprehensive reviews).

Since we initialise our simulations starting from the mass of the MBHs, in order to consider a self-consistent galactic environment we can exploit the mentioned scaling relations to set the properties of a stellar spheroid that hosts a MBH, or in our case a MBHB. Following Sesana and Khan (2015), the stellar velocity dispersion can be obtain from the mass-sigma relation (Kormendy and Ho, 2013) as

$$\frac{M_{\rm BH}}{10^9 {\rm M}_\odot} = 0.309\left(\frac{\sigma}{200\ {\rm km/s}}\right)^{4.38}, \tag{2.30}$$

while the total mass $M_\star$ of the stellar bulge is derived from

$$\frac{M_{\rm BH}}{10^9 {\rm M}_\odot} = 0.49\left(\frac{M_\star}{10^{11} {\rm M}_\odot}\right)^{1.16}. \tag{2.31}$$

In order to obtain the density profile, along with the total stellar mass $M_\star$, we need to specify a length scale r_0, which denotes the concentration of the stellar system. The task can be accomplished by, first assuming a Dehen profile (being γ the inner logarithmic slope; see Dehnen, 1993), i.e.,

$$\rho(r) = \frac{(3-\gamma)M_\star}{4\pi}\frac{r_0}{r^\gamma(r+r_0)^{4-\gamma}}, \tag{2.32}$$

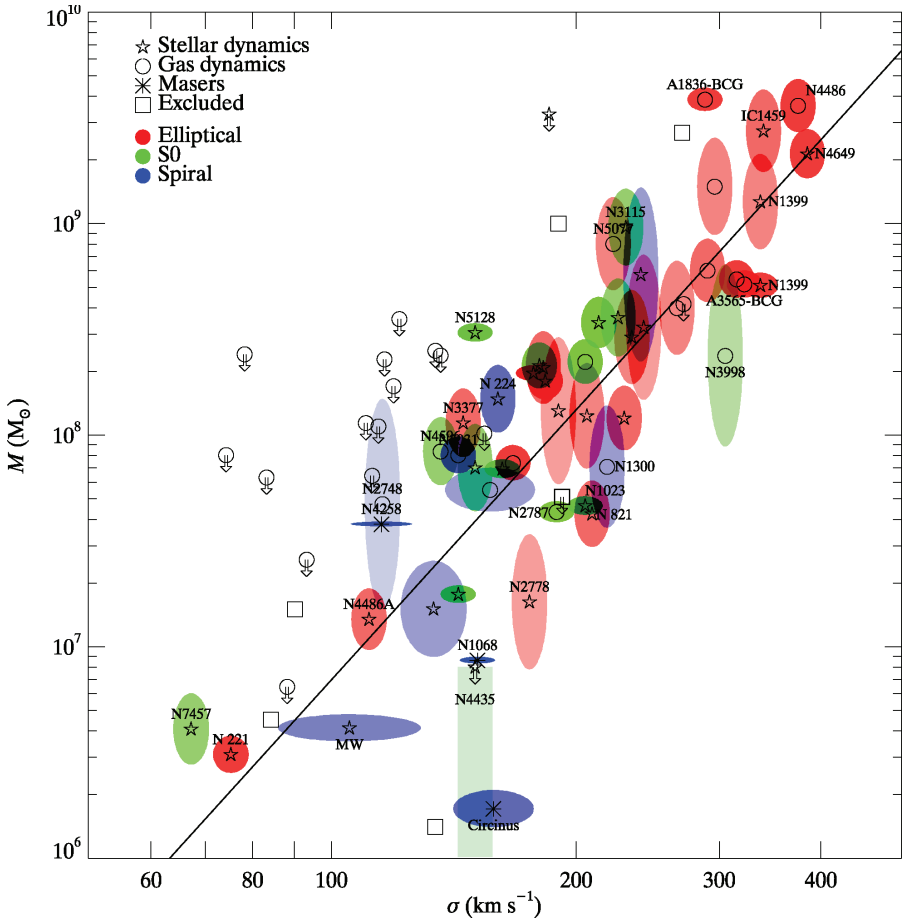

Figure 2.4: The mass-sigma relation that show the correlation between the mass of the MBH and the velcocity dispersion of the stellar spheroid hosting it. *Credit:* Gültekin et al. (2009)

and then employing the relation between r_0 and the galaxy effective radius $R_{\rm eff}$, i.e.,

$$R_{\rm eff} \approx 0.75 r_0 (2^{1/(2-\gamma)} - 1)^{-1}, \tag{2.33}$$

which, contrary to r_0, represents an observationally constrained quantity. In particular Dabringhausen, Hilker, and Kroupa (2008) found for elliptical galaxies

$$\frac{R_{\rm eff}}{\rm pc} = \max(2.95 M_{\star,6}^{0.596}, 34.8 M_{\star,6}^{0.399}), \tag{2.34}$$

whereas for bulges in spiral galaxies

$$\frac{R_{\rm eff}}{\rm pc} = 2.95 M_{\star,6}^{0.596}. \tag{2.35}$$

In the two last equations $M_{\star,6}$ represents the total stellar mass normalised to $10^6 \mathrm{M}_\odot$.

Finally the stellar density at the influence radius[4] of the MBHB is computed by evaluating eq. 2.32 at $r_{\rm inf} = r_0/\{[M_\star/(2M)]^{1/(3-\gamma)} - 1\}$.

[4]Throughout the literature the binary influence radius, $r_{\rm inf}$, is defined as the scale length that contains a mass in star equal to twice the mass of the hosted MBHB.

2.1.3 Stellar bulge

We describe the distribution of stars as an Hernquist profile (i.e., a Dehnen profile with $\gamma = 1$; see Hernquist, 1990) with an additional central core:

$$\rho(r) = \begin{cases} \dfrac{M_\star}{2\pi}\dfrac{r_0}{r(r+r_0)^3} & \text{if } r > r_c, \\ \\ \rho(r_c)\,(r/r_c)^{-1/2} & \text{if } r \leq r_c, \end{cases} \tag{2.36}$$

where $M_\star$ and r_0 can be consistently determined by observational scaling relations as described in the previous section and in Sesana and Khan (2015). The inner core is modelled as a shallower power-law with index $-1/2$ (Khan et al., 2012), aimed at mimicking the erosion of the central region of the bulge by the now-stalled inner MBHB (Ebisuzaki, Makino, and Okumura, 1991; Volonteri, Madau, and Haardt, 2003; Antonini, Barausse, and Silk, 2015a; Antonini, Barausse, and Silk, 2015b). Indeed, during its alleged hardening phase, the inner MBH ejects stars via the slingshot mechanism, hence producing a *mass deficit* in the stellar distribution that can be quantified as (Merritt, 2013; Antonini, Barausse, and Silk, 2015a; Antonini, Barausse, and Silk, 2015b)

$$\Delta M = M\left[0.7q^{0.2} + 0.5\ln\left(0.178\frac{c}{\sigma}\frac{q^{4/5}}{(1+q)^{3/5}}\right)\right], \tag{2.37}$$

where here M is the mass of the inner binary, and $q = m_2/m_1 \leq 1$ the binary mass ratio. The core radius r_c can be easily obtained by imposing that ΔM equals the mass difference, within r_c, between the original Hernquist and $r^{-1/2}$ profiles .

The bulge mass M_b is given by integration of eq. 2.36, i.e.,

$$M_b(r) = \begin{cases} M_\star r_0\left[\dfrac{4r_c^2}{5(r_c+r_0)^3} + \dfrac{(r-r_c)(2r_c r + r_0(r_c+r))}{(r_c+r_0)^2(r+r_0)^2}\right] & \text{if } r > r_c \\ \\ \dfrac{4_\star r^{5/2} r_0}{5r_c^{1/2}(r_c+r_0)^3} & \text{if } r \leq r_c. \end{cases} \tag{2.38}$$

The core profile is then used to compute the hardening phase of the outer MBHB as detailed in the previous subsection, and to introduce a fixed analytical spherically symmetric potential in the equations of motion of the triplet, whose net effect is a Newtonian orbital precession with sign *opposite* to that induced by PN terms.

Note that also during this phase stars will be ejected from the bulge, eroding the density profile and hence slowing the hardening of the outer binary. On the other hand, it is conceivable that a similar amount of mass in stars is brought in by the intruder, so the net effect is difficult to asses. We therefore assume the outer binary to evolve in the full loss-cone limit, with the stellar distribution given by eq. 2.36.

2.1.4 Stellar dynamical friction

As a last effect acting already on kpc scale, we include the dynamical friction on the intruder of mass m in its way to the bulge centre. We adopt the simple Chandrasekhar's formula (Chandrasekhar, 1943), i.e.,

$$\dot{\boldsymbol{v}}_{\rm df} = -4\pi G\rho m \ln\Lambda \left[\mathrm{erf}(X) - \frac{2Xe^{-X^2}}{\sqrt{\pi}}\right] \frac{\boldsymbol{v}}{v^3}, \tag{2.39}$$

where here v is the velocity of the intruder, $\ln\Lambda$ is the Coulomb logarithm and $X = v/(\sqrt{2}\sigma)$.[5] Following Hoffman and Loeb (2007), we adopt

$$\ln\Lambda = \max\left\{\ln\left(\frac{r(\sigma^2+v^2)}{Gm}\right), 1\right\}, \tag{2.40}$$

and

$$\rho = \min\left\{\rho(r), \rho(r_{\rm inf})\right\}, \tag{2.41}$$

Dynamical friction is typically turned off in the code as soon as the intruder binds to the inner binary, when it becomes sub-dominant compared to the gravitational slingshot of background stars.

2.2 Code implementation and tests

We approached the computational problem from the most straightforward side, i.e., we employed a direct three-body integrator without any regularisation scheme to control round-off errors, rather, we selected a customised numerical precision suited for our goals.[6] Our numerical scheme directly integrates the three-body equations allowing for velocity-dependant forces (such as the PN dissipative terms and the binary hardening induced by the stellar background discussed in the previous section). The code leverages on a C++ implementation of the Bulirsch-Stoer (BS) method (Bulirsch and Stoer, 1966; Press et al., 2002) based on the Modified Midpoint algorithm and on the Richardson extrapolation (Richardson, 1911). The BS scheme advances the solution of a system of ordinary differential equations by "macroscopic" steps, i.e., the single step actually consists of many sub-steps of the Modified Midpoint method (i.e., the effective integrator scheme), which are then extrapolated to zero stepsize by the Richardson technique based on the Neville's algorithm (Press et al., 2002). The extrapolation, together with the dimension of the steps, provides a scheme to obtain high accuracy with minimised computational efforts.

[5] The functional form of the dynamical friction force can be consistently employed only when the stellar density distribution has a Maxwellian velocity distribution, as for the case of the SIS. However, as shown by Just et al. (2011) and Dosopoulou and Antonini (2017), the expected difference in the sinking time of a MBH when consistently evaluated using the correct distribution function of the density profile will not be larger than a factor of a few.

[6] We employed a direct three-body integrator since the secular equations of motion in some cases lead to inaccurate results, in particular when the eccentricities are very high (Antonini, Murray, and Mikkola, 2014). Note that recently Luo, Katz, and Dong (2016) proposed a correction to the secular equations in order to recover the results of direct integration.

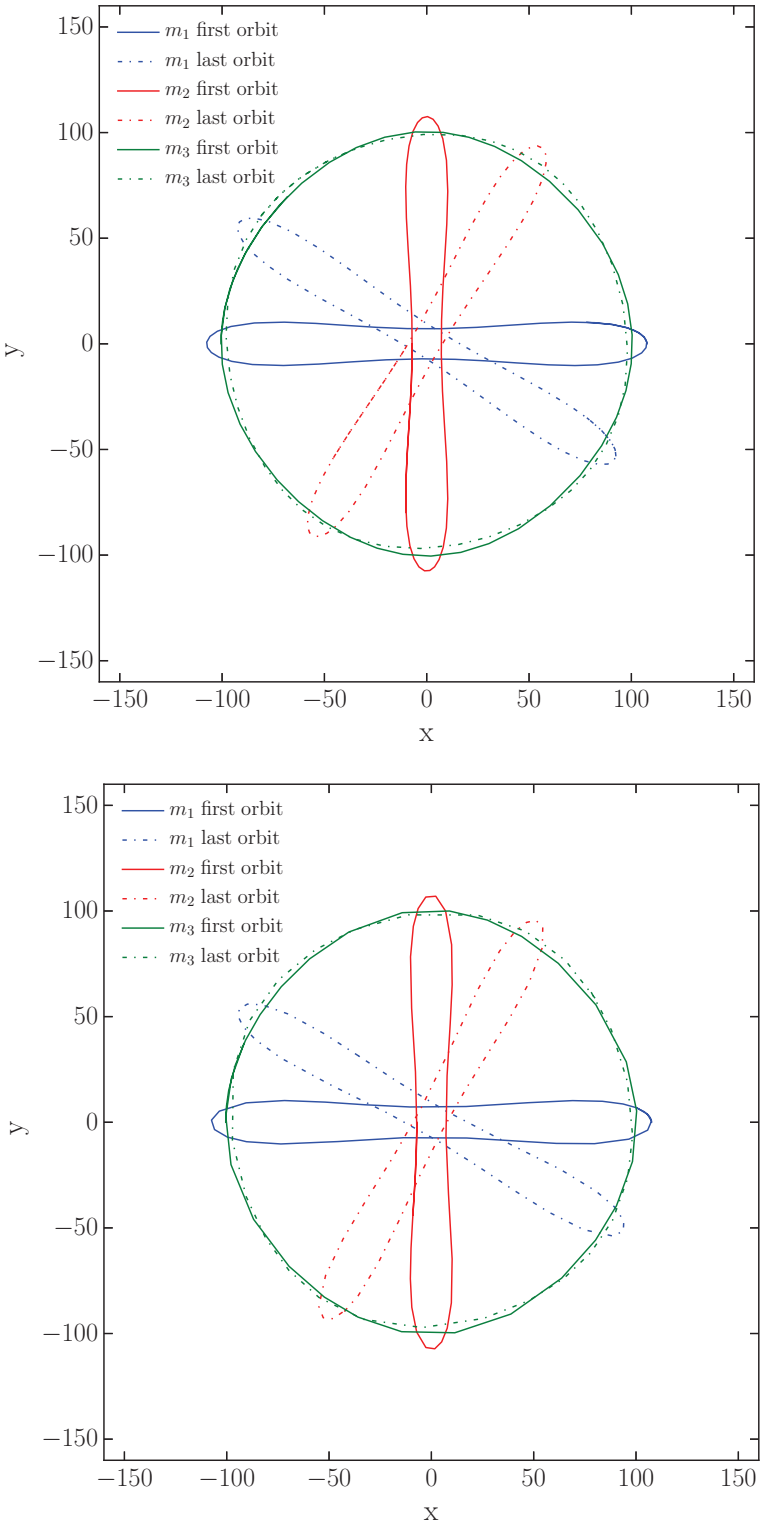

Figure 2.5: Test of energy and angular momentum conservation for the Henon's Criss Cross configuration. Purely Newtonian dynamics is stable against numerical errors for at least $10,000$ orbits. Integrations in quadruple (upper panel) or double precision (lower panel) do not show significant differences. The apparent orbital precession has to be ascribed to round-off errors in the initial conditions.

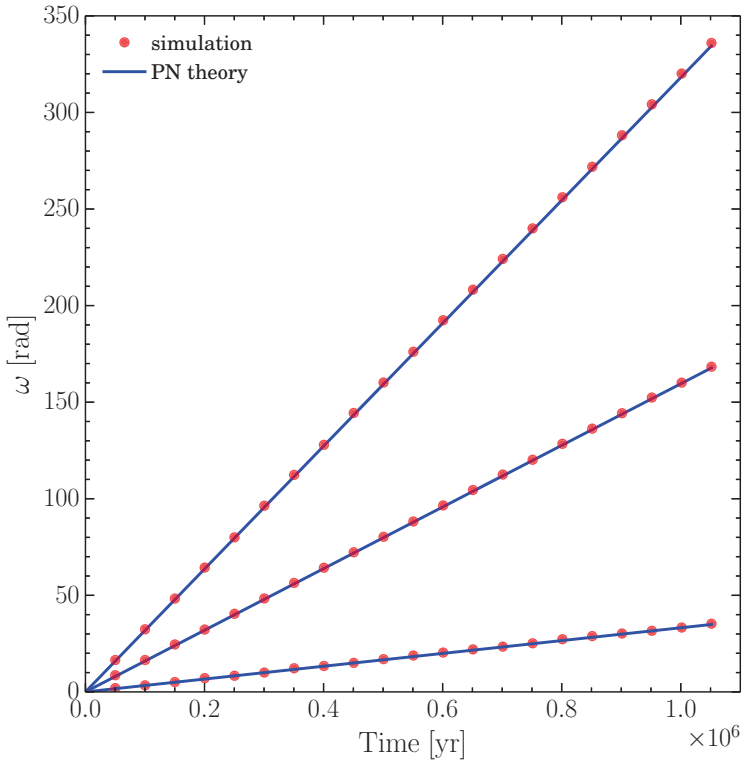

Figure 2.6: The periastron ω is shown against time for a two-body system consisting of a MBH of mass $m_{\rm BH} = 3.5 \times 10^6$ $\mathrm{M}_\odot$ and a star with $m_\star = 10$ $\mathrm{M}_\odot$ and semi-major axis $a = 1$ mpc. Red dots show every 1,000 orbits the advancement of the pericenter computed with our code, while the blue lines are the 2PN theoretical prediction. Three eccentricity are considered, $e = 0.9, 0.98, 0.99$, from bottom to top.

2.2.1 Test of Newtonian dynamics

In order to validate the code we performed some standard tests. We first tested the energy and angular momentum conservation at Newtonian order by means of a well known configuration for a three-body system, the so-called Henon's Criss-Cross (Henon, 1976; Moore and Nauenberg, 2006). We evolved the system for nearly $10,000$ orbits, and checked that both energy and angular momentum are conserved at a level of one part in 10^{13}. In fig. 2.5 we plot the first and last orbit of each of the three equal mass bodies of the test, comparing the results of integration in quadruple (left panel) and double (right panel) precision, and found no significant differences in the two runs. We will return later on this point. Note that the apparent orbital precession has to be ascribed to round-off errors in setting the appropriate initial conditions.

2.2.2 Tests of PN dynamics

We then proceeded to test our code against PN dynamics by performing some of the trial runs performed by Mikkola and Merritt (2008) using the

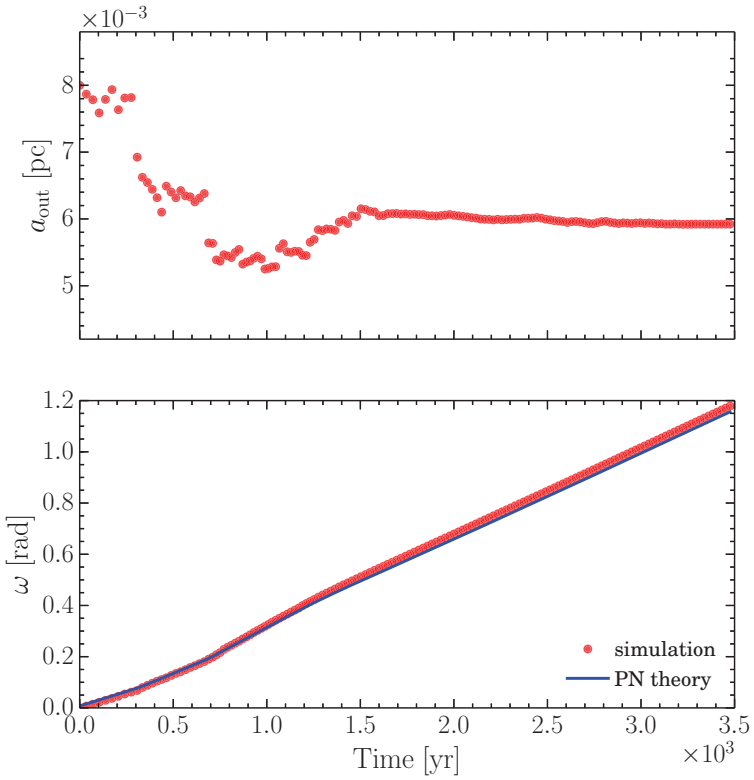

Figure 2.7: A three-body system with $m_1 = 3.5 \times 10^6$ M$_\odot$, $m_2 = 3.5 \times 10^3$ M$_\odot$, and $m_3 = 10$ M$_\odot$ is considered. The time evolution of the semi-major axis $a_{\rm out}$ (upper panel) and the argument of the pericenter ω of m_3 (lower panel) are shown as red dots. The blue line in the lower panel represents the 2PN theoretical predictions accounting for the time variations of $a_{\rm out}$ and $e_{\rm out}$.

ARCHAIN code. ARCHAIN, which includes non-dissipative 1PN, 2PN and dissipative 2.5PN corrections, employs a regularised chain structure and the time-transformed leapfrog scheme to accurately integrate the motions of arbitrarily close binaries with arbitrarily small mass-ratios. Recently, Antonini et al. (2016) used ARCHAIN to compute the evolution of hierarchical triplets formed in dense globular clusters.

We report on two tests analogous to those presented in Mikkola and Merritt (2008). The first one consisted in a two-body dynamics check, where a star of mass $m_\star = 10$ M$_\odot$ orbits a MBH of mass $m_{\rm BH} = 3.5 \times 10^6M_\odot$, with semi-major axis $a = 1$ mpc. We considered 3 different eccentricities ($e = 0.9, 0.98, 0.99$), and checked the progression of the periastron $\Delta\omega$ determined by the relativistic precession. As shown in fig. 2.6, we obtain in all tested cases a good agreement with the 2PN theoretical prediction, i.e.,

$$\Delta\omega = \frac{6\pi GM}{a(1-e^2)c^2} + \frac{3(18+e^2)\pi G^2 M^2}{2a^2(1-e^2)^2 c^4}, \tag{2.42}$$

where $M = m_\star + m_{\rm BH}$.

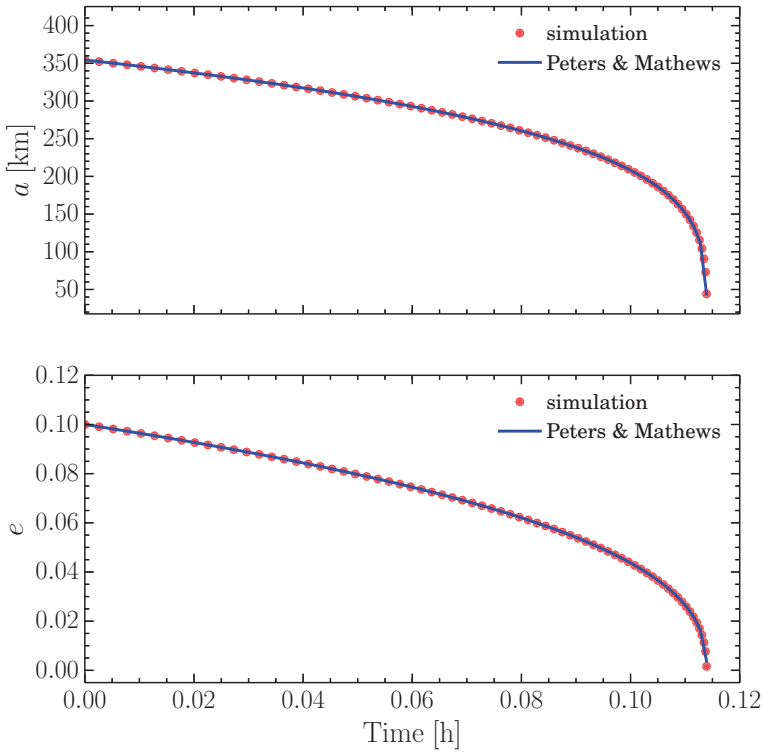

Figure 2.8: The orbital evolution of a binary system with masses $2m_2 = m_1 = 1\ \mathrm{M}_\odot$ including 2.5PN terms only (red dots) is compared to the evolution computed by employing the orbital averaged GW losses from Peters and Mathews (1963) (blue lines). The upper panels show the binary semi-major axis, the lower panels the binary eccentricity as a function of time (in hours). The initial binary eccentricity is set to $e = 0.1$.

As a second test we analysed a three-body case, in which a star of mass $m_3 = 10\mathrm{M}_\odot$ interacts with a MBHB, formed by a MBH of mass $m_1 = 3.5 \times 10^6\mathrm{M}_\odot$, and an intermediate mass BH with $m_2 = 3.5 \times 10^3\mathrm{M}_\odot$. The MBHB has semi-major axis $a_{\rm in} = 0.1$ mpc and eccentricity $e_{\rm in} = 0.9$, while the star is placed on an orbit with $a_{\rm out} = 8$ mpc and $e_{\rm out} = 0.974$. In fig. 2.7, upper panel, we show $a_{\rm out}$ as a function of time. Initially the star experiences close encounters with the MBHB, as apparent from the "noisy" pattern of $a_{\rm out}$. After $\simeq 1,500$ yrs the separation of the MBHs has greatly reduced because of GW emission, the star effectively "sees" an almost central potential at this stage, and its orbital separation stabilises. In fig. 2.7, lower panel, the argument of the star pericentre ω is compared to 2PN theoretical predictions accounting for the time variations of $a_{\rm out}$ and $e_{\rm out}$. Overall our results are in close agreement with those reported in Mikkola and Merritt (2008), although some minor numerical differences do exist, most probably due to the lack of regularization in our code. Given the quite chaotic behaviour in the initial phases of the evolution of system under study (confirmed by the large and erratic variations of $a_{\rm out}$), slightly numerical differences that arise during the integration can explain the observed (though small) discrepancy.

We then tested the implementation of the dissipative 2.5PN term, compar-

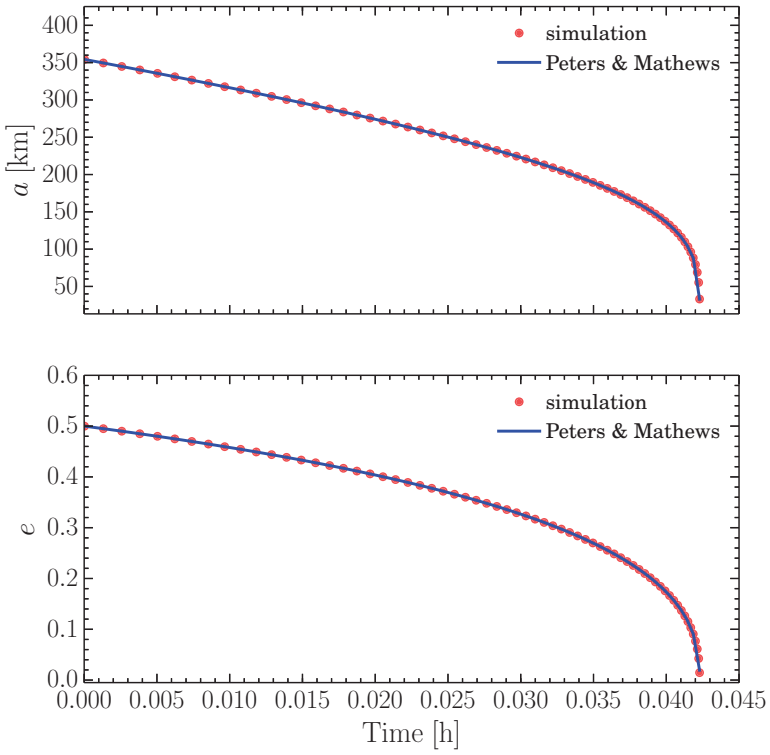

Figure 2.9: Same as fig. 2.8 except that the initial eccentricity is set to $e = 0.5$.

ing our results to the numerical integration of the orbit-averaged equation of Peters and Mathews (1963) for the time derivative of the semi-major axis and eccentricity, i.e.,

$$\dot{a} = -\frac{64G^3}{5c^5}\frac{m_1 m_2}{a^3(1-e^2)^{7/2}}\left(1 + \frac{73}{24}e^2 + \frac{37}{96}e^4\right) \tag{2.43}$$

$$\dot{e} = -\frac{304G^3}{15c^5}\frac{m_1 m_2}{a^4(1-e^2)^{5/2}}\left(e + \frac{121}{304}e^3\right). \tag{2.44}$$

We selected a stellar-size binary (see Galaviz and Brügmann, 2011) with $m_1 = 1\ \mathrm{M}_\odot$, $m_2 = m_1/2$, initial semi-major axis $a = 160G(m_1 + m_2)/c^2$, and two different values of the initial eccentricity, $e = 0.1$ and $e = 0.5$. We switched off the 1PN and 2PN terms, as eqs. 2.43 and 2.44 take into account only 2.5PN order corrections to the Newtonian dynamics. Figs. 2.8–2.10 shows the excellent agreement between simulations and analytical results.

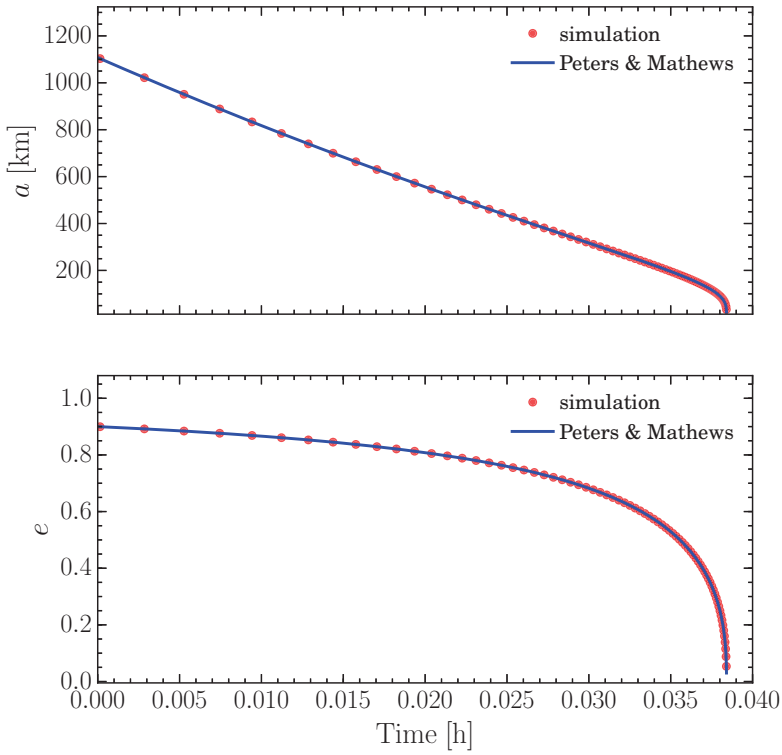

Figure 2.10: Same as fig. 2.8 except that the initial semi-major axis is set to $a = 500G(m_1 + m_2)/c^2$ and the initial eccentricity is set to $e = 0.9$.

2.2.3 Effects of numerical precision

We return here on the impact that the adopted numerical precision has on our results. We have already seen that in the Henon's Criss-Cross test the double and quadruple precisions give essentially the same output. We performed a further detailed analysis of the issue comparing simulations of the full dynamics of MBH triplets (i.e., all terms up to 2.5PN were considered). We found that the intrinsic chaotic nature of the three-body problem makes results quantitatively dependent upon the chosen numerical precision.[7] However, the qualitative behaviour of the simulated triplets appear to be fairly robust against round-off errors. This is shown in fig. 2.11, where we plot the relative separation (a,d panels), circularity (b,e panels) and inclination (c,f panels) of the inner binary. Note that single orbits are not recognisable on this time scale. The red line represents the semi-major axis of the inner binary. Results in quadruple (double) precision for a triple system with: $m_1 = 10^9 \mathrm{M}_\odot$, $m_2 = 3 \times 10^8 \mathrm{M}_\odot$, $m_3 = 5 \times 10^8 \mathrm{M}_\odot$, $a_{\rm out} = 4.43$ pc, $e_{\rm out} = 0.5$, $a_{\rm in} = 0.44$ pc, $e_{\rm in} = 0.8$, and $\iota = 80^\circ$ are shown in the a-c (d-f) panels.[8] In both cases the inner binary is bound to coalesce in few times 10^7 yrs, the precise timescale depending upon the adopted numerical precision. In fig. 2.12 we report the very same quantities for a similar triplet with initial $e_{\rm in} = 0$. In order to highlight the Kozai-Lidov oscillations experienced by the inner binary, we show a time zoom of the orbital evolution. Note that on this scale the only clear difference between quadruple and double precision integration is a slight temporal shift of the whole evolution.

We conclude our analysis of the effects of numerical precision by pointing out that quadruple precision typically takes, in terms of computer time, at least a factor $\gtrsim 10$ longer than double precision for the same set of parameters. Given this fact, the similar behaviour we witnessed in the test cases, and the fact that our final goal is a detailed survey of the parameter space of MBH triplets in a cosmological context, we decided to restrict our analysis to simulations in double numerical precision.

[7] This is known as the "shadowing" property of numerical solutions to deterministic chaotic systems. Indeed, for these systems, the details of a numerical solution are highly dependent on the round-off errors, but the calculated solution is very close to *some* trajectory of the system, i.e., it may not correspond exactly to the desired trajectory, but to another possible trajectory of the system (namely, one with slightly different initial conditions). See, e.g., Hilborn (1994).

[8] The initial conditions of the simulations performed in this thesis are determined according to Newtonian dynamics.

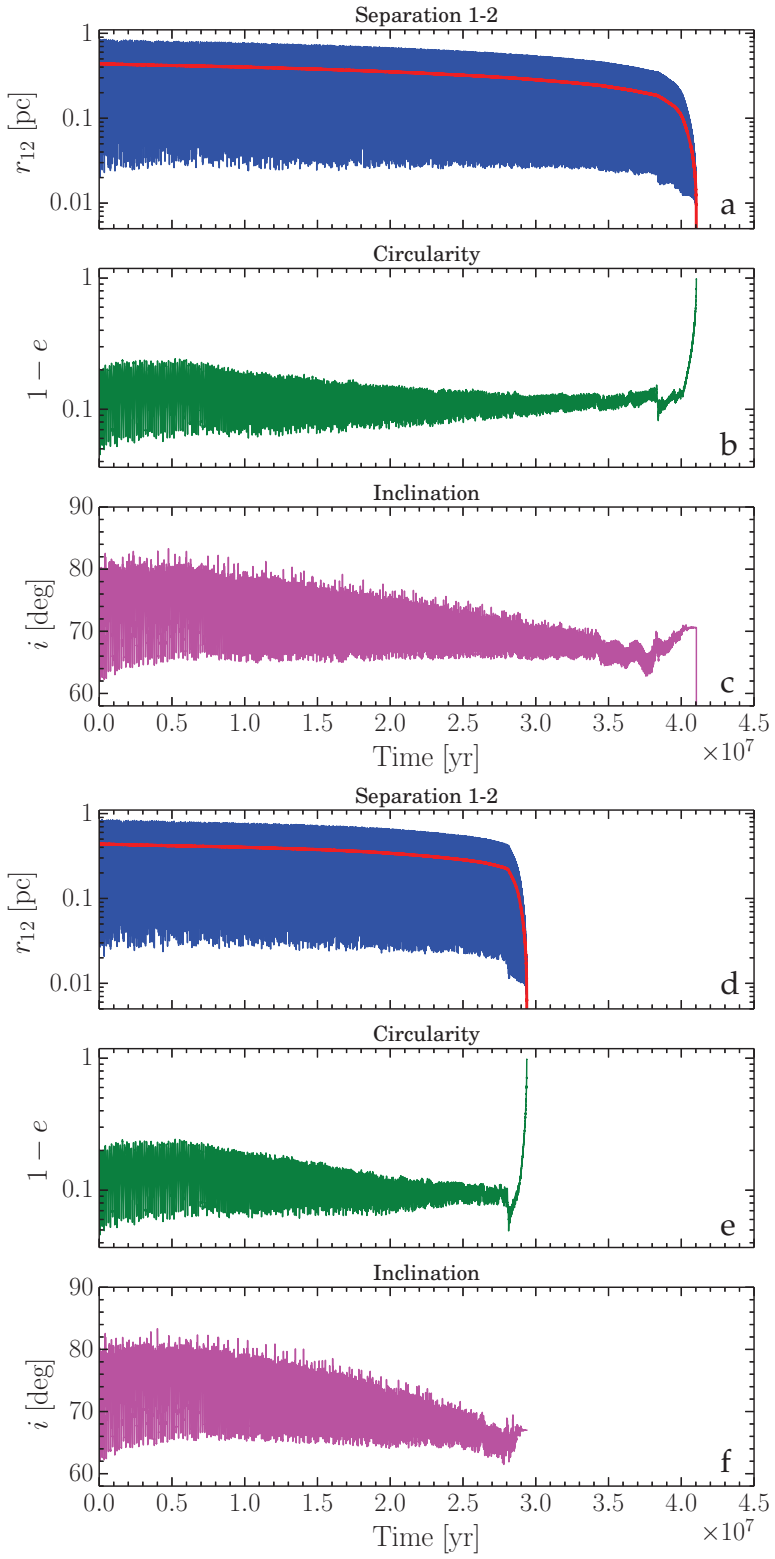

Figure 2.11: The relative separation (a,d panels), circularity (b,e panels) and inclination (c,f panels) are shown for the inner binary of a hierarchical triplet with $m_1 = 10^9 \mathrm{M}_\odot$, $m_2 = 3 \times 10^8 \mathrm{M}_\odot$, $m_3 = 5 \times 10^8 \mathrm{M}_\odot$, $a_{\rm out} = 4.43$pc, $e_{\rm out} = 0.5$, $a_{\rm in} = 0.44$pc, $e_{\rm in} = 0.8$, and $\iota = 80°$. The solid red line is $a_{\rm in}$. Quadruple (double) precision calculation in a-c (d-f) panels.

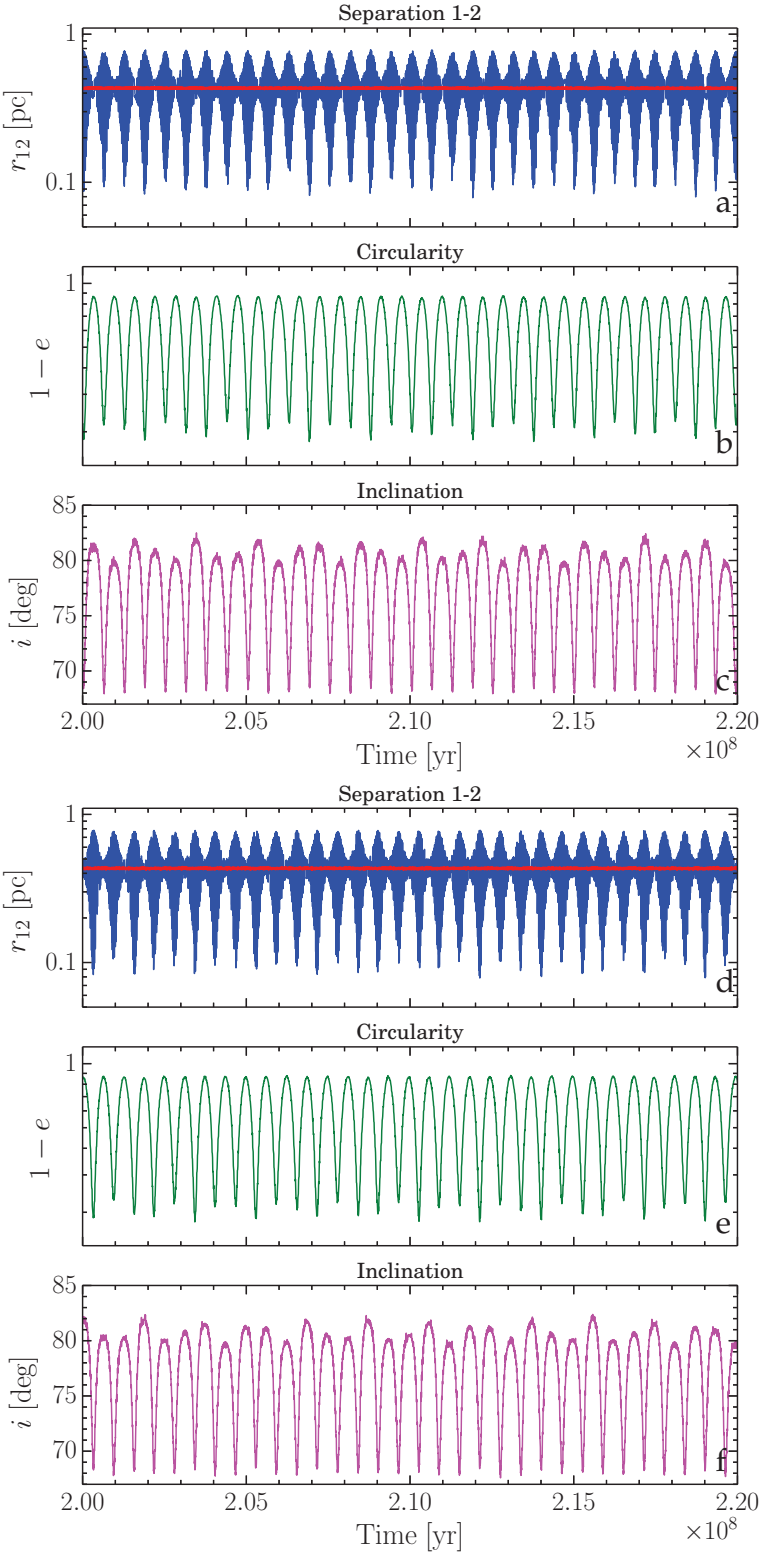

Figure 2.12: Same as fig. 2.11 but assuming an initial $e_{\rm in} = 0$. Note the different temporal scale compared to fig. 2.11.

2.3 Dynamics of MBH triplets

2.3.1 Standard three-body dynamics

We start by considering the standard three-body problem, i.e., the interaction of three MBHs (including relativistic corrections up to order 2.5PN) without the inclusion of any external force due to, e.g., the stellar environment. We study the particular case of (initially) hierarchical triplets, i.e., three-body systems that can be modelled as two separate binaries: an inner, close one (m_1 and m_2) and a much wider one formed by the intruder m_3 and the centre of mass of the former.

A hierarchical triplet is prone to a peculiar dynamical phenomenon of purely Newtonian origin, known as the Kozai-Lidov (K-L) mechanism (Kozai, 1962; Lidov, 1962). If the relative inclination between the inner and outer binary is larger than a critical angle ($\simeq 39.23°$), then a periodic exchange between the inclination and the eccentricity of the inner binary occurs on a timescale

$$t_{\rm KL} \sim \frac{a_{\rm out}^3(1-e_{\rm out}^2)^{3/2}\sqrt{m_1+m_2}}{G^{1/2}a_{\rm in}^{3/2}m_3} \simeq 2\times 10^6 \ \ {\rm yrs}, \tag{2.45}$$

where the numerical value reported above is for a MBHB with $m_1 = m_2 = m_3 = 10^8\ {\rm M}_\odot$, $a_{\rm in} = 1$ pc, $a_{\rm out} = 10$ pc, and $e_{\rm out} = 0$.

The most important feature of the K-L mechanism is the excitement of periodic oscillations of $e_{\rm in}$ at the expenses of the relative inclination of the two binaries: $e_{\rm in}$ has a maximum when the relative inclination of the two binaries reaches its minimum value and vice-versa. In this situation the emission of GWs is highly efficient, hence the K-L mechanism ultimately promotes the coalescence of the inner binary, possibly easing the final parsec problem. Indeed, the oscillations of $e_{\rm in}$ can in principle reduce the coalescence timescale by orders of magnitude.

However, as already pointed out, the K-L mechanism is a purely Newtonian phenomenon, and the inclusion of relativistic corrections to Newtonian dynamics can have dramatic consequences on the K-L mechanism itself (see Blaes, Lee, and Socrates, 2002). The very process relies on the libration of the pericenter argument of the inner binary. Since relativistic effects cause the precession of this orbital element, if the K-L timescale is longer than the relativistic precession timescale, the oscillations of $e_{\rm in}$ can be strongly inhibited compared to the purely Newtonian case.

As an example, we consider a triplet with the following parameters: $m_1 = 10^9{\rm M}_\odot$, $m_2 = 3\times 10^8{\rm M}_\odot$, $m_3 = 5\times 10^8{\rm M}_\odot$, $e_{\rm out} = 0.5$, $a_{\rm in} = 0.4$pc, $e_{\rm in} = 0.5$, and $\iota = 80°$, and two different values of $a_{\rm out}$. In fig. 2.13 we compare the 2.5PN (red lines) and purely Newtonian (green lines) dynamical evolution of the system, assuming $a_{\rm out} = 4$ pc. We plot the relative separation (upper panels), circularity (middle panels) and inclination (lower panels) of the inner binary. The top panels display the evolution for a time spanning almost 1 Gyr. The oscillations present in the Newtonian case are the modulation (ascribable to the octupole term) of the K-L oscillations (due instead to the quadrupole term).

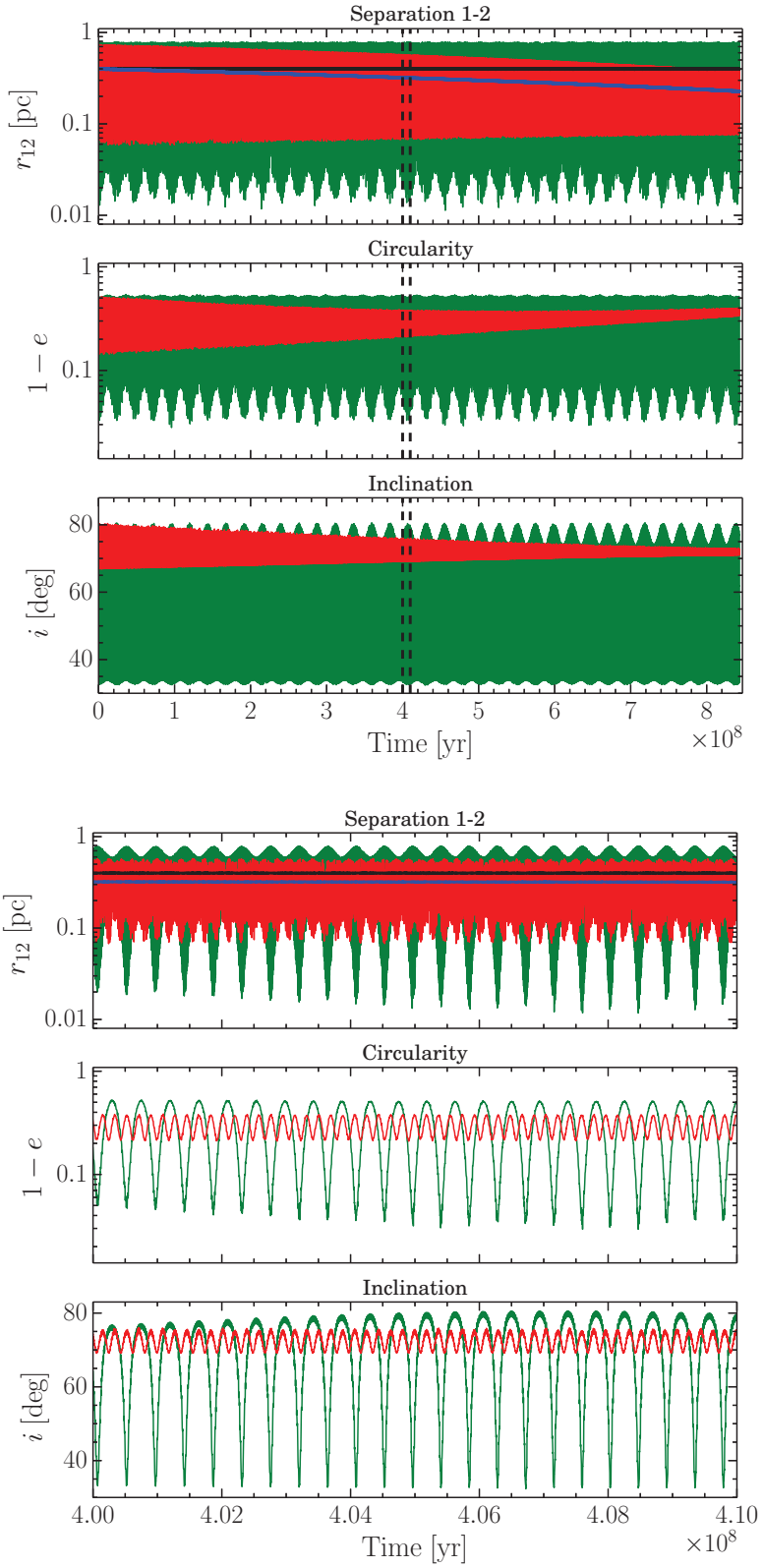

Figure 2.13: A triplet with $m_1 = 10^9 \mathrm{M}_\odot$, $m_2 = 3 \times 10^8 \mathrm{M}_\odot$, $m_3 = 5 \times 10^8 \mathrm{M}_\odot$, $a_{\rm out} = 4$ pc, $e_{\rm out} = 0.5$, $a_{\rm in} = 0.4$ pc, $e_{\rm in} = 0.5$, and $\iota = 80°$ is considered. Relative separation (upper panels), the circularity (middle panels) and the inclination (lower panels) of the inner binary are plotted against time. Red colour refers to results from 2.5PN calculations, while the corresponding Newtonian values are shown in green. The blue (black) line represents the 2.5PN (Newtonian) value of the semi-major axis $a_{\rm in}$. *Top*: entire run. The vertical dashed lines frame the time interval zoomed in the bottom panels. *Bottom*: the 10 Myr time zoom.

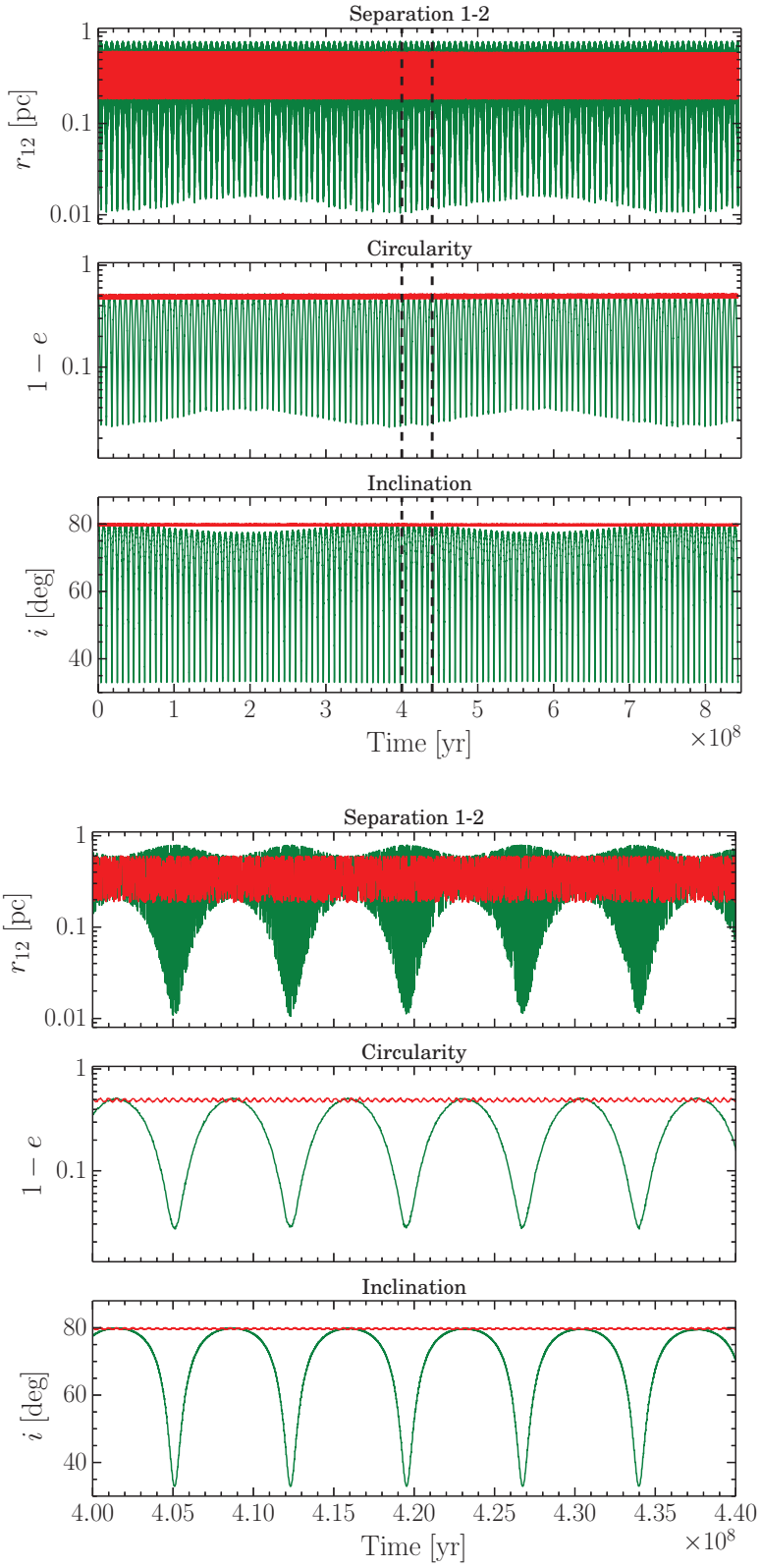

Figure 2.14: Same as fig. 2.13 but for $a_{\rm out} = 10$ pc. Here $a_{\rm in}$ is not plotted as it stays nearly constant even in the 2.5PN calculations. *Top*: entire run. The vertical dashed lines frame the time interval zoomed in the bottom panels. *Bottom*: the 40 Myr time zoom.

Note how the effect of GW emission manifests itself in the PN quantities, i.e., in a decrease of the semi-major axis (blue line) compared to the Newtonian case (black line), and in orbital circularisation. The K-L oscillations are resolved in the bottom panels, where a time zoom of 10 Myr highlights the significant damping of K-L oscillations when relativistic effects are included.

Fig. 2.14 shows the very same triplet, but assuming $a_{\rm out} = 10$ pc. Since the K-L timescale has a strong dependence upon $a_{\rm out}$ (see eq. 2.45), in this case relativistic precession is comparatively shorter, hence completely destroying the K-L oscillations.

2.3.2 Three-body dynamics in stellar environments

We finally analyse few examples of triplet dynamics including the effect of the stellar background, as discussed in section 2.1. Our initial conditions consist of an inner MBHB ($m_1 = 10^8 {\rm M}_\odot$, $m_2 = 3 \times 10^7 {\rm M}_\odot$) stalled on an elliptical orbit ($e_{\rm in} = 0.2$) at the centre of a spherical stellar distribution (cf. eqs. 2.36–2.38), and a third, initially far MBH ($m_3 = 5 \times 10^7 {\rm M}_\odot$) sinking in the global potential well because of dynamical friction. We initialise m_3 on an elliptical orbit ($e_{\rm out} = 0.3$) at a distance from the centre of the order of the bulge scale radius. The properties of the stellar distribution (see section 2.1.2 and section 2.1.3) are determined by the mass of the inner MBHB following the scaling relations described in section 2.1.2 (for full details see Sesana and Khan, 2015). Our choice of the inner binary mass then gives a stellar mass $M_\star = 3.2 \times 10^{10} {\rm M}_\odot$ (the corresponding velocity dispersion is $\sigma = 164$ km/s), a scale radius $r_0 = 1.2$ kpc, and a core radius $r_c = 270$ pc.

In the simulations, dynamical friction (section 2.1.4) operates on m_3 from the very beginning, while the hardening process (section 2.1.1) is activated when the intruder reaches the influence radius of the outer binary (i.e., for a hierarchical triplet, the radius containing a mass in stars twice the total mass of the three MBHs). As the triplet evolution proceeds, the hardening process on the outer binary becomes more important than dynamical friction on m_3. Then, we turn off effect of dynamical friction as soon as the intruder effectively binds to the inner binary, hence forming a genuine, hierarchical bound triplet.[9] Eventually, dynamical friction is re-activated when, after chaotic encounters, a MBH is kicked at greater distances and is again dominated by the stellar distribution.

The numerical implementation of the hardening process is switched off (and never re-activated) whenever the triplet, according to the stability criterion of Mardling and Aarseth (2001), is no longer hierarchical. When this occurs, in fact, the system dynamics is dominated by chaotic three-body interactions, and the hardening recipe described by eqs. 2.12 and 2.13, derived for isolated binary systems, is no longer valid.

[9] Note that a bound binary is not necessarily hard (indeed, dynamical friction operates on a light intruder well within the influence radius of the inner binary, see e.g., Antonini and Merritt, 2012). We therefore run test simulations allowing the dynamical friction to continuously operate after the formation of a bound triplet, and we checked that the overall evolution of the system is not qualitatively different compared to our standard cases.

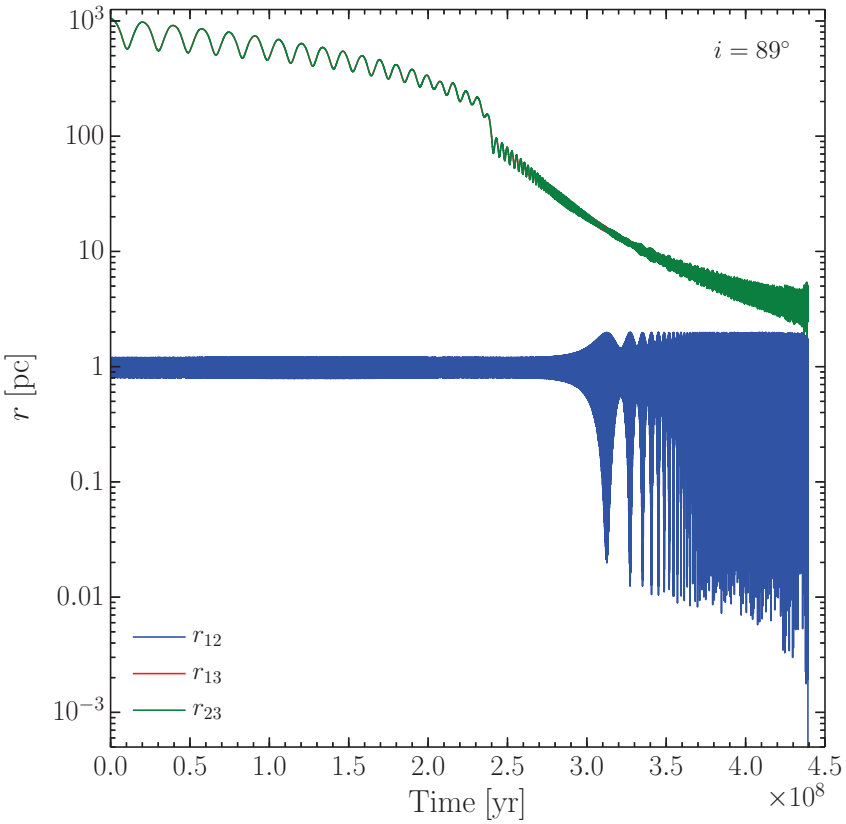

Figure 2.15: Full evolution of a MBH triplet ($m_1 = 10^8 \mathrm{M}_\odot$, $m_2 = 3 \times 10^7 \mathrm{M}_\odot$, $m_3 = 5 \times 10^7 \mathrm{M}_\odot$, $a_{\rm in} = 1$pc, $e_{\rm in} = 0.2$, $\iota = 89°$) in a stellar environment. The relative separation (in log scale) between m_1 and m_2 is shown in blue, that between m_2 and m_3 in green, and that (though not clearly visible, see text for details) between m_1 and m_3 in red.

At the beginning of our simulations, we assume that that the centre of the stellar potential always coincides with the inner binary centre of mass. When the third body actually forms a bound triplet, we instead consider that the centre of the stellar distribution lies in the triplet centre of mass. Physically, one expects the innermost stellar distribution to adjust, following the dominating MBH gravitational influence. Practically, for the examples here presented, the code moves the triplet (binary) centre of mass to the origin of the reference system, where the stellar distribution is centred. The process is replicated every 1000 time-steps (about every one hundred orbits of the inner binary).[10] In the following we discuss the evolution of triplet+stellar bulge system, assuming four different values of the initial relative inclination between the inner and the outer binary.

In fig. 2.15 we plot, as a function of time from the start of the simulation, the relative separation between the three MBH pairs (r_{12} in blue, r_{13} in red, and r_{23}

[10] See however next chapter for an alternative algorithm.

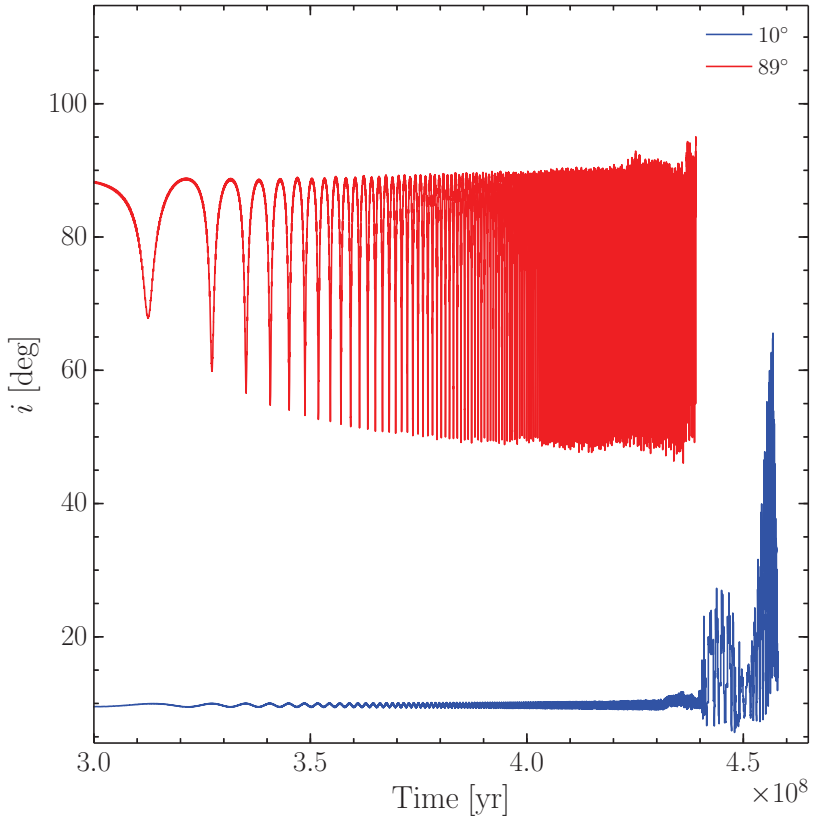

Figure 2.16: Time evolution of relative inclination ι of the two binaries. Upper red curve is for the case of an initial value $\iota = 89°$, lower blue curve is for $\iota = 10°$.

in green) assuming for the inclination a value of $\iota = 89°$. The evolution can be described by an initial phase lasting ≈ 230 Myr when the intruder sinks because of dynamical friction, while the inner binary is basically unperturbed. Then a bound triplet forms, and the outer binary keeps shrinking because of stellar hardening. At ≈ 300 Myr the outer binary has shrunk enough to excite K-L oscillations in the inner binary, as clearly shown by the huge periodic variations of r_{12}. The K-L mechanism is so effective in periodically increasing $e_{\rm in}$, that after $t = 439$ Myr from the start of the simulation the inner binary coalesces because of GW emission. It is worth noticing that, from the point of view of m_3, the inner binary is essentially a point mass, so that $r_{13} \simeq r_{23}$ (i.e., the green and red lines are coincident). Note also that single orbits of the inner binary are not recognisable in the figure. The relative inclination of the two binaries is plotted in fig. 2.16, upper red curve, as a function of time, clearly showing the oscillations that occur on the (reducing) K-L timescale.

A further interesting case is shown in fig. 2.17, where we set $\iota = 80°$. Though the inclination is large enough to excite the K-L oscillations (as clearly shown by the blue line in the top panel), the increase of $e_{\rm in}$ is sensitively lower compared to the $\iota = 89°$ case (note the different y-axis scale in fig. 2.15). This allows the outer binary to shrink more since the hardening process can operate for a

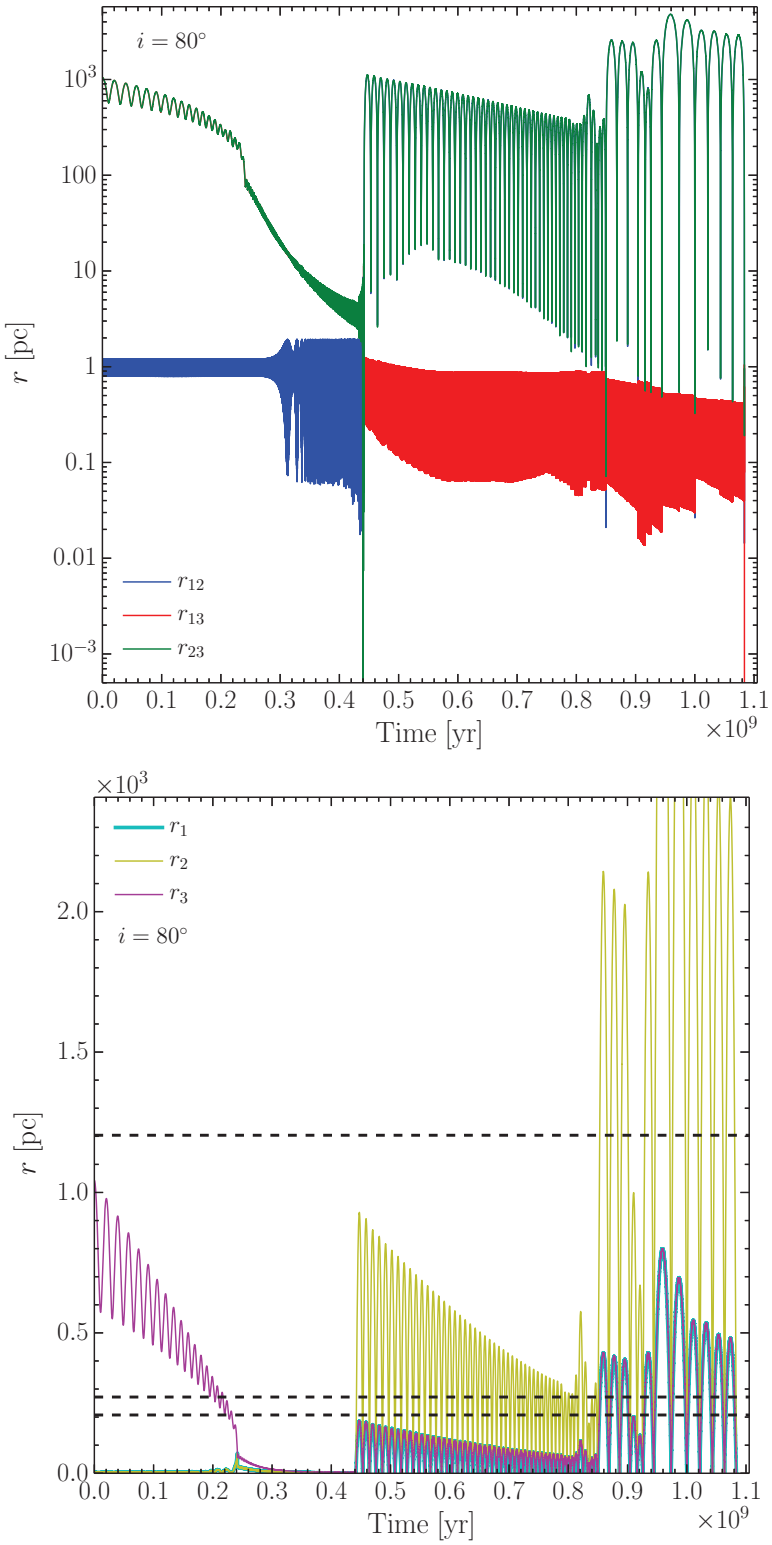

Figure 2.17: Same as fig. 2.15 but assuming an initial inclination $\iota = 80°$. *Top*: relative separations. *Bottom*: distance of the MBHs from the centre of the stellar distribution. The dashed black lines represent, from top to the bottom, the bulge scale radius, the bulge core radius, and the influence radius of the "original" inner binary (i.e., $m_1 + m_2$), respectively. Note in both panels the exchange event between m_2 and m_3 occurring at $t \simeq 440$ Myr.

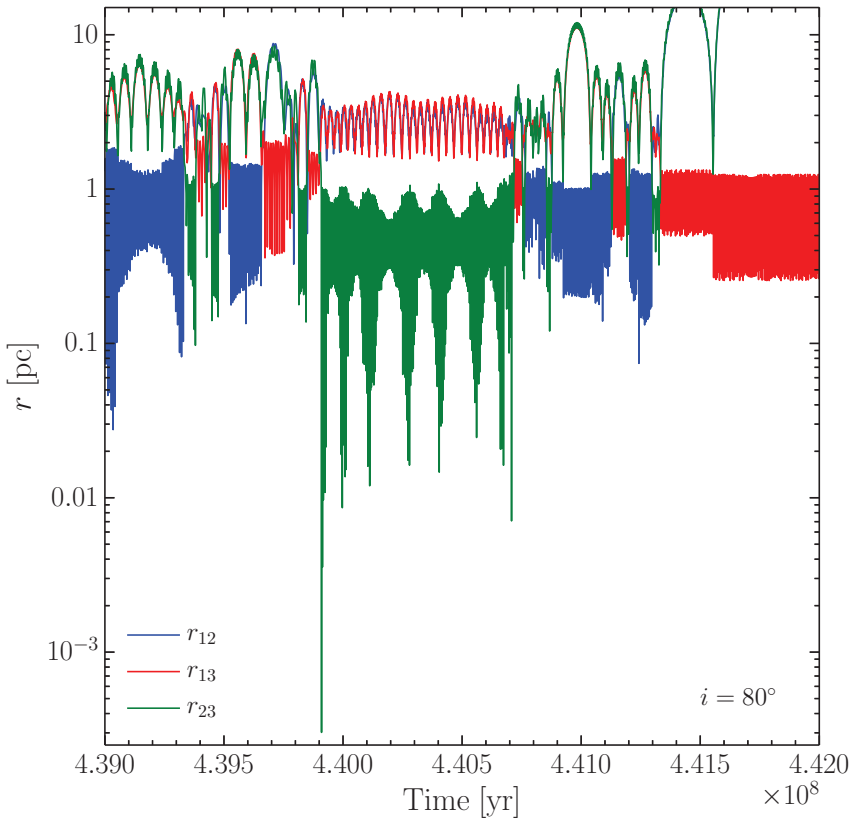

Figure 2.18: Same as top panel of fig. 2.17, zooming in the exchange event occurring at $t \simeq 440$ Myr.

longer time, undermining the secular stability of the triplet. Indeed, at $t \simeq 440$ Myr, an exchange event between m_2 and m_3 occurs, as seen by the sudden appearance of the red line, i.e., the inner binary is now $m_1 + m_3$. The exchange complexity is clearly shown in the time zoom-in of the event (see fig. 2.18). As a consequence of the exchange, m_2 is kicked on a very eccentric and much wider orbit, while at the same time the inner binary is relatively stable for the next $\simeq 500$ Myr. At this point a further close encounter with m_2 forces the inner binary eccentricity to greatly increase, then leading to coalescence after $\simeq 1$ Gyr from the start of the simulation. We must point out that in this particular case all the MBHs experience almost radial oscillations of large amplitude. This can be seen in the bottom panel of fig. 2.17, where we plot the time evolution of the distance of each of the three MBHs from the centre of the stellar distribution.

A case with $\iota = 20°$ is shown in fig. 2.19. K-L oscillations are not excited since the inclination is below the nominal threshold of $\simeq 39°$. The "original" inner binary is not going to coalesce, then. However, after $\simeq 420$ Myr, m_3 and the inner binary experience an energetic close encounter whose final outcome is an exchange between m_2 and m_3. While m_2 is kicked on a very eccentric and much wider orbit, the inner binary (now $m_1 + m_3$, shown again by the red line) is relatively stable for the next $\simeq 500$ Myr. At this point a fly-by of m_2

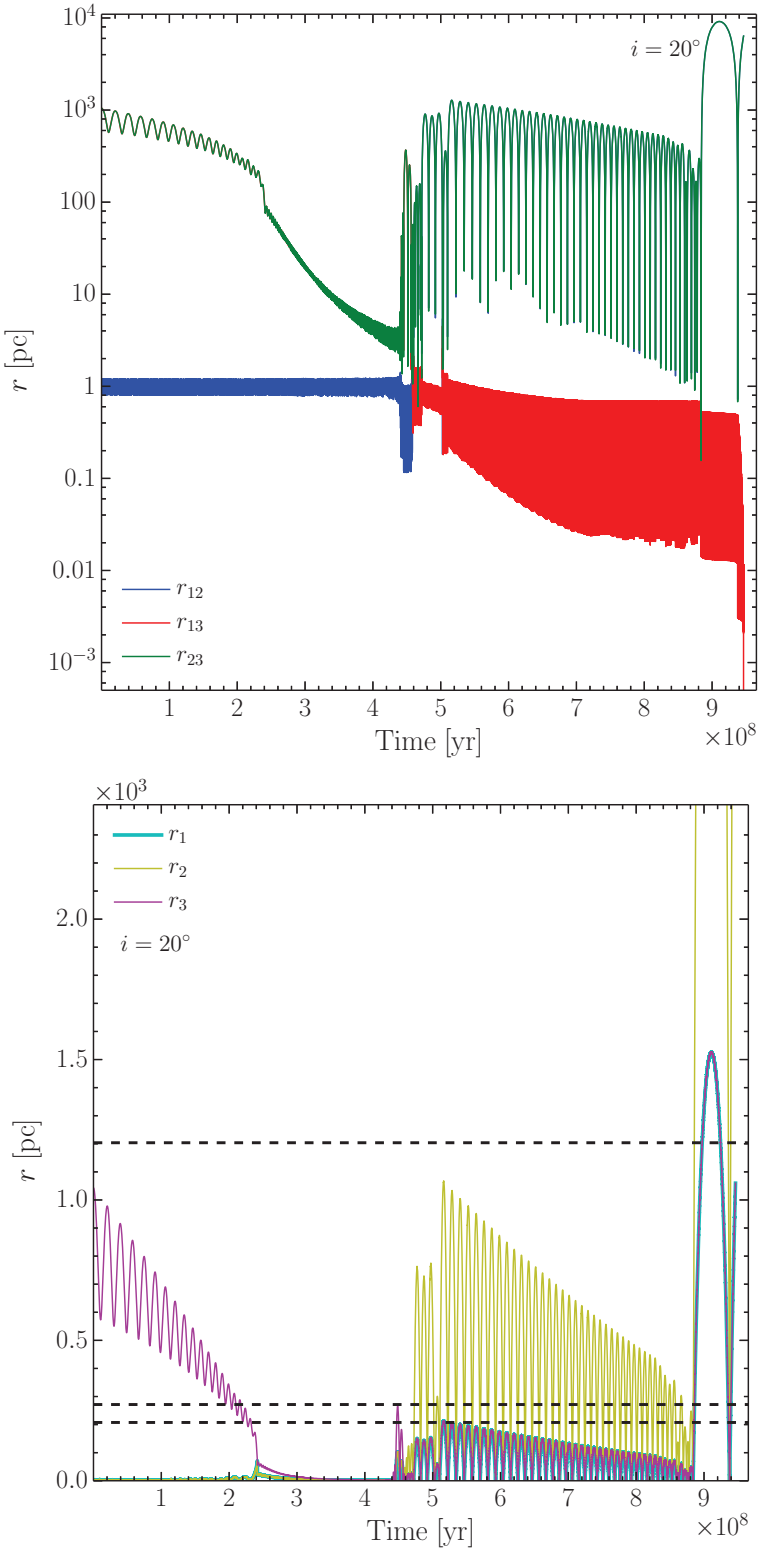

Figure 2.19: Same as fig. 2.17 but assuming an initial inclination $\iota = 20°$.

(which is on a very eccentric, shrinking orbit) forces the inner binary eccentricity to greatly increase, then leading to coalescence within the next $\simeq 10$ Myr (see fig. 2.20). Also in this case, the three MBHs are slingshot on almost radial orbits in the stellar potential. Indeed, the coalescence of the inner binary occurs when it lies at $\simeq 1$ kpc from the centre of the stellar distribution.

We must note that, whenever the MBHs are forced on almost radial kpc-scale orbits as in the last two cases discussed, the possible triaxiality of a more realistic stellar distribution could alter the dynamics of the triplet, possibly delaying any close encounter between m_2 and the inner binary. Another feature that could determine a delay in successive close encounters is a net rotation of the stellar structure. In this situation, when a MBH is kicked on a radial orbit it feels the gravitational pull generated by the bulk motion of the stars coming from a specific direction. The angular momentum of the MBH orbit gets increased and the pericentre of the next passage becomes larger, implying a less strong encounter with the binary. Finally, the granularity of real galaxies could also modify the returning time of a kicked MBH, but differently from the aforementioned processes, the interaction of a MBH with molecular clouds/spirals/globular clusters could instead result either in an increase or a decrease of the wandering time (Fiacconi et al., 2013; Roškar et al., 2015). We plan to include and analyse some of these additional features in the next implementation of our code.

We finally analyse a system with relative binary inclination set to $\iota = 10°$. Despite of the low initial inclination, the inner binary is bound to coalesce after $t = 458$ Myr, as shown in fig. 2.21. After $\simeq 440$ Myr, the triplet evolution is characterised by many close encounters (we also witness four exchanges) that increase the relative inclination above the K-L critical angle. The final outcome is most probably determined by K-L oscillations with contribution from higher orders (see Li et al., 2014). Note that during the last Myr before the binary merger, the pericenter is as small as $\simeq 1$ mpc, thus making the system a suitable candidate for a PTA burst-like signal.

The time evolution of the relative inclination of the two binaries is shown in fig. 2.16, lower blue curve. As the intruder gets close enough to the inner binary, small periodic variations of ι on long timescales (most probably led by high order K-L resonances) are excited. It is only when the three bodies experience the final close encounters at $t \simeq 440$ Myrs (eventually leading to the coalescence of the inner binary) that the rapid changes in inclination become large and erratic.

2.4 Discussion

2.4.1 Relevance of the dynamical ingredients included in the code

The test runs shown in the previous section reveal an extremely complex and diverse phenomenology, in which all the ingredients included in the modelling play a relevant role. Stellar hardening is crucial in bringing the intruder first down to a separation where K-L resonances can be effectively excited (~ 10 pc

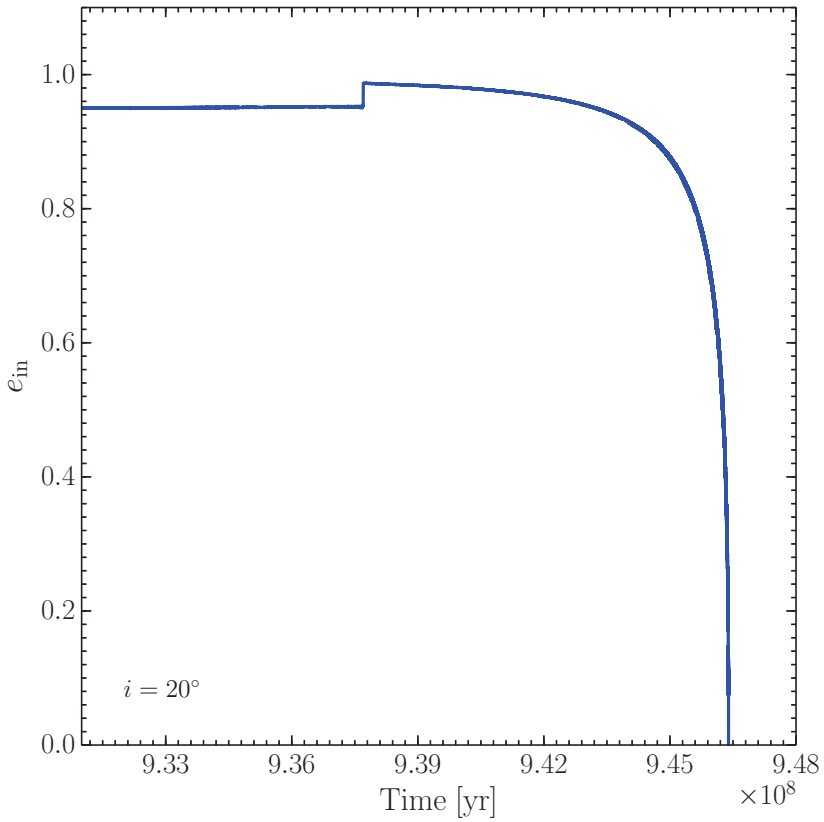

Figure 2.20: The final phase of the $\iota = 20°$ case. A fly-by of m_2 at $t \simeq 937$ Myr causes $e_{\rm in}$ to grow form $\simeq 0.95$ to $\simeq 0.99$, leading the inner binary to coalesce within the next $\simeq 10$ Myr.

for the specific masses examined), and then further down to experience strong interactions with individual components of the inner binary. K-L resonances require that the properties of the inner binary do not change over a time $t_{\rm KL}$ (eq. 2.45). Although this is a safe condition for a Newtonian system, it easily breaks down when general relativistic effects are included. In fact, as firstly demonstrated by Blaes, Lee, and Socrates, 2002, relativistic induced precession at 1PN and 2PN order can suppress K-L resonances. Considering only the leading 1PN order for simplicity, a comparison between the K-L and relativistic precession rates yields (Chen et al., 2011)

$$\frac{\dot{\omega}_{\rm KL}}{\dot{\omega}_{\rm GR}} \sim \frac{m_3}{m_1+m_2}\left(\frac{a_{\rm in}}{a_{\rm out}}\right)^3 \frac{a_{\rm in}}{R_{\rm S,in}} \frac{(1-e_{\rm in}^2)^{1/2}}{(1-e_{\rm out}^2)^{3/2}}, \tag{2.46}$$

where $R_{\rm S,in} = G(m_1+m_2)/c^2$ is the "equivalent" gravitational radius of a MBH with mass equal to the mass of the inner binary. The K-L mechanism is effective only when $\dot{\omega}_{\rm KL} > \dot{\omega}_{\rm GR}$. For example, given a specific inner binary, the intruder has to shrink to a small enough $a_{\rm out}$ to trigger it. This is what we have shown in figs. 2.13 and 2.14, where the system with smaller $a_{\rm out}$ (fig. 2.13)

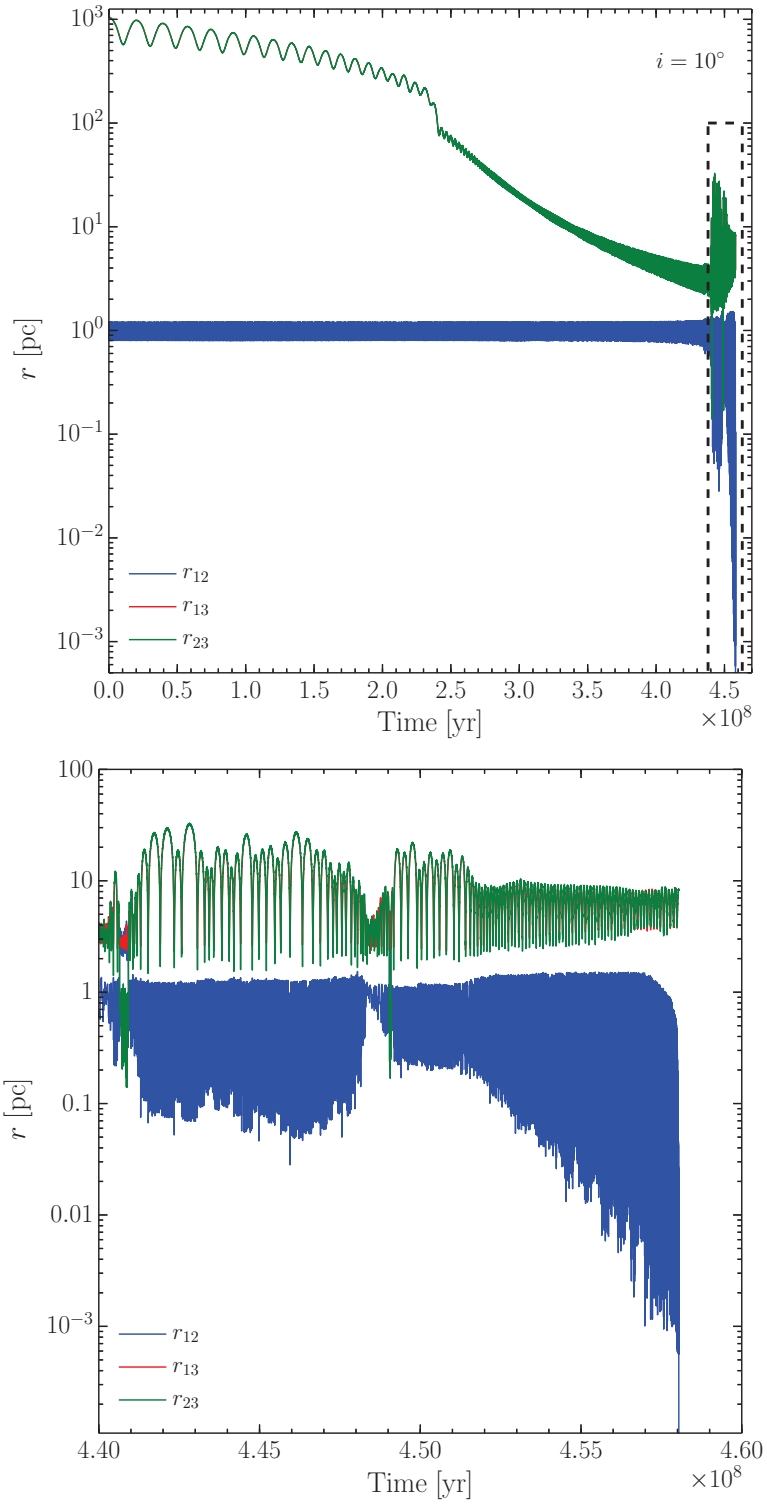

Figure 2.21: Same as fig. 2.15 but assuming $\iota = 10°$. *Top*: entire run. The vertical dashed lines frame the time interval zoomed in the bottom panel. *Bottom*: the 20 Myr time zoom.

undergoes more effective K-L cycles. Note how the GW driven hardening of the inner binary progressively suppresses the effect. This is because $a_{\rm in}$ decreases, bringing down the $\dot{\omega}_{\rm KL}/\dot{\omega}_{\rm GR}$ ratio in eq. 2.46. The exact point at which K-L becomes effective also depends on the mass ratio of the intruder with respect to the inner binary, and on the eccentricities of the inner vs. the outer binary. Note that as $e_{\rm in}$ increases, the ratio $\dot{\omega}_{\rm KL}/\dot{\omega}_{\rm GR}$ decreases. Therefore, the K-L mechanism might eventually self-regulate itself: as it grows the inner binary more eccentric, it also makes relativistic precession more effective. The condition $\dot{\omega}_{\rm KL} > \dot{\omega}_{\rm GR}$ might therefore not be satisfied any longer, thus suppressing the K-L effect and eventually altering the overall dynamics of the system.

Although our investigation is similar in spirit to that of Hoffman and Loeb, 2007, the above discussion highlights the importance of the differences in the two implementations. In particular, Hoffman and Loeb, 2007 did not include 1PN and 2PN relativistic precession in their equations. This might significantly alter the overall statistical properties of merging binaries (e.g., eccentricities, coalescence timescales) because, as we just discussed, the conditions for triggering K-L resonances, and thus the general dynamics of the system, are different. Moreover, our treatment of the hardening in the stellar background is more accurate, since it also reproduces the eccentricity evolution in the hardening phase. This is important because i), it affects the triggering point of K-L cycles (eq. 2.46), and ii), it has a strong impact on the stability of the hierarchical triplet and on the probability of close encounters leading to chaotic behaviour.

2.4.2 Astrophysical implications

The few cases examined here already provide some interesting astrophysical insights that we briefly outline in the following.

In all our simulations, two of the MBHs (not necessarily those originally forming the inner binary) coalesce in less than 1 Gyr from the start of the dynamical friction phase of the intruder. Therefore, triple interactions might provide a viable channel to merge MBH binaries in massive, low density galaxies, where hardening against the stellar and gaseous background might act on a timescale of several Gyrs (Khan, Just, and Merritt, 2011; Vasiliev, Antonini, and Merritt, 2015; Sesana and Khan, 2015). At least a fraction of massive elliptical galaxies, which host the most massive binaries targeted by PTAs, might realistically undergo multiple mergers at $z \lesssim 1$ (see Gerosa and Sesana, 2015, and references therein). If the typical coalescence timescale of the formed MBHBs is several Gyrs, then the occurrence of a second merger will bring in an intruder, typically leading to coalescence on a much shorter timescale. Triple interactions might therefore be an important channel for merging very massive, gas-poor low redshift binaries. Whether it is also important for lower mass system at higher redshifts is less clear. The larger availability of cold gas, together with extremely high density environments (Khan et al., 2016) might in fact result in more efficient coalescences on a timescale $\lesssim 10^8$yr. Note, however, that mergers are way more common at high z, and that the relevant dynamical timescales are also much shorter. If seed black holes are abundant in high

redshift protogalaxies, it is then possible that many triple systems will form following subsequent galaxy mergers.

The dynamics of individual triplets presents in itself extremely interesting features. For example, the system shown in fig. 2.17 undergoes a close encounter at $T \approx 440$Myr, with a closest passage at $\lesssim 10^{-3}$ pc. On the other hand, all the other cases show a late phase when $e_{\rm in} \gtrsim 0.99$, eventually promoting the final coalescence of the inner binary. In particular, in fig. 2.21 we see that the inner system spends its last million years of life with $e_{\rm in} \approx 0.999$ before coalescence. If this behaviour is general, then it carries important consequences for the GW signals expected from these sources. Indeed, Amaro-Seoane et al. (2010) showed that a very eccentric binary emits relatively broad-band bursts centred at frequency $f \propto [a(1-e)]^{-3/2}$ (which is the frequency of a circular binary with semimajor axis equal to the periastron of the eccentric system), which we can parametrise as (see Wen, 2003; Antonini et al., 2016)

$$f \approx 4 \times 10^{-7}\mathrm{Hz} \left(\frac{M}{10^8 \mathrm{M}_\odot}\right)^{-1} \left(\frac{\alpha}{100}\right)^{-3/2}. \tag{2.47}$$

Here $\alpha = r_p/R_{\rm S,in}$, where r_p is the binary periastron. Note that, for $M = 10^8 M_\odot$, $\alpha = 100$ corresponds to $r_p \approx 1$ mpc, which is the typical value found in our test cases. Therefore, right before coalescence or during extremely close encounters (such as the one shown in fig. 2.17), these systems will emit intense bursts of gravitational radiation of the duration of ≈ 1 month (for the masses considered here), which might be detectable by PTAs. Moreover, if binaries typically coalesce with resonance-induced high eccentricities (as in most of the cases shown here), there might be other profound consequences for the overall GW signal that PTAs are hunting. In the most extreme scenario, very high eccentricities will dramatically suppress the low frequency signal, shifting most of the emitted power at higher frequencies. Moreover, the statistical properties of the signal might look quite different, featuring a collection of burst-like events of duration of months-to-years, rather than the superposition of continuous periodic sources. Although eq. 2.47 gives the central frequency of the signal, the burst is expected to be broad-band, possibly extending to frequencies more than an order of magnitude higher (for $e \gtrsim 0.99$). Although Amaro-Seoane et al., 2010 found that massive ($M \gtrsim 10^8 \mathrm{M}_\odot$) systems are extremely unlikely to burst in the LISA band, if triplets are also common among low mass systems in the high redshift Universe, burst-like signals may also be a relatively frequent occurrence in the LISA band.

2.5 Summary

We devoted this second chapter to the description and validation of a new, original numerical code able to treat the relativistic dynamics of MBH triplets up to 2.5PN order. We included a simple prescription for dynamical friction, and an ad-hoc designed fictitious force that reproduces both the semi-major axis and the eccentricity evolution of MBHB hardening in a stellar background.

The effect of the stellar background itself is included in the equations of motion, providing additional insight in the dynamics. We tested the stability of the code with a number of standard tests and by comparing the dynamical outcome of complex cases to results obtained by other groups with the ARCHAIN code, finding in general a fairly good agreement. We also tested the importance of non-dissipative 1PN and 2PN terms in the dynamical evolution of the system, showing how they alter the excitation of K-L resonances.

Our code includes most of the physics relevant to the dynamics of massive triplets in stellar systems, and it can be expanded (as we have planned) to include further dynamical features, such as the effects of a non-spherical potential. The code is versatile and fast enough to allow an efficient exploration of the parameter space relevant to astrophysical triplets, which will be the topic of the next chapter.

Chapter 3

MBH triplets: exploration of the parameter space

The present chapter is devoted to a systematic study of the parameter space of MBH triple systems, necessary to quantify the cosmological and astrophysical relevance of such systems. In practice, we explore different MBH masses, mass ratios, eccentricities and relative inclinations, characterising the statistics of coalescing MBHB, i.e, quantifying the dependence on the physical parameters, and hinting at possible signatures imprinted on the emitted GW signal.

The chapter is organised as follows: we begin by describing the computational setup used to perform the simulations. We next proceed in presenting the results of our wide set of simulations, reporting a detailed analysis about merger fractions, timescales and eccentricity distribution. Finally, in more detail, we discuss the strengths and caveats of our work.

3.1 Methodology

We numerically integrate the orbits of MBH triplets formed by a stalled MBHB at the centre of a stellar spherical potential, and by a third MBH approaching the system from kpc-scale distances.

The host's stellar distribution is modelled by an Hernquist profile (Hernquist, 1990) with a central core, where the total mass and the scale length are consistently determined from empirical scaling relations (e.g., Dabringhausen, Hilker, and Kroupa, 2008; Kormendy and Ho, 2013), as detailed in chapter 2. The shallow density core mimics the erosion of the central region caused by the stalled inner binary (see, e.g., Ebisuzaki, Makino, and Okumura, 1991; Volonteri, Madau, and Haardt, 2003; Antonini, Barausse, and Silk, 2015a; Antonini, Barausse, and Silk, 2015b), with the mass deficit quantified as in Merritt (2013), Antonini, Barausse, and Silk (2015a), and Antonini, Barausse, and Silk (2015b).

Table 3.1: Parameter space sampling

Initial conditions	
$\log(m_1)$ [$M_\odot$]	5, 6, 7, 8, 9, 10
$\log(q_{\rm in})$	-1.5, -1.0, -0.5, 0.0
$\log(q_{\rm out})$	-1.5, -1.0, -0.5, 0.0
$e_{\rm in}$	0.2, 0.4, 0.6, 0.8
$e_{\rm out}$	0.3, 0.6, 0.9
$\cos\iota$	13 values equally spaced in $(-1, 1)$

We do not consider any dark matter (DM) extended component associated to the stellar background.

In principle, the complete characterisation of a MBH triplet requires to specify 14 initial conditions: the three MBH masses; the two semi-major axes and eccentricities; the argument of pericentre, the node and the orbital phase for both the inner binary and the intruder; and the relative inclination of the two orbital planes. However, given the initial hierarchical nature of the triplet, the parameters that have the largest impact on the dynamics are the MBH masses, the eccentricities and the relative inclination, thus defining a 6-dimensional sub-space. As for the two semi-major axes, while their effect is potentially important, in astrophysically relevant situations we can safely assume that the inner MBHB stalls at a separation just below its hardening radius, while the distance of the intruder to the inner binary can be initially set approximately to the scale radius of the stellar bulge, without loss of generality.

In generating the initial conditions, for the mass of the heavier MBH of the inner binary (m_1) we choose 6 values uniformly selected in logarithmic space, from 10^5 $M_\odot$ to 10^{10} $M_\odot$. The inner and outer binary mass ratios $q_{\rm in} \equiv m_2/m_1$ and $q_{\rm out} \equiv m_3/(m_1+m_2)$ can take 4 values each, uniformly spaced (logarithmically) from 0.03 to 1. The eccentricity of the inner binary, $e_{\rm in}$, takes 4 values uniformly spaced from 0.2 to 0.8, while the eccentricity of the outer binary, $e_{\rm out}$, is chosen among $0.3, 0.6, 0.9$.

Finally, in order to average our results over an isotropic orientation of the angular momenta of the two binaries, we sample the relative inclination of the two orbital planes, $0^\circ < \iota < 180^\circ$, in 13 values equally spaced in $\cos\iota$.

When presenting results marginalised over $e_{\rm in}$ and $e_{\rm out}$, those are simply obtained by summing up simulations with different eccentricities, which corresponds to a uniform weight in $e_{\rm in}$ and $e_{\rm out}$. Similarly, results marginalised over $q_{\rm in}$ and $q_{\rm out}$ are also obtained by direct summation, which corresponds to a uniform weight in the logarithm of the mass ratios. The sampling of the 6-dimensional space is summarised in tab. 3.1, and consists of a grand total of 14,976 different initial conditions.

Simulations are run with the code presented in chapter 2, which we briefly summarise here. The employed numerical scheme directly integrates the three-body (Hamiltonian) equations of motion through 2.5PN order (i.e., through 2PN

order in the conservative dynamics and leading order in the dissipative one), introducing velocity-dependant forces to account for the dynamical friction on the intruder during its initial orbital decay toward the galactic centre, and for the stellar hardening (Quinlan, 1996) of the outer binary. Unlike for the representative tests of chapter 2, the centre of mass of the triplet is not re-centred every 1000 integration steps, but we rather apply the following algorithm: when the MBH dynamics is dominated by the stellar background, dynamical friction acts on the binary *and* on the perturber separately. When m_3 later binds to the inner binary (thus forming the outer binary), the dynamical friction force is instead applied to the centre of mass of the triplet, and the stellar hardening of the outer binary is simultaneously activated. Stellar hardening is eventually switched off (and never re-activated) as the first close three-body MBH encounter occurs and the dynamics becomes chaotic. In case of ejections, dynamical friction is again applied to the binary and the third body separately. Moreover, in order speed up our computations, we switch off the conservative 2PN terms in the Hamiltonian dynamics. We have checked that 2PN corrections are indeed negligible, at least in a statistical sense, although extremely time-consuming computationally.

We stop the orbital integration when one of the following conditions is first met: a minimum approach between two members of the triplet is reached; one of the MBHs is ejected; or the time spent exceeds the (present) Hubble time. Regarding the first condition, the minimum separation is set to 15 gravitational radii. When that separation is reached, we count the event as a "binary coalescence". An ejection, instead, is counted whenever one of the MBHs is kicked to a distance in excess of 10 stellar bulge scale radii, irrespective of its binding energy. Note that this threshold is rather conservative compared to, e.g., Hoffman and Loeb (2007)[1], and has been chosen to avoid overestimating the interaction rate between the inner binary and the returning kicked MBH. Indeed, in a perfect spherically symmetric potential like ours, an MBH bound to the galaxy potential would always return to the centre of the stellar distribution. In more realistic situations, however, any deviation from spherical symmetry would prevent further interactions of the kicked MBH with the inner binary (see, e.g., Guedes et al., 2009). Our combined choices of, i) neglecting the DM component of the galactic potential, and ii) counting kicked MBHs as ejected once they reach a relatively short distance from the centre, are then conservative in terms of predicted MBHB coalescences. We plan to analyse in details the effects of triaxiality on the dynamics of MBH triple systems in the future.

3.2 Results

3.2.1 Merger fraction

Our full results, in terms of merger fractions as functions of different triplet parameters, are reported in a series of tables presented in Appendix C.

[1] In Hoffman and Loeb (2007) a MBH is considered as ejected if it reaches a distance greater than 500 kpc with $E > 0$.

Table 3.2: Merger percentage

$\log m_1$ $[\mathrm{M}_\odot]$	% Mergers m_1-m_2	m_1-m_3	m_2-m_3	Total
5	16.8	0.9	0.8	18.5(1.6)
6	16.2	1.4	1.0	18.5(1.9)
7	15.4	2.5	1.4	19.4(4.4)
8	14.7	4.0	2.5	21.2(6.3)
9	15.2	4.1	3.2	22.5(11.2)
10	21.1	7.6	3.3	31.9(12.7)

Table 3.2 shows in particular the dependence of the merger fraction, i.e., the fraction of simulations ending with a merger of any two members of the triplet, on the mass of the primary MBH (m_1). As can be seen, the merger fraction is almost constant and around $\simeq 20\%$ for the entire sampled mass range, except for the most massive case, where $\gtrsim 30\%$ of the systems are bound to coalescence. Averaged over m_1, the merger fraction is $\simeq 22\%$. The merger excess for $m_1 = 10^{10}\,\mathrm{M}_\odot$ is most probably due to the way we generate the initial conditions. Since the inner binary is initialised with a separation of the order of its hardening radius, $a_h = Gm_2/(4\sigma^2)$, and since the efficiency of GW emission scales with the binary mass, high-mass/low-$q_{\rm in}$ systems are not technically stalled. Indeed, their coalescence timescale under GW emission, albeit of several Gyrs, is still shorter than the Hubble time (Sesana, 2010; Dvorkin and Barausse, 2017).

In tab. 3.2 we also report, as an ancillary entry in the column "Total", the fraction of MBHBs that are bound to coalesce within a Hubble time *after* an ejection event. Note that since we stop our simulations whenever an ejection occurs, we compute *a posteriori* the time the remaining MBHB needs to coalesce because of GW losses. These "post-ejection" coalescences add a further $\simeq 6\%$ to the overall merger fraction (hence accounting for $\simeq 1/5$ of the total number of mergers), which is then $\simeq 30\%$. Taken at face values, our results confirm that triple interactions represent a possible, albeit partial, solution to the final-parsec problem.

In fig. 3.1 the merger fraction (*not* inclusive of the post-ejection coalescences discussed above) is plotted as a function of the initial relative inclination of the two binaries. The merger fraction peaks around $\simeq 90^\circ$, which is indeed the angle yielding the maximal eccentricity excitation in the standard (i.e., quadrupole-order) K-L mechanism. K-L oscillations have therefore a strong impact on the dynamics of our simulated MBHBs.

In a two-dimensional map (fig. 3.2) we show again the merger fraction, but now as a function of the initial values of $q_{\rm in}$ and $q_{\rm out}$.[2] The peak of the merger fraction occurs for equal-mass triplets, but there is a large plateau in the upper

[2]Note that an equal-mass triplet (i.e., $m_1 = m_2 = m_3$) is characterised by $\log q_{\rm in} = 0$ and $\log q_{\rm out} = -0.3$.

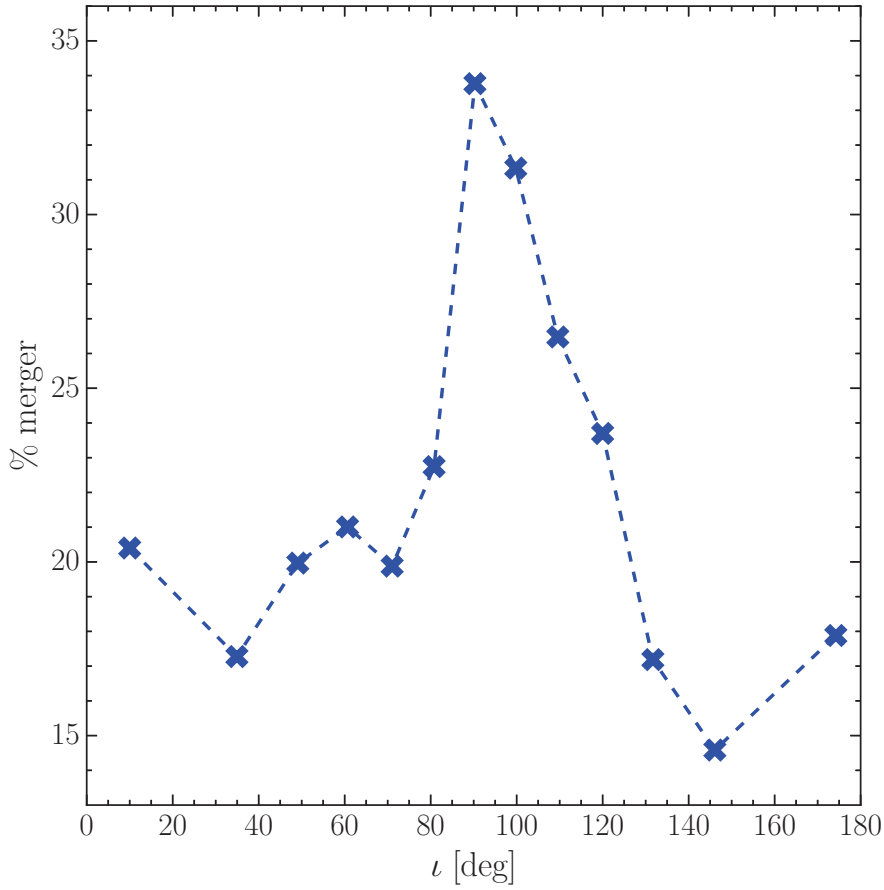

Figure 3.1: Merger fraction as a function of the initial relative inclination between the inner and outer binary. Post-ejection coalescences are not included. The prominent peak at $\iota \approx 90°$ confirms the important role of the K-L mechanism in driving the merger of MBHBs.

part of the plot, with hints of two distinct maxima. A simple interpretation is that the inner binary, in order to be perturbed, needs to interact with an intruder of at least comparable mass (i.e., $\log q_{\rm out} \approx -0.3$). A light m_3 is most probably simply kicked out by the heavier inner binary, as hinted at by the rapid decline of the merger fraction as $q_{\rm out}$ gets $\ll 1$. Note, however, that even for low values of $q_{\rm out}$ the merger fraction is significant when $q_{\rm in}$ is also small (thus, when $m_2 \approx m_3$).

A finer understanding of the results of fig. 3.2 can be gained by considering that, at the octupole level, the K-L oscillations are more easily triggered when the inner binary has a small mass ratio. In this case, the inner binary can merge when the triplet is still in the initial hierarchical phase, and the eccentricity growth responsible for the coalescence is primarily driven by secular processes. This is the cause of the leftmost peak in the merger fraction, indeed occurring for $\log q_{\rm out} \approx -0.3$ and $\log q_{\rm in} \ll 0$. A second channel to coalescence is represented by merger-inducing strong non-secular close encounters that the original inner binary experiences once the triplet becomes unstable. This happens for almost equal-mass triplets, i.e., when the intruder carries a mass sufficiently large to perturb the inner binary, but, at the same time, the K-L mechanism is not easily

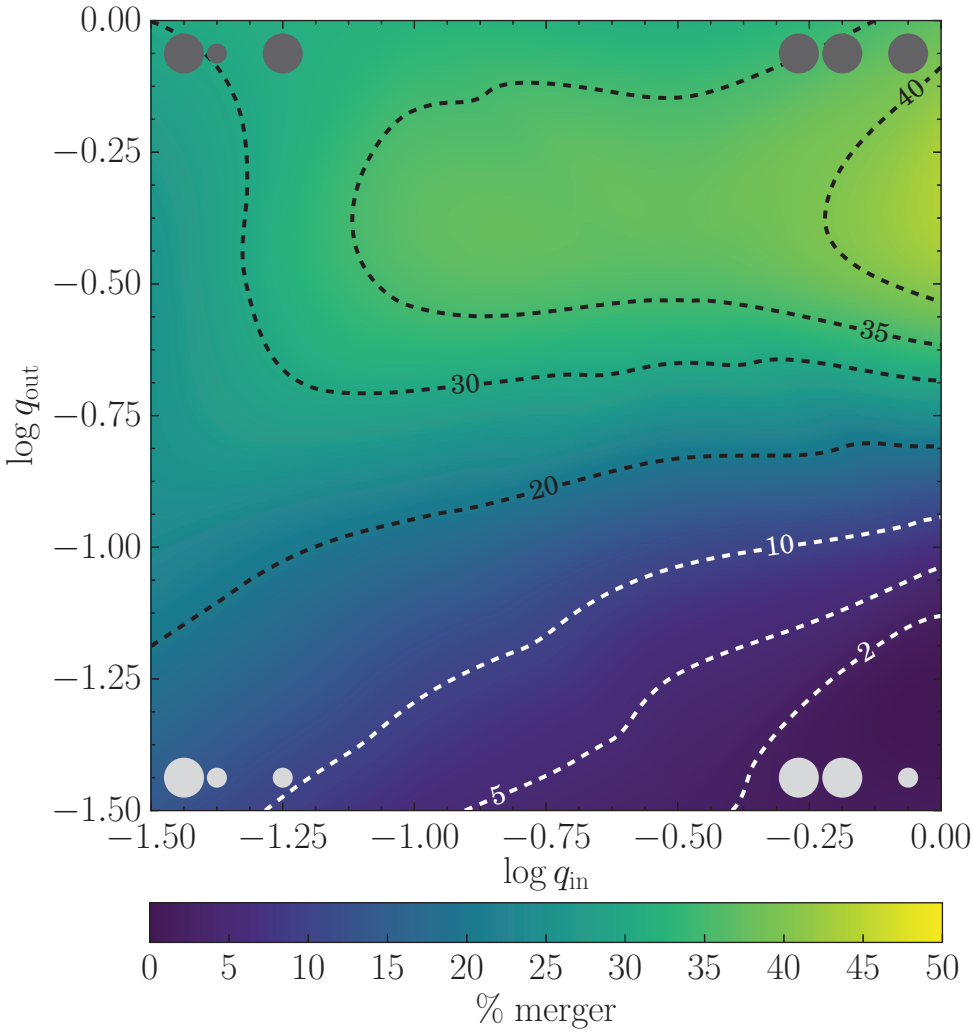

Figure 3.2: Merger fraction (colour coded) as a function of the inner ($q_{\rm in} = m_2/m_1$) and outer ($q_{\rm out} = m_3/(m_1+m_2)$) mass ratios. The merger fraction is larger ($\gtrsim 30$ %) in the upper region, corresponding to $q_{\rm out} \gtrsim 0.3$ and $0.1 \lesssim q_{\rm in} \lesssim 1$. The circles in the four corners of the plot represent, in cartoon-like fashion, the corresponding mass hierarchy of the triplets.

triggered. During the process, prior to coalescence, several exchanges[3] may occur, and therefore the final merger does not necessarily involve the members of the original inner binary. This second channel is responsible for the rightmost peak of the merger fraction in fig. 3.2.

In order to better understand the role played by these two different channels in the merger fraction, we separately analyse the systems in which no exchange occurs during the evolution, and the rest of the systems that instead experience strong encounters, ultimately leading to one or more exchange events. In addition, we single out systems with initial inclination in the range ($70° < \iota < 110°$), hence dividing our simulations into four subsets.

The relative merger fraction of these subsets (i.e., relative to the number of

[3] An exchange is an event in which the intruder kicks one body (usually the lightest one) out of the inner binary, and binds to the other to form a new two-body system.

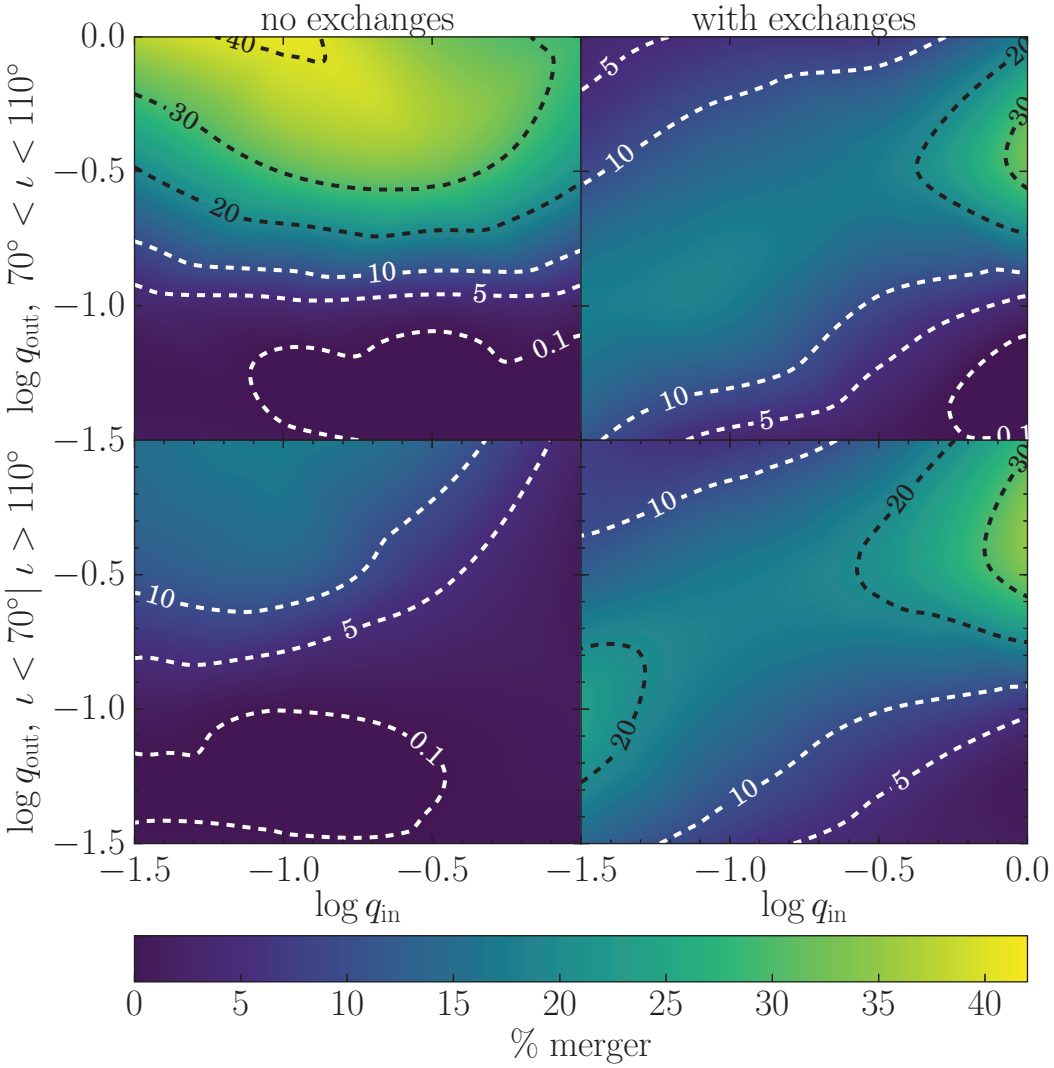

Figure 3.3: Break-up of fig. 3.2 into different sub-populations. The two columns distinguish between merging binaries that underwent at least one close encounter leading to an exchange (right) and merging binaries that experienced no such encounters (left). The two rows identify sub-populations starting off with relative inclinations $70^\circ < \iota < 110^\circ$ (top) and $\iota < 70^\circ$ or $\iota > 110^\circ$ (bottom). Merger fractions are normalized with respect to the total number of simulations in the respective inclination range.

simulations performed in a particular inclination range) is shown in fig. 3.3. Left panels represent the systems in which no exchange occurs. In these cases the coalescence is mainly due to secular K-L oscillations, a fact confirmed by the comparatively much higher merger fraction (factor of ≈ 3) at high initial inclinations (upper left panel). Moreover, we note that low $q_{\rm in}$ are more likely to lead to mergers, irrespective of the inclination. As already mentioned, this is to be ascribed to the octupole terms of the K-L resonances, whose amplitude is proportional to the mass difference $m_1 - m_2$, hence vanishing for $q_{\rm in} \to 1$. Note that, unlike in the standard quadrupole K-L resonances, the introduction of the octupole terms can excite high eccentricities even at low inclinations, a fact responsible for the non-negligible merger fraction in the lower left panel of fig. 3.3. At high inclinations, the region of both low $q_{\rm out}$ and low $q_{\rm in}$ should be prone to the K-L mechanism, but our results show no significant merger fraction (fig. 3.3, upper left panel). This can be understood by noting that if the timescale of the relativistic precession is shorter than that of the K-L oscillations, the latter are damped. Since the K-L timescale increases as m_3 decreases, in the limit $q_{\rm out} \ll 1$ the process is largely suppressed by relativistic precession. The relatively large merger fraction visible in the lower left area of fig. 3.2 is then due to non-secular processes.

The right panels of fig. 3.3 show the non-secular channel to merger. The first thing to notice is that the pattern of the merger fraction is almost independent of the inclination angle, consistent with the fact that exchanges occur when chaotic interactions take place and secular processes play no significant role. The merger fraction is larger when the three MBHs have similar masses, and in general has non-negligible values ($> 10\%$) only along a broad band stretching from the upper right to the lower left sides of the $q_{\rm in} - q_{\rm out}$ plane. This can be understood by considering that when $q_{\rm in} \simeq 1$ and $q_{\rm out} \ll 1$ (i.e., in the lower right corner of the plot), the intruder cannot perturb significantly the much more massive inner binary. On the other extreme (i.e., $q_{\rm in} \ll 1$ and $q_{\rm out} \simeq 1$, upper left corner of the plot), m_3 simply kicks the much lighter m_2 out of the inner binary, taking its place. It is only when $m_3 \sim m_2$ that genuinely chaotic dynamics can take place, in some cases leading to coalescence.

Finally, fig. 3.4 shows the merger fraction as a function of the initial eccentricity of the inner and outer binary. We note that the merger fraction increases with increasing $e_{\rm in}$, while it decreases with increasing $e_{\rm out}$. The dependence upon $e_{\rm in}$ is readily understood, since highly eccentric inner binaries are closer to the efficient GW-emission stage and can easily be driven to coalescence by a relatively mild perturbation from a third body. The dependence upon $e_{\rm out}$ is likely due to the fact that quasi-circular outer binaries form a stable hierarchical triplet for a comparatively longer time during the inspiral of m_3, hence leaving more room to the development of K-L resonances, which are efficient at driving the inner binary to coalescence. Conversely, in very eccentric outer binaries, m_3 soon interacts with the inner binary at pericentre, entering the chaotic phase. Chaotic interactions are more likely to result in ejections rather than mergers, hence suppressing the overall merger fraction.

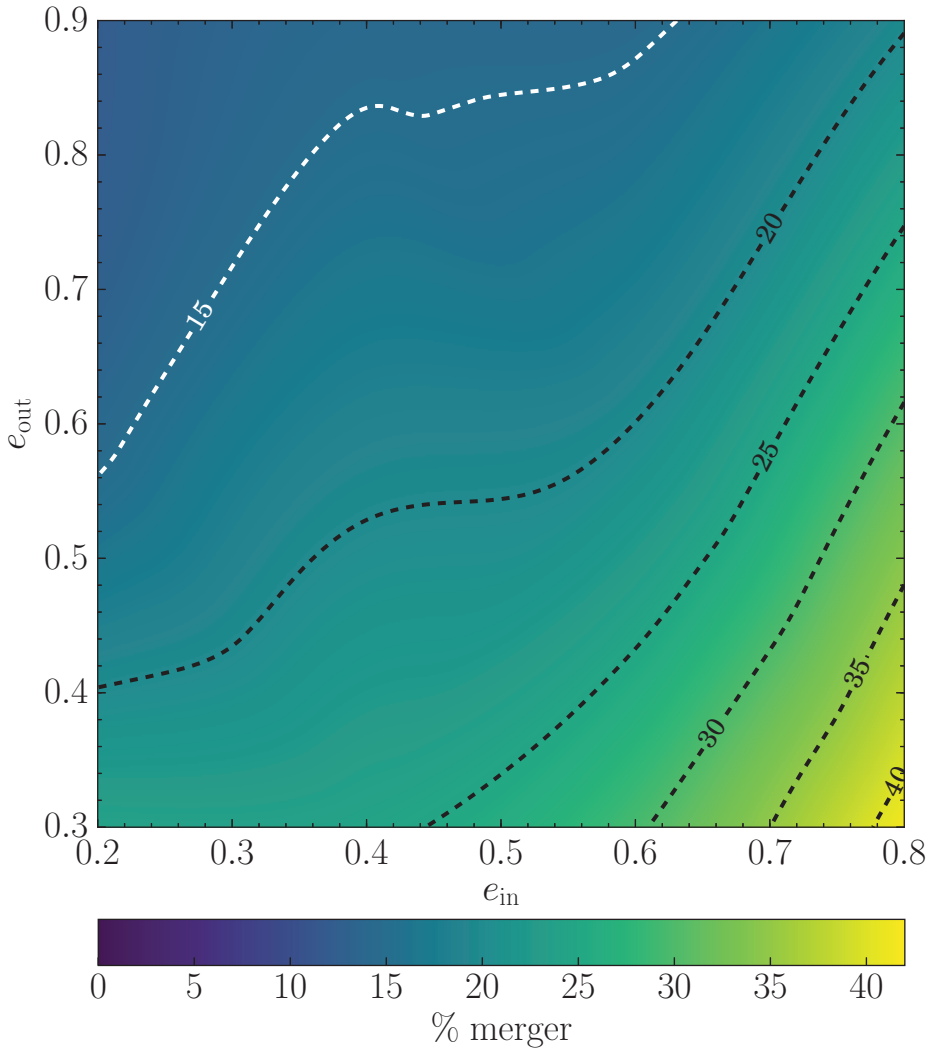

Figure 3.4: Merger fraction (colour coded) as a function of the initial inner ($e_{\rm in}$) and outer ($e_{\rm out}$) binary eccentricities.

Importance of PN corrections

As pointed out in the previous section, the K-L mechanism can be suppressed by general relativistic effects. In particular, relativistic precession tends to destroy the coherent pile-up of the perturbation that the third body induces on the inner binary, hence effectively damping the K-L resonances.[4] In order to quantify the impact of the relativistic precession on the merger fraction and to compare our results with previous work that neglected this effect (e.g., Iwasawa, Funato, and Makino, 2006; Hoffman and Loeb, 2007), in tab. 3.3 and in fig. 3.5 we compare, only for the case $m_1 = 10^9$ M$_\odot$, the merger fraction obtained with and without 1PN corrections. Overall, the merger fraction is substantially higher in the case without 1PN terms (right panel of fig. 3.5). As can be seen, the largest differences compared to the full case occur for $q_{\rm in} \ll 1$, where, because of octupole-order terms, the K-L mechanism is maximally effective. On the contrary, for large $q_{\rm in}$ the merger fractions with or without 1PN corrections are similar, because, as

[4]More precisely, any kind of precession tends to suppress the K-L mechanism.

previously discussed, coalescences are mainly due to chaotic strong encounters, rather than to K-L oscillations. Our results highlight the importance of K-L resonances in inducing MBH mergers in triple systems, and the need to account at least for 1PN corrections.

Table 3.3: Comparison of the merger fraction from the simulations with $m_1 = 10^9$ M$_\odot$, run with and without conservative 1PN corrections.

$m_1 = 10^9$ M$_\odot$	% Mergers including 1PN				% Mergers without 1PN			
$q_{\rm in}/q_{\rm out}$	m_1-m_2	m_1-m_3	m_2-m_3	Total	m_1-m_2	m_1-m_3	m_2-m_3	Total
0.0316/0.0316	9.0	5.1	0.0	14.1(20.5)	44.2	5.8	0.0	50.0(5.1)
0.0316/ 0.1	23.7	3.2	0.0	26.9(13.5)	59.0	1.9	0.0	60.9(5.1)
0.0316/0.3162	9.0	1.3	0.6	10.9(3.8)	41.0	3.2	0.0	44.2(3.8)
0.0316/ 1	25.0	0.0	1.9	26.9(0.0)	62.2	0.0	0.6	62.8(0.0)
0.1/0.0316	4.5	1.9	0.0	6.4(16.7)	29.5	1.9	0.0	31.4(12.8)
0.1/ 0.1	16.0	5.8	0.6	22.4(17.3)	35.9	6.4	1.3	43.6(17.9)
0.1/0.3162	24.4	3.2	1.3	28.8(11.5)	44.9	4.5	0.6	50.0(7.7)
0.1/ 1	25.6	0.0	7.1	32.7(1.3)	40.4	0.6	7.7	48.7(0.0)
0.3162/0.0316	2.6	0.6	0.0	3.2(7.1)	9.0	0.0	0.6	9.6(5.8)
0.3162/ 0.1	12.8	2.6	0.6	16.0(14.1)	17.3	5.8	0.0	23.1(9.6)
0.3162/0.3162	26.3	14.1	3.8	44.2(16.0)	30.1	13.5	4.5	48.1(16.0)
0.3162/ 1	17.3	1.9	4.5	23.7(5.8)	29.5	3.2	5.8	38.5(6.4)
1/0.0316	1.3	0.0	0.0	1.3(5.1)	3.2	0.6	0.0	3.8(1.3)
1/ 0.1	5.8	0.0	0.6	6.4(8.3)	18.6	1.3	1.3	21.2(10.3)
1/0.3162	26.9	12.2	14.1	53.2(16.0)	33.3	9.6	6.4	49.4(13.5)
1/ 1	13.5	14.1	15.4	42.9(21.8)	19.9	16.0	18.6	54.5(11.5)
Average	15.2	4.1	3.2	22.5(11.2)	32.4	4.6	3.0	40.0(7.9)

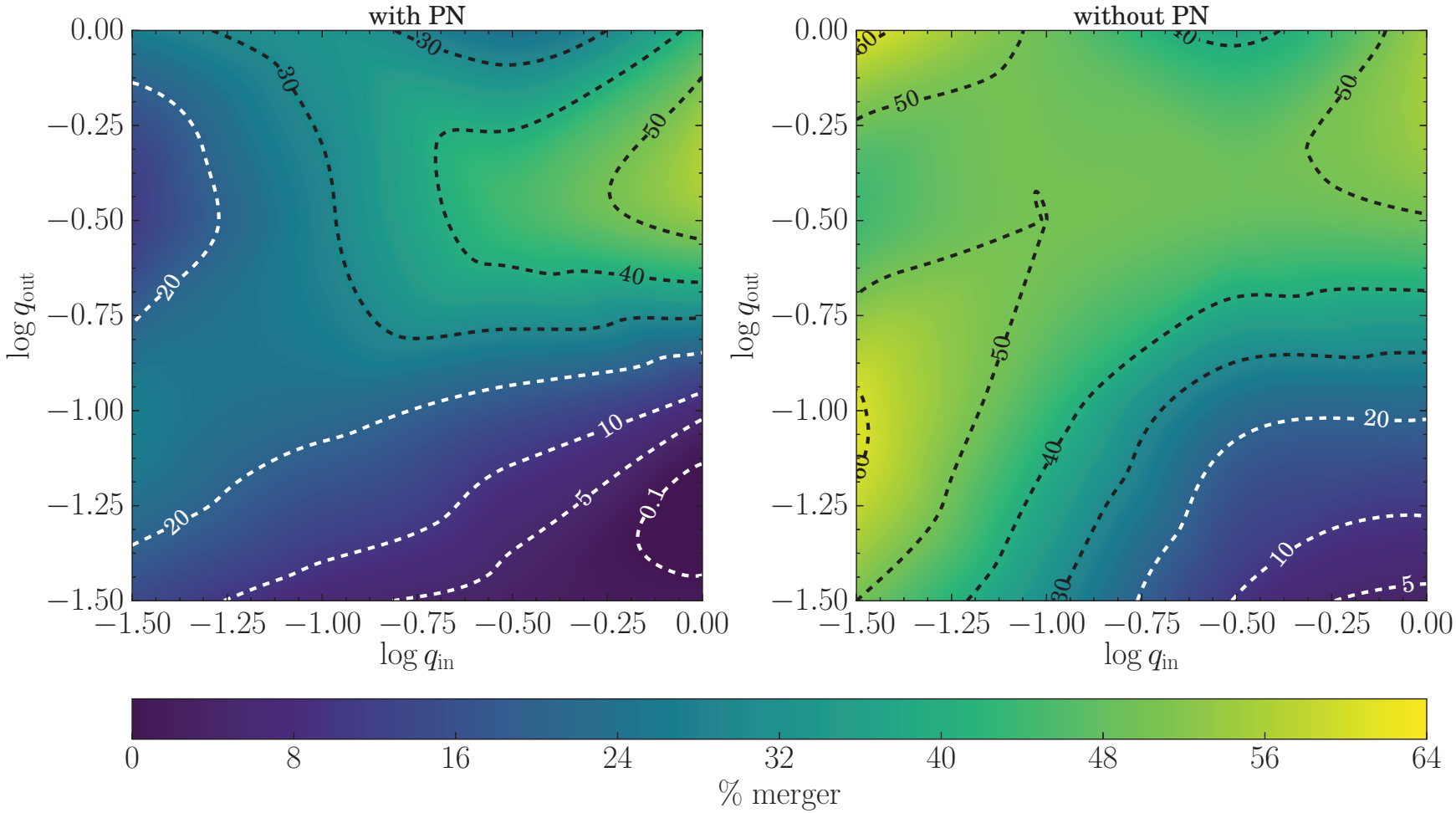

Figure 3.5: Comparison between the merger fraction in the case $m_1 = 10^9$ M$_\odot$, when the dynamics is evolved with (left panel) and without (right panel) 1PN term. The suppression of the merger fraction for low q_{in}, due to 1PN precession, is clearly visible (see discussion in main text).

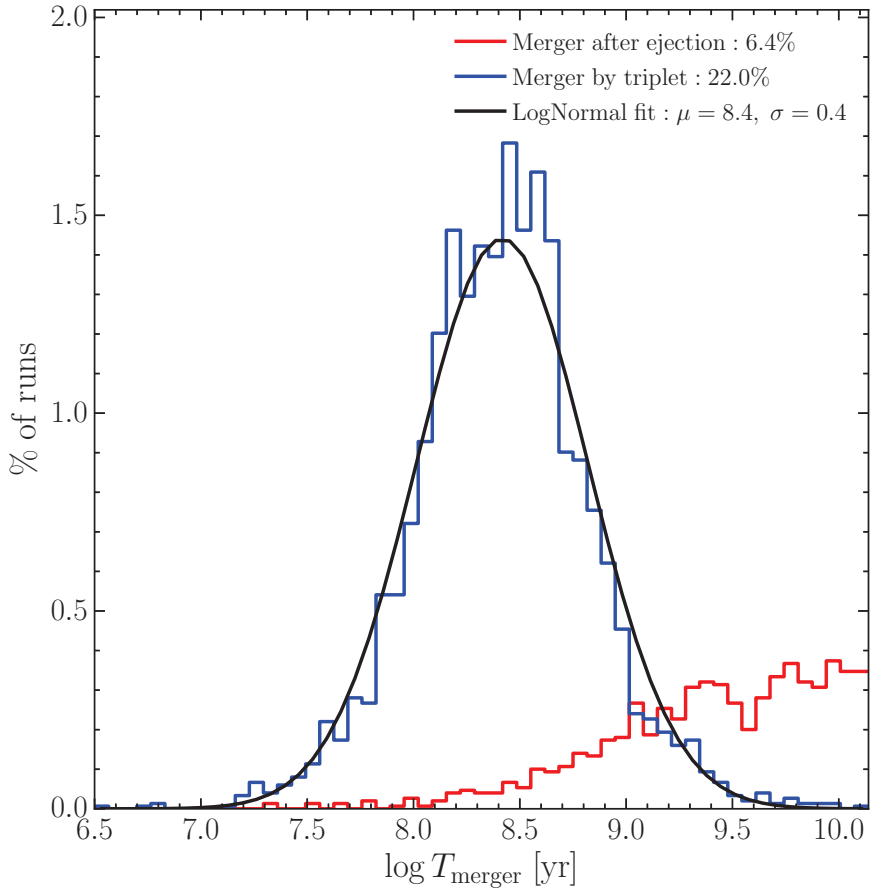

Figure 3.6: Distribution of merger-times. The blue histogram represents binaries that merge because of the prompt interaction with a third body (chaotic dynamics and/or K-L resonances plus GWs), and the black line is a log-normal fit to the distribution. The red histogram, instead, represents the binaries that are driven to merger by GW emission alone after the ejection of one of the MBHs (always the lightest one).

3.2.2 Merger timescales

The time spent by triplets before coalescence is shown in fig. 3.6. The merger-time distribution is remarkably well fit by a log-normal, with mean $\mu = 8.4$ and standard deviation $\sigma = 0.4$ in $\log(T/\mathrm{yrs})$. The mean value $\mu = 8.4$ corresponds to $\simeq$ 250 Myr, i.e., a timescale substantially shorter than the Hubble time, indicating that the triplet channel can lead to fast mergers. Indeed, most of the time prior to merger is spent in the dynamical friction and stellar hardening dominated regimes, i.e., most of the time the intruder is far from the inner binary. Once a genuinely bound triplet is formed, secular and (in some cases) chaotic interactions drive the system to coalescence on a much shorter timescale.

In fig. 3.6 we also show, as a lower red histogram, the merger-time distribution of the "post-ejection" coalescences discussed in section 3.2.1. These events, which account for approximatively 1/5 of the total merger fraction and which are relatively more probable for high m_1 values (see tab. 3.2), involve an ejection, and a leftover inner binary that coalesces within a Hubble time under the effect

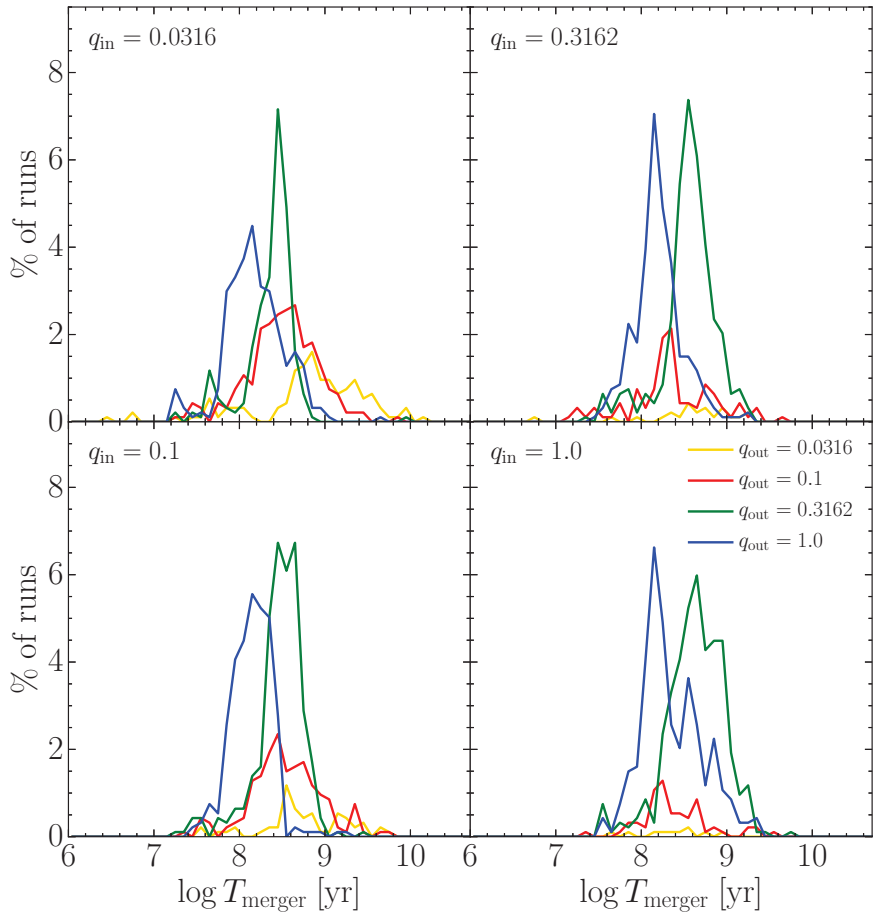

Figure 3.7: Distribution of merger-times, grouped according to the initial mass ratio of the inner (as labelled in the upper left corner of all panels) and outer binary (differentiated by colors as indicated in the lower right panel). The merger timescale only has a weak dependence on the outer mass ratio.

of GW emission alone. The merger-time distribution is quite broad for these systems, and these MBHBs typically need a few Gyrs to merge.

In fig. 3.7 the merger-time distribution is shown for the different sampled values of $q_{\rm in}$ (in the four panels) and $q_{\rm out}$ (indicated by different colours in each panel). While there is no clear dependence of the merger timescale on $q_{\rm in}$, we note a weak dependence on $q_{\rm out}$, with $q_{\rm out} \simeq 1$ systems coalescing faster because of the stronger perturbations exerted by m_3 on the inner binary.

3.2.3 Eccentricity distribution

Of particular importance for GW emission from MBHBs in a cosmological setting is the study of the eccentricity evolution of merging binaries. In the left panels of fig. 3.8 we track the evolution of the merging binaries in the orbital frequency vs circularity plane $(f, 1-e)$, colour coding the probability of finding a binary at given values of eccentricity and frequency. We first discretise the $(\log f, \log(1-e))$ space in the range $-14 \leq \log f \leq -2$ and $-4 \leq \log(1-e) \leq 0$ on a 150×150 grid equally spaced along each direction. Then, we evaluate the

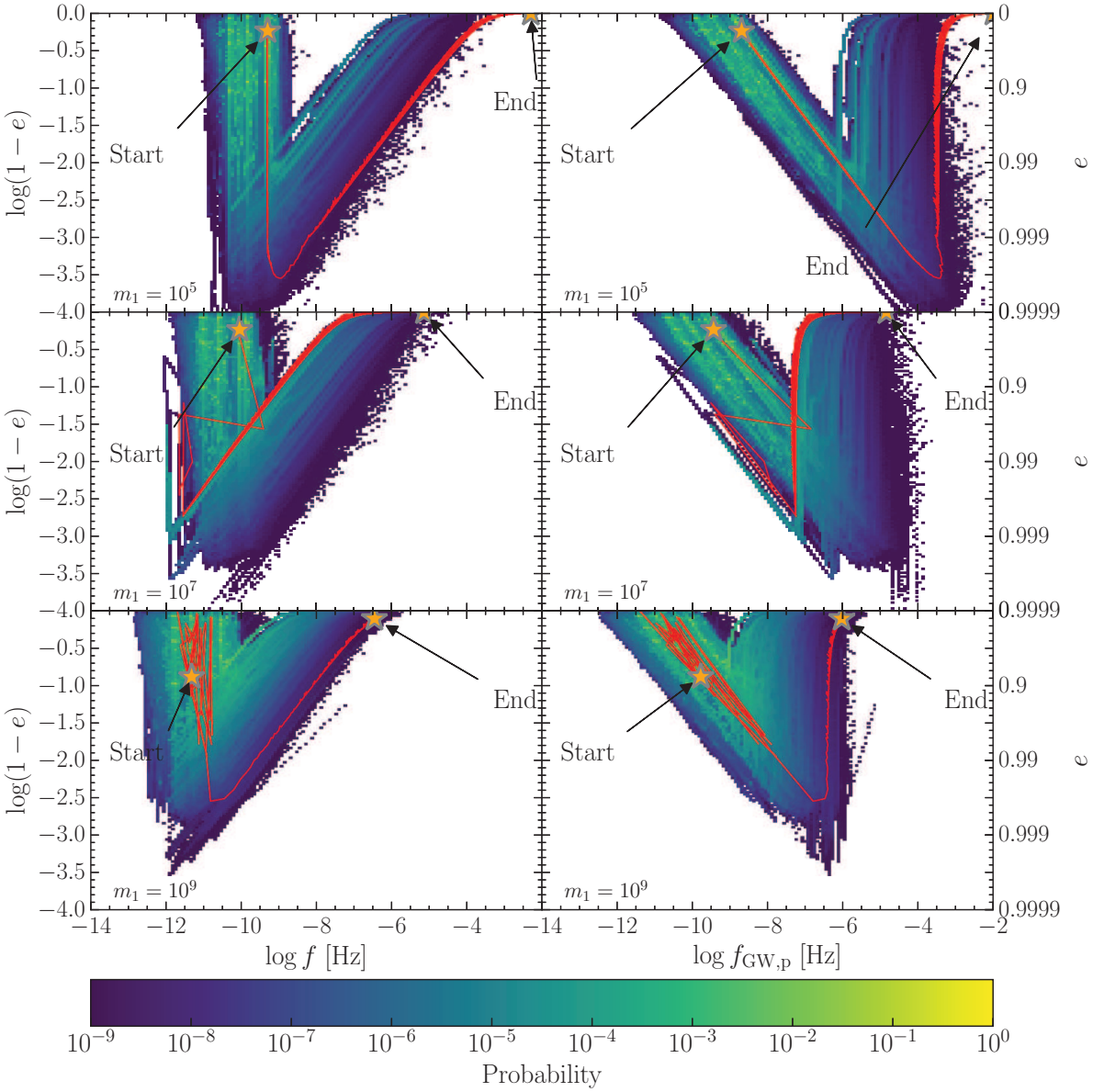

Figure 3.8: Evolution in the plane $(f, 1-e)$ (left panels) and $(f_{\rm GW,p}, 1-e)$ (right panels) of all merging binaries for three selected values of $m_1 = 10^5, 10^7, 10^9 \mathrm{M}_\odot$ (from top to bottom). Colour-coded is the probability (see text for details about the computation) of finding a binary at given values of frequency and eccentricity. For each mass, superimposed in red is the evolutionary track of a representative binary that reached final coalescence. In the top panels such representative binary merges when the triplet is still in the hierarchical phase, while in the lower panels the binary experiences strong chaotic three-body interactions, clearly visible in the noisy change of orbital elements. The primary effects of the triple interactions (secular or chaotic) is the great increase of the orbital eccentricity, leading one of the pairs in the triplet to coalescence.

time spent by each merging binary in each of the 22,500 bins of the grid during its evolution, then sum over all merging binaries, and normalise to the total time spent over all bins by all binaries. In this way, we obtain a bivariate normalised function that gives the probability of finding a binary in a given logarithmic two-dimensional interval of frequency and circularity. We construct this function for the six sampled values of m_1, and show in fig. 3.8, left panels, three cases ($m_1 = 10^5, 10^7, 10^9$ M$_\odot$). The evolutionary tracks of single illustrative merging binaries are shown as a red line.

In the orbital frequency-eccentricity plane, a typical stalled inner binary starts its evolution in the upper left corner, i.e., at large separation (i.e., low f) and with an eccentricity given by one of the 4 values of $e_{\rm in}$ that we sample (see tab. 3.1). As soon as the perturbations due to the approaching third body become significant, the inner binary becomes more eccentric. If the system undergoes K-L resonances, the eccentricity actually oscillates on the K-L timescale between high and low values (these oscillations are not visible in fig. 3.8 due to the scale used), with a secular shift to higher values because of the perturbation exerted by an increasingly closer m_3. The orbital frequency (i.e., the separation) of the inner binary stays nearly constant during this evolutionary phase. An example is given by the red line shown in the $m_1 = 10^5$ M$_\odot$ case (fig. 3.8, upper left panel). When chaotic interactions are instead the main driver of the binary evolution, f can show large, random variations, as exemplified by the tracks in the middle and lower left panels of fig. 3.8.

In any case, when the eccentricity becomes very high, $\gtrsim 0.99$, GW emissions starts dominating the dynamics, increasing the orbital frequency and circularising the orbit until coalescence, as can be seen from the rising branch of the red tracks. The colour code shows that this circularisation phase is much shorter than the preceding evolution. The maximum eccentricity reached (the turnover point in the evolutionary tracks) mainly depends on the mass of the inner binary, i.e., the lower the mass, the higher the maximum eccentricity. In fact, for more massive binaries GWs start dominating sooner during the evolution, hence determining the earlier orbital circularisation. This behaviour is clearly visible in fig. 3.8, moving from the top panel ($m_1 = 10^5$ M$_\odot$) to the bottom one ($m_1 = 10^9$ M$_\odot$). Note that for more massive systems the orbital frequency at merger is necessarily lower, since it scales as M^{-1}, where $M \equiv m_1 + m_2$.

It is of a certain interest to analyse the same evolution not in terms of the orbital frequency, but rather in terms of the peak frequency of the GW power spectrum (Wen, 2003)

$$f_{\rm GW,p} = \frac{1}{\pi}\sqrt{\frac{GM}{[a(1-e^2)]^3}}(1+e)^{1.1954}, \tag{3.1}$$

which is clearly larger for more eccentric binaries. (Note that this equation essentially means that GWs are mainly emitted at the pericentre passages). The probability distribution in the $(\log f_{\rm GW,p}, \log(1-e))$ plane is shown in the right panels of fig. 3.8, for the same three values of m_1 considered before.

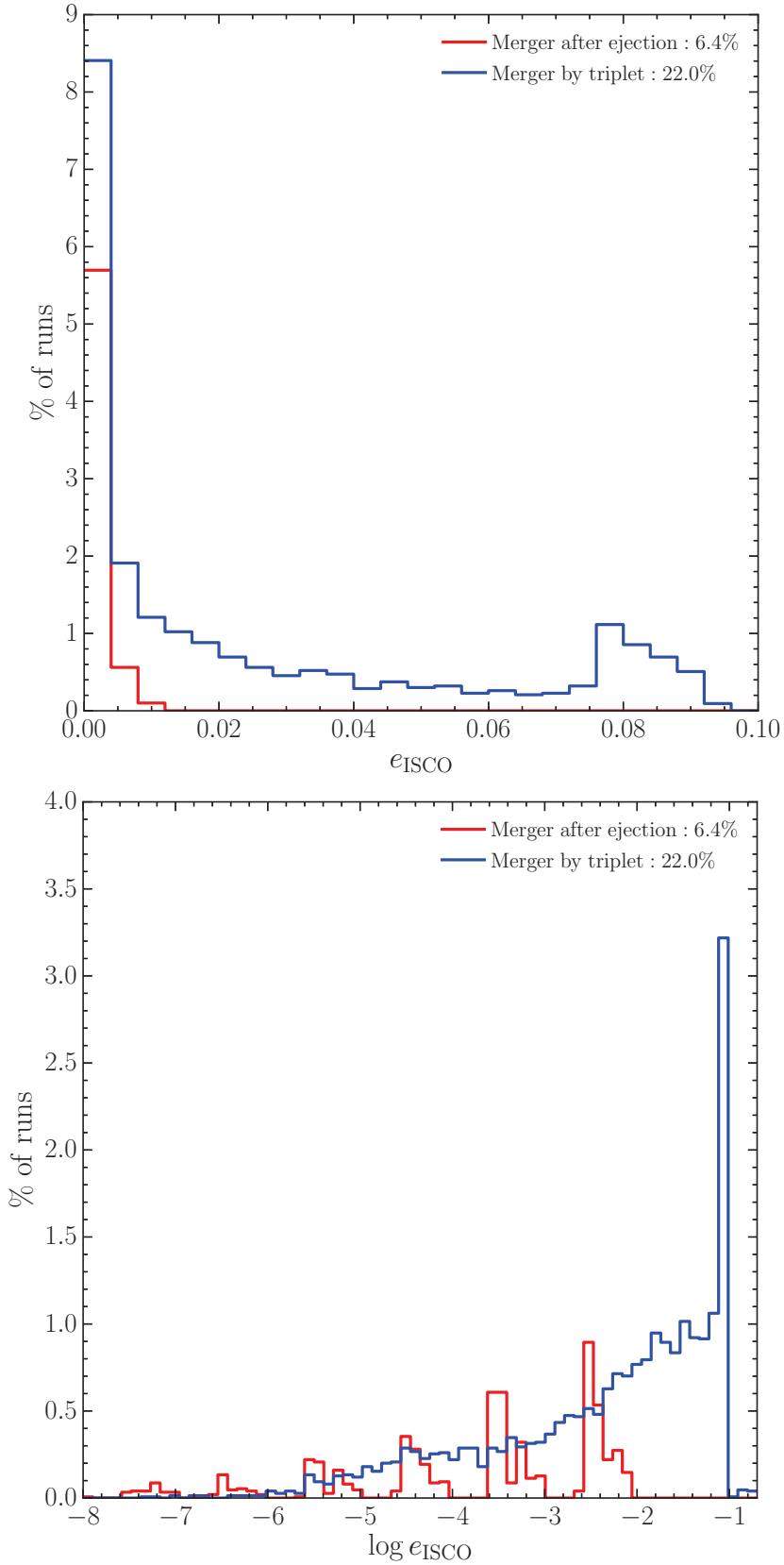

Figure 3.9: Distribution of $e_{\rm ISCO}$ of all merging binaries. Colour code as in fig. 3.6. The binaries that merge after a strong interaction with the third body retain a larger eccentricity close to merger compared to those that are GW-driven. *Top*: linear scale. *Bottom*: log scale. Note the peculiar clustering of the red distribution in six different blocks corresponding to the six different values of m_1, i.e., from, left to right, $10^5 {\rm M}_\odot$ to $10^{10} {\rm M}_\odot$.

During the initial phase of eccentricity growth, irrespective of the evolution driver (K-L resonances or chaotic interactions), the orbital frequency does not change (left panels in fig. 3.8), but $f_{\rm GW,p}$ increases because of its dependence on e. As soon as GWs take over, the orbit circularises fast while maintaining an almost constant $f_{\rm GW,p}$ until the very last phase of the evolution. This means that during the circularisation phase, the binaries maintain a fixed pericentre separation while their the semi-major axis shrinks. Once the circularisation is completed, GW losses keep shrinking the semi-major axis. Therefore, $f_{\rm GW,p}$ increases and eventually becomes twice the orbital frequency ($f_{\rm GW,p} = 2f$), as expected for circular binaries at leading PN order. Like the orbital frequency, in the GW dominated regime $f_{\rm GW,p}$ is lower for larger masses. A particularly interesting result of our simulations is that more massive binaries merge with a slightly larger eccentricity compared to their low mass counterparts, despite their maximum eccentricity being comparatively lower. This is essentially due to the shorter timescale of the inspiral phase, which results in a sizeable residual eccentricity, as can be seen in fig. 3.8 by observing the positions marked as "End".

Fig. 3.9 shows the distribution of the eccentricity of merging MBHBs at an arbitrary separation chosen equal to the innermost stable circular orbit of a non-spinning MBH with the same mass of the binary, i.e., at a separation $r_{\rm ISCO} = 6R_G$, where the gravitational radius is defined as $R_G = GM/c^2$. In the top panel, we plot the distribution on a linear scale, while in the bottom panel we show the logarithmic version of the same distribution. It is remarkable that the distribution extends up to $e_{\rm ISCO} \simeq 0.1$, as shown by the blue histogram.

In the same figure, the red histogram refers to the "post-ejection" coalescences, which we recall account for $\simeq 1/5$ of the total. As expected, given that the final coalescence is purely driven by GW emission, these mergers are much less eccentric. Their low residual eccentricity has a marked dependence of the mass of the triplet, as can be inferred from the logarithmic version of the plot. Indeed, the bottom panel of fig. 3.9 shows that the $e_{\rm ISCO}$ distribution clusters around 6 different values, corresponding to the 6 values of m_1 that we have sampled, with m_1 increasing from left to right. Note that the distribution of $e_{\rm ISCO}$ for the mergers driven by triple interactions instead does not show any clustering.

Finally, in fig. 3.10 we plot the eccentricity distribution, for the four different initial values considered, of the inner binaries that did not merge within a Hubble time after the kick of one of the three bodies. The distribution is approximatively thermal (i.e., $p(e) \propto e$), typical of binaries that have experienced strong dynamical encounters during their evolution (Jeans, 1919; Heggie, 1975), in the range from $e_{\rm in} = 0$ to its initial value. Above this value of the eccentricity the distribution shows a turnover, which is simply due to the fact that binaries with a higher eccentricity merge within a Hubble time, and are therefore not counted in the shown distribution. In fig. 3.11 the same distribution is plotted summing over all values of the initial eccentricity. In this case the slope results steeper than thermal because of the contribution of binaries with low initial eccentricity.

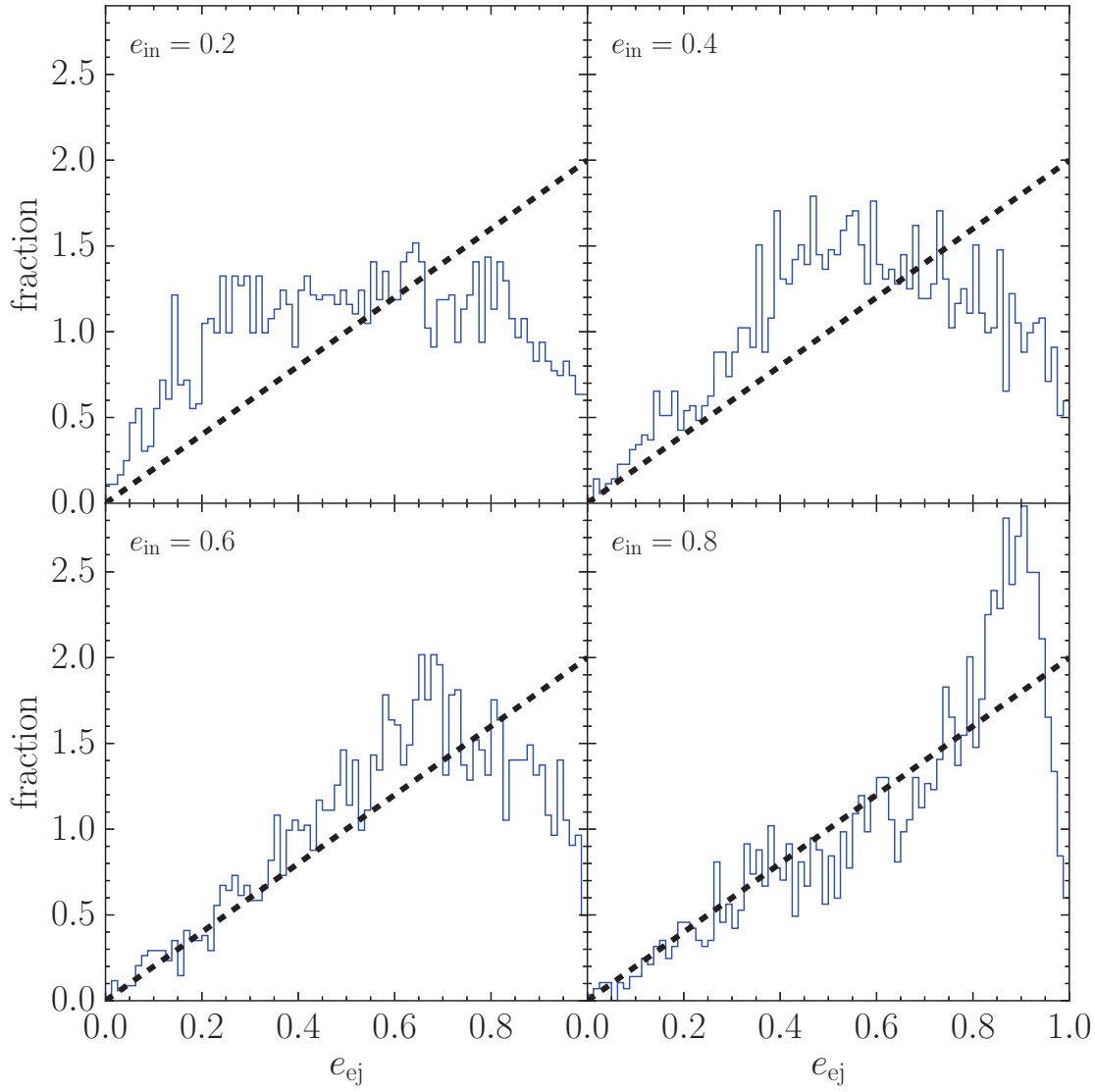

Figure 3.10: Eccentricity distribution according to the initial value of $e_{\rm in}$ of those binaries that, after the ejection of one of the MBHs, *would not* merge within a Hubble time. For each panel, the eccentricity approximately follows a thermal distribution (i.e., $f(e) = 2e$, represented as a black dashed line in the figure) from $e_{\rm in} = 0$ to the starting values of the inner eccentricity. At high eccentricities some of the binaries are missing because they are driven to coalescence (and therefore counted as mergers) by GW emission, causing a turnover in the distribution.

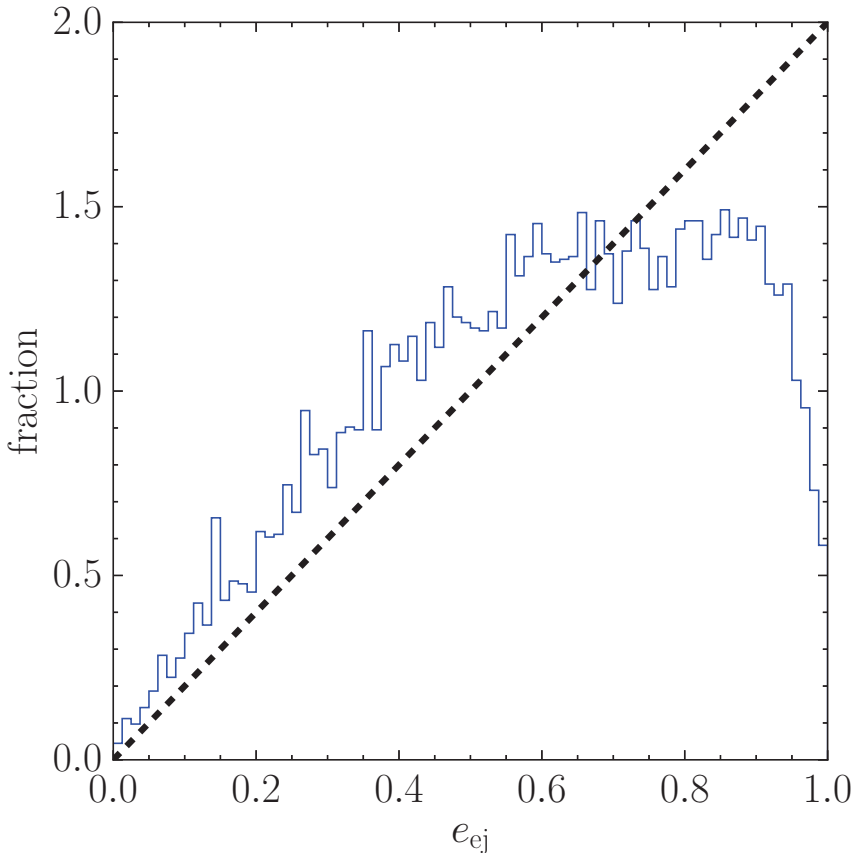

Figure 3.11: Same as fig. 3.10, but considering all simulations with a non-coalescing binary. Note that the slope results steeper than thermal because of the contribution of binaries with low initial eccentricity which does not resemble a thermal character in the whole eccentricity range.

3.3 Discussion

3.3.1 Implications for the emission of gravitational waves

The results presented in the previous section suggest that MBH triplets might have a critical impact on the emission and detection of low-frequency gravitational waves. Although a detailed analysis of the relevant implications for PTAs (and briefly for LISA) will be presented in the next chapters, we preview here some relevant points.

The fact that about 30% of triple systems lead to coalescence of a MBHB implies that this is an effective "last resort" to overcome the final-parsec problem, should all other dynamical mechanisms fail. If the average galaxy undergoes a fairly large number of mergers during its cosmic history, then triple MBH interactions guarantee that at least 30% of the galaxy mergers would end up with a MBHB coalescence. Therefore, compared to a scenario where MBHBs merge efficiently, the merger rate should be at most suppressed by a factor of $\simeq 3$. This is particular encouraging for low-frequency GW probes. Indeed, even if MBHB stalling turns out to be a problem, LISA detection rates would be affected by a factor $\simeq 3$ only, while the stochastic GW background in the PTA

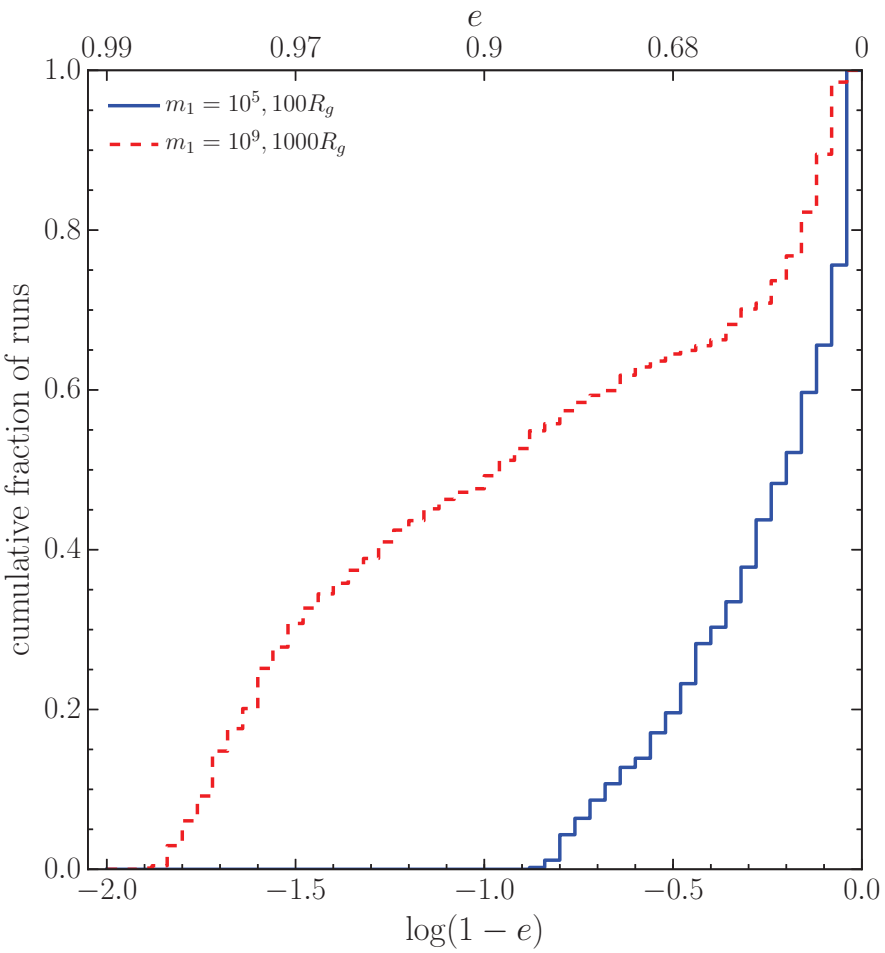

Figure 3.12: Cumulative distribution of $1-e$ of all merging binaries with $m_1 = 10^5\mathrm{M}_\odot$ (blue solid line) and $m_1 = 10^9\mathrm{M}_\odot$ (red dashed line). In the case of $m_1 = 10^5\mathrm{M}_\odot$ ($10^9\mathrm{M}_\odot$) the distribution is evaluated when the separation is 100 (1000) R_G, most relevant for LISA (PTAs).

band would only be suppressed by a factor $\sqrt{3}$ (since the GW background is proportional to the square root of the number of mergers). Conversely, if the average galaxy undergoes $\lesssim 1$ merger during its cosmic history, MBH triplets would not form frequently. In this scenario, MBHB stalling would result in a severe suppression of any low-frequency GW signals, posing a potential threat to PTAs (and LISA). In the following chapters, we will explore which of the two scenarios is more likely to occur in Nature by coupling the results presented here to a state-of-the-art semi-analytical galaxy formation model.

Triple interactions also leave a distinctive imprint in the eccentricity distribution of merging MBHBs. In fact, whether secular processes or chaotic dynamics dominate the evolution, the coalescence is triggered when one of the MBH pairs is eccentric enough that a significant amount of GWs is emitted at subsequent pericentre passages. The net result is that triplet-induced MBHB coalescences typically involve eccentric systems. Even at separation $\sim r_{\rm ISCO}$, eccentricity can still be as high as 0.1, and is $\gtrsim 0.01$ for more than 50% of the binaries.

LISA is mostly sensitive to $10^5\mathrm{M}_\odot - 10^6\mathrm{M}_\odot$ MBHBs throughout the Universe.

Table 3.4: Extended parameter space sampling for the case $m_1 = 10^9$.

Initial conditions	
$\log(q_{\rm in})$	-1.5, -1.0, -0.5, 0.0
$\log(q_{\rm out})$	-1.5, -1.0, -0.5, 0.0, 0.5, 1.0
$e_{\rm in}$	0.0, 0.2, 0.4, 0.6, 0.8
$e_{\rm out}$	0.0, 0.3, 0.6, 0.9
$\cos\iota$	13 values equally spaced in $(-1, 1)$

Those systems typically enter the detector band at separations around $100R_G$. The cumulative eccentricity distribution of merging systems for all simulations with $m_1 = 10^5 \mathrm{M}_\odot$ is shown in fig. 3.12. Although skewed towards $e = 0$, the distribution extends to $e \approx 0.8$, with about 30% of the systems having $e \gtrsim 0.5$. Therefore, high eccentricities in the LISA band might be the smoking gun of triple-driven coalescences, and waveforms accurate up to high eccentricities might be necessary for proper recovery of the source parameters. Conversely, PTAs are sensitive to masses $\gtrsim 10^8 \mathrm{M}_\odot$ at low redshift. In fig. 3.12 we also show the eccentricity distribution of merging systems for all simulations with $m_1 = 10^9 \mathrm{M}_\odot$ at a separation of $1000R_G$, which are representative of the sources dominating the GW signal in the nHz band. Note that the distribution extends to $e \approx 0.99$, and about 50% of the systems have eccentricity in excess of 0.9. Thus, in a Universe dominated by triple interactions, the PTA signal is expected to be dominated by very eccentric binaries.

A further consequence of high eccentricities is the possibility of generating bursts of GWs. In practice, binaries with high e mostly emit GWs at every pericentre passage, resulting in a "burst signal" well localised in time and spread (in frequency) over a large number of harmonics (Amaro-Seoane et al., 2010). As an example, massive binaries with orbital periods of hundreds of years can emit month-long bursts in the PTA frequency band, while lighter binaries with periods of several months can emit bursts detectable by LISA. This latter case is particularly interesting, because it might enhance the number of LISA detections well beyond the nominal MBHB merger rate. We will investigate this possibility in a planned forthcoming work.

3.3.2 Extended survey

In order to explore in greater detail the dependence of the merger fraction on the various parameters that characterise a MBH triplet, only for the case $m_1 = 10^9$ $\mathrm{M}_\odot$ we run additional simulations that covered a wider portion of the parameter space. In particular, as shown in tab. 3.4, we extended the surveyed values of $q_{\rm out}$ up to 10 and those of $e_{\rm in}$ and $e_{\rm out}$ to 0, for a total of 6240 simulations for this particular m_1 value.

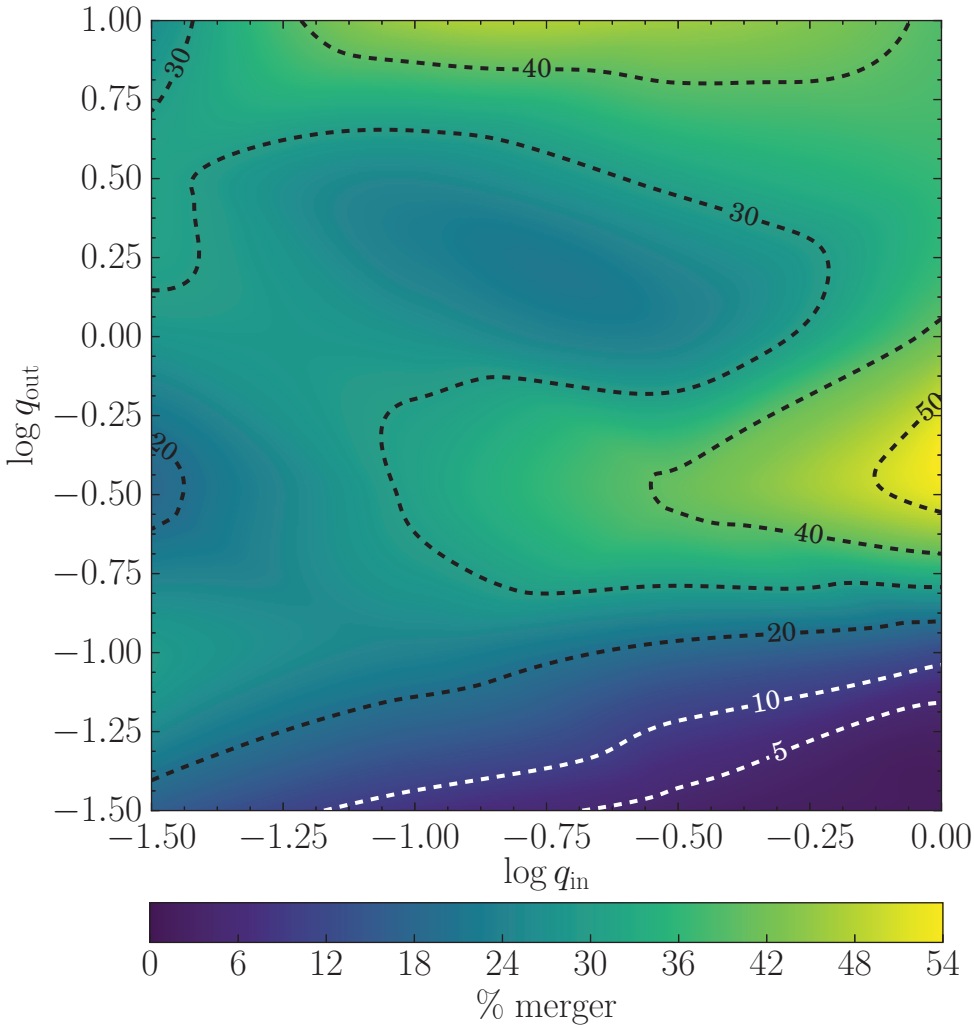

Figure 3.13: Same as fig. 3.2, but now extended up to $q_{\rm out} = 10$. Only the case $m_1 = 10^9 {\rm M}_\odot$ is considered.

Effect of a massive intruder

Although the inner mass ratio is $q_{\rm in} \leq 1$ by definition, the outer mass ratio $q_{\rm out} = m_3/(m_1+m_2)$ can be > 1 if the intruder is more massive than the bound binary. This can be relevant in a hierarchical structure-formation scenario, where a pre-existing stalled binary can interact with a third, more massive black hole following a major galaxy merger. To explore the possible outcomes of this kind of configurations, we run two additional sets of simulations characterised by $q_{\rm out} = 3$ and $q_{\rm out} = 10$. Although the stellar potential is likely dominated by the host galaxy of the intruder m_3 in these cases, we ignore this fact and simply centre the stellar potential in the (initial) centre of mass of the bound inner binary. This should not significantly affect the outcome of the simulations, at least qualitatively and in a statistical sense, since we find that the stellar potential has little effect on both the secular K-L evolution and the later chaotic phase (if present).

Results are shown in fig. 3.13, where the original parameter space of fig. 3.3 is extended up to $q_{\rm out} = 10$. As one might expect, the merger fraction is still

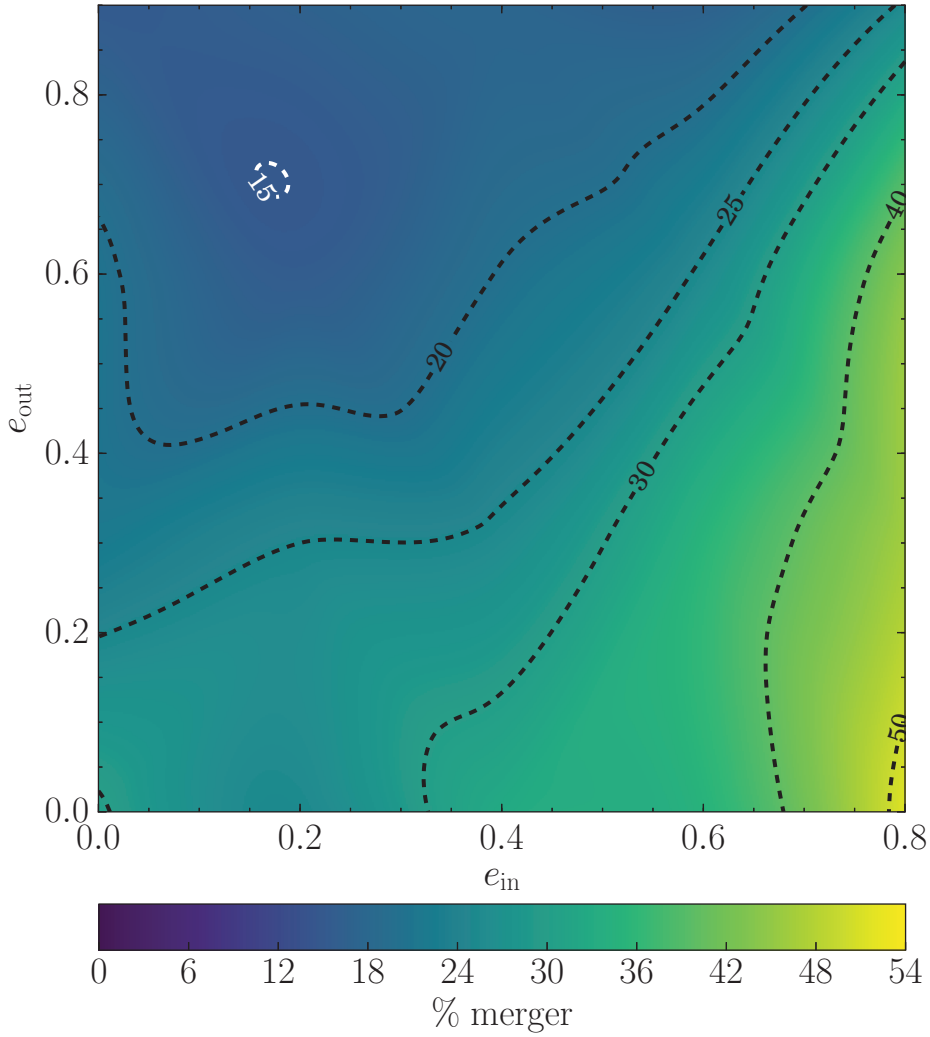

Figure 3.14: Same as fig. 3.4, but now extended to $e_{\rm in} = 0$ and $e_{\rm out} = 0$. Only the case $m_1 = 10^9 {\rm M}_\odot$ is considered.

high, around 30-40% when $q_{\rm out} \gtrsim 1$. This is the result of two competing effects. On the one hand the K-L timescale is inversely proportional to $m_3/(m_1 + m_2)$, i.e., a massive intruder can excite the eccentricity of the inner binary several times, favouring its prompt coalescence. On the other hand, at inclinations where K-L resonances are not very efficient, the unequal mass ratio favours the ejection of the lightest black hole, suppressing the fraction of systems that can merge because chaotic interactions.

Effect of low outer eccentricity

An interesting trend, already noted in fig. 3.4, concerns the increase of the merger fraction witnessed for low values of $e_{\rm out}$. By extending our survey to $e_{\rm out} = 0$ (and $e_{\rm in} = 0$), we have found that such trend is robust. Indeed, as indicated by the left corner of fig. 3.14, the merger fraction stays around 25-30% as already hinted by results shown in fig. 3.4. The reason of the trend has to ascribed to the enhanced stability of a less eccentric hierarchical triplet. A low

value of $e_{\rm out}$ can delay strong encounters, in which MBHs are more likely ejected and lost, i.e., actually avoiding any further three-body interaction. Therefore, stretching the lapse of time in which the K-L oscillation are active, it could lead the inner binary to coalescence.

3.3.3 Comparison with previous work

We compare the results of the analysis of our simulations with the work of Hoffman and Loeb (2007), to which our investigations are similar in spirit, although we introduce some important novelties. The major differences are, i) the surveyed parameter space, which we extend to a wider range of masses, mass ratios and initial eccentricities, ii) our conservative choice of not considering a DM component and, iii) the introduction of the conservative 1PN dynamics.

By comparing the merger fractions (their tab. 1 compared to our tab. 3.2), we immediately note that their values are typically a factor $\simeq 3$ larger than our results, even if "post-ejection" merger binaries are added to our total. The discrepancy can be understood by analysing the differences in the two implementations:

- All the simulations in Hoffman and Loeb (2007) have nearly the same total mass ($\simeq 6\times10^8{\rm M}_\odot$), and moreover they considered systems, except in one case, in which the MBHs are nearly equal-mass. The interaction of nearly equal-mass objects produces the highest merger fraction, as can be seen from, e.g., our tab. 3.3, where in the nearly equal-mass case the merger fraction is $\simeq 50\%$. In the only case in which Hoffman and Loeb (2007) consider a lower mass ratio, the merger fraction decreases below $\lesssim 70\%$, suggesting that the chosen mass ratio is in fact one of the reasons of the higher merger percentage. In practice, when restricting to comparable mass ratios, the merger fractions differ by less than a factor $\simeq 1.7$ ($\approx 50\%$ vs $\approx 85\%$).

- The value of the initial outer eccentricity can mildly influence the merger fraction, which increases as $e_{\rm out}$ decreases (see fig. 3.4 and fig. 3.14). All the simulations in Hoffman and Loeb (2007) have an initial $e_{\rm out}$ that at most is 0.3, i.e., the region of the parameter space where the merger fraction is higher.

- The 1PN dynamics can further contribute to the difference. Even though it is mostly effective at low mass ratios (as can be appreciated from fig. 3.5), the merger fraction can still be about 10% higher even at comparable mass ratios when the 1PN relativistic precession is neglected.

- The absence of a DM halo and the conservative threshold for MBH ejection assumed in our simulations also plays a role. As already discussed in section 3.1, our choice implies that a larger number of MBHs are ejected, compared to Hoffman and Loeb (2007). This is confirmed by their run featuring a less massive DM halo, where the merger fraction drops to $\sim 70\%$. As already discussed, our choice is meant to be conservative, in the

sense that outside the stellar bulge significant triaxiality and asymmetries in the potential will likely prevent the ejected MBH from returning back to the centre (Guedes et al., 2009; Sijacki, Springel, and Haehnelt, 2011). We will explore this issue in greater detail in a future work.

In summary, we argue that the combination of the four points above fully explains the differences between the two studies.

3.4 Summary

In the present chapter we have utilised the three-body integrator presented in chapter 2 to investigate the outcome of MBH triple interactions over a large parameter space. The code evolves the dynamics of MBH triplets including a variety of relevant factors, such as an external galactic potential, the dynamical friction against the stellar background, the stellar hardening, and the PN corrections to the equations of motion consistently derived from the three-body PN Hamiltonian. The set-up of the code is tuned to capture the physics relevant to three-body interactions of MBHs originated by repeated galaxy mergers in hierarchical cosmologies. We have explored the parameter space relevant to this specific context by considering primary MBH masses in the range $10^5\mathrm{M}_\odot \leq m_1 \leq 10^{10}\mathrm{M}_\odot$, a variety of inner and outer binary mass ratios in the range $0.03 - 1$, and several inner and outer binary initial eccentricities and mutual orbit inclinations as detailed in tab. 3.1. We have integrated a grand total of 14,976 configurations with the goal of deriving the fraction of merging systems as a function of the relevant parameters, as well as the typical merger timescales and properties of the coalescing MBHs.

Our main results can be summarised as follows:

- The fraction of systems experiencing the merger of one of any pair of MBHs in the triplet is about 30%. About 4/5 of these mergers are promptly induced during the three-body interaction, whereas about 1/5 are driven by GW emission following the ejection of the lightest black hole.

- Prompt mergers are induced both by secular K-L evolution and chaotic dynamics. The former is more efficient for massive intruders (large $q_{\rm out}$) and eccentric inner binaries, while the latter is most efficient for nearly equal-mass systems. Overall, the merger fraction is higher for large $q_{\rm out}$, reaching 40% of the systems.

- The 1PN terms in the equations of motion are important at low $q_{\rm in}/q_{\rm out}$. Neglecting such correction, the fraction of low-q systems leading to a merger goes from $\approx 20\%$ to about 40%. This happens because the relativistic precession implied by the 1PN term destroys the K-L resonances, preventing the inner binary from reaching eccentricities high enough to lead to coalescence because of GW back-reaction.

- The typical timescale for prompt mergers is well described by a log-normal distribution centred around $\log(T/\mathrm{yrs}) = 8.4$ with a dispersion of 0.4 dex,

almost independent of the masses and mass ratios involved. Note that this timescale is dominated by the orbital decay of the intruder, driven by dynamical friction and stellar hardening. Once the chaotic phase starts, mergers can be triggered within a few Myrs. Mergers following a MBH ejection occur on much longer timescales, of the order of several Gyrs.

- Merging binaries are generally driven to eccentricities in excess of 0.9 and up to 0.9999 in some cases, and even at coalescence binaries can retain a significant eccentricity, up to 0.1. Binaries driven by triple MBH interactions can therefore have eccentricities in excess of 0.5 when entering the LISA band, and in excess of 0.9 in the PTA frequency range.

Compared to the merger fractions found in previous studies (Hoffman and Loeb, 2007), our numbers are significantly lower. This is because our parameter space includes lower mass ratios (which give a lower merger fraction), PN dynamics (which partially suppresses K-L resonances) and a conservative prescription for ejection (which does not include the galactic DM potential). Essentially, we consider a MBH as ejected forever once it reaches the outskirts of the stellar bulge. This is justified by the fact that triaxiality and potential asymmetries will likely prevent the MBH from sinking back to the centre in less than a few Gyrs. In a future work, we plan to include a triaxial potentials in our simulations, in order to quantify the effects on the MBHB merger fraction.

The aforementioned results indicate that MBH triplets can have a significant impact on the evolution of a cosmic population of MBHs, and as a consequence, on the event detection rate expected for LISA and PTAs. In particular, three-body interactions provide a partial solution to the final-parsec problem, should all other binary shrinking mechanisms fail. This should guarantee a fairly large number of detectable GW sources, both by LISA and PTAs, regardless of the details of the interaction between MBHBs and their environment in galactic nuclei. In the next chapters, we investigate such issue in great detail, coupling our extensive library of MBH triplet simulations to a state-of-the-art semi-analytical model of galaxy and MBH cosmic evolution.

Appendix C

Merger fractions

In this appendix we report the tables of the merger fraction per range of m_1 sliced according to various IC parameters, i.e., mass ratios, eccentricities and relative inclination.

Table C.1: Results $m_1 = 10^{10}\mathrm{M}_\odot$

$m_1 = 10^{10}$ M$_\odot$	% Mergers			
$q_{\rm in}/q_{\rm out}$	m_1-m_2	m_1-m_3	m_2-m_3	Total
0.0316/0.0316	21.2	9.6	0.0	30.8(32.7)
0.0316/ 0.1	33.3	6.4	0.0	39.7(11.5)
0.0316/0.3162	19.9	4.5	0.0	24.4(7.7)
0.0316/ 1	32.1	1.3	5.8	39.1(7.7)
0.1/0.0316	7.7	7.7	0.0	15.4(15.4)
0.1/ 0.1	21.8	13.5	1.9	37.2(23.1)
0.1/0.3162	36.5	8.3	3.2	48.1(10.3)
0.1/ 1	18.6	4.5	4.5	27.6(7.1)
0.3162/0.0316	4.5	1.3	0.0	5.8(10.9)
0.3162/ 0.1	16.7	3.8	1.3	21.8(12.2)
0.3162/0.3162	37.2	14.7	1.9	53.8(15.4)
0.3162/ 1	19.2	7.7	7.1	34.0(7.1)
1/0.0316	0.6	1.3	0.6	2.6(5.1)
1/ 0.1	9.6	1.3	0.0	10.9(12.2)
1/0.3162	32.7	16.7	10.9	60.3(9.6)
1/ 1	25.6	18.6	15.4	59.6(14.7)
Average	21.1	7.6	3.3	31.9(12.7)

$m_1 = 10^{10}$ M$_\odot$	% Mergers			
$e_{\rm in}/e_{\rm out}$	m_1-m_2	m_1-m_3	m_2-m_3	Total
0.2/0.3	18.3	6.7	5.8	30.8(18.3)
0.2/0.6	8.2	9.6	2.9	20.7(6.7)
0.2/0.9	8.2	13.9	3.8	26.0(3.8)
0.4/0.3	24.5	4.8	3.4	32.7(7.2)
0.4/0.6	15.9	4.8	2.9	23.6(14.9)
0.4/0.9	13.9	11.5	2.9	28.4(7.2)
0.6/0.3	28.8	8.2	1.9	38.9(9.6)
0.6/0.6	19.2	6.2	2.9	28.4(10.6)
0.6/0.9	14.4	10.6	2.9	27.9(13.0)
0.8/0.3	47.1	3.4	2.4	52.9(3.4)
0.8/0.6	32.7	4.3	3.4	40.4(7.7)
0.8/0.9	21.6	6.7	4.3	32.7(5.8)
Average	21.1	7.6	3.3	31.9(12.7)

$m_1 = 10^{10}$ M$_\odot$	% Mergers			
ι	m_1-m_2	m_1-m_3	m_2-m_3	Total
10	14.6	9.4	7.8	31.8(14.1)
34.9323	11.5	8.9	3.6	24.0(14.6)
49.0917	16.7	7.3	4.2	28.1(12.0)
60.6678	20.8	7.8	2.1	30.7(14.6)
71.0409	23.4	9.4	3.6	36.5(10.4)
80.7981	23.4	8.9	3.6	35.9(12.5)
90.2902	29.7	6.2	2.1	38.0(12.5)
99.7903	33.9	4.7	2.6	41.1(10.9)
109.574	27.1	6.2	1.0	34.4(12.0)
120	25.5	5.7	1.6	32.8(15.1)
131.681	13.5	9.9	2.1	25.5(9.9)
146.094	15.1	5.7	3.6	24.5(12.0)
174.231	18.8	8.3	4.7	31.8(14.1)
Average	21.1	7.6	3.3	31.9(12.7)

Table C.2: Results $m_1 = 10^9 \mathrm{M}_\odot$

$m_1 = 10^9$ M$_\odot$	% Mergers			
$q_{\rm in}/q_{\rm out}$	m_1-m_2	m_1-m_3	m_2-m_3	Total
0.0316/0.0316	9.0	5.1	0.0	14.1(20.5)
0.0316/ 0.1	23.7	3.2	0.0	26.9(13.5)
0.0316/0.3162	9.0	1.3	0.6	10.9(3.8)
0.0316/ 1	25.0	0.0	1.9	26.9(0.0)
0.1/0.0316	4.5	1.9	0.0	6.4(16.7)
0.1/ 0.1	16.0	5.8	0.6	22.4(17.3)
0.1/0.3162	24.4	3.2	1.3	28.8(11.5)
0.1/ 1	25.6	0.0	7.1	32.7(1.3)
0.3162/0.0316	2.6	0.6	0.0	3.2(7.1)
0.3162/ 0.1	12.8	2.6	0.6	16.0(14.1)
0.3162/0.3162	26.3	14.1	3.8	44.2(16.0)
0.3162/ 1	17.3	1.9	4.5	23.7(5.8)
1/0.0316	1.3	0.0	0.0	1.3(5.1)
1/ 0.1	5.8	0.0	0.6	6.4(8.3)
1/0.3162	26.9	12.2	14.1	53.2(16.0)
1/ 1	13.5	14.1	15.4	42.9(21.8)
Average	15.2	4.1	3.2	22.5(11.2)

$m_1 = 10^9$ M$_\odot$	% Mergers			
$e_{\rm in}/e_{\rm out}$	m_1-m_2	m_1-m_3	m_2-m_3	Total
0.2/0.3	18.3	3.8	3.4	25.5(9.1)
0.2/0.6	7.7	3.8	3.4	14.9(8.7)
0.2/0.9	5.3	5.3	2.4	13.0(2.4)
0.4/0.3	16.3	3.4	3.8	23.6(13.5)
0.4/0.6	13.0	3.8	2.4	19.2(12.0)
0.4/0.9	7.7	5.3	3.4	16.3(8.2)
0.6/0.3	22.6	2.4	6.2	31.2(6.2)
0.6/0.6	12.0	5.3	2.9	20.2(11.1)
0.6/0.9	9.1	3.8	1.0	13.9(13.0)
0.8/0.3	34.1	1.9	1.9	38.0(5.3)
0.8/0.6	24.5	4.3	4.3	33.2(7.2)
0.8/0.9	12.0	6.2	2.9	21.2(13.0)
Average	15.2	4.1	3.2	22.5(11.2)

$m_1 = 10^9$ M$_\odot$	% Mergers			
ι	m_1-m_2	m_1-m_3	m_2-m_3	Total
10	10.9	4.2	6.2	21.4(14.6)
34.9323	10.4	4.2	3.1	17.7(10.4)
49.0917	10.4	1.6	7.8	19.8(14.1)
60.6678	10.4	2.1	7.3	19.8(13.0)
71.0409	8.3	5.7	3.6	17.7(8.3)
80.7981	17.7	6.2	0.5	24.5(12.5)
90.2902	26.6	6.2	1.0	33.9(8.3)
99.7903	27.1	2.1	1.0	30.2(8.9)
109.574	18.2	4.7	0.5	23.4(12.5)
120	22.4	2.6	3.1	28.1(13.0)
131.681	14.1	4.2	1.0	19.3(8.9)
146.094	10.4	5.2	2.1	17.7(10.9)
174.231	10.9	4.7	3.6	19.3(9.9)
Average	15.2	4.1	3.2	22.5(11.2)

Table C.3: Results $m_1 = 10^8 \mathrm{M}_\odot$

$m_1 = 10^8$ M$_\odot$	% Mergers			
$q_{\rm in}/q_{\rm out}$	m_1-m_2	m_1-m_3	m_2-m_3	Total
0.0316/0.0316	9.6	8.3	0.0	17.9(5.1)
0.0316/ 0.1	14.1	2.6	0.0	16.7(8.3)
0.0316/0.3162	28.2	0.6	0.6	29.5(1.9)
0.0316/ 1	14.7	1.3	2.6	18.6(3.2)
0.1/0.0316	4.5	3.2	0.0	7.7(5.8)
0.1/ 0.1	9.6	6.4	0.0	16.0(12.8)
0.1/0.3162	22.4	6.4	1.3	30.1(5.1)
0.1/ 1	21.8	0.0	1.9	23.7(2.6)
0.3162/0.0316	1.3	1.3	0.0	2.6(3.2)
0.3162/ 0.1	10.3	1.3	0.6	12.2(7.1)
0.3162/0.3162	25.6	9.0	1.9	36.5(11.5)
0.3162/ 1	23.1	3.2	8.3	34.6(5.1)
1/0.0316	0.0	0.6	0.0	0.6(3.2)
1/ 0.1	5.8	0.0	0.0	5.8(5.1)
1/0.3162	25.0	9.6	10.9	45.5(11.5)
1/ 1	19.2	10.3	11.5	41.0(9.0)
Average	14.7	4.0	2.5	21.2(6.3)

$m_1 = 10^8$ M$_\odot$	% Mergers			
$e_{\rm in}/e_{\rm out}$	m_1-m_2	m_1-m_3	m_2-m_3	Total
0.2/0.3	15.9	4.3	4.8	25.0(3.4)
0.2/0.6	12.0	4.3	3.4	19.7(6.2)
0.2/0.9	4.3	3.8	2.4	10.6(2.4)
0.4/0.3	18.3	3.4	1.9	23.6(5.3)
0.4/0.6	14.9	4.8	1.4	21.2(11.1)
0.4/0.9	4.8	5.8	2.9	13.5(5.3)
0.6/0.3	20.7	2.9	1.4	25.0(1.4)
0.6/0.6	13.0	3.8	1.4	18.3(4.3)
0.6/0.9	3.4	5.3	2.9	11.5(1.4)
0.8/0.3	34.6	1.4	2.4	38.5(1.0)
0.8/0.6	23.6	4.3	1.9	29.8(2.4)
0.8/0.9	11.1	3.8	2.9	17.8(5.8)
Average	14.7	4.0	2.5	21.2(6.3)

$m_1 = 10^8$ M$_\odot$	% Mergers			
ι	m_1-m_2	m_1-m_3	m_2-m_3	Total
10	10.4	3.1	3.6	17.2(6.8)
34.9323	8.9	3.1	3.1	15.1(6.2)
49.0917	6.8	5.2	4.2	16.1(8.3)
60.6678	13.0	5.7	2.6	21.4(4.7)
71.0409	11.5	3.1	2.6	17.2(8.9)
80.7981	14.6	2.6	4.2	21.4(6.8)
90.2902	27.6	0.5	1.6	29.7(3.1)
99.7903	28.1	2.1	1.0	31.2(3.1)
109.574	20.3	4.2	2.1	26.6(6.8)
120	19.3	2.6	1.6	23.4(5.2)
131.681	13.5	4.2	2.1	19.8(5.2)
146.094	7.8	7.3	0.0	15.1(8.9)
174.231	9.4	8.3	3.6	21.4(7.8)
Average	14.7	4.0	2.5	21.2(6.3)

Table C.4: Results $m_1 = 10^7 \mathrm{M}_\odot$

$m_1 = 10^7$ M$_\odot$	% Mergers			
$q_{\rm in}/q_{\rm out}$	m_1-m_2	m_1-m_3	m_2-m_3	Total
0.0316/0.0316	5.1	4.5	0.0	9.6(6.4)
0.0316/ 0.1	23.1	1.9	0.0	25.0(1.9)
0.0316/0.3162	23.7	3.2	0.6	27.6(7.7)
0.0316/ 1	23.7	5.8	0.0	29.5(1.9)
0.1/0.0316	3.2	0.6	0.0	3.8(3.2)
0.1/ 0.1	9.6	2.6	0.0	12.2(6.4)
0.1/0.3162	32.1	1.3	0.6	34.0(5.1)
0.1/ 1	22.4	1.9	0.6	25.0(3.2)
0.3162/0.0316	0.0	0.6	0.0	0.6(0.6)
0.3162/ 0.1	10.3	0.0	1.3	11.5(5.8)
0.3162/0.3162	23.1	6.4	0.6	30.1(4.5)
0.3162/ 1	23.1	0.0	7.1	30.1(0.6)
1/0.0316	1.3	0.0	0.0	1.3(0.6)
1/ 0.1	6.4	1.3	0.6	8.3(2.6)
1/0.3162	24.4	3.8	5.1	33.3(9.0)
1/ 1	14.7	6.4	6.4	27.6(11.5)
Average	15.4	2.5	1.4	19.4(4.4)

$m_1 = 10^7$ M$_\odot$	% Mergers			
$e_{\rm in}/e_{\rm out}$	m_1-m_2	m_1-m_3	m_2-m_3	Total
0.2/0.3	18.8	2.4	2.4	23.6(2.4)
0.2/0.6	6.7	2.4	1.9	11.1(0.0)
0.2/0.9	3.4	4.8	1.4	9.6 (1.4)
0.4/0.3	21.6	1.4	2.4	25.5(3.8)
0.4/0.6	13.9	1.0	1.0	15.9(6.2)
0.4/0.9	5.8	2.9	1.4	10.1(4.8)
0.6/0.3	21.6	2.4	1.0	25.0(1.4)
0.6/0.6	13.5	1.9	1.9	17.3(5.8)
0.6/0.9	8.7	2.9	0.5	12.0(3.8)
0.8/0.3	39.4	0.5	0.5	40.4(1.4)
0.8/0.6	22.6	4.8	1.4	28.8(1.9)
0.8/0.9	8.7	2.9	1.4	13.0(4.3)
Average	15.4	2.5	1.4	19.4(4.4)

$m_1 = 10^7$ M$_\odot$	% Mergers			
ι	m_1-m_2	m_1-m_3	m_2-m_3	Total
10	12.5	2.6	1.6	16.7(5.7)
34.9323	10.4	1.0	2.1	13.5(6.8)
49.0917	12.0	2.1	3.1	17.2(3.6)
60.6678	11.5	3.1	1.6	16.1(4.7)
71.0409	14.6	2.6	1.6	18.8(5.2)
80.7981	14.1	4.2	1.0	19.3(4.7)
90.2902	31.2	1.6	1.0	33.9(3.6)
99.7903	26.0	1.0	1.0	28.1(3.1)
109.574	24.0	3.6	0.0	27.6(2.6)
120	17.2	1.6	1.0	19.8(4.7)
131.681	11.5	2.1	1.6	15.1(4.2)
146.094	8.3	3.6	1.0	13.0(4.2)
174.231	6.8	3.6	2.1	12.5(4.7)
Average	15.4	2.5	1.4	19.4(4.4)

Table C.5: Results $m_1 = 10^6 \mathrm{M}_\odot$

$m_1 = 10^6$ M$_\odot$	% Mergers			
$q_{\rm in}/q_{\rm out}$	m_1-m_2	m_1-m_3	m_2-m_3	Total
0.0316/0.0316	4.5	0.6	0.0	5.1(1.3)
0.0316/ 0.1	11.5	0.0	0.0	11.5(0.0)
0.0316/0.3162	25.6	0.0	0.0	25.6(2.6)
0.0316/ 1	39.7	0.0	1.9	41.7(0.6)
0.1/0.0316	1.3	0.6	0.0	1.9(1.9)
0.1/ 0.1	9.0	1.3	0.0	10.3(6.4)
0.1/0.3162	38.5	0.0	0.0	38.5(2.6)
0.1/ 1	43.6	0.0	0.6	44.2(0.6)
0.3162/0.0316	0.6	0.6	0.0	1.3(1.3)
0.3162/ 0.1	3.2	0.6	0.0	3.8(0.0)
0.3162/0.3162	19.9	1.3	0.0	21.2(1.9)
0.3162/ 1	26.3	1.3	2.6	30.1(1.9)
1/0.0316	0.6	0.0	0.0	0.6(0.6)
1/ 0.1	1.9	0.6	0.6	3.2(1.3)
1/0.3162	17.9	6.4	4.5	28.8(5.1)
1/ 1	14.7	8.3	5.8	28.8(1.9)
Average	16.2	1.4	1.0	18.5(1.9)

$m_1 = 10^6$ M$_\odot$	% Mergers			
$e_{\rm in}/e_{\rm out}$	m_1-m_2	m_1-m_3	m_2-m_3	Total
0.2/0.3	16.3	2.9	1.4	20.7(1.4)
0.2/0.6	6.7	0.5	0.5	7.7 (1.4)
0.2/0.9	6.2	1.0	1.4	8.7 (3.4)
0.4/0.3	18.8	1.4	1.4	21.6(1.9)
0.4/0.6	14.4	1.4	1.9	17.8(3.4)
0.4/0.9	7.7	1.0	1.0	9.6 (3.4)
0.6/0.3	27.4	0.5	0.5	28.4(0.0)
0.6/0.6	13.9	2.4	0.0	16.3(0.0)
0.6/0.9	9.1	1.4	0.5	11.1(0.0)
0.8/0.3	38.0	1.4	1.4	40.9(0.0)
0.8/0.6	22.6	0.5	0.5	23.6(0.0)
0.8/0.9	13.0	1.9	1.4	16.3(0.5)
Average	16.2	1.4	1.0	18.5(1.9)

$m_1 = 10^6$ M$_\odot$	% Mergers			
ι	m_1-m_2	m_1-m_3	m_2-m_3	Total
10	13.0	3.1	1.0	17.2(3.6)
34.9323	13.5	0.0	2.1	15.6(1.6)
49.0917	15.6	2.1	1.0	18.8(1.0)
60.6678	17.7	0.5	1.6	19.8(2.6)
71.0409	14.1	0.5	1.0	15.6(1.6)
80.7981	18.2	0.5	0.0	18.8(1.6)
90.2902	33.3	0.5	0.5	34.4(0.5)
99.7903	25.5	0.5	0.0	26.0(1.6)
109.574	20.3	1.0	0.5	21.9(2.1)
120	15.6	2.6	1.6	19.8(0.5)
131.681	9.9	1.6	0.0	11.5(4.2)
146.094	5.7	1.6	3.1	10.4(1.0)
174.231	7.8	3.1	0.5	11.5(2.6)
Average	16.2	1.4	1.0	18.5(1.9)

Table C.6: Results $m_1 = 10^5 \mathrm{M}_\odot$

$m_1 = 10^5$ M$_\odot$	% Mergers			
$q_{\rm in}/q_{\rm out}$	m_1-m_2	m_1-m_3	m_2-m_3	Total
0.0316/0.0316	1.9	1.9	0.0	3.8(2.6)
0.0316/ 0.1	19.2	1.3	0.0	20.5(0.0)
0.0316/0.3162	34.6	0.0	0.0	34.6(1.3)
0.0316/ 1	23.1	0.0	1.3	24.4(3.8)
0.1/0.0316	0.6	0.0	0.0	0.6(1.3)
0.1/ 0.1	8.3	0.6	0.6	9.6(3.2)
0.1/0.3162	35.3	0.6	0.0	35.9(1.3)
0.1/ 1	40.4	0.0	0.0	40.4(0.0)
0.3162/0.0316	1.9	0.0	0.0	1.9(0.0)
0.3162/ 0.1	2.6	0.6	0.0	3.2(3.8)
0.3162/0.3162	28.2	0.6	0.6	29.5(3.2)
0.3162/ 1	30.8	0.6	3.8	35.3(0.0)
1/0.0316	0.0	0.0	0.0	0.0(0.6)
1/ 0.1	5.8	0.0	0.0	5.8(1.3)
1/0.3162	19.2	3.8	5.1	28.2(2.6)
1/ 1	16.7	4.5	1.9	23.1(1.3)
Average	16.8	0.9	0.8	18.5(1.6)

$m_1 = 10^5$ M$_\odot$	% Mergers			
$e_{\rm in}/e_{\rm out}$	m_1-m_2	m_1-m_3	m_2-m_3	Total
0.2/0.3	17.3	0.5	1.4	19.2(1.0)
0.2/0.6	10.1	0.5	0.5	11.1(0.5)
0.2/0.9	2.9	1.9	1.0	5.8 (1.4)
0.4/0.3	17.8	0.0	1.9	19.7(0.5)
0.4/0.6	12.5	1.4	1.0	14.9(1.4)
0.4/0.9	6.7	1.0	0.5	8.2 (1.4)
0.6/0.3	26.4	1.4	1.0	28.8(0.5)
0.6/0.6	18.8	0.5	0.5	19.7(1.0)
0.6/0.9	10.1	0.5	0.5	11.1(2.4)
0.8/0.3	38.5	0.0	0.5	38.9(1.0)
0.8/0.6	26.0	1.0	1.0	27.9(1.4)
0.8/0.9	14.4	2.4	0.5	17.3(2.4)
Average	16.8	0.9	0.8	18.5(1.6)

$m_1 = 10^5$ M$_\odot$	% Mergers			
ι	m_1-m_2	m_1-m_3	m_2-m_3	Total
10	16.7	0.0	1.6	18.2(3.1)
34.9323	15.6	1.6	0.5	17.7(2.6)
49.0917	18.2	0.0	1.6	19.8(1.6)
60.6678	15.1	0.5	2.6	18.2(1.6)
71.0409	12.5	0.5	0.5	13.5(2.6)
80.7981	16.1	0.0	0.5	16.7(1.0)
90.2902	31.8	0.5	0.5	32.8(1.6)
99.7903	30.7	0.5	0.0	31.2(1.0)
109.574	21.4	1.6	2.1	25.0(1.0)
120	17.7	0.5	0.0	18.2(1.0)
131.681	9.9	1.6	0.5	12.0(0.5)
146.094	5.2	1.6	0.0	6.8(2.1)
174.231	7.3	3.1	0.5	10.9(1.6)
Average	16.8	0.9	0.8	18.5(1.6)

Chapter 4

Cosmological framework

The results obtained in previous chapters provide a complete and detailed description of three-body interactions involving MBHs in galactic nuclei. However, the simulated sample, although very large when compared to similar exiting studies, lacks an important point in order to represent a truly realisation of our Universe. Indeed, the information that misses is the cosmological "weight" that each combination of the surveyed parameters has, e.g., how likely are low mass systems with respect to the most massive ones or the evolution of the merger rate with time. These information are crucial to asses the shape and the strength of the expected cosmic GW signal. Since MBHs are intimately connected to the evolution of their hosts, we therefore need a tool that can reproduce the symbiotic evolution of both.

One of the main difficulties met in tackling the problem of galaxy formation and evolution is the huge dynamical spatial range involved, which spans form several Gpc, i.e., the present cosmological horizon, to even fractions of micro-pc, i.e., the scale at which MBH mergers actually take place. The extremely large dynamical range and the complex nature of the involved process, often non-linear and dissipative, prevent to attain a comprehensive solution of the problem in full generality. Therefore, in order to overcome these difficulties, one can rely on various methods with different levels of approximations.

The approaches employed in any study of galaxy formation and evolution are essentially two. On one side, hydrodynamical simulations, in which the evolution of particles that form the cosmic structure (DM and baryons, see fig. 4.1) is computed by numerically solving the equations of hydrodynamics and gravity, offer a very powerful tool (Springel and Hernquist, 2003; Springel, 2005; Di Matteo, Springel, and Hernquist, 2005; Scannapieco et al., 2009; Kravtsov and Gnedin, 2005; Tassis et al., 2003; Tassis, Kravtsov, and Gnedin, 2008; Dubois and Teyssier, 2008; Blecha et al., 2011; Guedes et al., 2011; Sijacki, Springel, and Haehnelt, 2009; Sijacki, Springel, and Haehnelt, 2011; Teyssier et al., 2011; DeGraf et al., 2012; Dubois et al., 2014; Hirschmann et al., 2014; Vogelsberger et al., 2014; Khandai et al., 2015; Feng et al., 2016; Volonteri et al., 2016).

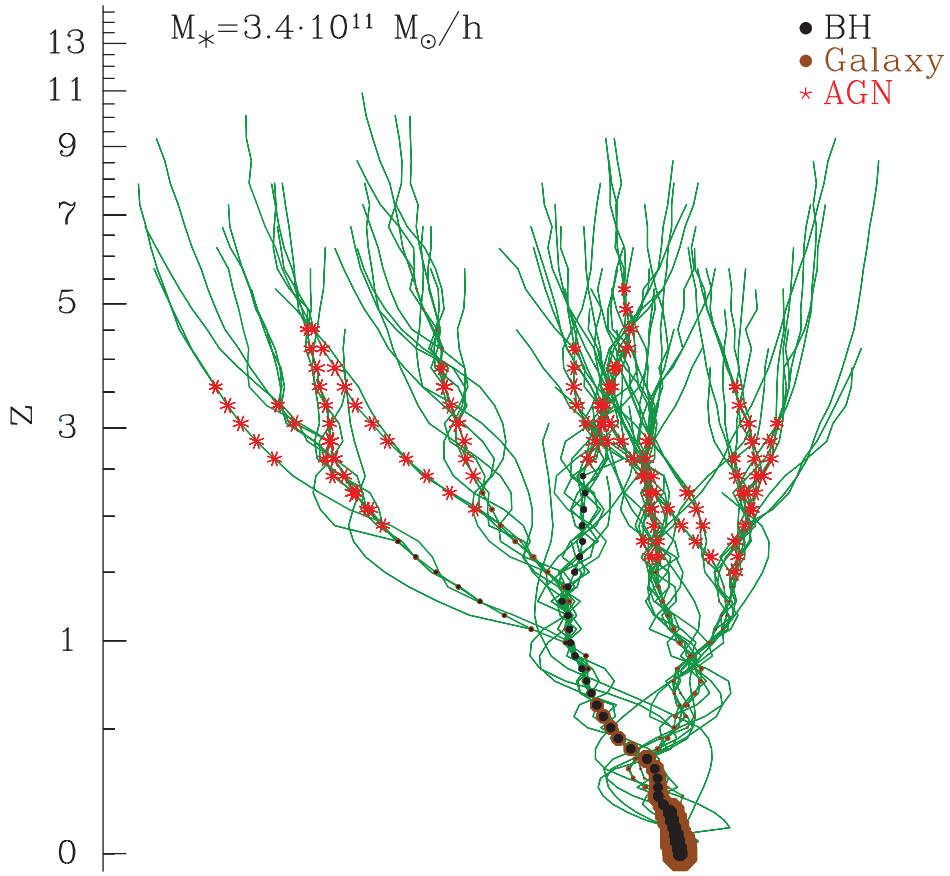

Figure 4.1: Example of a cosmological merger tree that leads to the formation of a galaxy hosting a MBH within $z = 0$. Shown is the merger history of all the DM halos containing galaxies and MBHs that merge with each other in forming the final structure. *Credit:* Marulli et al. (2009).

On the other side, in the so-called "semi-analytical models" (SAMs) a different approach is adopted. The DM halo formation and merger history relies on analytical theories of structure formation (the so-called "Press and Schechter" formalism, Press and Schechter, 1974), coupled to Monte-Carlo methods, while the physics of the baryonic component of the cosmic fluid is treated with simplified recipes tuned to match observational constraints (e.g., the specific star formation rate. See, e.g., Kauffmann, White, and Guiderdoni, 1993; Cole et al., 1994; Cole et al., 2000; Somerville and Primack, 1999; Somerville et al., 2008; Croton et al., 2006; Bower et al., 2006; Benson and Bower, 2010; Monaco, Fontanot, and Taffoni, 2007; Barausse, 2012).

SAMs are optimally suited to perform statistical studies of the formation and evolution of binary and multiple MBH systems at a fairly modest computational cost, especially when compared to the more informative, but much dearer, hydro-simulations of statistically significant cosmological boxes. In particular, we simulate the co-evolution of MBHs and their host galaxies adopting the SAM originally proposed by Barausse (2012), with later improvements described in Sesana et al. (2014), Antonini, Barausse, and Silk (2015a), Antonini, Barausse, and Silk (2015b), and Barausse et al. (2017). The main novelty we employ

here is the implementation in the SAM of our results regarding multiple MBH interactions, in terms of merger fraction, timescales, eccentricity distribution, etc., as described in the previous chapters of this thesis. The coupling of our statistical study of triplets to the SAM allows us to put our detailed, PN calculations in the context of cosmic structure formation.

4.1 Description of the SAM

Here we summarise the main features of the SAM we adopt. For full details, the interested readers are addressed to Barausse et al. (2017), and references therein.

The evolution of DM halos is modelled via merger trees produced with an extended Press-Schechter formalism, suitably modified so as to reproduce the results of N-body simulations (Press and Schechter, 1974; Parkinson, Cole, and Helly, 2008). The baryonic components of galaxies are then evolved along the branches of these merger trees, while the nodes of the trees correspond to the moment when two halos touch, thus initiating the processes leading to halo, galaxy and possibly MBH coalescence.

In more detail, galaxies form from either the cooling of an unprocessed "hot" gas component shock-heated to the halo virial temperature, or (especially in low-mass systems and at high redshift) from accretion flows of colder gas (Dekel and Birnboim, 2006; Cattaneo et al., 2006; Dekel et al., 2009). When the gas has reached the halo centre as a result of either of these channels it forms a disc, simply by conservation of angular momentum, and eventually starts forming stars. Galactic spheroids form instead when the gaseous and galactic discs are destroyed either by bar instabilities or by major galactic mergers. Both these processes are also assumed to drive cold gas to the galactic centre, thus enhancing star formation. During star formation episodes (in both discs and spheroids) the feedback from supernova explosions on the surrounding gas is accounted for.

MBHs are formed from high-redshift seeds, with several possible choices for their initial mass function and halo occupation fraction. In this thesis, we consider a "light-seed" (*LS*) scenario, where seeds of a few hundred $M_\odot$ are provided by the remnants of popIII stars forming in low-metallicity high-redshift galaxies (Madau and Rees, 2001), and a "heavy-seed" (*HS*) scenario where larger ($\sim 10^5 M_\odot$) seeds form from the collapse of protogalactic discs due to, e.g., to bar instabilities. In the *LS* scenario we populate with seeds only the most massive halos (i.e., those collapsing from the $3.5\,\sigma$ peaks of the primordial density field) at redshift $15 < z < 20$. The mass of each seed is assumed to be $\simeq 2/3$ of the initial mass of the popIII star (to account for mass losses during the collapse of the star). The mass of the star is drawn randomly from a log-normal distribution centred at 300 $M_\odot$ with rms equal 0.2 dex and an exclusion region between 140 and 260 $M_\odot$, since in this mass range stars end their life as pair-instability supernovae leaving no relic (Heger and Woosley, 2002).

For the *HS* scenario, we follow Volonteri, Lodato, and Natarajan (2008), who model the formation of massive seeds from disc bar instabilities at redshift

$15 < z < 20$. The model has just one free parameter, i.e., the critical Toomre parameter Q_c at which the instability sets in. The most likely values for Q_c range between 2 and 3. Here, we adopt $Q_c = 2.5$.

After their formation, black-hole seeds grow via accretion and mergers. For the former channel, we assume that a gas reservoir forms in the nuclear region of each galaxy as a result of cold gas being funnelled to the centre during major galactic mergers or bar instabilities of the gaseous galactic discs. Because both kinds of events are also thought to trigger spheroid formation, we follow Granato et al. (2004) and Lapi et al. (2014) and assume that the feeding of the nuclear gas reservoir is linearly correlated with the star formation rate in the spheroid component.

The MBH then accretes from this reservoir on the viscous timescale, and we cap the accretion rate at the Eddington rate in the *HS* scenario, at twice the Eddington rate in the *LS* one.[1] As a result, a MBH undergoes periods of quiescent activity interrupted by quasar/AGN phases. The feedback of the MBH on the surrounding gas is taken into account in both the quasar-mode and radio-mode phases. The former is mainly due to radiative feedback and is connected to high accretion rate. The latter instead is linked to radio-jets where the transfer of the AGN energy to gas proceeds via momentum exchanges. The nuclear gas reservoir not only feeds the MBH, it forms stars too, producing a nuclear star cluster (Antonini, Barausse, and Silk, 2015a; Antonini, Barausse, and Silk, 2015b). We assume that nuclear star clusters can form and grown also via a second channel, namely the migration of globular clusters to the nuclear region induced by dynamical friction (Antonini, Barausse, and Silk, 2015a; Antonini, Barausse, and Silk, 2015b).

After two halos start coalescing (at the nodes of the merger tree), the smaller halo (the "satellite") initially retains its identity within the bigger one (the "host"), slowly falling towards the centre driven by dynamical friction. We account for this phase by using the expression for the dynamical-friction time taken from Boylan-Kolchin, Ma, and Quataert (2008), which is calibrated against numerical simulations, and accounts for the effect of both DM and baryons. We also model the mass loss suffered by the satellite halo and its galaxy due to tidal stripping and evaporation (Taffoni et al., 2003). When the satellite subhalo and its galaxy merge with the host, the MBHs contained in the two galaxies may still be very far apart (at $\sim$ kpc distances). Nevertheless, at least when the satellite and the host have mass ratios $\gtrsim 0.1$ (the most relevant case for our results, cf. section 5.4), dynamical friction against the gas and stars of the newly formed galaxy quickly drives the two MBHs toward the centre (Callegari et al., 2009). This process is particularly efficient because, at least in its initial stages, the MBHs are expected to be still surrounded by a stellar core from their host galaxy, resulting in a shorter dynamical-friction timescale. Therefore, for the purpose of this work, we can safely neglect this phase and assume that whenever the host and satellite galaxies coalesce, the MBHs are efficiently driven down to a

[1] Note that, in order to reproduce the high-redshift active galactic nuclei (AGN) luminosity function in an *LS* scenario, periods of super-Eddington accretion are required, cf. Madau, Haardt, and Dotti (2014).

separation comparable to the primary MBH influence radius $r_i \approx 2Gm_1/\sigma^2$ (m_1 being the primary black hole mass and σ the velocity dispersion of the host spheroid).

The subsequent evolution of the MBHs is accounted for with the simple prescriptions outlined in (Antonini, Barausse, and Silk, 2015a; Antonini, Barausse, and Silk, 2015b). Briefly, in a gas-rich nuclear environment we assume that the MBH binary is driven to sub-pc separation (where GW emission is sufficiently efficient to trigger the merger) by planetary-like migration within the nuclear disc, and we assume that this phase lasts one viscous time (evaluated at the influence radius of the binary), i.e., $\sim 10^7 - 10^8$ yr.[2]

In gas-poor environments (more relevant for PTAs), the MBH binary is instead driven to sub-pc separations by stellar hardening, i.e., by three-body interactions with stars. We model this phase by assuming that its duration is given by the hardening timescale evaluated at the influence radius of the MBH binary (Sesana and Khan, 2015), or to the timescale of the hardening from the nuclear star cluster, whichever the shorter. In practice, these hardening timescales are typically of a few Gyr.

We account for the possibility that while a MBH binary is still evolving under gas-driven migration or hardening, another galaxy merger may take place. This would bring a third MBHs down to pc-scale separations, possibly triggering the coalescence of the inner binary via K-L resonances (Kozai, 1962; Lidov, 1962) or chaotic three-body interactions (see examples in chapter 2).

Clearly, the importance of these MBH triple systems in triggering MBH coalescences depends sensitively on the "delays" between the time halos start merging and the time MBHs eventually coalesce. In our study, we consider two different possible situations, one in which the delays are implemented as described above (*Model-delayed* hereinafter), and a second case in which the delays are artificially set to values larger than the age of the Universe (i.e., MBH mergers never take place unless triggered by three-body MBH interactions) dubbed *Model-stalled* hereinafter. Coupled with the different MBH seeding prescription, we therefore have four distinct models: *Model-delayed-LS*, *Model-stalled-LS*, *Model-delayed-HS*, *Model-stalled-HS*.

As outlined in the next section, we model triple interactions by using the results described in chapter 3 obtained with the three-body PN code presented in chapter 2.

[2]This prescription is strictly valid for low mass MBHBs, i.e., with total mass lower than $\sim 10^7$ $M_\odot$ (see, e.g., Haiman, Kocsis, and Menou, 2009). Indeed, the orbital shrinking of more massive binaries is dominated by other physical process (dynamical friction and/or three-body interactions with stars). In any case, very massive systems are usually gas-poor, therefore this prescription would not be applied at all to high mass binaries. Indeed, looking at tab. 5.1 in the next chapter the fraction of high mass binaries that merge because of gas-driven dynamics is practically negligible, thus confirming the validity of the employed simplified recipe.

4.2 Treatment of triple and quadruple MBH systems

The backbone for a consistent treatment of multiple (i.e., triple and quadruple) MBH interactions in the semi-analytical model described above is the large suite of numerical simulations described in chapter 3. We have collected the outcome of triple MBH interactions on a grid of primary MBH mass, m_1, sampled in the range $[10^5\,\mathrm{M}_\odot, 10^{10}\,\mathrm{M}_\odot]$, and inner and outer binary mass ratio $q_{\rm in} \in [0.03, 1]$ and $q_{\rm out} \in [0.03, 10]$.[3] For each point in the 3D grid (m_1, $q_{\rm in}$, $q_{\rm out}$), we simulate several systems with different inner and outer orbit eccentricities, and different relative inclinations, and we use the results to compute merger fractions, merger-time distributions and MBHB eccentricity distributions just before merger (more precisely, we record eccentricities at separations of $100R_{\rm G}$, where $R_G = GM/c^2$ is the gravitational radius associated with the merging MBHB total mass $M = m_i + m_j$, with $i \neq j : 1, 2, 3$). In particular, we isolate three distinct outcomes (see fig. 4.2) and their associated occurrence probabilities:

1. A prompt coalescence triggered by a triple interaction. The coalescence can involve any one pair of MBHs in the triplet. We identify here with body 1 and 2 the two MBHs of the inner binary ($m_1 \geq m_2$ by definition) and with body 3 the intruder. For each grid point in our simulation suite, we record three numbers a, b and c identifying the fractions of simulations in which bodies 1-2, 1-3 and 2-3 merge, respectively.

2. An ejection of one of the MBHs (the lighter, in the overwhelming majority of the cases) and a delayed merger of the remaining binary (shrunk or made more eccentric by the 3-body interaction) under the effect of GW emission. This occurs in a fraction d of the realizations.

3. An ejection and a left-over binary unable to merge alone within the Hubble time. Such binary can potentially undergo new multiple MBH interactions following later galaxy mergers, or it can coalesce under the effect of gas-driven migration or stellar hardening (*Model-delayed* only).

The relative occurrence of the different outcomes depend on the chosen point in the 3-D grid (m_1, $q_{\rm in}$, $q_{\rm out}$). We also stress that our treatment of triple interactions is conservative, because the ejected MBH may fall back to the galactic nucleus after the left-over binary merged, thus potentially providing an additional MBH merger in a minority of cases (around $\sim 10 - 20\%$, see, Hoffman and Loeb, 2007).

In any given triple interaction produced by the semi-analytical model, the probability of a given outcome is obtained by using a trilinear interpolation

[3] While we define $q_{\rm in} \leq 1$ by construction, the intruder might be more massive than the pre-existent MBHB (even though this occurs in a minority of cases). Note that for $q_{\rm out} > 1$ we performed a restricted set of simulations for $m_1 = 10^9\,\mathrm{M}_\odot$ only. Given that none of the results for $q_{\rm out} < 1$ has a strong dependence on the mass scale, we extrapolate the $q_{\rm out} > 1$ results obtained for $m_1 = 10^9\,\mathrm{M}_\odot$ to all masses.

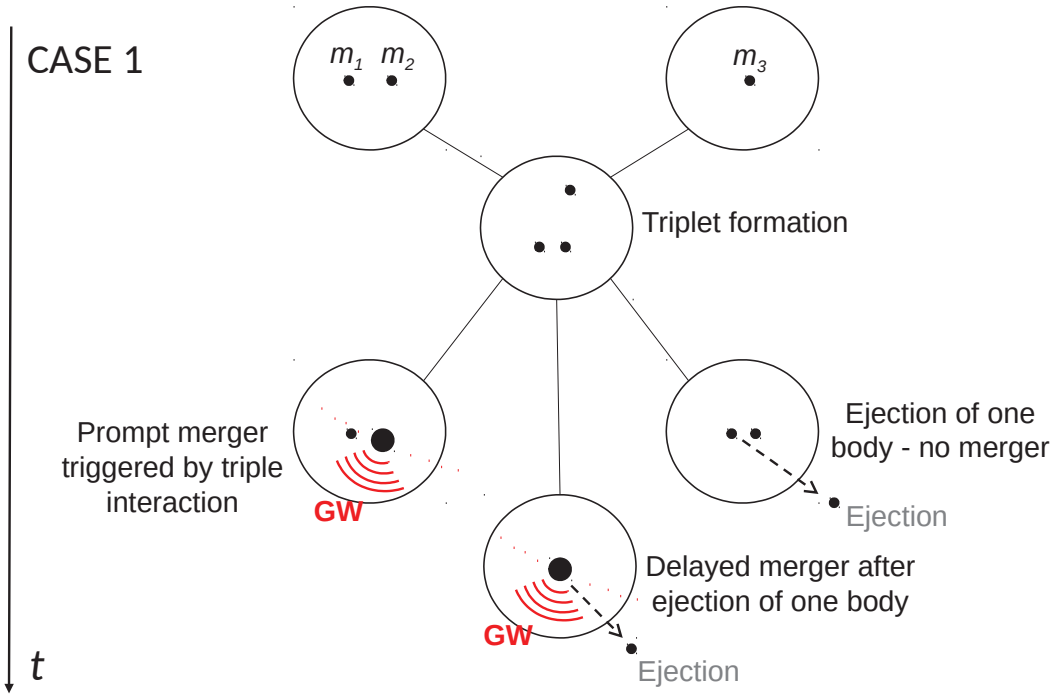

Figure 4.2: Cartoon representation of how triple MBH interactions are treated in the semi-analytical model described in section 4.1.

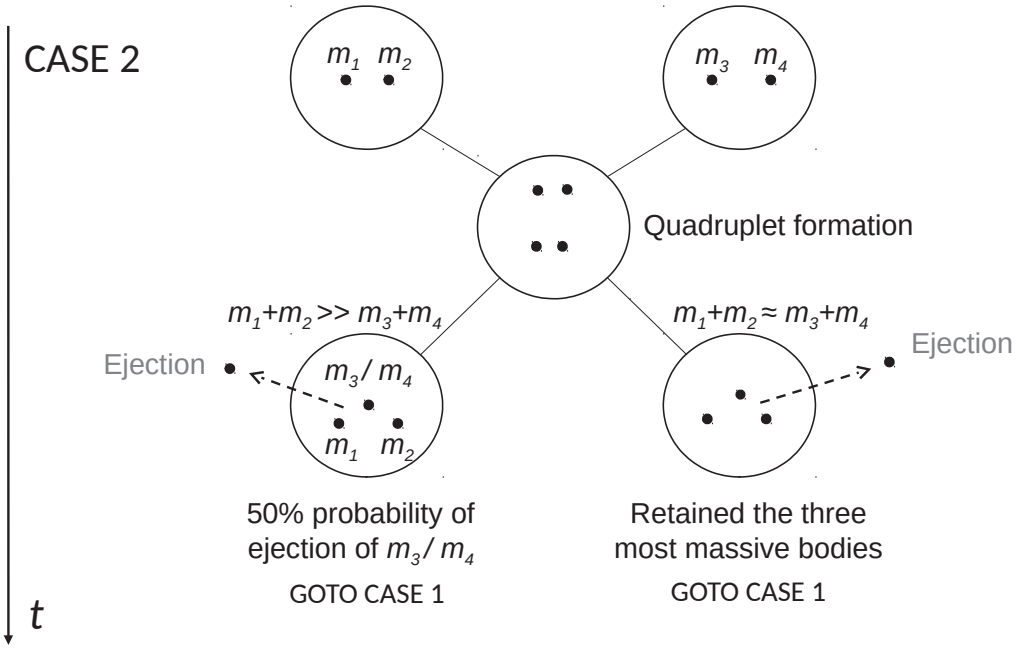

Figure 4.3: Same as figure 4.2, but for quadruple interactions.

between the surveyed grid points, in order to estimate the fractions a, b, c, d for that specific system. A random number P between 0 and 1 is then drawn and, according to its value, one of the following choices is selected:

- If $P < a + b + c \rightarrow$ prompt merger:
  - If $P \leq a \rightarrow$ merger of bodies 1-2.
  - If $a < P \leq a + b \rightarrow$ merger of bodies 1-3.
  - If $a + b < P \leq a + b + c \rightarrow$ merger of bodies 2-3.
- If $a + b + c < P \leq a + b + c + d \rightarrow$ delayed merger (of the two most massive bodies).
- If $a + b + c + d < P \rightarrow$ no merger (left-over binary formed by the two most massive bodies).

In the case of a merger, the relevant timescale is obtained by sampling the distribution of merger timescales for the two cases of prompt and delayed mergers, respectively (see chapter 3, fig. 3.6). We also note that the parameters of a given triplet can lie outside the grid sampled in chapter 3. In particular, we can have $q_{\rm in} < 0.03$ and/or $q_{\rm out} < 0.03$ or $q_{\rm out} > 10$. In these cases we simply apply the fractions and timescale distributions of the closest grid point. Although this is certainly a crude approximation, in the next chapter we will show that the GW signal is much weaker for low mass-ratio binaries, and our treatment of those systems does not change our results significantly.

Besides the formation of triplets, quadruple interactions (caused by the merger of two galaxies, both hosting a binary) are a natural occurrence, especially in *Model-stalled*. In absence of a library of simulations of quadruple interactions, we reduce the problem to the triplet case, as shown in fig. 4.3. If one of the two binaries is much lighter than the other (we arbitrarily choose a threshold mass ratio of 0.1), we expel one of its two members with 50% probability, irrespectively of the mass ratio of the binary, retaining only one intruder and reducing the problem to the triplet case. This assumption is made in analogy to the problem of a stellar binary interacting with a much more massive object (usually a MBH or an intermediate MBH, see, e.g., Bromley et al., 2006). If the two binaries have comparable total mass (mass ratio larger than 0.1), we retain the three most massive bodies, again reducing the problem to the triplet case. We stress that this assumption is conservative, mostly because it neglects the possibility of multiple mergers. If the four MBHs form a hierarchical system of two binaries, for example, K-L oscillations might induce mergers of both binaries.

Each of our semi-analytical models thus produces a catalogue of MBH mergers containing the masses of the two merging MBHs and the merger redshift. If the merger involved a standard MBHB, we flag the event either as "star" or "gas", depending on whether the binary evolved in a stellar (i.e., gas-poor) or gaseous (i.e., gas-rich) environment. If the merger was instead triggered by a multiple (triple or quadruple) interaction, we also record $q_{\rm in}$ and $q_{\rm out}$ of the progenitor triplet, and we flag the system as "Tr" if the merger

was promptly triggered during the triple interaction, or as "Tr-ej" if the merger was driven by GW emission after the ejection of one MBH during the triple interaction. In the "Tr" case, we also record whether the progenitor system was originally a triple or a quadruple, to assess the relative importance of the two populations. The catalogues are then used to construct differential distributions of merging binaries, which we use to compute the GW signal, as detailed in the next chapter.

Chapter 5

Predictions for the nHz gravitational wave signal

In the present chapter we analyse the implications that our results of the cosmic evolution of the MBH population have for the stochastic GW background (GWB). Our study is performed employing the catalogues of merging MBHBs obtained with the numerical setup presented in previous chapters, which embeds the results of our large set of simulations of MBH triplets in a cosmological framework. As already pointed out, we consider four different models according to the mass of the initial MBH seeds (*LS* vs *HS*) and to the delay between the merger of the host galaxies and the coalescence of a MBHB (*Model-delayed* vs *Model-stalled*). However, as we will show in the following, we find that low and high mass seeds yield very similar results in the MBH mass range relevant to PTAs (but not at the low masses relevant to LISA, see, Klein et al., 2016, as we are exploring in a still on-going project.). For this reason, unless otherwise stated, we always show results for the *LS* models.

We start by providing a very brief description of the concept of PTA experiments. We then present our detailed analysis of the catalogues of the merging MBHBs, and we evaluate the characteristic strain of the stochastic GWB for each of the considered models. We next discuss the implications for the detectability of GWs by PTA, and we estimate the detection probability as a function of the number of monitored pulsars and of the total observation time. Finally, we analyse the major caveats of our work and we argue about the robustness of our conclusions.

5.1 The concept of pulsar timing array

Since their discovery (Hewish et al., 1968), pulsars have always represented a powerful tool for modern astrophysics. One of the most striking characteristic is the precision of the emitted pulses, which actually makes the pulsars the

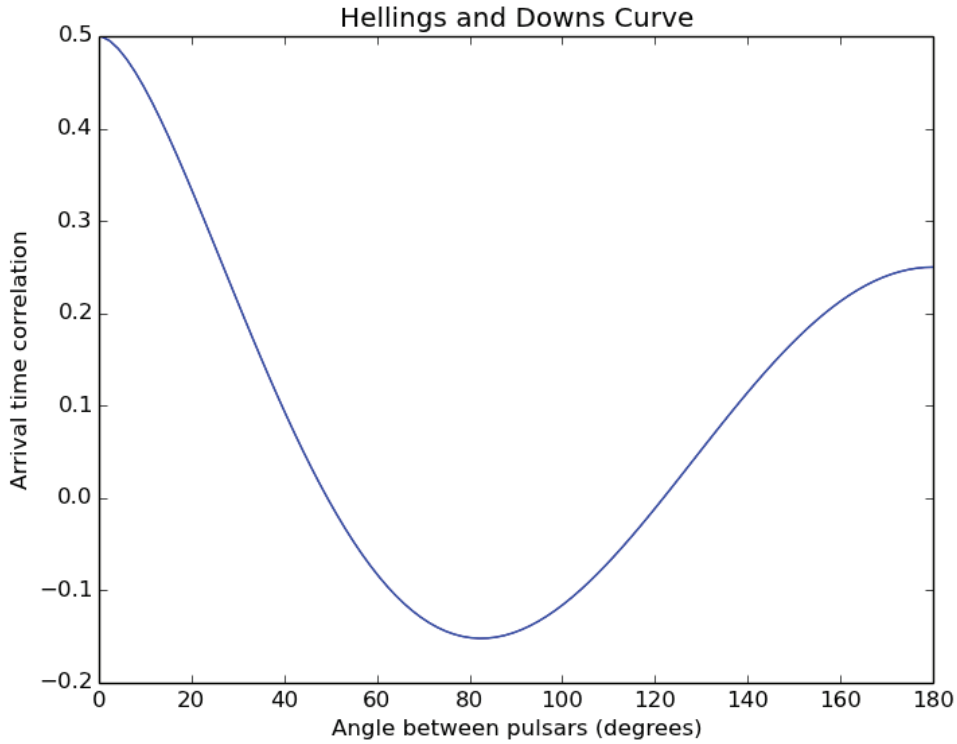

Figure 5.1: The Hellings-and-Downs curve that describe the correlation pattern between each pair of pulsar of the timing residual induced by an isotropic background of GWs.

most stable macroscopic clocks in Nature. This remarkable property can be exploited for a considerable number of interesting tasks, one of which is in fact the detection of GWs. Through the constant monitoring of the time-of-arrival (TOA) of the pulses coming from many pulsars (a technique denoted as pulsar timing, see, Lorimer and Kramer, 2004, for an extensive review), the tiny signature imprinted by the passage of GWs could be discovered.

In brief, the TOAs of the observed pulses are compared with a model that predicts their arrival time. The model contains the details about the proper physics of the pulsars, the effects induced on the emitted radiation by the propagation through the interstellar medium towards us, and the peculiar motion of the Earth. Deviations between the predicted and observed TOAs are denoted as timing residuals, and they represent the smoking gun of the presence of unaccounted phenomena, like, e.g., GWs. The expected residuals induced by GWs are very small, $\lesssim 100$ ns, and therefore are quite challenging to be detected, especially because lots of pulsar are subjected to local instabilities that generate residuals at even the microsecond level. However, there exists a particular subclass of pulsars, the milliseconds pulsars (MSP), which emit pulses that instead present a much greater and remarkable stability, thus allowing for a exquisite TOA precision, in some cases at the order of tens of nanoseconds.

The possibility of detecting GWs using this kind of technique was first pointed out by Sazhin (1978) and Detweiler (1979), who showed that gravita-

tional radiation leaves a peculiar Doppler shift imprint in the timing residuals at time t from the start of the observation given by

$$R(t) = -\int_0^t \frac{\delta\nu}{\nu}\mathrm{d}t, \tag{5.1}$$

where $\delta\nu/\nu$ is

$$\frac{\delta\nu}{\nu} = H^{ij}(h^e_{ij} - h^p_{ij}), \tag{5.2}$$

being h^e_{ij} the GW strain at the Earth, h^p_{ij} that at the pulsar when the radio signal was emitted and H^{ij} a geometrical factor depending on the two GW polarizations and on the relative direction of the pulsar and the GW source.

The detection of GWs is performed by monitoring several pulsars and looking for a coherent correlation pattern in the timing residuals of all of them, i.e., the whole array. For an isotropic GW background, the correlation pattern as a function of the pulsars angular separation was first determined by Hellings and Downs (1983), who showed that the correlation between each pulsar pair is described by (see fig. 5.1)

$$\Gamma_{ij} = \frac{3}{2}\gamma_{ij}\ln(\gamma_{ij}) - \frac{\gamma_{ij}}{4} + \frac{1}{2} + \frac{1}{2}\delta_{ij}, \tag{5.3}$$

where $\gamma_{ij} = (1-\cos\theta_{ij})/2$, θ_{ij} is the relative angular separation between pulsar i and pulsar j, while δ_{ij} is the Kronecker delta.

A convincing detection should follow this predicted correlation pattern.

5.2 Computation of the gravitational-wave signal

We adopt two different techniques for the computation of the GWB in the case of "regular" mergers (i.e., determined by the interaction with stellar or gaseous environments), and mergers induced by triple interactions. For regular MBHBs, we assume circular orbits for simplicity. Therefore, the characteristic strain can be expressed as

$$h_c^2(f) = \frac{4G}{\pi c^2 f^2}\int \mathrm{d}z \int \mathrm{d}m_1 \int \mathrm{d}q\, \frac{\mathrm{d}^3 n}{\mathrm{d}z\,\mathrm{d}m_1\,\mathrm{d}q}\frac{1}{(1+z)}\,\frac{\mathrm{d}E_{\rm gw}}{\mathrm{d}\ln f_r}, \tag{5.4}$$

where $\mathrm{d}^3 n/(\mathrm{d}z\,\mathrm{d}m_1\,\mathrm{d}q)$ is the differential number density of MBHB merger per unit redshift, primary MBH mass and binary mass ratio (to be derived from SAM-generated catalogues), and $\mathrm{d}E_{\rm gw}/\mathrm{d}\ln f_r$ is the differential energy spectrum that can be written as

$$\frac{\mathrm{d}E_{\rm gw}}{\mathrm{d}\ln f_r} = \frac{\mathrm{d}E_{\rm gw}}{\mathrm{d}t_r}\frac{\mathrm{d}t_r}{\mathrm{d}f_r}f_r. \tag{5.5}$$

Note that time and frequency are evaluated in the source rest-frame, so that compared to the time and frequency at the observer, we have $t_r = t/(1+z)$

and $f_r = f(1+z)$. The first term on the right-hand side of eq. 5.5 is the GW luminosity, which is given by

$$\frac{\mathrm{d}E_{\rm gw}}{\mathrm{d}t_r} = \frac{32G^{7/3}}{5c^5}\mathcal{M}^{10/3}(\pi f_r)^{10/3}, \tag{5.6}$$

where $\mathcal{M} = (m_1 m_2)^{3/5}/(m_1+m_2)^{1/5}$ is the binary chirp mass. The term $\mathrm{d}t_r/\mathrm{d}f_r$ represents the time a given binary spends emitting at a specific frequency f_r. The main contributors to the GWB are moderately heavy binaries merging in massive galaxies at relatively low redshift. Since most of those mergers are gas poor (cf. tab. 5.1), we assume that MBHBs evolve exclusively because of three-body interactions against the stellar environment and emission of GW, and we write

$$\frac{\mathrm{d}f_r}{\mathrm{d}t_r} = \frac{\mathrm{d}f_r}{\mathrm{d}t_r}\Big|_{3b} + \frac{\mathrm{d}f_r}{\mathrm{d}t_r}\Big|_{\rm gw} = \mathcal{A}f^{1/3} + \mathcal{B}f^{11/3}, \tag{5.7}$$

where (Chen, Sesana, and Del Pozzo, 2017)

$$\mathcal{A} = \frac{3}{2(2\pi)^{2/3}}\frac{HG\rho_i}{\sigma}M^{1/3}, \tag{5.8}$$

$$\mathcal{B} = \frac{96G^{5/3}}{5c^5}(\pi)^{8/3}\mathcal{M}^{5/3}. \tag{5.9}$$

Here, $M = m_1 + m_2$ is the MBHB total mass, σ is the velocity dispersion of the host galaxy, ρ_i is the stellar density at the binary influence radius (both of which are evaluated from the output of the SAM), and $H \approx 15$ is the hardening rate defined in chapter 2 (see also, Quinlan, 1996; Sesana, Haardt, and Madau, 2006). The binary evolution is dominated by three-body scattering in the early phase, whereas GW emission takes over at higher frequencies. The transition frequency f_t can be computed by equating the two contributions to $\mathrm{d}f/\mathrm{d}t$, and for typical PTA sources lies in the nHz regime.

Triple interactions can result in extremely eccentric binaries, making the analytic computation of the GWB somewhat time consuming (see however, Taylor, Simon, and Sampson, 2017). Moreover, the eccentricity evolution can be highly chaotic, and thus the construction of a simple analytic $\mathrm{d}E/\mathrm{d}f$ is not possible. We note, however, that in the PTA frequency range MBHBs show a rather regular behaviour, following $f - e$ tracks dictated by GW back-reaction and hardly affected by the third body (cf. fig. 3.8). We can therefore consider, to first approximation, a population of eccentric MBHBs evolving solely because of GW emission. Chen, Sesana, and Del Pozzo (2017) showed that the stochastic GWB for an arbitrary population of GW-driven eccentric binaries can be simply obtained by evaluating the single spectrum of a fiducial system, and rescaling it appropriately to match the parameter of the considered sources. The total GWB can be written as:

$$h_c^2(f) = \int \mathrm{d}z \int \mathrm{d}m_1 \int \mathrm{d}q \int \mathrm{d}e \frac{\mathrm{d}^4 n}{\mathrm{d}z\ \mathrm{d}m_1\ \mathrm{d}q\ \mathrm{d}e} h^2_{c,\mathrm{fit}}\left(f\frac{f_{p,0}}{f_p}\right) \left(\frac{f_p}{f_{p,0}}\right)^{-4/3}\left(\frac{\mathcal{M}}{\mathcal{M}_0}\right)^{5/3}\left(\frac{1+z}{1+z_0}\right)^{-1/3}, \tag{5.10}$$

where $\mathrm{d}^4 n/(\mathrm{d}z\ \mathrm{d}m_1\ \mathrm{d}q\ \mathrm{d}e)$ is now the differential number density of MBHB mergers per unit redshift, primary mass, mass ratio and eccentricity. This quantity is constructed from the catalogue produced by the semi-analytical model. Since we do not follow the eccentricity evolution of MBHBs self-consistently, for each event we draw a value of e from the distribution corresponding to the appropriate parent triplet properties, interpolating the distributions obtained at the grid points of our suite of numerical integrations (cf. section 4.2; as mentioned earlier, eccentricity distributions are recorded at a reference binary separation of $100R_{\mathrm{G}}$). $h_{c,\mathrm{fit}}$ is a reference spectrum for a binary with parameters $(\mathcal{M}_0, z_0, f_0, e(f_0))$, which is adapted to arbitrary MBHB parameters via the scaling factors reported in parenthesis. The factor $f_{p,0}/f_p$ is the ratio of the peak frequencies of the two binary spectra. An eccentric binary, in fact, has a peak in the emission spectrum that is uniquely determined by specifying $e(f)$ at a given frequency f (details given in Chen, Sesana, and Del Pozzo, 2017). Therefore, if we know e at $100R_G$, we can compute f_p and rescale the fiducial spectrum accordingly. We also recall that triple interactions can result in either a 'Tr' or 'Tr-ej' merger, as described in the previous section. In general, 'Tr' and 'Tr-ej' events have very different eccentricity probability distributions, and we therefore distinguish between the two cases and sample from the respective distributions.

Although qualitatively different, the two GWB computations of eq. 5.4 and eq. 5.10 are perfectly consistent with each other. We have checked that by artificially setting arbitrarily small e in the triplet population, the GWB obtained via eq. 5.10 coincides with that obtained via eq. 5.4, assuming purely GW-driven circular binaries.

Summarising, to practically evaluate the GWB in the two models, we proceed as follow. We flag the origin of each MBHB as merging because of:

1. Standard dynamical processes (flag 'star').
2. Dynamical processes during a triple interaction (flag 'Tr').
3. GW emission after the ejection of the lighter MBH involved in the triple interaction (flag 'Tr-ej').

For each subset of systems we construct the relevant differential number density $\mathrm{d}^3 n/(\mathrm{d}z\ \mathrm{d}m_1\ \mathrm{d}q)$ for case (1), or $\mathrm{d}^4 n/(\mathrm{d}z\ \mathrm{d}m_1\ \mathrm{d}q\ \mathrm{d}e)$ for cases (2) and (3). In *Model-delayed*, all subsets contribute to the GWB, and we therefore write $h_c^2 = h^2_{c,\mathrm{star}} + h^2_{c,\mathrm{Tr}} + h^2_{c,\mathrm{Tr-ej}}$, where $h^2_{c,\mathrm{star}}$ is computed via eq. 5.4 and $h^2_{c,\mathrm{Tr}}$, $h^2_{c,\mathrm{Tr-ej}}$ are obtained via eq. 5.10. In *Model-stalled*, only triple interactions can drive MBHB coalescences; the GWB is therefore computed as $h_c^2 = h^2_{c,\mathrm{Tr}} + h^2_{c,\mathrm{Tr-ej}}$, where both terms are obtained via eq. 5.10.

LS

$\mathcal{M}$ [$M_\odot$]	*Model-delayed* Rate [yr^{-1}]	binaries star	binaries gas	triplets Tr (quad)	triplets Tr-ej	*Model-stalled* Rate [yr^{-1}]	binaries star	binaries gas	triplets Tr (quad)	triplets Tr-ej
$10^7 - 10^8$	0.118	81.1%	6.0%	10.4%(0.8%)	2.6%	0.028	–	–	88.9%(72.4%)	11.1%
$10^8 - 10^9$	0.022	76.5%	2.6%	16.0%(3.1%)	4.8%	4.4×10^{-3}	–	–	85.0%(65.0%)	15.0%
10^9	1.8×10^{-4}	48.1%	0.7%	40.9%(16.3%)	10.3%	1.9×10^{-4}	–	–	82.1%(62.4%)	17.9%

HS

$\mathcal{M}$ [$M_\odot$]	*Model-delayed* Rate [yr^{-1}]	binaries star	binaries gas	triplets Tr (quad)	triplets Tr-ej	*Model-stalled* Rate [yr^{-1}]	binaries star	binaries gas	triplets Tr (quad)	triplets Tr-ej
$10^7 - 10^8$	0.079	82.2%	6.5%	8.9%(0.9%)	2.4%	0.044	–	–	88.5%(34.0%)	11.5%
$10^8 - 10^9$	0.020	81.7%	2.5%	12.0%(1.5%)	3.8%	5.4×10^{-3}	–	–	85.8%(42.2%)	14.2%
10^9	2.4×10^{-4}	63.1%	0.7%	28.6%(7.1%)	7.6%	1.9×10^{-4}	–	–	84.8%(52.1%)	15.3%

Table 5.1: Merger rate and population composition of the MBHBs with chirp mass in the three most massive mass bins. The number in parenthesis refer to the fraction of prompt mergers originated by a quadruple system.

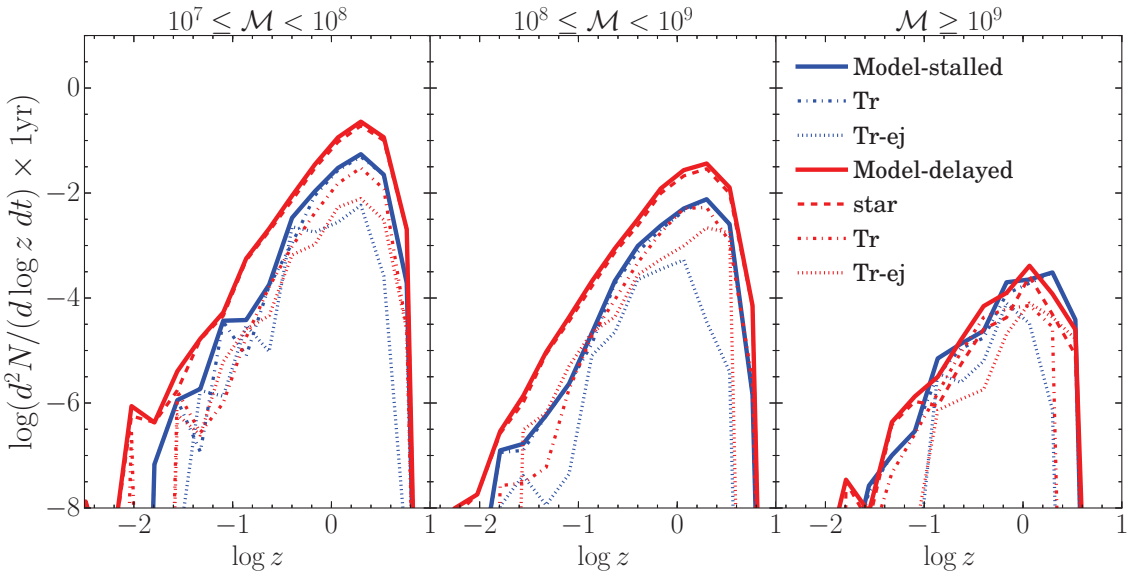

Figure 5.2: Redshift distribution of merging MBHBs in different chirp mass bins, as labelled at the top of the right panel. Line styles are described in the figure.

5.3 Results

5.3.1 MBH merger rates

We first focus on the MBHB merger rates predicted by *Model-delayed* and *Model-stalled*. Being interested primarily in the PTA signal, we concentrate on systems with $\mathcal{M} > 10^7 \mathrm{M}_\odot$. Results are reported for both *HS* and *LS* models in tab.5.1 and plotted for the *LS* model (our default choice) in fig. 5.2. The table lists the total merger rates for selected chirp-mass ranges, and highlights the relative contributions of different MBHB sub-populations, providing a number of useful information:

1. As anticipated, there is little difference between the *HS* and *LS* models; rates are very similar for all mass ranges and so are the fractions of mergers due to individual channels.

2. The only exception is the fraction of mergers due to quadruple interactions, which is larger in the *LS* model. This is due to this model large occupation fraction of MBHs with $M < 10^5 \mathrm{M}_\odot$, which is also responsible for the presence of a significant number of very low mass ratio binaries (Dvorkin and Barausse, 2017), which are absent in the *HS* model. We stress, however, that these low mass ratio systems have little effect on the level of the GWB.

3. In *Model-delayed*, more than 80% of all merging systems with $\mathcal{M} < 10^9 \mathrm{M}_\odot$ are 'regular' binaries, the vast majority of which reside in gas poor environments. This validates our assumption that regular binaries evolve via stellar hardening only.

4. The importance of triple interactions is a monotonically increasing function of mass. For $\mathcal{M} > 10^9 \mathrm{M}_\odot$, about half of the mergers are due to this

channel. This is because very massive galaxies experience several mergers in their lifetime, hence typical MBHB merger timescales are longer than the time occurring between subsequent galaxy mergers. *Model-delayed* is therefore similar to *Model-stalled* at such high masses, but we checked that systems with $\mathcal{M} > 10^9 \mathrm{M}_\odot$ (which are quite rare, see the 'Rate' column in the table) contribute less than 10% to the overall GWB signal.

5. For $\mathcal{M} < 10^9 \mathrm{M}_\odot$, merger rates of *Model-delayed* are about four times higher than those of *Model-stalled*. Triple interactions have therefore limited efficiency (about 30%) in solving the final-parsec problem, since many of them simply end up with the ejection of one of the MBHs (about 70%) without the left-over binary merging. Note that, conversely, rates are comparable for $\mathcal{M} > 10^9 \mathrm{M}_\odot$, for the reasons discussed in the previous point.

6. In general, $\approx 85\%$ of triplet-induced mergers are prompt (Tr), whereas only about 15% are due to GW hardening following the ejection of the lighter of the three MBHs (Tr-ej). This is true for both *Model-delayed* and *Model-stalled*.

The redshift distribution of merging systems is shown in fig. 5.2 for the *LS* model. Counter intuitively, mergers do not appear to be shifted, on average, to lower redshifts in *Model-stalled*. This is likely because typical MBHB merger timescales in *Model-delayed* are of the order of Gyr, especially when systems are stellar driven (which are the vast majority at $\mathcal{M} > 10^7 \mathrm{M}_\odot$), similar to the timescale of subsequent mergers that trigger triple interaction. Within the triple-induced mergers, however, the Tr-ej sub-group (dotted curves in figure) tends to coalesce at lower redshifts than the Tr one (dashed curves in the figure). This is because the former is comprised of left-over systems that merge because of GW emission only, and their coalescence timescale is skewed towards values of several Gyr (cf. fig. 3.6), thus shifting the peak of the merger rate to lower z. The Tr binaries, conversely, typically coalesce in few hundred Myr. The overall shape and normalisation of the rates are in line with estimates from other authors (e.g., Blecha et al., 2016), and the implied total merger rate of MBHBs with $\mathcal{M} > 10^7 \mathrm{M}_\odot$ is about 0.14 yr^{-1} in *Model-delayed* and 0.032 yr^{-1} in *Model-stalled*.

5.3.2 Stochastic GW background

Fig. 5.3 shows the stochastic GWB produced by the two models. The figure is obtained by combining 100 Monte Carlo sampling of the $\mathrm{d}^4 n/(\mathrm{d}z\ \mathrm{d}m_1\ \mathrm{d}q\ \mathrm{d}e)$ distribution. To assess the overall effect of MBHB stalling in the normalisation of the expected GWB, we ignore any effect due to stellar hardening and eccentricity and compute the GWB as a pure $f^{-2/3}$ power law, which is shown by the gold line. Considering the standard parametrisation $h_c = A[f/(1\ \mathrm{yr}^{-1})]^{-2/3}$, we find $A = 1 \times 10^{-15}, 0.7 \times 10^{-15}$ for *Model-delayed* and *Model-stalled* respectively, implying a suppression of 30% only.

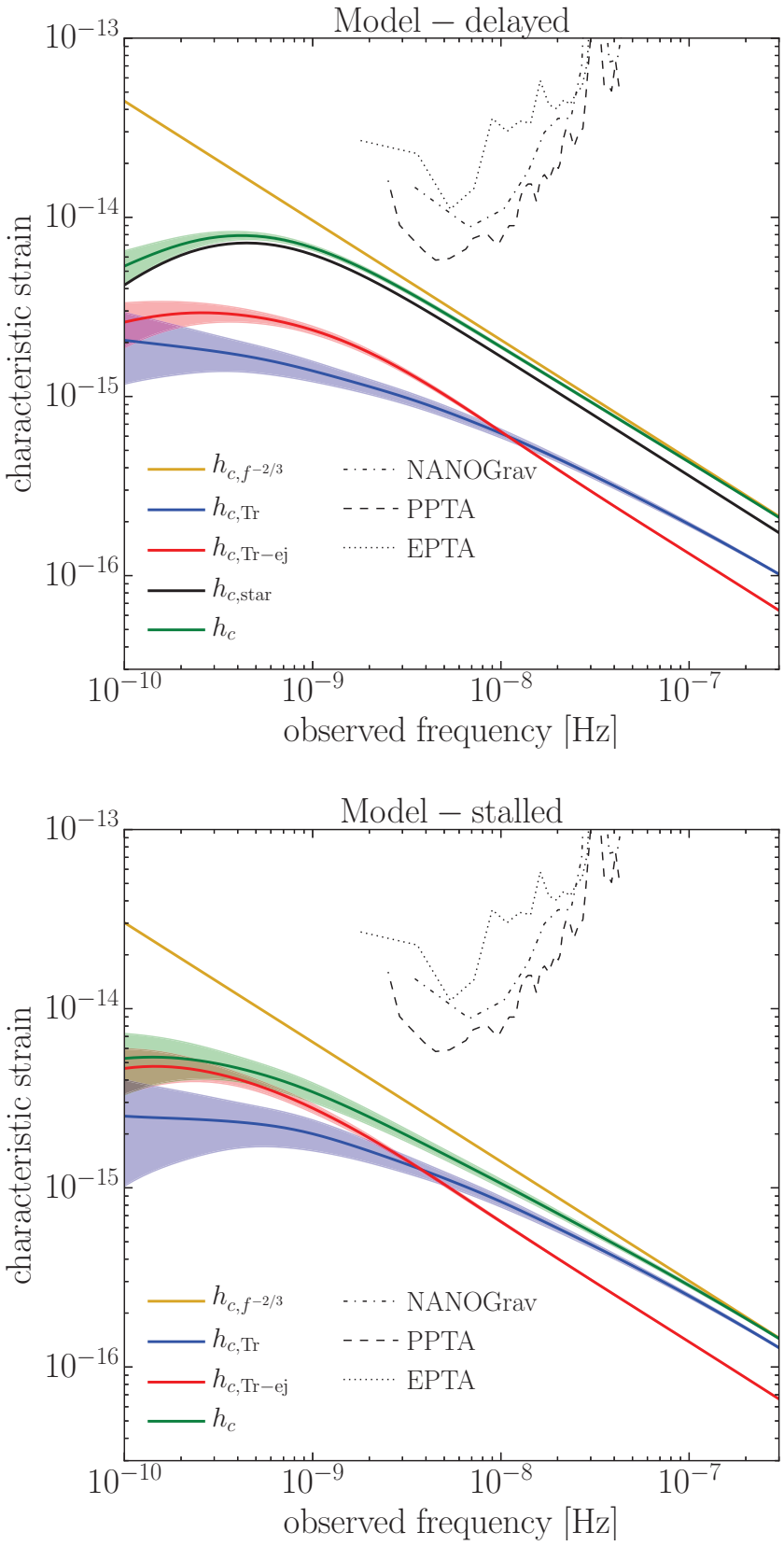

Figure 5.3: Stochastic GWB from MBHBs, divided in each of the contributing components, as indicated in each panel. Solid lines show the mean values of the characteristic strain h_c of each component, whereas the shaded area marks the standard deviation inferred from 100 Monte Carlo simulations of the MBHB population. Current sensitivities of major PTA experiments are also shown. *Top: Model-delayed. Bottom: Model-stalled.*

In *Model-delayed*, the vast majority of the GWB ($h_{c,\mathrm{star}} \approx 0.9 h_c$) is produced by regular binaries evolving via stellar hardening, with triplet-induced mergers (either prompt or following ejection) playing a sub-dominant role. As long as MBHBs are not highly eccentric, the spectral turnover is at $f < 1$ nHz (black and green lines in the lower panel of fig. 5.3), and the signal only mildly departs from the $f^{-2/3}$ power law at frequencies relevant to PTA detection. This is certainly true in our model, which assumes circular binaries, but the shape of the spectrum is hardly affected by eccentricity up to $e \approx 0.5$ (Sesana, 2015; Taylor, Simon, and Sampson, 2017; Chen, Sesana, and Del Pozzo, 2017). We note, however, that the evolution of the eccentricity of stellar driven binaries strongly depends on its initial value at binary formation, which is a poorly understood parameter, with N-body simulations of merging galactic bulges resulting in a wide range of MBHB eccentricities (see Dotti, Sesana, and Decarli, 2012, for a review). Conversely, the signal in *Model-stalled* already departs from the $f^{-2/3}$ power law at $f \approx 3 \times 10^{-8}$ Hz, and at 1 nHz it is already a factor ~ 2 below its nominal $f^{-2/3}$ value. This is due to the non-negligible eccentricity of MBHBs merging via triple interactions. Unlike in the stellar hardening scenario, the presence of binaries with high eccentricities is not just a possibility in this case, but an *inevitable* outcome of the three-body MBH dynamics (cf. chapter 2 and chapter 3). Note the relative contribution of promptly induced coalescences ($h_{c,\mathrm{Tr}}$) and GW-driven coalescences following ejection of one of the triplet members ($h_{c,\mathrm{Tr-ej}}$). The normalisation of the latter contribution is a factor ~ 2 lower, being Tr-ej systems about 20% of the overall triplet-induced coalescences. However, the contributions of the two sub-populations have different spectral shapes, crossing at $f \approx 3 \times 10^{-9}$Hz, below which Tr-ej becomes dominant. This is due to the different eccentricity distribution of the two sub-populations, as we will see in the next subsection.

Figure 5.4 visualises the difference between the simple $f^{-2/3}$ power law, *Model-delayed* and *Model-stalled*. Results are shown for both *LS* and *HS* models, to stress their similarity. The plot clearly shows that *Model-delayed* closely follows the simple power law model at least down to 2×10^{-9}Hz, with a low-frequency drop due to stellar driven evolution. The ratio between *Model-stalled* and the single power-law model, as already mentioned, is about 0.7 at high frequencies, monotonically decreasing to about 0.1 at ~ 0.1 nHz. Compared to *Model-delayed*, *Model-stalled* produces a GWB that is a fraction 2-to-3 smaller in the frequency range 1-10 nHz, most relevant to PTA experiments. The result holds for both *LS* and *HS* models, with minimal differences.

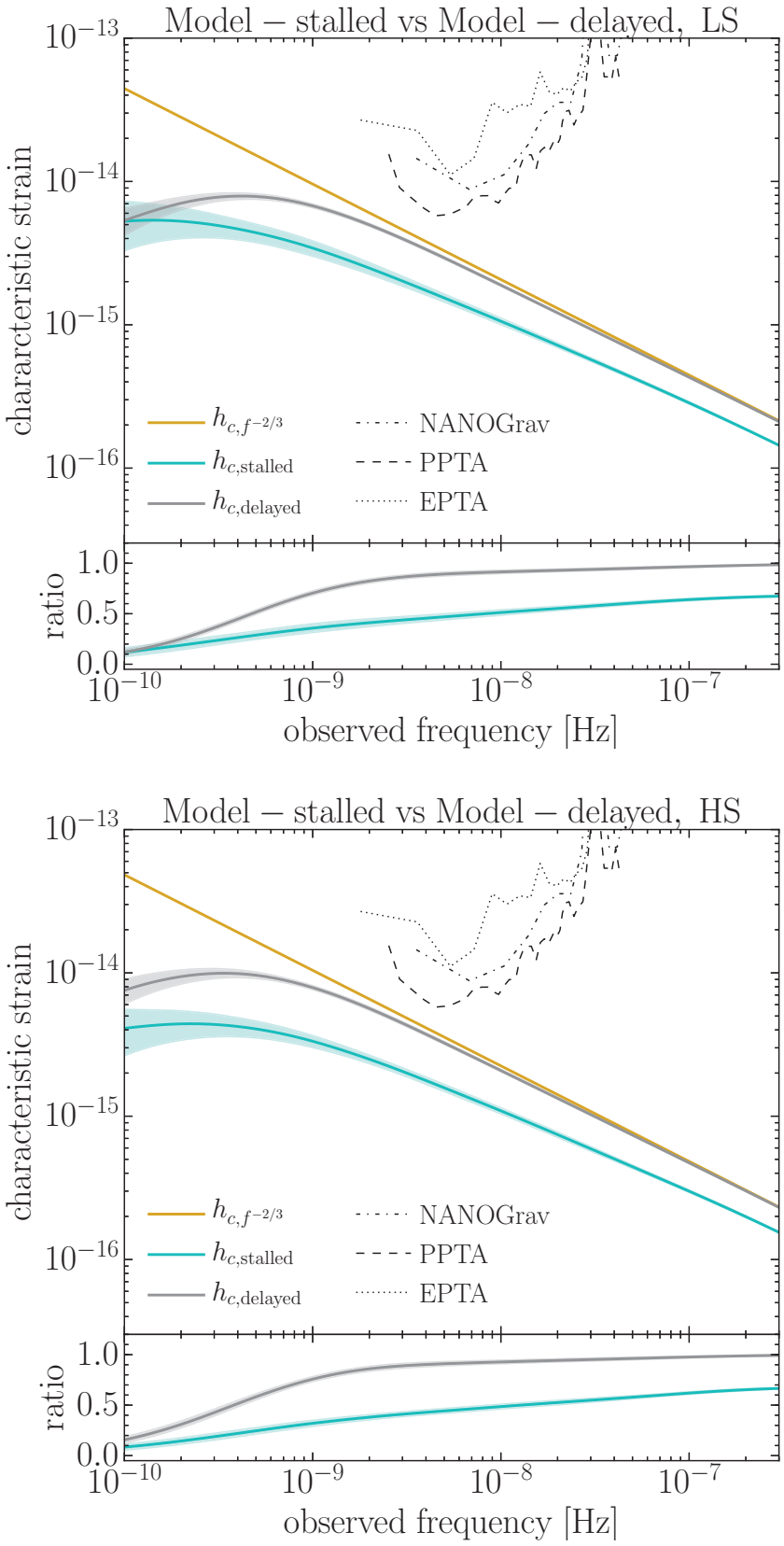

Figure 5.4: Comparison of the stochastic GWB generated by *Model-delayed* (grey) and *Model-stalled* (light-blue). Lines and shaded areas have the same meaning as in fig. 5.3. The bottom inset shows the ratio between either models and a reference $f^{-2/3}$ power law generated by a GW-driven population of circular binaries, shown as an orange line in the main plots. Here, we present results for both *LS* (top) and *HS* (bottom) seed models.

Eccentricity distribution

As mentioned above, the occurrence of high eccentricities is a critical and inevitable feature of triple-induced inspirals. This might be relevant for the detection of individually resolvable binaries, for which eccentric templates might be necessary (Taylor et al., 2016b). To investigate the actual distribution of individual MBHB eccentricities, we need to convert the merger number densities in eq. 5.10 into the instantaneous number of systems in the sky at a given frequency, i.e.,

$$\frac{\mathrm{d}^5 N}{\mathrm{d}z\ \mathrm{d}m_1\ \mathrm{d}q\ \mathrm{d}e\ \mathrm{d}\ln f} = \frac{\mathrm{d}^4 n}{\mathrm{d}z\ \mathrm{d}m_1\ \mathrm{d}q\ \mathrm{d}e'} \frac{\mathrm{d}V_c}{\mathrm{d}z} \frac{\mathrm{d}z}{\mathrm{d}t} \frac{\mathrm{d}t}{\mathrm{d}\ln f}, \tag{5.11}$$

where e' is the eccentricity computed at $100R_G$, V_c is the comoving volume, $\mathrm{d}V_c/\mathrm{d}z$, $\mathrm{d}z/\mathrm{d}t$ are known once a cosmology is assumed (Hogg, 1999), and

$$\frac{\mathrm{d}t}{\mathrm{d}\ln f} = \frac{5}{96}(2\pi)^{-8/3}\mathcal{M}^{-5/3}f^{-11/3}F(e)^{-1} \tag{5.12}$$

$$F(e) = \frac{1 + (73/24)e^2 + (37/96)e^4}{(1-e^2)^{7/2}}. \tag{5.13}$$

The eccentricity e at the desired frequency f is obtained by evolving e' backwards from $100R_G$ to f by using the standard evolution of eccentric binaries in the quadrupole approximation (Peters and Mathews, 1963; Chen, Sesana, and Del Pozzo, 2017). Note that $F(e)$ is a strong increasing function of e, thus $\mathrm{d}t/\mathrm{d}\ln f$ is much shorter for very eccentric binaries, down-weighing their relative number at a given observed frequency.

The distribution of the number of emitting binaries of *Model-stalled*, integrated in redshift, in the circularity[1]-mass plane is shown in fig. 5.5 and fig. 5.6 at two observed *orbital* reference frequencies, $f = 1$ nHz and $f = 10$ nHz respectively. The number of sources is obviously dominated by low mass MBHBs, with a long tail of few sources extending up to $\mathcal{M} = 10^{10}\mathrm{M}_\odot$. The overall distribution is dominated by light, rather circular binaries, but possible eccentricities extend up to $e > 0.99$.

Marginalised source distributions are shown in the lower panel as a function of chirp mass, circularity and redshift. As expected, the number of sources is dominated by low-mass systems (which, however, do not contribute much to the total GWB) and the redshift distribution peaks around $z \sim 1$, consistent with, e.g, Sesana, Vecchio, and Volonteri (2009) and Blecha et al. (2016). As already noticed, the Tr and Tr-ej sub-populations behave quite differently, the latter peaking at lower redshifts (because of the long coalescence timescales). Moreover, the circularity distributions are also distinct: the Tr population extends to $1 - e \approx 0.003(0.03)$ at $f = 1(10)$ nHz, whereas the the Tr-ej populations hardly goes below $1 - e \approx 0.1$, preferentially selecting rather circular binaries. This can be understood by looking at fig. 3.9 of chapter 3. Prompt coalescences (i.e.,

[1]The circularity is defined as 1-e. Its logarithm is often used for plotting purposes, to highlight tails of high eccentricities.

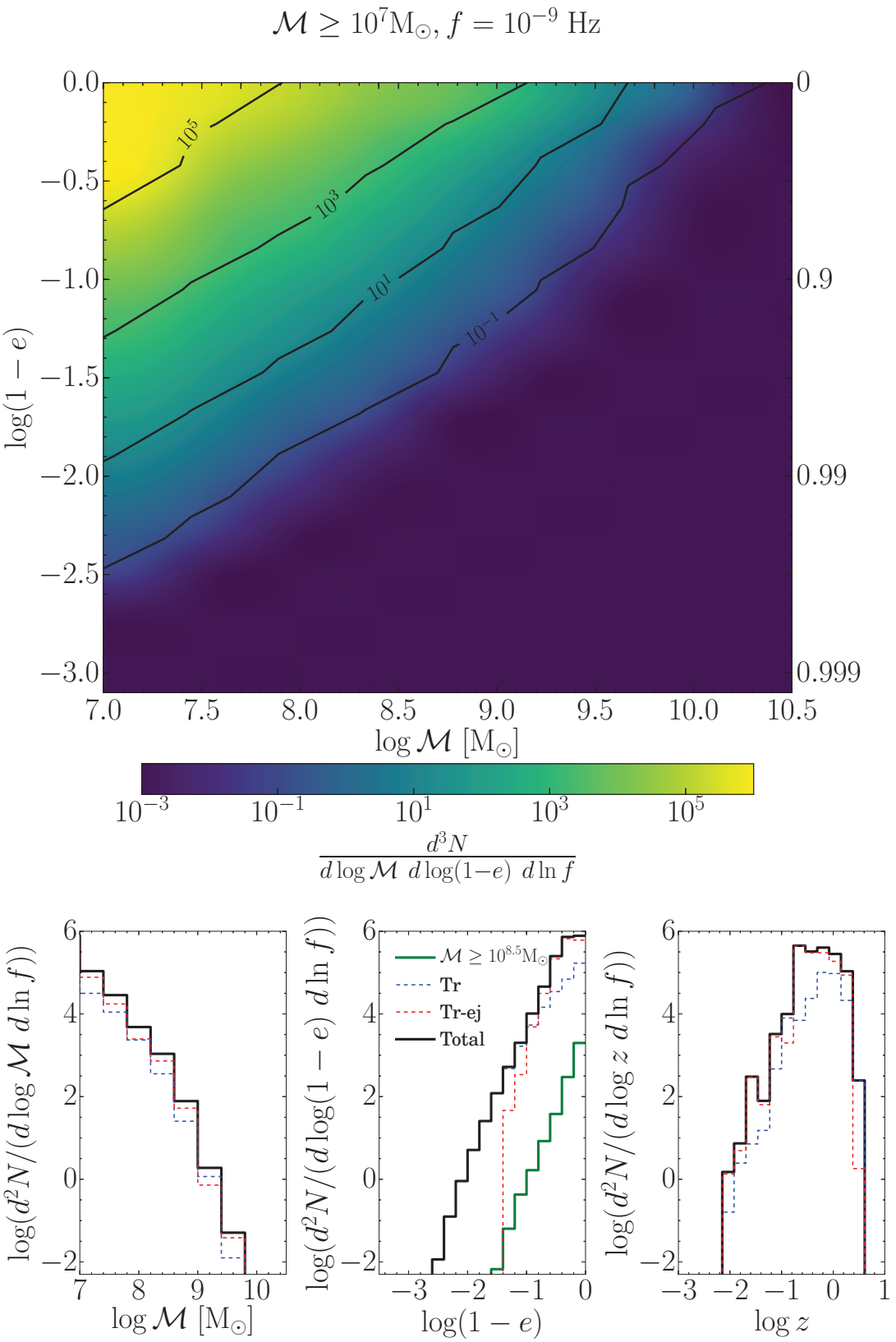

Figure 5.5: Properties of individual MBHBs of *Model-stalled* contributing to the GW signal within an observed orbital frequency $\Delta f = f$ around $f = 1$ nHz. The upper panel shows the differential distribution of sources in the chirp mass – circularity plane (with the eccentricity e shown on the right of each figure). The lower panels show the marginalised distributions of the number of sources as a function of chirp mass (left), circularity (centre) and redshift (right). The legend of the histogram linestyles is shown in the central panels.

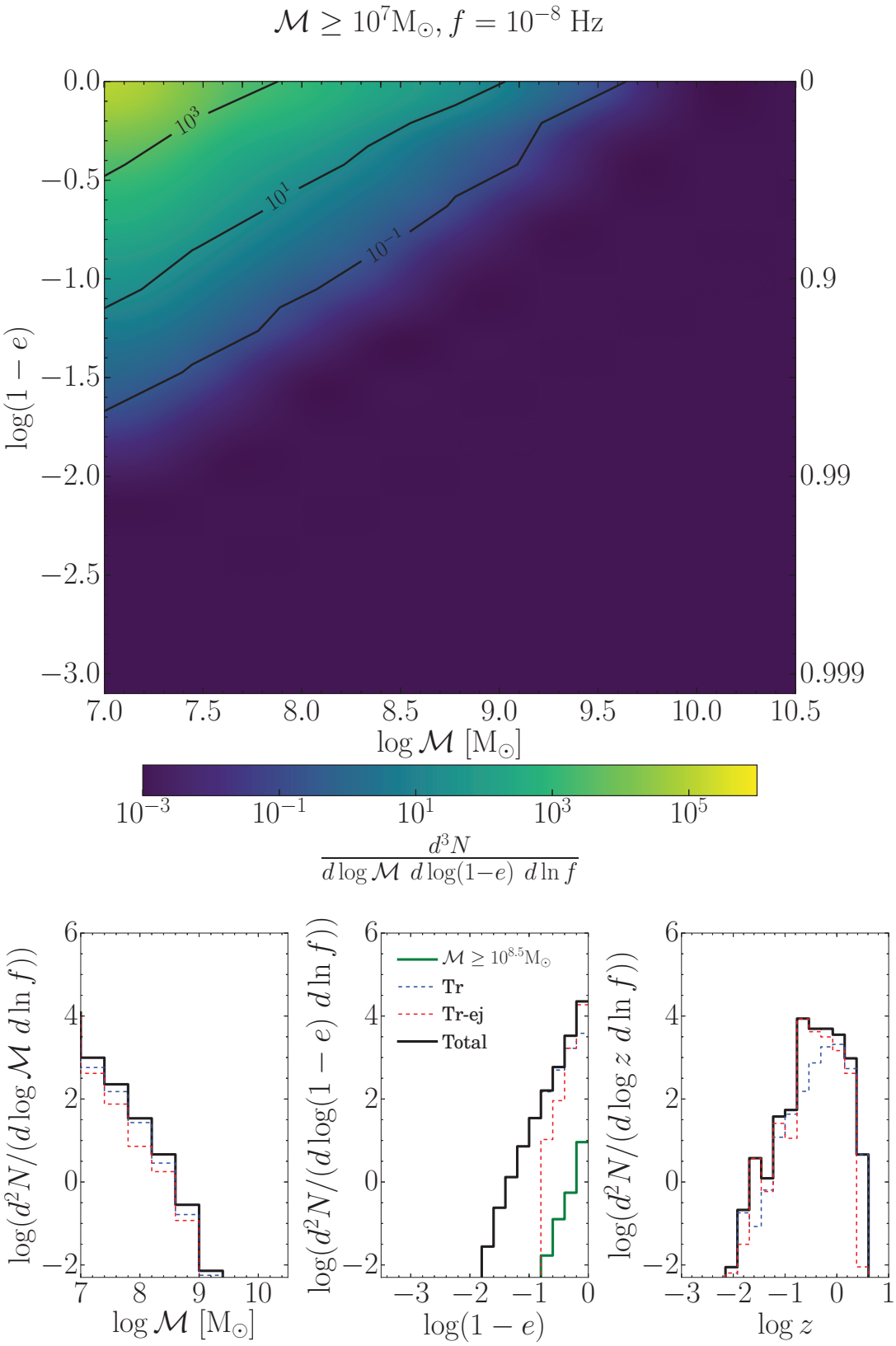

Figure 5.6: Same as fig. 5.5 except that an observed orbital frequency of 10 nHz is chosen.

the Tr population) are generally caused by the formation of either a temporarily highly eccentric binary (mostly as a result of secular Kozai-Lidov oscillations), or a compact system of moderate eccentricity (in the case of chaotic energy and angular momentum exchanges). The resulting eccentricity distribution is therefore extremely broad, spanning several orders of magnitude at the innermost circular stable orbit (cf. fig. 3.9). Conversely, coalescences driven by GW emission after an ejection (i.e., the Tr-ej population) preferentially select the systems that did not reach sufficiently high eccentricities to promptly coalesce, but which are still sufficiently eccentric that their coalescence time is shorter than the Hubble time. The result is a much narrower (and mass dependent) allowed eccentricity range, which does not reach the high values of the Tr population. The green curves in the lower central panels of both fig. 5.5 and fig. 5.6 select binaries with $\mathcal{M} > 10^{8.5}\mathrm{M}_{\odot}$, which are the loudest GW sources and which are thus more likely to be individually resolved. Although the distribution favours circular binaries, $\mathcal{O}(10)$ systems have eccentricities higher than 0.7 at $f \approx 1$ nHz. Eccentric resolvable sources are therefore a rather common occurrence if merging MBHBs are mostly driven by triple interactions. These kind of sources could produce bursts of GWs that may enter the PTA band. Although in this thesis we mainly focus on the GWB, we plan to investigate this point in a future work.

5.3.3 A realistic lower bound to the GWB: implications for PTA detectability

Our results imply that triple interactions efficiently counteract the effect of stalling and drive a significant fraction of MBHBs to coalescence, the resulting GWB being reduced by a factor of 2-to-3 only in the PTA band. We can now use this fact to derive a robust lower limit to the amplitude distribution of the expected GWB, based on our best astrophysical knowledge of MBH assembly and dynamics following galaxy mergers.

Our scope is not to make realistic predictions of time to detection (see, e.g., Siemens et al., 2013; Taylor et al., 2016a), but to assess the impact of the most pessimistic scenario on GWB detectability by PTAs. As such, we consider a simple model based on the following assumptions:

1. We take a GWB amplitude distribution predicted by a MBHB population model based on the MBH-galaxy scaling relations proposed by Shankar et al. (2016), which are based on a putative observational selection bias on the resolvability of the MBH influence sphere. This choice is solely based on the fact that those relations provide a very conservative estimate of the stochastic GWB. In fact, Sesana et al. (2016) showed that they result in a 95% confidence GWB amplitude distribution in the range $1.4 \times 10^{-16} < A < 1.1 \times 10^{-15}$, with a median value of $A = 4 \times 10^{-16}$, well below current PTA limits. Also, consistently with this choice, the semi-analytical galaxy formation model utilised in this thesis reproduces the scaling relations of Shankar et al. (2016) (cf. Barausse et al., 2017).

2. We draw A from this distribution and apply a correction factor $C(f)_{\rm delayed} = h_{c,{\rm delayed}}(f)/h_{c,f^{2/3}}(f)$ and $C(f)_{\rm stalled} = h_{c,{\rm stalled}}(f)/h_{c,f^{2/3}}(f)$, shown in the lower panels of fig. 5.4. In both cases, the GWB then takes the form $h_{c,X} = C(f)_X \times A(f/1\ {\rm yr}^{-1})^{-2/3}$.

3. We consider an idealised SKA-type PTA. Following Janssen et al. (2015), we make the conservative assumption that SKA will be able to monitor up to 50 MSPs with rms precision of 100 ns. We then explore the detection probability (DP, also indicated as γ in the following) as a function of observing time T and number of pulsars N_p in the array.

In particular, assumptions (1) and (2) provide a realistic projection of how low the GWB can get, by combining the existence of moderately light MBHBs to stalling.

PTA detectability under assumption (3) is computed using the framework developed by Rosado, Sesana, and Gair (2015). The authors define the detection statistics S as the cross-correlation between the data collected by two detectors, i.e., in practice the cross-correlation of the TOAs coming from a pair of pulsars.

If no GWB signal is present in the cross-correlated data, then the outputs of the detectors just reflects the properties of noise, which is assumed to be a stochastic process whose probability density function is a Gaussian distribution with zero mean and standard deviation σ_0, i.e.,

$$p_0(S) = \frac{1}{\sqrt{2\pi\sigma_0^2}}\, {\rm e}^{-\dfrac{S^2}{2\sigma_0^2}}. \tag{5.14}$$

If a GWB is instead present, the detection statistic is assumed to be again described by a Gaussian distribution, but with mean μ_1 different from zero and standard deviation $\sigma_1 \neq \sigma_0$,

$$p_1(S) = \frac{1}{\sqrt{2\pi\sigma_1^2}}\, {\rm e}^{-\dfrac{(S-\mu_1)^2}{2\sigma_1^2}}. \tag{5.15}$$

A detection of the GWB may be claimed when a measured value of S is such that $S \geq S_T$, where S_T is a detection threshold determined by the experimental setup. Integrating the noise distribution over all $S \geq S_T$ gives the false alarm probability (FAP), whereas that of $p_1(S)$ over the same range gives instead the DP. More explicitly, the integral

$$\alpha = \int_{S_T}^{\infty} p_0(S){\rm d}S \tag{5.16}$$

defines the probability of a spurious detection in the absence of a GWB, while

$$\gamma = \int_{S_T}^{\infty} p_1(S){\rm d}S \tag{5.17}$$

represents the probability of a true detection of the GWB. When the above integrals are recast in terms of the complementary error function (erfc) eq. 5.16 and eq. 5.17 read

$$\alpha = \frac{1}{2}\mathrm{erfc}\left(\frac{S_T}{\sqrt{2}\sigma_0}\right), \tag{5.18}$$

$$\gamma = \frac{1}{2}\mathrm{erfc}\left(\frac{S_T - \mu_1}{\sqrt{2}\sigma_1}\right). \tag{5.19}$$

Finally, once the value of the FAP is fixed ($\alpha_0 = 0.001$ in our case) and solving eq. 5.18 for S_T, the DP can be rewritten as

$$\gamma = \frac{1}{2}\mathrm{erfc}\left(\frac{\sqrt{2}\sigma_0 \mathrm{erfc}^{-1}(2\alpha_0) - \mu_1}{\sqrt{2}\sigma_1}\right). \tag{5.20}$$

Under the simplifying assumptions of an array of equal pulsars, randomly distributed in the sky and monitored for the same timespan T, the quantities μ_1, σ_0 and σ_1 take the form

$$\mu_1 = N_p(N_p-1)T\int \mathrm{d}f \frac{\Gamma^2 S_h^2}{(P+S_h)^2 + \Gamma^2 S_h^2}, \tag{5.21}$$

$$\sigma_0^2 = N_p(N_p-1)T\int \mathrm{d}f \frac{\Gamma^2 S_h^2 P^2}{\left[(P+S_h)^2 + \Gamma^2 S_h^2\right]^2}, \tag{5.22}$$

$$\sigma_1^2 = N_p(N_p-1)T\int \mathrm{d}f \frac{\Gamma^2 S_h^2 \left[(P+S_h)^2 + \Gamma^2 S_h^2\right]}{\left[(P+S_h)^2 + \Gamma^2 S_h^2\right]^2}, \tag{5.23}$$

where P represents the power spectral density (PSD) of the noise, while S_h is the PSD of the signal for which we have made the further assumption that the signal spectrum S_h is known and matched to a template $S_{h0} = S_h$. Moreover, we have replaced the pulsar-pair dependent correlation function Γ_{ij} (the Hellings & Downs function, Hellings and Downs, 1983) with the square root of its variance, i.e., $\Gamma = 1/(4\sqrt{3})$. The signal PSD S_h is related to the characteristic strain derived in section 5.2 via

$$S_h = \frac{h_c^2}{12\pi^2 f^3}, \tag{5.24}$$

whereas, for the PSD of the noise P, assumed to be the same for all pulsars, we use the form

$$P = 2\sigma^2 \Delta t + \frac{\delta}{f^5}, \tag{5.25}$$

where $\sigma = 100$ ns is the rms residual of the measured TOAs, Δt is the assumed cadence of individual MSPs observations, and

$$\delta = 5 \times 10^{-49} \left(\frac{10\ \mathrm{yr}}{T}\right)^5 \left(\frac{\sigma}{100\mathrm{ns}}\right)^2 \frac{\Delta t}{2\,\mathrm{weeks}}. \tag{5.26}$$

With this prescription, the second term on the right-hand side of eq. 5.25 mimics the loss of sensitivity seen in current PTAs at low frequency and due to fitting of the MSP spin and spin derivative in the timing model. Note that we do not include any red-noise contribution to the noise PSD, which can be easily accounted for by adding a suitable term $P_{\rm rn}(f)$ in eq. 5.25. For each value of A drawn from the GWB-amplitude distribution reported in Sesana et al. (2016), we compute the expected $h_c(f)$ for *Model-delayed* and *Model-stalled* as explained in point (2) above, and for each value of N_p and T we compute the DP using eq. 5.20.

Results are shown in fig. 5.7 and fig. 5.8. Fig. 5.7 shows the distribution of the expected amplitudes as a function of frequency. In *Model-stalled*, the signal is generally flatter than the canonical $f^{-2/3}$ power law in the relevant PTA frequency range, thus it is not sufficient to simply report GWB amplitudes A when quoting results. This is also true in *Model-delayed*, even though the departure from $f^{-2/3}$ is minimal at $f > 1$nHz. The *Model-stalled* amplitude range still spans more than an order of magnitude and is shifted down by about a factor of two at the currently most relevant PTA frequencies (marked by the stars) compared to the fiducial model. The whole predicted range (99.7% confidence region) is below the current best PTA limit (Shannon et al., 2015), but well within the reach of a putative SKA array under our conservative assumptions.

This is better quantified in fig. 5.8, that shows the DP in the observation time (T) – number of pulsars (N_p) plane. For a given N_p, the 50% DP timescale is delayed by only 3-to-6 years in the *Model-stalled* scenario. The plot highlights the importance of having a sufficiently large N_p, i.e., a larger array helps to narrow this time gap. In fact, detection is based on correlation statistics, which is very sensitive to the number of pulsar pairs that can be correlated. We see that if $N_p = 5$, even at $T = 20$ yr we still have only DP ≈ 0.3. A larger array of $N_p = 50$, instead, reaches the same DP value after only 10 yr and by $T = 20$ yr has DP > 0.95. Overall, these findings support the statement that PTAs *will* eventually detect the stochastic GWB from MBHBs, regardless of possible binary stalling issues.

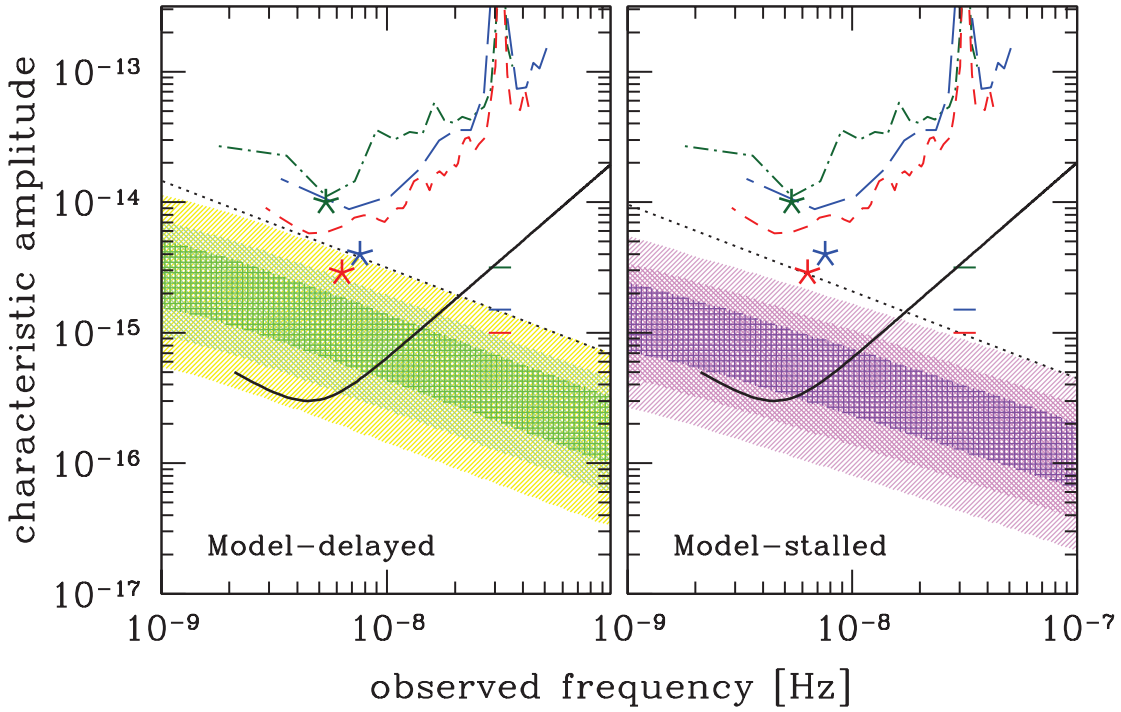

Figure 5.7: h_c vs f for *Model-delayed* (left panel) and *Model-stalled* (right panel) assuming the conservative MBH population model from Shankar et al. (2016). In each panel, the shaded areas represent the 68%, 95% and 99.7% confidence intervals of the signal amplitude. The jagged curves are current PTA sensitivities: EPTA (dot-dashed green), NANOGrav (long-dashed blue), and PPTA (short-dashed red). For each sensitivity curve, stars represent the integrated upper limits to an $f^{-2/3}$ background, i.e., a GWB with the particular normalisation A_0 such that its signal-to-noise ratio (SNR, i.e., the integral of the characteristic strain squared weighted by the sensitivity curve) allows claiming a detection at the 95% level with the current experimental status. Stars are placed at the frequency that contribute most to the SNR, while the horizontal ticks are their extrapolation at $f = 1$ yr^{-1}. The solid black line represent the typical sensitivity level of a conservative SKA-type array formed by 50 pulsars monitored at 100 ns precision for 15 years. A dotted black line with slope $f^{-2/3}$ is also added to guide the eye.

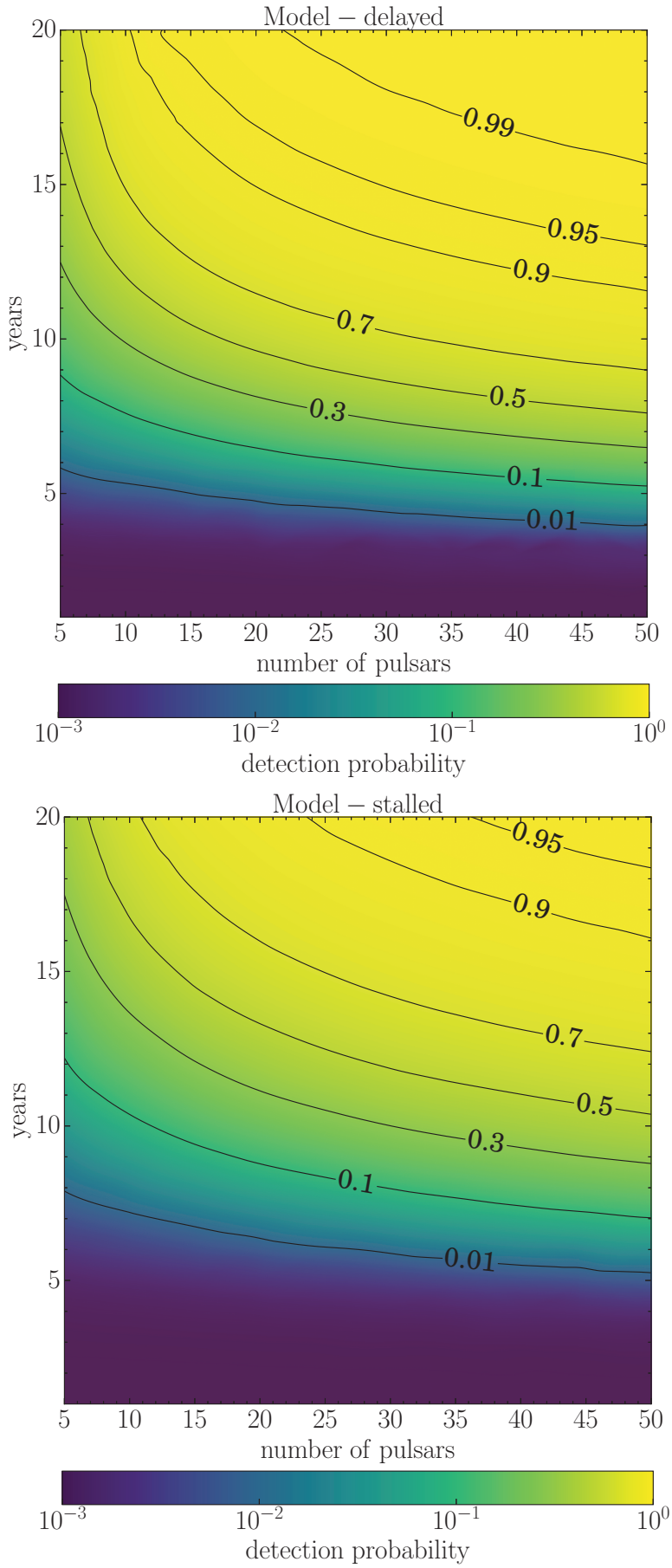

Figure 5.8: Detection probability contour plot in the number of pulsar vs observation time plane. All pulsars are assumed to have an equal rms residual of 100 ns. *Top: Model-delayed. Bottom: Model-stalled.*

5.4 Caveats

Although employing an accurate treatment of the three-body dynamics including an external potential, dynamical friction, stellar hardening and PN equations of motion consistently derived from the three-body PN Hamiltonian (chapter 1), the results presented here are subject to a number of caveats that we discuss in the following.

First, we did not attempt to model the interaction of quadruple MBH systems. This is an important point, especially in *Model-stalled* where, necessarily, most galaxy mergers contain pairs of MBHBs instead of pairs of single MBHs. In fact, in this case mergers are dominated by quadruple systems (cf. tab. 5.1). As already mentioned, by removing one body and thus recovering a triplet, our estimation of the quadruple contribution to the GWB is conservative. We also stress that even if for some (unexpected) reasons quadruple interactions were to lead to no mergers, the total GWB would be further suppressed by a factor of two only, and we therefore conclude that our results are robust against this instance.

Second, in the simulations presented in chapter 3 we did not account for the later evolution of the MBHs that are ejected in triple systems. As shown by Hoffman and Loeb (2007), those MBHs may fall back to the galactic nucleus on timescales shorter than the Hubble time, thus giving rise to an additional MBH merger in about $10 - 20\%$ of cases. For this reason, however, this effect is sub-dominant relative to the main one (the prompt and GW-driven triplet-induced mergers that we account for in this thesis), and is likely to depend on the exact modelling of the galactic potential (and namely its triaxiality, which is unknown). Moreover, as already mentioned, since we neglect this effect our results should be regarded as conservative.

Third, as stressed in chapter 4, our semi-analytical galaxy formation model only includes the dynamical friction timescale of galaxy satellites in the potential well of the primary galaxy until the two merge, but does not model the early migration of MBHs driven by dynamical friction against the gaseous and stellar distribution, in the early epochs following the merger. We do this on the grounds that this timescale is generally short relative to that of the dynamical friction between the two halos and galaxies, and relative to the timescales that describe the evolution of MBHBs at separations $\lesssim$ a few pc (stellar hardening, gas-driven migration, triple MBH interactions), at least for the comparable-mass MBHBs that provide the bulk of the PTA signal (Dvorkin and Barausse, 2017; Dosopoulou and Antonini, 2017). For this reason, the results of this chapter are robust against this assumption, which anyway affects only the *Model-delayed* results and not directly the *Model-stalled* ones (where the MBH merger timescales are set to values larger than the Hubble time). Nevertheless, N-body simulations of galaxy pairs find that merging within an Hubble time might be difficult for MBH systems with mass ratios $\lesssim 0.1$. Therefore this issue, while formally absent in *Model-stalled*, may have consequences also for that scenario, because the simulations of chapter 3 *assume* (as initial conditions) that MBHs are efficiently brought down to separations comparable to the primary MBH sphere of influence. However, we have checked that low mass ratio

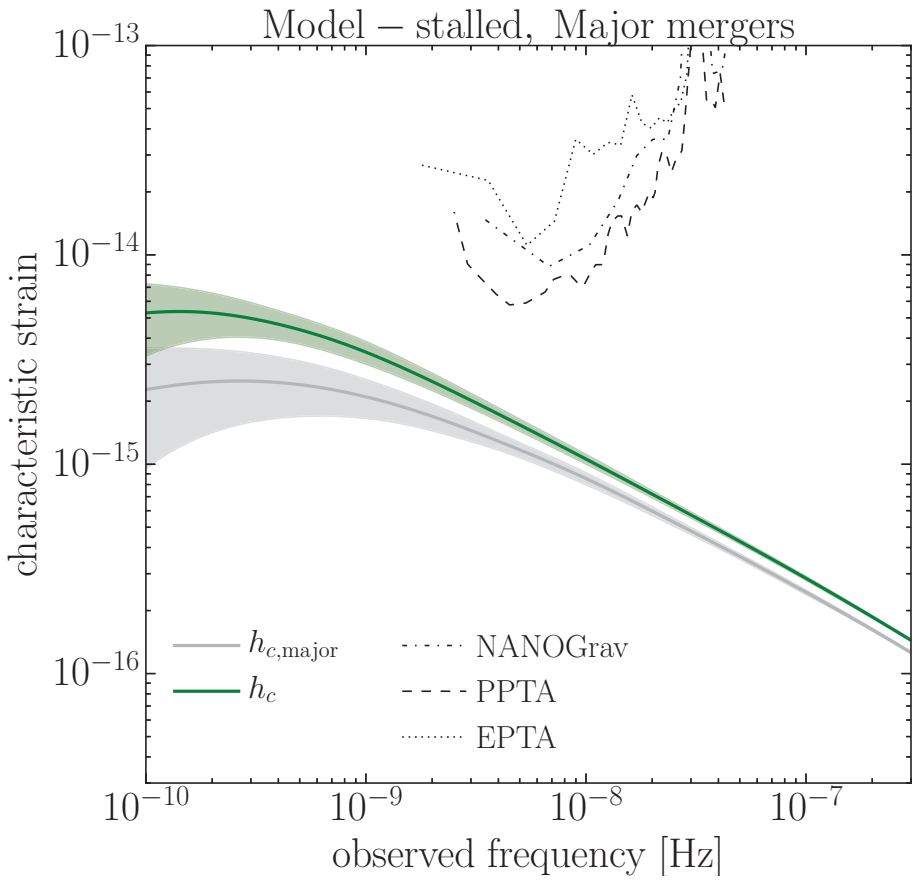

Figure 5.9: GWB spectrum h_c of *Model-stalled* when considering only major mergers, i.e., when $q_{\mathrm{in}} \geq 0.1$ and $q_{\mathrm{out}} \geq 0.1$ (grey line and area) compared to the total GWB predicted by the model (green line and area). Lines and shaded areas have the same meaning as in fig. 5.3.

systems do not contribute significantly to our results, even in *Model-stalled*, by removing all triplets with either q_{in} or q_{out} lower than 0.1 from the GWB calculation. Results are shown in fig. 5.9. It is clear that low q systems do not significantly contribute to the GWB normalisation, being the signal at high frequencies only about 10% lower after their removal. It appears, however, that high q triplets tend to produce more eccentric binaries, causing a higher frequency flattening and spectral turnover when low q systems are not included in the calculation. The difference in GWB amplitude is however still less than 50% at frequencies of few nHz, relevant to PTA experiments.

Last, when applying our results to the Sesana et al. (2016) GWB signal distribution, we are implicitly assuming that the signal correction factor $C(f)$ due to stalling directly applies to MBHB populations that are different from those produced by our semi-analytical model. Indeed, even though the two models both assume observational selection effects on the scaling relations, the intrinsic MBH-galaxy scaling relations of the populations are not necessarily exactly the same (Barausse et al., 2017). Although changing ingredients such the employed scaling relation should not change the occurrence of mergers due to

triple interactions (our triplet-induced merger fractions are fairly independent on the mass scale of the problem, see chapter 3), things can be different for MBH evolution models relying on radically different merger histories. For example, if galaxy merger rates (which are relatively poorly constrained by observations) are significantly lower, then the occurrence of subsequent mergers is much rarer, implying a lower triplet formation rate. This, in turn, will cause a larger suppression of the GWB. We note, however, that in *Model-stalled* the majority of mergers actually involve quadruple systems. This means that mergers are frequent enough that, in *Model-stalled*, the vast majority of galaxies hosts a MBHB *at any time* along cosmic history.[2] Although we cannot check this within our current framework, we conjecture that the cosmic galaxy merger rate must be much lower than predicted by our semi-analytical model to significantly diminish the occurrence of triple interactions in *Model-stalled* compared to 'standard' MBHB mergers in *Model-delayed*. In support to our conjecture, we note that by employing a completely different framework and MBH evolution model, Ryu et al. (2017) find a very similar suppression in the GWB normalisation of about 30%.

Although these are substantial caveats, we argue that they are unlikely to strongly influence the results obtained here and our conclusions are thus robust.

5.5 Summary

We have explored for the first time the effect of MBH triple interactions on the GW signal produced by a cosmic population of MBHs. To this purpose, we have coupled a large library of numerical simulations of triple interactions (chapter 3) to a state-of-the-art semi-analytical model for galaxy- and MBH-evolution (Barausse, 2012).

The numerical simulations solve the three-body equations of motion consistently derived from the three-body PN Hamiltonian (chapter 1) through 2.5PN order, and include the effects of the galactic potential and an analytic treatment of dynamical friction and stellar hardening. The library of outcomes is then implemented within the SAM, which keeps track of the evolution of individual MBHs and the formation of MBH binaries, triplets and quadruplets following galaxy mergers along the cosmic history of structure formation. This comprehensive framework has allowed us to assess the effect of triple (and quadruple) interactions on the MBHB cosmic merger rate, and to asses the expected GWB in the PTA band.

[2]Observational constraints that could confirm or rule out this particular scenario are limited. Indeed, since binaries are stalled, the environment cannot be gas rich and therefore the search of peculiar electromagnetic signatures (e.g., periodicities in the AGN luminosity) may not represent a feasible route. Though, even at very low accretion rates, the jet-launching mechanism can still be effective, thus possible precession features of relativistic jets could still be used to hint at the presence of a MBHB. Finally, although limited to nearby galaxies, another constraint could be the search for kinematic signatures imprinted in the innermost stellar distribution, where the presence of a MBHB can significantly alter the local dynamics (see, e.g., Meiron and Laor, 2010). For an extensive discussion see also section 5.1 of Dosopoulou and Antonini (2017).

We have considered two models for the dynamics of MBHBs. In our fiducial model (labelled *Model-delayed*) MBHBs merge on timescales of millions-to-billions years, consistently estimated from the properties of the host galaxy. In the PTA band, most mergers occur in gas-poor galaxies and typical merger timescales due to stellar-driven hardening (assuming efficient loss cone replenishment) are of the order of Gyr. Though the formation of several triple MBH systems due to subsequent galaxy mergers is common, the formation of "standard" MBHBs is still the dominant coalescence channel.

We have then considered a rather extreme model in which all standard dynamical processes are inefficient at driving MBHBs to sub-pc scales, and as a consequence MBHBs stall close to their hardening radius (*Model-stalled*). The rationale behind this model was to investigate the outcome of the most pessimistic scenario from the GW generation standpoint. Naively, if all MBHBs stall, no GW signal is expected in the PTA band. However, mergers can still be triggered by triple (and quadruple) MBH interactions following subsequent galaxy mergers, a possibility not accounted for in Dvorkin and Barausse (2017) that we have explored for the first time.

Our main results can be summarised as follows:

1. Even in the eventuality that the final-parsec problem is not solved by the interaction of MBHBs with their stellar and gaseous environment (i.e., in *Model-stalled*), triple interactions can still lead a large number of MBHBs to final coalescence. In the mass range relevant to PTA observations, MBHB stalling suppresses the MBHB merger rate only by a factor of ≈ 4 (cf. tab. 5.1). Those mergers are the result of triple interactions.

2. The implied GWB background is only suppressed by a factor of about 2-to-3 in the relevant PTA frequency range ($1\ \mathrm{nHz} \lesssim f \lesssim 10\ \mathrm{nHz}$).

3. Triple MBH interactions naturally produce eccentric binaries. This causes the GWB to be generally flatter than the standard $f^{-2/3}$ power law. However, no clear turnover is seen, at least above $\gtrsim 0.1$ nHz, due to the wide range of eccentricities of the binaries.

4. The most massive MBHBs, $\mathcal{M} > 10^{8.5}\mathrm{M}_{\odot}$, which are the most likely to be individually resolved, can have eccentricities $\gtrsim 0.9$ at the relevant PTA frequencies. Still, the majority of them tends to be circular or mildly eccentric.

5. When coupling the GWB suppression due to stalling to a pessimistic MBHB population model that predicts a particularly low GWB, we still obtain amplitude normalisations at the level $A \gtrsim 10^{-16}$.

6. The predicted amplitude is well within the reach of SKA. We find that a putative array monitoring 50 pulsars at 100 ns level has a 90% chance of detection after 15 years of observation. In general, we find that stalling will delay GWB detection by only about 3-to-6 years depending on the number of pulsars in the array.

A particularly relevant result is that signal amplitudes below $A \approx 10^{-16}$ are extremely unlikely even in the most pessimistic scenario in which (1) MBHs are intrinsically less massive than predicted by standard MBH-host galaxy relations *and*, (2) MBHBs stall. Our main claim is therefore that, because of triple interactions, stalling does not strongly decrease the level of the GWB in the PTA frequency range.

The only other way to pose a threat to future PTA detections is if the opposite of stalling is realised in Nature, i.e., if an extremely efficient coupling with the environment swiftly drives MBHBs through the PTA band, which would cause a low-frequency turnover in the GWB. In order to severely affect GW detectability, such turnover should be at frequencies well above 10 nHz, which for realistic environments is never the case, unless *all* MBHBs are extremely eccentric ($e \gtrsim 0.99$). This eventuality seems very unlikely, since simulations of MBHBs in stellar environments generally find a *range* of eccentricities $0 \leq e < 1$. The most important implication is that with the advent of MeerKAT, FAST and SKA, PTAs *will* detect a GW signal from merging MBHBs, provided that those instruments bring an-order-of-magnitude improvement over current PTA sensitivities.

Our results are subject to a number of caveats that we have extensively discussed: a very approximate treatment of quadruple interactions, our assumption that MBHBs are driven to separations comparable with their influence radius on timescales shorter than the Hubble time, the direct application of our findings to different MBHB populations to derive a lower limit for the expected GWB amplitude. We have argued that none of those caveats is however critical, and that the our results are therefore robust. Even if everything conspires to produce the lowest possible GWB amplitude, a typical SKA-based PTA will still have a $\gtrsim 90\%$ probability of detecting a signal within 15 years of data collection, which strengthens the scientific case of this observatory and which is a good reason to look with optimism at the future of GW astrophysics in the nHz band.

Chapter 6

Prospects for LISA

A natural extension of our work is the analysis of the triple interaction in the framework of the LISA mission. This is the subject of a project still in progress at the time this thesis was written. Therefore, here we simply give a brief description of the main points.

6.1 The concept of LISA

The laser interferometer space antenna (LISA, see, e.g., Amaro-Seoane et al., 2017, for full details) will be the first mission to study the high-redshift Universe through observation of GWs. The science case of the mission is extremely rich and ambitious, having the possibility of observing gravitational radiation from objects spanning a huge range in mass (from few to billion of solar masses) and redshift (from galactic sources to an early epoch of the Universe when it was only few hundreds of Myr old).

The concept of the mission relies on the laser interferometry technique. The experiment essentially is a super-wide interferometer in space, formed by three satellites in equilateral triangular configuration, each arm-length being of the order of millions of kilometres. GWs are detected by monitoring the changes in distance between free falling test masses inside the spacecrafts. These tiny changes could be detected by analysing the interference pattern of the recombined light that beams back and forth among the satellites. Because of the space-borne nature of the mission and the wide arm-length, an important low frequency window could be for the first time extensively surveyed.

Differently from PTA, the main targets of LISA are single resolvable sources, which through an accurate parameter estimation analysis, could provide a precise demographics of our Universe, perform cosmological measurements and test GR at its most extreme levels.

Concerning MBHs, the frequency window of LISA allows the detection of coalescences of relatively small mass MBHBs, i.e., with $10^4 \lesssim \mathcal{M} \lesssim 10^7$, which

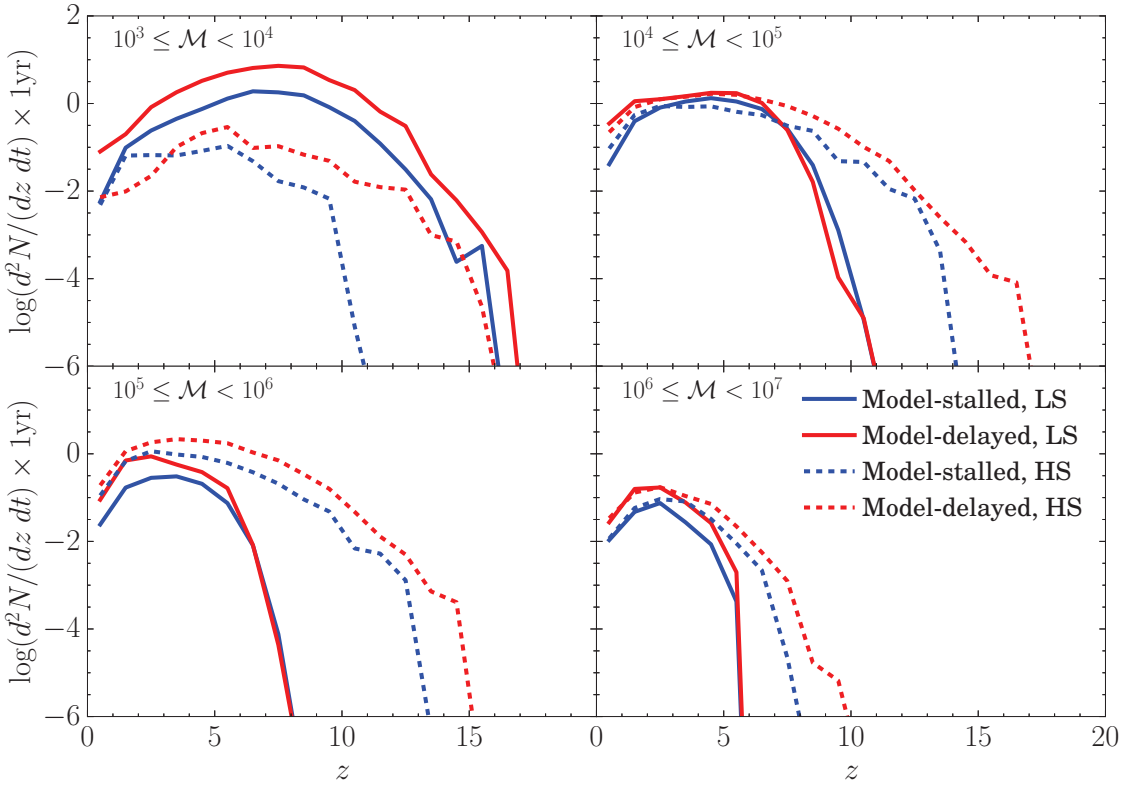

Figure 6.1: Redshift distribution of merging MBHBs in different chirp mass bins relevant for LISA. Line styles are described in the figure.

emit GWs in the range $10^{-5} - 1$ Hz. Therefore, LISA represents the perfect counterpart of PTA, which instead is most sensitive to very massive binaries. Together, these two experiments can fully cover the relevant frequency domain of the GW sources studied and discussed in this thesis.

6.2 MBH triplets and LISA

By means of the catalogues of merging MBHBs presented in previous chapters, we can perform a detailed analysis of the impact of triple interactions in the LISA band. Contrary to the PTA framework, the details about the MBH seed prescriptions result to be quite relevant and can moderately affect the global merger rate and its redshift distribution in the mass range observable by the experiment.

Indeed, as shown in tab. 6.1 (and fig. 6.1), the merger rate in the lowest chirp mass bin results to be more than one order of magnitude higher for the *LS* scenario compared to the *HS* case. Another remarkable difference between the two seed models appears in the *Model-delayed* case, where for the *LS* scenario, the primary merger channel is interactions with a gaseous environment, in strike contrast with typical PTA sources, where stellar-driven coalescences are more likely. This is not the case for the *HS* model, the stellar channel still being the preferred coalescence-driving mechanism also at low masses. Moreover, the fraction of triple interactions leading to coalescences is globally higher in the

HS scenario.

From fig. 6.1, we can see that the merger rate redshift distribution features different signatures according to the seed model. In particular, it can be inferred that the *HS* model shows prominent tails at higher redshift,[1] not shown in case of light seeds. At lower redshift, instead, the two models predict a quite similar merger rate (except, as already pointed out, in the lowest mass bin). Hence, in principle, LISA could place important constraints on the characteristics of the MBH seeding at early times.

A reliable analysis cannot be disentangled from an estimation of the signal-to-noise ratio (SNR) of the merging MBHBs. The goal can be achieved by assuming a waveform model and a sensitivity curve for LISA. This is one of the main points we are currently investigating.

A second important point we are working on is a careful analysis of the effects of non-negligible eccentricities. Indeed, as previously discussed, a distinct characteristic of triple interactions can be found in the extreme eccentricity values that binaries can acquire. Generally, we do not expect that MBHBs in the LISA band would have the extremely high eccentricities found in the PTA frequency window, still a significant number of coalescing MBHBs could have eccentricity in excess of $\simeq 0.5$ when entering the LISA band (see fig. 3.12). In order to quantify the expected GW signal, we are performing a detailed analysis of the higher harmonics excited by the non-zero eccentricity, as a relevant fraction of the emitted power is indeed radiated at such high frequencies. As an example, in fig. 6.2 we report a representative source extracted from our catalogues of MBH mergers. It is apparent that high harmonics play a relevant role in forging the GW signal, and LISA ability to detect it.[2]

Finally, a further consequence connected to the excitation of higher frequencies is the possibility that wide, highly eccentric binaries could emit a detectable signal in the LISA band. Should such particular binaries have a merger timescale longer than the nominal duration of the mission, then they could represent a new class of burst-like sources, calling for extra care in the process of signal extraction and in the data analysis.

[1] Note that the higher-z tails present in the mass bin $10^4 - 10^5$ $M_\odot$ and not in the $10^3 - 10^4$ $M_\odot$ one are likely due to the MBH seeding recipe which produce seed MBHs around $\sim 10^5$ $M_\odot$ (see, Volonteri, Lodato, and Natarajan, 2008, for further details).

[2] For the estimation of the SNR we have followed the approach of Barack and Cutler (2004).

LS

$\mathcal{M}$ [$M_\odot$]	*Model-delayed*					*Model-stalled*				
	Rate [yr^{-1}]	binaries		triplets		Rate [yr^{-1}]	binaries		triplets	
		star	gas	Tr (quad)	Tr-ej		star	gas	Tr (quad)	Tr-ej
$10^3 - 10^4$	38.12	17.2%	75.0%	5.7% (0.4%)	1.7%	9.444	–	–	76.9% (19.2%)	3.94%
$10^4 - 10^5$	8.937	18.9%	76.5%	3.9% (0.08%)	0.7%	5.899	–	–	50.7% (42.3%)	7.02%
$10^5 - 10^6$	2.788	38.4%	55.7%	4.9% (0.2%)	0.8%	1.087	–	–	28.0% (64.1%)	7.93%
$10^6 - 10^7$	0.461	68.1%	21.9%	8.1% (0.3%)	1.6%	0.176	–	–	18.3% (72.2%)	9.52%

HS

$\mathcal{M}$ [$M_\odot$]	*Model-delayed*					*Model-stalled*				
	Rate [yr^{-1}]	binaries		triplets		Rate [yr^{-1}]	binaries		triplets	
		star	gas	Tr (quad)	Tr-ej		star	gas	Tr (quad)	Tr-ej
$10^3 - 10^4$	0.980	53.7%	32.1%	14.1% (0.0%)	0.0%	0.452	–	–	100.0% (0.0%)	0.0%
$10^4 - 10^5$	9.977	51.6%	26.3%	21.3% (0.3%)	0.4%	5.050	–	–	97.0% (1.7%)	1.3%
$10^5 - 10^6$	11.39	54.2%	25.9%	16.4% (2.1%)	1.4%	5.098	–	–	81.7% (14.1%)	4.2%
$10^6 - 10^7$	0.533	62.8%	24.2%	10.0% (1.3%)	1.8%	0.289	–	–	67.0% (26.5%)	6.5%

Table 6.1: Same as tab. 5.1, except that we consider MBHBs with chirp mass in the four least massive mass bins.

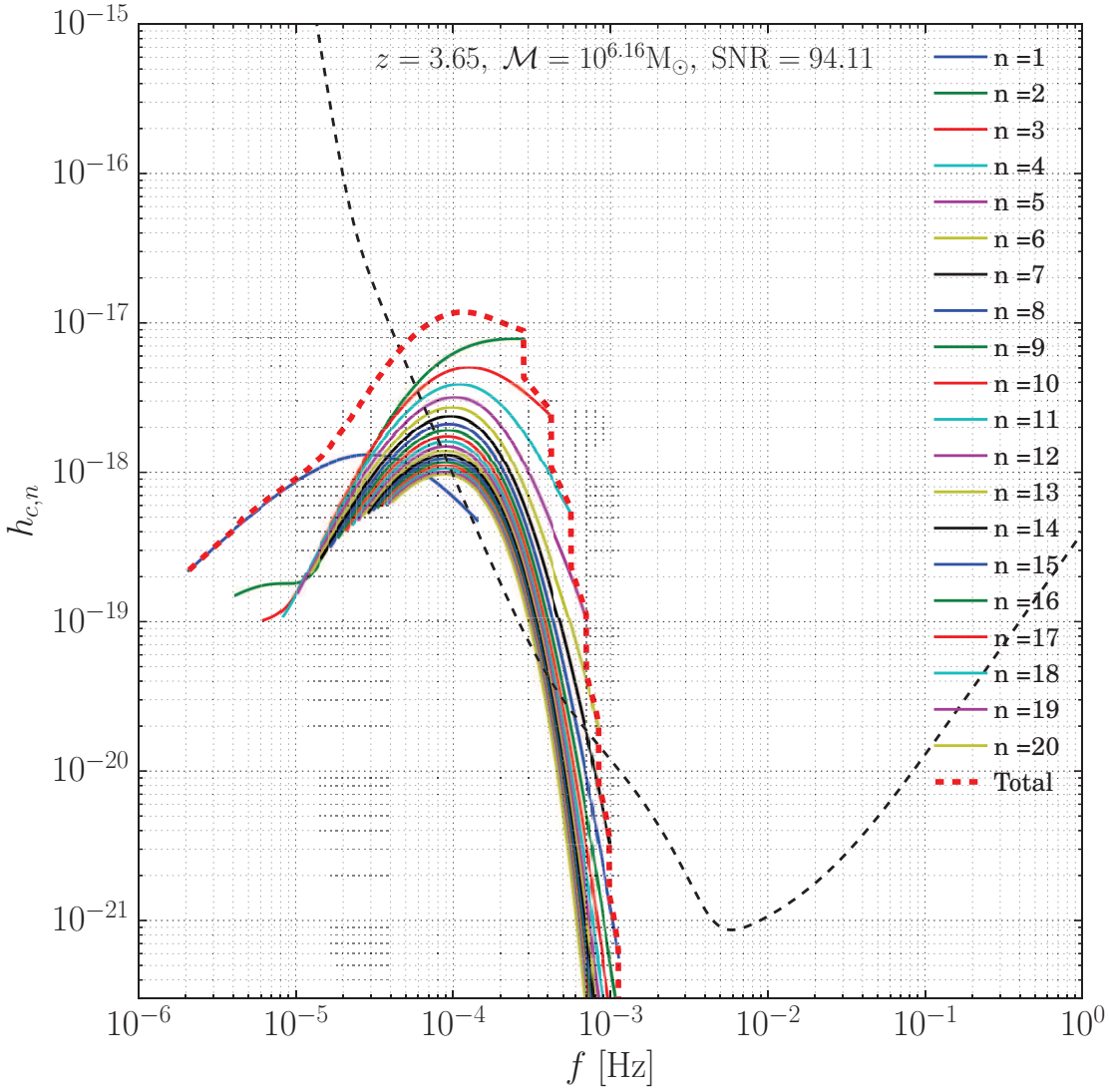

Figure 6.2: Representative evolution of the characteristic strain (red dashed line) of a merging MBHB in which higher harmonics (labelled according to their colour code) are excited by a non-zero orbital eccentricity. The dashed black line is the expected LISA sensitivity curve for six laser links and an arm-length of 2.5 millions of kilometres (see, e.g., Babak et al., 2017).

Conclusions

In this thesis I presented a detailed analysis of the formation and evolution of massive black hole (MBH) triplets. Such systems are expected to form in galactic nuclei as a consequence of, i) the hierarchical formation of the cosmic structure and, ii) the possible stalling of MBH binaries (MBHBs) at $\lesssim$ pc-scale separations. I summarise in the following our major findings.

We developed a three-body integrator that includes the relevant physics necessary to accurately describe the relativistic dynamics of MBH triplets embedded in a stellar system. In particular, we implemented and tested the relativistic corrections up to 2.5PN order, as consistently derived from a three-body PN Hamiltonian. We then analysed the emission of gravitational waves (GWs) for the specific case of triple interactions, highlighting some peculiar subtle behaviours that arise when computing the GW emission of triple system by simply employing that standard GW generation formalism.

In order to properly account for the effects of the environment, the MBH triplets were modelled as embedded in a galactic potential, considering the roles played in the evolution by dynamical friction and by stellar hardening. Stellar hardening was inserted through the introduction of a phase dependent fictitious force able to reproduce the results of scattering experiments. We tested the stability and accuracy of our code with a number of tests and comparisons with other similar existing codes, and we generally found very good agreement.

Next, we performed a detailed survey of the parameter space of astrophysical MBH triplets, spanning a wide range in terms of masses, mass ratios, eccentricities and inclinations. We analysed the fraction of merging systems as a function of the relevant parameters, as well as the typical merger timescales and properties of the coalescing MBHs. Remarkably, we found that around 30% of the simulated systems undergo a coalescence of one of any pair of MBHs. The major part of these mergers (around 20% independent on mass) are promptly induced during the three-body interaction, whereas a minor fraction is driven toward coalescence by GW emission alone following the ejection of the lightest black hole. Among prompt mergers, we could identify two major physical channels, i.e., secular K-L resonances and chaotic interactions, respectively. The K-L mechanism is more effective for more massive intruders (large $q_{\rm out}$), more eccentric inner binaries, and relative inclination close to 90°, while chaotic dy-

namics is proportionally more relevant in case of (almost) equal-mass system. The merger timescale, around 250 Myr, is dominated by the orbital decay of the intruder, driven by dynamical friction and stellar hardening. When a chaotic interaction starts, the possible coalescence follows after few Myrs.

We also verified that conservative relativistic corrections can have dramatic effects at low $q_{\rm in}/q_{\rm out}$. Neglecting such corrections, the merger fraction results a factor $\simeq 2$ larger, highlighting the importance of low order PN terms when studying the dynamics of MBH triple systems.

A further remarkable consequence of merger-inducing triple interactions is the high eccentricity acquired by MBHBs, generally above 0.9, and up to 0.9999 in some cases. Remarkably, such very high eccentricities can be retained until the very last phases of the evolution. Binaries driven to coalescence by triple MBH interactions can therefore have eccentricities in excess of 0.5 when entering the LISA band, and in excess of 0.9 in the PTA frequency range.

Compared to the merger fractions found in previous studies (e.g., Hoffman and Loeb, 2007), our figures are significantly lower. This can be explained by the fact that we included lower mass ratios (which give a lower merger fraction), PN dynamics (which partially suppresses K-L resonances), and by a conservative prescription for MBHs ejections.

In order to assess the signature of triple systems on the GW signal, we coupled our catalogue of MBH triplets with a semi-analytical model of galaxy formation and evolution. We implemented an ad-hoc recipe to resolve multiple MBH interactions occurring during the assembling path of the cosmic structure, exploring two different scenarios: an idealised picture in which MBH mergers can actually happen only as a consequence of triple (multiple) interactions (*Model-stalled*, i.e., where all MBHBs stall and coalescence can be triggered only after the interaction with a third body), and a more standard model, where MBHBs coalescences can also be driven by stellar and/or gaseous interactions (*Model-delayed*). We released catalogues of merging MBHBs, discriminating among the different drivers of MBHB coalescences.

For the first time we could evaluate the impact of triple interactions on the level of the nHz stochastic GW background, relevant to PTAs. Even in the pessimistic scenario implied by *Model-stalled*, mergers can still be triggered by triple (and quadruple) MBH interactions. This represents a partial solution to the final-parsec problem, as the MBHB merger rate results to be only suppressed by a factor of $\simeq 4$ compared to *Model-delayed*. This translates into a GW background only a factor of about 2-to-3 dimmer in the relevant PTA frequency range (1 nHz $\lesssim f \lesssim 10$ nHz). We also showed that, as triple MBH interactions naturally produce eccentric binaries, the resulting background spectrum results to be flatter than the standard $f^{-2/3}$ power law.

Finally, we could estimate that a putative array monitoring 50 pulsars, with time-of-arrival of the radio signals tracked at the 100 ns accuracy level, would have a $\gtrsim 90\%$ chance of detection after 15 years of observation. In this context, we proved that MBH stalling would delay the background detection by only about 3-to-6 years, depending on the number of pulsars in the array. Therefore, although the detection of GW background may still remain challenging for

present PTA configurations, the amplitude we predicted by our conservative study lies well within the reach of future experiments, like, e.g., SKA. Our work strengthens the scientific case of GW searches in the nHz regime, clearly showing that the detection of the GW background from the cosmic population of MBHB is within reach in few years.

Finally, we sketched the relevance of a sizeable population of MBHBs forced to merge by a triple interaction on the LISA mission. As our work on this subject is still in progress, some promising preliminary results seem to suggest that triple interaction should be taken into account in any assessment of the LISA data stream.

Bibliography

Abbott, B. P. et al. (Feb. 2016). "Observation of Gravitational Waves from a Binary Black Hole Merger". In: *Physical Review Letters* 116.6, 061102, p. 061102. DOI: 10.1103/PhysRevLett.116.061102. arXiv: 1602.03837 [gr-qc] (cit. on p. 1).

Alcubierre, M. (2008). *Introduction to 3+1 Numerical Relativity*. Oxford University Press (cit. on p. 1).

Amaro-Seoane, P. et al. (Mar. 2010). "Triplets of supermassive black holes: astrophysics, gravitational waves and detection". In: MNRAS 402, pp. 2308–2320. DOI: 10.1111/j.1365-2966.2009.16104.x. arXiv: 0910.1587 (cit. on pp. xvii, 63, 86).

Amaro-Seoane, P. et al. (Feb. 2017). "Laser Interferometer Space Antenna". In: *ArXiv e-prints*. arXiv: 1702.00786 [astro-ph.IM] (cit. on pp. xi, 137).

Antognini, J. M. O. and T. A. Thompson (Mar. 2016). "Dynamical formation and scattering of hierarchical triples: cross-sections, Kozai-Lidov oscillations, and collisions". In: MNRAS 456, pp. 4219–4246. DOI: 10.1093/mnras/stv2938. arXiv: 1507.03593 [astro-ph.SR] (cit. on p. xv).

Antonini, F., E. Barausse, and J. Silk (Oct. 2015a). "The Coevolution of Nuclear Star Clusters, Massive Black Holes, and Their Host Galaxies". In: ApJ 812, 72, p. 72. DOI: 10.1088/0004-637X/812/1/72. arXiv: 1506.02050 (cit. on pp. 39, 65, 102, 104, 105).

Antonini, F., E. Barausse, and J. Silk (June 2015b). "The Imprint of Massive Black Hole Mergers on the Correlation between Nuclear Star Clusters and Their Host Galaxies". In: ApJ 806, L8, p. L8. DOI: 10.1088/2041-8205/806/1/L8. arXiv: 1504.04033 (cit. on pp. 39, 65, 102, 104, 105).

Antonini, F. and D. Merritt (Jan. 2012). "Dynamical Friction around Supermassive Black Holes". In: ApJ 745, 83, p. 83. DOI: 10.1088/0004-637X/745/1/83. arXiv: 1108.1163 (cit. on p. 53).

Antonini, F., N. Murray, and S. Mikkola (Jan. 2014). "Black Hole Triple Dynamics: A Breakdown of the Orbit Average Approximation and Implications for Gravitational Wave Detections". In: ApJ 781, 45, p. 45. DOI: 10.1088/0004-637X/781/1/45. arXiv: 1308.3674 [astro-ph.HE] (cit. on p. 40).

Antonini, F. et al. (Jan. 2016). "Black Hole Mergers and Blue Stragglers from Hierarchical Triples Formed in Globular Clusters". In: ApJ 816, 65, p. 65. DOI: 10.3847/0004-637X/816/2/65. arXiv: 1509.05080 (cit. on pp. xv, 43, 63).

Arnowitt, R., S. Deser, and C. W. Misner (Dec. 1959). "Dynamical Structure and Definition of Energy in General Relativity". In: *Physical Review* 116, pp. 1322–1330. DOI: 10.1103/PhysRev.116.1322 (cit. on p. 10).

Babak, S. et al. (May 2017). "Science with the space-based interferometer LISA. V. Extreme mass-ratio inspirals". In: Phys. Rev. D 95.10, 103012, p. 103012. DOI: 10.1103/PhysRevD.95.103012. arXiv: 1703.09722 [gr-qc] (cit. on p. 141).

Baker, John G. et al. (2006). "Gravitational wave extraction from an inspiraling configuration of merging black holes". In: *Phys. Rev. Lett.* 96, p. 111102. eprint: gr-qc/0511103 (cit. on p. 1).

Barack, L. and C. Cutler (Dec. 2004). "Confusion noise from LISA capture sources". In: Phys. Rev. D 70.12, 122002, p. 122002. DOI: 10.1103/PhysRevD.70.122002. eprint: gr-qc/0409010 (cit. on p. 139).

Barausse, E. (July 2012). "The evolution of massive black holes and their spins in their galactic hosts". In: MNRAS 423, pp. 2533–2557. DOI: 10.1111/j.1365-2966.2012.21057.x. arXiv: 1201.5888 (cit. on pp. xi, 102, 133).

Barausse, E. et al. (July 2017). "Selection bias in dynamically measured supermassive black hole samples: scaling relations and correlations between residuals in semi-analytic galaxy formation models". In: MNRAS 468, pp. 4782–4791. DOI: 10.1093/mnras/stx799. arXiv: 1702.01762 (cit. on pp. 102, 103, 125, 132).

Begelman, M. C., R. D. Blandford, and M. J. Rees (Sept. 1980). "Massive black hole binaries in active galactic nuclei". In: Nature 287, pp. 307–309. DOI: 10.1038/287307a0 (cit. on p. xi).

Benson, A. J. and R. Bower (July 2010). "Galaxy formation spanning cosmic history". In: MNRAS 405, pp. 1573–1623. DOI: 10.1111/j.1365-2966.2010.16592.x. arXiv: 1003.0011 (cit. on p. 102).

Berczik, P. et al. (May 2006). "Efficient Merger of Binary Supermassive Black Holes in Nonaxisymmetric Galaxies". In: ApJ 642, pp. L21–L24. DOI: 10.1086/504426. eprint: astro-ph/0601698 (cit. on p. xiii).

Blaes, O., M. H. Lee, and A. Socrates (Oct. 2002). "The Kozai Mechanism and the Evolution of Binary Supermassive Black Holes". In: ApJ 578, pp. 775–786. DOI: 10.1086/342655. eprint: astro-ph/0203370 (cit. on pp. xv, xvi, 50, 60).

Blanchet, L. (1998). "On the multipole expansion of the gravitational field". In: *Class. Quant. Grav.* 15.7, pp. 1971–1999. eprint: gr-qc/9801101. URL: http://stacks.iop.org/0264-9381/15/i=7/a=013 (cit. on p. 20).

Blanchet, L. (Dec. 2002). "Gravitational Radiation from Post-Newtonian Sources and Inspiralling Compact Binaries". In: *Living Reviews in Relativity* 5, 3, p. 3. DOI: 10.12942/lrr-2002-3. eprint: gr-qc/0202016 (cit. on p. 10).

Blanchet, L. and T. Damour (1986). "Radiative gravitational fields in general relativity. I. general structure of the field outside the source". In: *Phil. Trans. Roy. Soc. Lond. A* 320, pp. 379–430. DOI: 10.1098/rsta.1986.0125. URL:

http://rsta.royalsocietypublishing.org/content/320/1555/379 (cit. on p. 20).

Blanchet, Luc (Feb. 2014). "Gravitational Radiation from Post-Newtonian Sources and Inspiralling Comp act Binaries". In: *Living Reviews in Relativity* 17.1, p. 2. ISSN: 1433-8351. DOI: 10.12942/lrr-2014-2. URL: http://dx.doi.org/10.12942/lrr-2014-2 (cit. on pp. 1, 6, 9, 19, 22).

Blanchet, Luc and Thibault Damour (1989). "Post-Newtonian generation of gravitational waves". In: *Annales Inst. H. Poincaré Phys. Théor.* 50, pp. 377–408. URL: http://www.numdam.org/item/AIHPA_1989__50_4_377_0 (cit. on p. 20).

Blanchet, Luc, Thibault Damour, and Bala R. Iyer (May 1995). "Gravitational waves from inspiralling compact binaries: Energy loss and waveform to second-post-Newtonian order". In: *Phys. Rev. D* 51 (10), pp. 5360–5386. DOI: 10.1103/PhysRevD.51.5360. URL: https://link.aps.org/doi/10.1103/PhysRevD.51.5360 (cit. on p. 20).

Blanchet, Luc et al. (May 1995). "Gravitational-Radiation Damping of Compact Binary Systems to Second Post-Newtonian Order". In: *Phys. Rev. Lett.* 74 (18), pp. 3515–3518. DOI: 10.1103/PhysRevLett.74.3515. URL: https://link.aps.org/doi/10.1103/PhysRevLett.74.3515 (cit. on p. 20).

Blecha, L. et al. (Apr. 2011). "Recoiling black holes in merging galaxies: relationship to active galactic nucleus lifetimes, starbursts and the M_{BH}-σ_* relation". In: MNRAS 412, pp. 2154–2182. DOI: 10.1111/j.1365-2966.2010.18042.x. arXiv: 1009.4940 (cit. on p. 101).

Blecha, L. et al. (Feb. 2016). "Recoiling black holes: prospects for detection and implications of spin alignment". In: MNRAS 456, pp. 961–989. DOI: 10.1093/mnras/stv2646. arXiv: 1508.01524 (cit. on pp. 118, 122).

Bower, R. G. et al. (Aug. 2006). "Breaking the hierarchy of galaxy formation". In: MNRAS 370, pp. 645–655. DOI: 10.1111/j.1365-2966.2006.10519.x. eprint: astro-ph/0511338 (cit. on p. 102).

Boylan-Kolchin, M., C.-P. Ma, and E. Quataert (Jan. 2008). "Dynamical friction and galaxy merging time-scales". In: MNRAS 383, pp. 93–101. DOI: 10.1111/j.1365-2966.2007.12530.x. arXiv: 0707.2960 (cit. on p. 104).

Bromley, B. C. et al. (Dec. 2006). "Hypervelocity Stars: Predicting the Spectrum of Ejection Velocities". In: ApJ 653, pp. 1194–1202. DOI: 10.1086/508419. eprint: astro-ph/0608159 (cit. on p. 108).

Bulirsch, Roland and Josef Stoer (Mar. 1966). "Numerical treatment of ordinary differential equations by extrapolation methods". In: *Numerische Mathematik* 8.1, pp. 1–13. ISSN: 0029-599X (print), 0945-3245 (electronic) (cit. on p. 40).

Callegari, S. et al. (May 2009). "Pairing of Supermassive Black Holes in Unequal-Mass Galaxy Mergers". In: ApJ 696, pp. L89–L92. DOI: 10.1088/0004-637X/696/1/L89. arXiv: 0811.0615 (cit. on p. 104).

Campanelli, Manuela et al. (2006). "Accurate evolutions of orbiting black-hole binaries without excision". In: *Phys. Rev. Lett.* 96, p. 111101. eprint: gr-qc/0511048 (cit. on p. 1).

Cattaneo, A. et al. (Aug. 2006). "Modelling the galaxy bimodality: shutdown above a critical halo mass". In: MNRAS 370, pp. 1651–1665. DOI: 10.1111/j.1365-2966.2006.10608.x. eprint: astro-ph/0601295 (cit. on p. 103).

Chandrasekhar, S. (Mar. 1943). "Dynamical Friction. I. General Considerations: the Coefficient of Dynamical Friction." In: ApJ 97, p. 255. DOI: 10.1086/144517 (cit. on pp. xii, 40).

Chen, S., A. Sesana, and W. Del Pozzo (Sept. 2017). "Efficient computation of the gravitational wave spectrum emitted by eccentric massive black hole binaries in stellar environments". In: MNRAS 470, pp. 1738–1749. DOI: 10.1093/mnras/stx1093. arXiv: 1612.00455 (cit. on pp. 114, 115, 120, 122).

Chen, X. et al. (Mar. 2011). "Tidal Stellar Disruptions by Massive Black Hole Pairs. II. Decaying Binaries". In: ApJ 729, 13, p. 13. DOI: 10.1088/0004-637X/729/1/13. arXiv: 1012.4466 (cit. on p. 60).

Cole, S. et al. (Dec. 1994). "A Recipe for Galaxy Formation". In: MNRAS 271, p. 781. DOI: 10.1093/mnras/271.4.781. eprint: astro-ph/9402001 (cit. on p. 102).

Cole, S. et al. (Nov. 2000). "Hierarchical galaxy formation". In: MNRAS 319, pp. 168–204. DOI: 10.1046/j.1365-8711.2000.03879.x. eprint: astro-ph/0007281 (cit. on p. 102).

Colpi, Monica (2014). "Massive binary black holes in galactic nuclei and their path to coalescence". In: *Space Sci. Rev.* 183.1-4, pp. 189–221. DOI: 10.1007/s11214-014-0067-1. arXiv: 1407.3102 [astro-ph.GA] (cit. on p. xiii).

Croton, D. J. et al. (Jan. 2006). "The many lives of active galactic nuclei: cooling flows, black holes and the luminosities and colours of galaxies". In: MNRAS 365, pp. 11–28. DOI: 10.1111/j.1365-2966.2005.09675.x. eprint: astro-ph/0508046 (cit. on p. 102).

Cuadra, J. et al. (Mar. 2009). "Massive black hole binary mergers within subparsec scale gas discs". In: MNRAS 393, pp. 1423–1432. DOI: 10.1111/j.1365-2966.2008.14147.x. arXiv: 0809.0311 (cit. on p. xiii).

Cui, X. and Q. Yu (Jan. 2014). "Orbital orientation evolution of massive binary black holes at the centres of non-spherical galaxies". In: MNRAS 437, pp. 777–789. DOI: 10.1093/mnras/stt1936. arXiv: 1310.2309 (cit. on p. 34).

Dabringhausen, J., M. Hilker, and P. Kroupa (May 2008). "From star clusters to dwarf galaxies: the properties of dynamically hot stellar systems". In: MNRAS 386, pp. 864–886. DOI: 10.1111/j.1365-2966.2008.13065.x. arXiv: 0802.0703 (cit. on pp. 38, 65).

Damour, T. and G. Schäfer (Sept. 1985). "Lagrangians for n point masses at the second post-Newtonian approximation of general relativity." In: *General Relativity and Gravitation* 17, pp. 879–905 (cit. on p. 10).

DeGraf, C. et al. (Aug. 2012). "Early black holes in cosmological simulations: luminosity functions and clustering behaviour". In: MNRAS 424, pp. 1892–1898. DOI: 10.1111/j.1365-2966.2012.21294.x. arXiv: 1107.1254 (cit. on p. 101).

Dehnen, W. (Nov. 1993). "A Family of Potential-Density Pairs for Spherical Galaxies and Bulges". In: MNRAS 265, p. 250. DOI: 10.1093/mnras/265.1.250 (cit. on p. 37).

Dekel, A. and Y. Birnboim (May 2006). "Galaxy bimodality due to cold flows and shock heating". In: MNRAS 368, pp. 2–20. DOI: 10.1111/j.1365-2966.2006.10145.x. eprint: astro-ph/0412300 (cit. on p. 103).

Dekel, A. et al. (Jan. 2009). "Cold streams in early massive hot haloes as the main mode of galaxy formation". In: Nature 457, pp. 451–454. DOI: 10.1038/nature07648. arXiv: 0808.0553 (cit. on p. 103).

Detweiler, S. (Dec. 1979). "Pulsar timing measurements and the search for gravitational waves". In: ApJ 234, pp. 1100–1104. DOI: 10.1086/157593 (cit. on p. 112).

Di Matteo, T., V. Springel, and L. Hernquist (Feb. 2005). "Energy input from quasars regulates the growth and activity of black holes and their host galaxies". In: Nature 433, pp. 604–607. DOI: 10.1038/nature03335. eprint: astro-ph/0502199 (cit. on p. 101).

Dosopoulou, F. and F. Antonini (May 2017). "Dynamical Friction and the Evolution of Supermassive Black Hole Binaries: The Final Hundred-parsec Problem". In: ApJ 840, 31, p. 31. DOI: 10.3847/1538-4357/aa6b58. arXiv: 1611.06573 (cit. on pp. 40, 131, 133).

Dotti, M., A. Sesana, and R. Decarli (2012). "Massive Black Hole Binaries: Dynamical Evolution and Observational Signatures". In: *Advances in Astronomy* 2012, 940568, p. 940568. DOI: 10.1155/2012/940568. arXiv: 1111.0664 (cit. on p. 120).

Dotti, M. et al. (Aug. 2007). "Supermassive black hole binaries in gaseous and stellar circumnuclear discs: orbital dynamics and gas accretion". In: MNRAS 379, pp. 956–962. DOI: 10.1111/j.1365-2966.2007.12010.x. eprint: astro-ph/0612505 (cit. on p. xiii).

Dubois, Y. and R. Teyssier (Jan. 2008). "On the onset of galactic winds in quiescent star forming galaxies". In: A&A 477, pp. 79–94. DOI: 10.1051/0004-6361:20078326. arXiv: 0707.3376 (cit. on p. 101).

Dubois, Y. et al. (Oct. 2014). "Dancing in the dark: galactic properties trace spin swings along the cosmic web". In: MNRAS 444, pp. 1453–1468. DOI: 10.1093/mnras/stu1227. arXiv: 1402.1165 (cit. on p. 101).

Dvorkin, I. and E. Barausse (Feb. 2017). "The nightmare scenario: measuring the stochastic gravitational-wave background from stalling massive black-hole binaries with pulsar-timing arrays". In: *ArXiv e-prints*. arXiv: 1702.06964 (cit. on pp. 68, 117, 131, 134).

Ebisuzaki, T., J. Makino, and S. K. Okumura (Nov. 1991). "Merging of two galaxies with central black holes". In: Nature 354, pp. 212–214. DOI: 10.1038/354212a0 (cit. on pp. 39, 65).

Einstein, A., L Infeld, and B Hoffmann (Jan. 1938). "The gravitational equations and the problem of motions". In: *Ann. Math.* 39, p. 65 (cit. on p. 1).

Einstein, Albert (Feb. 1918). "Über Gravitationswellen". In: *Sitzungsberichte der Königlich Preußischen Akademie der Wissenschaften (Berlin)*, pp. 154–167. URL: http://echo.mpiwg-berlin.mpg.de/MPIWG:8HSP60BU (cit. on p. 6).

Enoki, M. et al. (Nov. 2004). "Gravitational Waves from Supermassive Black Hole Coalescence in a Hierarchical Galaxy Formation Model". In: ApJ 615, pp. 19–28. DOI: 10.1086/424475. eprint: astro-ph/0404389 (cit. on p. xi).

Feng, Y. et al. (Jan. 2016). "The BlueTides simulation: first galaxies and reionization". In: MNRAS 455, pp. 2778–2791. DOI: 10.1093/mnras/stv2484. arXiv: 1504.06619 (cit. on p. 101).

Ferrarese, L. and D. Merritt (Aug. 2000). "A Fundamental Relation between Supermassive Black Holes and Their Host Galaxies". In: ApJ 539, pp. L9–L12. DOI: 10.1086/312838. eprint: astro-ph/0006053 (cit. on p. 37).

Fiacconi, D. et al. (Nov. 2013). "Massive Black Hole Pairs in Clumpy, Self-gravitating Circumnuclear Disks: Stochastic Orbital Decay". In: ApJ 777, L14, p. L14. DOI: 10.1088/2041-8205/777/1/L14. arXiv: 1307.0822 (cit. on p. 59).

Ford, E. B., B. Kozinsky, and F. A. Rasio (May 2000). "Secular Evolution of Hierarchical Triple Star Systems". In: ApJ 535, pp. 385–401. DOI: 10.1086/308815 (cit. on p. xiv).

Galaviz, P. and B. Brügmann (Apr. 2011). "Characterization of the gravitational wave emission of three black holes". In: Phys. Rev. D 83.8, 084013, p. 084013. DOI: 10.1103/PhysRevD.83.084013. arXiv: 1012.4423 [gr-qc] (cit. on pp. 2, 3, 7, 8, 17, 19, 23, 45).

Georg, I. and G. Schäfer (July 2015). "Canonical center and relative coordinates for compact binary systems through second post-Newtonian order". In: *Classical and Quantum Gravity* 32.14, 145001, p. 145001. DOI: 10.1088/0264-9381/32/14/145001. arXiv: 1503.04618 [gr-qc] (cit. on p. 10).

Gerosa, D. and A. Sesana (Jan. 2015). "Missing black holes in brightest cluster galaxies as evidence for the occurrence of superkicks in nature". In: MNRAS 446, pp. 38–55. DOI: 10.1093/mnras/stu2049. arXiv: 1405.2072 (cit. on p. 62).

Goicovic, F. G. et al. (Nov. 2017). "Infalling clouds on to supermassive black hole binaries - II. Binary evolution and the final parsec problem". In: MNRAS 472, pp. 514–531. DOI: 10.1093/mnras/stx1996. arXiv: 1602.01966 [astro-ph.HE] (cit. on p. xiii).

Goldstein, H. (1950). *Classical mechanics* (cit. on p. 10).

Granato, G. L. et al. (Jan. 2004). "A Physical Model for the Coevolution of QSOs and Their Spheroidal Hosts". In: ApJ 600, pp. 580–594. DOI: 10.1086/379875. eprint: astro-ph/0307202 (cit. on p. 104).

Gualandris, A., M. Dotti, and A. Sesana (Feb. 2012). "Massive black hole binary plane reorientation in rotating stellar systems". In: MNRAS 420, pp. L38–L42. DOI: 10.1111/j.1745-3933.2011.01188.x. arXiv: 1109.3707 (cit. on p. 34).

Gualandris, A. and D. Merritt (Jan. 2012). "Long-term Evolution of Massive Black Hole Binaries. IV. Mergers of Galaxies with Collisionally Relaxed Nuclei". In: ApJ 744, 74, p. 74. DOI: 10.1088/0004-637X/744/1/74. arXiv: 1107.4095 (cit. on p. xiii).

Gualandris, A. et al. (Jan. 2017). "Collisionless loss-cone refilling: there is no final parsec problem". In: MNRAS 464, pp. 2301–2310. DOI: 10.1093/mnras/stw2528. arXiv: 1609.09383 (cit. on p. xiii).

Guedes, J. et al. (Sept. 2009). "Simulations of Recoiling Massive Black Holes in the Via Lactea Halo". In: ApJ 702, pp. 890–900. DOI: 10.1088/0004-637X/702/2/890. arXiv: 0907.0892 [astro-ph.GA] (cit. on pp. 67, 90).

Guedes, J. et al. (Mar. 2011). "Recoiling Massive Black Holes in Gas-rich Galaxy Mergers". In: ApJ 729, 125, p. 125. DOI: 10.1088/0004-637X/729/2/125. arXiv: 1008.2032 (cit. on p. 101).

Gültekin, K. et al. (June 2009). "The M-σ and M-L Relations in Galactic Bulges, and Determinations of Their Intrinsic Scatter". In: ApJ 698, pp. 198–221. DOI: 10.1088/0004-637X/698/1/198. arXiv: 0903.4897 [astro-ph.GA] (cit. on pp. 37, 38).

Haehnelt, M. G. (July 1994). "Low-Frequency Gravitational Waves from Supermassive Black-Holes". In: MNRAS 269, p. 199. DOI: 10.1093/mnras/269.1.199. eprint: astro-ph/9405032 (cit. on p. xi).

Haiman, Z., B. Kocsis, and K. Menou (Aug. 2009). "The Population of Viscosity- and Gravitational Wave-driven Supermassive Black Hole Binaries Among Luminous Active Galactic Nuclei". In: ApJ 700, pp. 1952–1969. DOI: 10.1088/0004-637X/700/2/1952. arXiv: 0904.1383 [astro-ph.CO] (cit. on pp. xiii, 105).

Heger, A. and S. E. Woosley (Mar. 2002). "The Nucleosynthetic Signature of Population III". In: ApJ 567, pp. 532–543. DOI: 10.1086/338487. eprint: astro-ph/0107037 (cit. on p. 103).

Heggie, D. C. (Dec. 1975). "Binary evolution in stellar dynamics". In: MNRAS 173, pp. 729–787. DOI: 10.1093/mnras/173.3.729 (cit. on p. 82).

Hellings, R. W. and G. S. Downs (Feb. 1983). "Upper limits on the isotropic gravitational radiation background from pulsar timing analysis". In: ApJ 265, pp. L39–L42. DOI: 10.1086/183954 (cit. on pp. 113, 127).

Henon, M. (May 1976). "A family of periodic solutions of the planar three-body problem, and their stability". In: *Celestial Mechanics* 13, pp. 267–285. DOI: 10.1007/BF01228647 (cit. on p. 42).

Hernquist, L. (June 1990). "An analytical model for spherical galaxies and bulges". In: ApJ 356, pp. 359–364. DOI: 10.1086/168845 (cit. on pp. 39, 65).

Hewish, A. et al. (Feb. 1968). "Observation of a Rapidly Pulsating Radio Source". In: Nature 217, pp. 709–713. DOI: 10.1038/217709a0 (cit. on p. 111).

Hilborn, R. C. (1994). *Chaos and Nonlinear Dynamics: An Introduction for Scientists and Engineers* (cit. on p. 47).

Hills, J. G. (Aug. 1983). "The effect of low-velocity, low-mass intruders (collisionless gas) on the dynamical evolution of a binary system". In: AJ 88, pp. 1269–1283. DOI: 10.1086/113418 (cit. on pp. 29, 30).

Hirschmann, M. et al. (Aug. 2014). "Cosmological simulations of black hole growth: AGN luminosities and downsizing". In: MNRAS 442, pp. 2304–2324. DOI: 10.1093/mnras/stu1023. arXiv: 1308.0333 (cit. on p. 101).

Hoffman, L. and A. Loeb (May 2007). "Dynamics of triple black hole systems in hierarchically merging massive galaxies". In: MNRAS 377, pp. 957–976. DOI: 10.1111/j.1365-2966.2007.11694.x. eprint: astro-ph/0612517 (cit. on pp. xv, 40, 62, 67, 73, 89, 91, 106, 131, 144).

Hogg, D. W. (May 1999). "Distance measures in cosmology". In: *ArXiv Astrophysics e-prints*. eprint: astro-ph/9905116 (cit. on p. 122).

Holley-Bockelmann, K. and F. M. Khan (Sept. 2015). "Galaxy Rotation and Rapid Supermassive Binary Coalescence". In: ApJ 810, 139, p. 139. DOI: 10.1088/0004-637X/810/2/139. arXiv: 1505.06203 (cit. on p. xiii).

Holman, M., J. Touma, and S. Tremaine (Mar. 1997). "Chaotic variations in the eccentricity of the planet orbiting 16 Cygni B". In: Nature 386, pp. 254–256. DOI: 10.1038/386254a0 (cit. on p. xv).

Hut, P. and J. N. Bahcall (May 1983). "Binary-single star scattering. I - Numerical experiments for equal masses". In: ApJ 268, pp. 319–341. DOI: 10.1086/160956 (cit. on p. 30).

Iwasawa, M., Y. Funato, and J. Makino (Nov. 2006). "Evolution of Massive Black Hole Triples. I. Equal-Mass Binary-Single Systems". In: ApJ 651, pp. 1059–1067. DOI: 10.1086/507473. eprint: astro-ph/0511391 (cit. on pp. xv, 73).

Iwasawa, M., Y. Funato, and J. Makino (Jan. 2008). "Evolution of Massive Black-hole Triples II – The effect of the BH triples dynamics on the structure of the galactic nuclear". In: *ArXiv e-prints*. arXiv: 0801.0859 (cit. on p. xv).

Jaffe, A. H. and D. C. Backer (Feb. 2003). "Gravitational Waves Probe the Coalescence Rate of Massive Black Hole Binaries". In: ApJ 583, pp. 616–631. DOI: 10.1086/345443. eprint: astro-ph/0210148 (cit. on p. xi).

Janssen, G. et al. (Apr. 2015). "Gravitational Wave Astronomy with the SKA". In: *Advancing Astrophysics with the Square Kilometre Array (AASKA14)*, 37, p. 37. arXiv: 1501.00127 [astro-ph.IM] (cit. on p. 126).

Jeans, J. H. (Apr. 1919). "The origin of binary systems". In: MNRAS 79, p. 408. DOI: 10.1093/mnras/79.6.408 (cit. on p. 82).

Jenet, F. A. et al. (June 2005). "Detecting the Stochastic Gravitational Wave Background Using Pulsar Timing". In: ApJ 625, pp. L123–L126. DOI: 10.1086/431220. eprint: astro-ph/0504458 (cit. on p. xi).

Just, A. et al. (Feb. 2011). "Dynamical friction of massive objects in galactic centres". In: MNRAS 411, pp. 653–674. DOI: 10.1111/j.1365-2966.2010.17711.x. arXiv: 1009.2455 [astro-ph.CO] (cit. on p. 40).

Katz, B., S. Dong, and R. Malhotra (Oct. 2011). "Long-Term Cycling of Kozai-Lidov Cycles: Extreme Eccentricities and Inclinations Excited by a Distant Eccentric Perturber". In: *Physical Review Letters* 107.18, 181101, p. 181101. DOI: 10.1103/PhysRevLett.107.181101. arXiv: 1106.3340 [astro-ph.EP] (cit. on p. xv).

Kauffmann, G., S. D. M. White, and B. Guiderdoni (Sept. 1993). "The Formation and Evolution of Galaxies Within Merging Dark Matter Haloes". In: MNRAS 264, p. 201. DOI: 10.1093/mnras/264.1.201 (cit. on p. 102).

Khan, F. M., A. Just, and D. Merritt (May 2011). "Efficient Merger of Binary Supermassive Black Holes in Merging Galaxies". In: ApJ 732, 89, p. 89. DOI: 10.1088/0004-637X/732/2/89. arXiv: 1103.0272 (cit. on pp. xiii, 62).

Khan, F. M. et al. (Apr. 2012). "Mergers of Unequal-mass Galaxies: Supermassive Black Hole Binary Evolution and Structure of Merger Remnants". In: ApJ 749, 147, p. 147. DOI: 10.1088/0004-637X/749/2/147. arXiv: 1202.2124 (cit. on p. 39).

Khan, F. M. et al. (Sept. 2016). "Swift Coalescence of Supermassive Black Holes in Cosmological Mergers of Massive Galaxies". In: ApJ 828, 73, p. 73. DOI: 10.3847/0004-637X/828/2/73. arXiv: 1604.00015 (cit. on pp. xiii, 62).

Khandai, N. et al. (June 2015). "The MassiveBlack-II simulation: the evolution of haloes and galaxies to z = 0". In: MNRAS 450, pp. 1349–1374. DOI: 10.1093/mnras/stv627. arXiv: 1402.0888 (cit. on p. 101).

Klein, A. et al. (Jan. 2016). "Science with the space-based interferometer eLISA: Supermassive black hole binaries". In: Phys. Rev. D 93.2, 024003, p. 024003.

DOI: 10.1103/PhysRevD.93.024003. arXiv: 1511.05581 [gr-qc] (cit. on pp. xi, 111).

Königsdörffer, C., G. Faye, and G. Schäfer (Aug. 2003). "Binary black-hole dynamics at the third-and-a-half post-Newtonian order in the ADM formalism". In: Phys. Rev. D 68.4, 044004, p. 044004. DOI: 10.1103/PhysRevD.68.044004. eprint: gr-qc/0305048 (cit. on pp. 2, 3).

Kormendy, J. and L. C. Ho (Aug. 2013). "Coevolution (Or Not) of Supermassive Black Holes and Host Galaxies". In: ARA&A 51, pp. 511–653. DOI: 10.1146/annurev-astro-082708-101811. arXiv: 1304.7762 (cit. on pp. xi, 37, 65).

Kozai, Y. (Nov. 1962). "Secular perturbations of asteroids with high inclination and eccentricity". In: AJ 67, p. 591. DOI: 10.1086/108790 (cit. on pp. xiv, 50, 105).

Kravtsov, A. V. and O. Y. Gnedin (Apr. 2005). "Formation of Globular Clusters in Hierarchical Cosmology". In: ApJ 623, pp. 650–665. DOI: 10.1086/428636. eprint: astro-ph/0305199 (cit. on p. 101).

Kulkarni, G. and A. Loeb (May 2012). "Formation of galactic nuclei with multiple supermassive black holes at high redshifts". In: MNRAS 422, pp. 1306–1323. DOI: 10.1111/j.1365-2966.2012.20699.x. arXiv: 1107.0517 (cit. on p. xvi).

Landau, L. D. and E. M. Lifshitz (1975). *The classical theory of fields*. Oxford: Pergamon Press (cit. on pp. 6, 10, 19).

Lapi, A. et al. (Feb. 2014). "The Coevolution of Supermassive Black Holes and Massive Galaxies at High Redshift". In: ApJ 782, 69, p. 69. DOI: 10.1088/0004-637X/782/2/69. arXiv: 1312.3751 (cit. on p. 104).

Lehner, Luis and Frans Pretorius (2014). "Numerical Relativity and Astrophysics". In: *Annual Review of Astronomy and Astrophysics* 52.1, pp. 661–694. DOI: 10.1146/annurev-astro-081913-040031. eprint: https://doi.org/10.1146/annurev-astro-081913-040031. URL: https://doi.org/10.1146/annurev-astro-081913-040031 (cit. on p. 1).

Li, G. et al. (Apr. 2014). "Eccentricity Growth and Orbit Flip in Near-coplanar Hierarchical Three-body Systems". In: ApJ 785, 116, p. 116. DOI: 10.1088/0004-637X/785/2/116. arXiv: 1310.6044 [astro-ph.EP] (cit. on p. 59).

Lidov, M. L. (Oct. 1962). "The evolution of orbits of artificial satellites of planets under the action of gravitational perturbations of external bodies". In: Planet. Space Sci. 9, pp. 719–759. DOI: 10.1016/0032-0633(62)90129-0 (cit. on pp. xiv, 50, 105).

Lodato, G. et al. (Sept. 2009). "Black hole mergers: can gas discs solve the 'final parsec' problem?" In: MNRAS 398, pp. 1392–1402. DOI: 10.1111/j.1365-2966.2009.15179.x. arXiv: 0906.0737 (cit. on p. xiii).

Lorimer, D. R. and M. Kramer (Dec. 2004). *Handbook of Pulsar Astronomy* (cit. on p. 112).

Lousto, C. O. and H. Nakano (Oct. 2008). "Three-body equations of motion in successive post-Newtonian approximations". In: *Classical and Quantum Gravity* 25.19, 195019, p. 195019. DOI: 10.1088/0264-9381/25/19/195019. arXiv: 0710.5542 [gr-qc] (cit. on pp. 2, 3).

Luo, L., B. Katz, and S. Dong (May 2016). "Double-averaging can fail to characterize the long-term evolution of Lidov-Kozai Cycles and derivation of an

analytical correction". In: MNRAS 458, pp. 3060–3074. DOI: 10.1093/mnras/stw475. arXiv: 1601.04345 [astro-ph.EP] (cit. on p. 40).

Madau, P., F. Haardt, and M. Dotti (Apr. 2014). "Super-critical Growth of Massive Black Holes from Stellar-mass Seeds". In: ApJ 784, L38, p. L38. DOI: 10.1088/2041-8205/784/2/L38. arXiv: 1402.6995 (cit. on p. 104).

Madau, P. and M. J. Rees (Apr. 2001). "Massive Black Holes as Population III Remnants". In: ApJ 551, pp. L27–L30. DOI: 10.1086/319848. eprint: astro-ph/0101223 (cit. on p. 103).

Maggiore, Michele (2007). *Gravitational Waves. Vol. 1: Theory and Experiments*. Oxford Master Series in Physics. Oxford University Press. ISBN: 9780198570745, 9780198520740 (cit. on pp. 7, 9–11, 13, 14, 21, 25).

Magorrian, J. et al. (June 1998). "The Demography of Massive Dark Objects in Galaxy Centers". In: AJ 115, pp. 2285–2305. DOI: 10.1086/300353. eprint: astro-ph/9708072 (cit. on p. 37).

Mardling, R. A. and S. J. Aarseth (Mar. 2001). "Tidal interactions in star cluster simulations". In: MNRAS 321, pp. 398–420. DOI: 10.1046/j.1365-8711.2001.03974.x (cit. on p. 53).

Marulli, F. et al. (July 2009). "The spatial distribution of X-ray selected AGN in the Chandra deep fields: a theoretical perspective". In: MNRAS 396, pp. 1404–1414. DOI: 10.1111/j.1365-2966.2009.14851.x. arXiv: 0904.0256 (cit. on p. 102).

Meiron, Y. and A. Laor (Sept. 2010). "The stellar kinematic signature of massive black hole binaries". In: MNRAS 407, pp. 1497–1513. DOI: 10.1111/j.1365-2966.2010.17031.x. arXiv: 1005.2917 (cit. on p. 133).

Merritt, D. (Apr. 2002). "Rotational Brownian Motion of a Massive Binary". In: ApJ 568, pp. 998–1003. DOI: 10.1086/339035. eprint: astro-ph/0107569 (cit. on p. 34).

Merritt, D. (July 2013). *Dynamics and Evolution of Galactic Nuclei*. Princeton University Press, 2013 (cit. on pp. 39, 65).

Merritt, D., S. Mikkola, and A. Szell (Dec. 2007). "Long-Term Evolution of Massive Black Hole Binaries. III. Binary Evolution in Collisional Nuclei". In: ApJ 671, pp. 53–72. DOI: 10.1086/522691. arXiv: 0705.2745 (cit. on p. xiii).

Mikkola, S. and D. Merritt (June 2008). "Implementing Few-Body Algorithmic Regularization with Post-Newtonian Terms". In: AJ 135, pp. 2398–2405. DOI: 10.1088/0004-6256/135/6/2398. arXiv: 0709.3367 (cit. on pp. 42–44).

Mikkola, S. and M. J. Valtonen (Nov. 1992). "Evolution of binaries in the field of light particles and the problem of two black holes". In: MNRAS 259, pp. 115–120. DOI: 10.1093/mnras/259.1.115 (cit. on p. 30).

Milosavljević, M. and D. Merritt (Oct. 2003). "The Final Parsec Problem". In: *The Astrophysics of Gravitational Wave Sources*. Ed. by J. M. Centrella. Vol. 686. American Institute of Physics Conference Series, pp. 201–210. DOI: 10.1063/1.1629432. eprint: astro-ph/0212270 (cit. on pp. xii, xiii).

Misner, C. W., K. S. Thorne, and J. A. Wheeler (1973). *Gravitation*. San Francisco: W.H. Freeman and Co. (cit. on pp. 7, 9, 10, 19, 20, 26).

Monaco, P., F. Fontanot, and G. Taffoni (Mar. 2007). "The MORGANA model for the rise of galaxies and active nuclei". In: MNRAS 375, pp. 1189–1219.

DOI: 10.1111/j.1365-2966.2006.11253.x. eprint: astro-ph/0610805 (cit. on p. 102).

Moore, C. and M. Nauenberg (Oct. 2006). "New Periodic Orbits for the n-Body Problem". In: *Journal of Computational and Nonlinear Dynamics, Volume 1, Issue 4, p. 307-311* 1, pp. 307–311. DOI: 10.1115/1.2338323. eprint: math/0511219 (cit. on p. 42).

Mortlock, D. J. et al. (June 2011). "A luminous quasar at a redshift of z = 7.085". In: Nature 474, pp. 616–619. DOI: 10.1038/nature10159. arXiv: 1106.6088 [astro-ph.CO] (cit. on p. xi).

Naoz, S. (Sept. 2016). "The Eccentric Kozai-Lidov Effect and Its Applications". In: ARA&A 54, pp. 441–489. DOI: 10.1146/annurev-astro-081915-023315. arXiv: 1601.07175 [astro-ph.EP] (cit. on p. xiv).

Naoz, S., W. M. Farr, and F. A. Rasio (Aug. 2012). "On the Formation of Hot Jupiters in Stellar Binaries". In: ApJ 754, L36, p. L36. DOI: 10.1088/2041-8205/754/2/L36. arXiv: 1206.3529 [astro-ph.EP] (cit. on p. xv).

Naoz, S. et al. (May 2013). "Secular dynamics in hierarchical three-body systems". In: MNRAS 431, pp. 2155–2171. DOI: 10.1093/mnras/stt302. arXiv: 1107.2414 [astro-ph.EP] (cit. on p. xv).

Nixon, C. J. et al. (Apr. 2011). "Retrograde accretion and merging supermassive black holes". In: MNRAS 412, pp. 1591–1598. DOI: 10.1111/j.1365-2966.2010.17952.x. arXiv: 1011.1914 [astro-ph.HE] (cit. on p. xiii).

Parkinson, H., S. Cole, and J. Helly (Jan. 2008). "Generating dark matter halo merger trees". In: MNRAS 383, pp. 557–564. DOI: 10.1111/j.1365-2966.2007.12517.x. arXiv: 0708.1382 (cit. on p. 103).

Pati, M. E. and C. M. Will (Dec. 2000). "Post-Newtonian gravitational radiation and equations of motion via direct integration of the relaxed Einstein equations: Foundations". In: Phys. Rev. D 62.12, 124015, p. 124015. DOI: 10.1103/PhysRevD.62.124015. eprint: gr-qc/0007087 (cit. on p. 19).

Peters, P. C. and J. Mathews (July 1963). "Gravitational Radiation from Point Masses in a Keplerian Orbit". In: *Phys. Rev.* 131 (1), pp. 435–440. DOI: 10.1103/PhysRev.131.435. URL: http://link.aps.org/doi/10.1103/PhysRev.131.435 (cit. on pp. xvi, 44, 45, 122).

Planck Collaboration et al. (Sept. 2016). "Planck 2015 results. I. Overview of products and scientific results". In: A&A 594, A1, A1. DOI: 10.1051/0004-6361/201527101. arXiv: 1502.01582 (cit. on p. xi).

Poisson, E. and C. M. Will (May 2014). *Gravity* (cit. on p. 28).

Poisson, Eric (2004). "The motion of point particles in curved spacetime". In: *Living Rev. Relativity* 7, p. 6. eprint: gr-qc/0306052. URL: http://www.livingreviews.org/lrr-2004-6 (cit. on p. 2).

Poujade, Olivier and Luc Blanchet (June 2002). "Post-Newtonian approximation for isolated systems calculated by matched asymptotic expansions". In: *Phys. Rev. D* 65 (12), p. 124020. DOI: 10.1103/PhysRevD.65.124020. URL: https://link.aps.org/doi/10.1103/PhysRevD.65.124020 (cit. on p. 20).

Press, W. H. (Feb. 1977). "Gravitational radiation from sources which extend into their own wave zone". In: Phys. Rev. D 15, pp. 965–968. DOI: 10.1103/PhysRevD.15.965 (cit. on p. 10).

Press, W. H. and P. Schechter (Feb. 1974). "Formation of Galaxies and Clusters of Galaxies by Self-Similar Gravitational Condensation". In: ApJ 187, pp. 425–438. DOI: 10.1086/152650 (cit. on pp. 102, 103).

Press, W. H. et al. (2002). *Numerical recipes in C++ : the art of scientific computing* (cit. on p. 40).

Preto, M. et al. (May 2011). "Fast Coalescence of Massive Black Hole Binaries from Mergers of Galactic Nuclei: Implications for Low-frequency Gravitational-wave Astrophysics". In: ApJ 732, L26, p. L26. DOI: 10.1088/2041-8205/732/2/L26. arXiv: 1102.4855 (cit. on p. xiii).

Pretorius, Frans (2005). "Evolution of binary black hole spacetimes". In: *Phys. Rev. Lett.* 95, p. 121101. eprint: gr-qc/0507014 (cit. on p. 1).

Quinlan, G. D. (July 1996). "The dynamical evolution of massive black hole binaries I. Hardening in a fixed stellar background". In: New A 1, pp. 35–56. DOI: 10.1016/S1384-1076(96)00003-6. eprint: astro-ph/9601092 (cit. on pp. xii, 29–31, 34, 67, 114).

Rhook, K. J. and J. S. B. Wyithe (Aug. 2005). "Realistic event rates for detection of supermassive black hole coalescence by LISA". In: MNRAS 361, pp. 1145–1152. DOI: 10.1111/j.1365-2966.2005.08987.x. eprint: astro-ph/0503210 (cit. on p. xi).

Richardson, L. F. (1911). "The Approximate Arithmetical Solution by Finite Differences of Physical Problems Involving Differential Equations, with an Application to the Stresses in a Masonry Dam". In: *Philosophical Transactions of the Royal Society of London A: Mathematical, Physical and Engineering Sciences* 210.459-470, pp. 307–357. ISSN: 0264-3952. DOI: 10.1098/rsta.1911.0009. eprint: http://rsta.royalsocietypublishing.org/content/210/459-470/307.full.pdf. URL: http://rsta.royalsocietypublishing.org/content/210/459-470/307 (cit. on p. 40).

Rosado, P. A., A. Sesana, and J. Gair (Aug. 2015). "Expected properties of the first gravitational wave signal detected with pulsar timing arrays". In: MNRAS 451, pp. 2417–2433. DOI: 10.1093/mnras/stv1098. arXiv: 1503.04803 [astro-ph.HE] (cit. on pp. xvii, 126).

Roškar, R. et al. (May 2015). "Orbital decay of supermassive black hole binaries in clumpy multiphase merger remnants". In: MNRAS 449, pp. 494–505. DOI: 10.1093/mnras/stv312. arXiv: 1406.4505 (cit. on p. 59).

Ryu, T. et al. (Sept. 2017). "Interactions between multiple supermassive black holes in galactic nuclei: a solution to the final parsec problem". In: *ArXiv e-prints*. arXiv: 1709.06501 (cit. on p. 133).

Saslaw, W. C., M. J. Valtonen, and S. J. Aarseth (June 1974). "The Gravitational Slingshot and the Structure of Extragalactic Radio Sources". In: ApJ 190, pp. 253–270. DOI: 10.1086/152870 (cit. on p. 30).

Sazhin, M. V. (Feb. 1978). "Opportunities for detecting ultralong gravitational waves". In: Soviet Ast. 22, pp. 36–38 (cit. on p. 112).

Scannapieco, C. et al. (June 2009). "The formation and survival of discs in a ΛCDM universe". In: MNRAS 396, pp. 696–708. DOI: 10.1111/j.1365-2966.2009.14764.x. arXiv: 0812.0976 (cit. on p. 101).

Schäfer, G. (Aug. 1987). "Three-body hamiltonian in general relativity". In: *Physics Letters A* 123, pp. 336–339. DOI: 10.1016/0375-9601(87)90389-6 (cit. on pp. 2, 3).

Sesana, A. (Aug. 2010). "Self Consistent Model for the Evolution of Eccentric Massive Black Hole Binaries in Stellar Environments: Implications for Gravitational Wave Observations". In: ApJ 719, pp. 851–864. DOI: 10.1088/0004-637X/719/1/851. arXiv: 1006.0730 [astro-ph.CO] (cit. on p. 68).

Sesana, A. (June 2013). "Systematic investigation of the expected gravitational wave signal from supermassive black hole binaries in the pulsar timing band". In: MNRAS 433, pp. L1–L5. DOI: 10.1093/mnrasl/slt034. arXiv: 1211.5375 (cit. on p. xvii).

Sesana, A. (2015). "Pulsar Timing Arrays and the Challenge of Massive Black Hole Binary Astrophysics". In: *Gravitational Wave Astrophysics*. Ed. by C. F. Sopuerta. Vol. 40. Astrophysics and Space Science Proceedings, p. 147. DOI: 10.1007/978-3-319-10488-1_13. arXiv: 1407.5693 (cit. on p. 120).

Sesana, A., F. Haardt, and P. Madau (Nov. 2006). "Interaction of Massive Black Hole Binaries with Their Stellar Environment. I. Ejection of Hypervelocity Stars". In: ApJ 651, pp. 392–400. DOI: 10.1086/507596. eprint: astro-ph/0604299 (cit. on pp. xii, 29–35, 37, 114).

Sesana, A. and F. M. Khan (Nov. 2015). "Scattering experiments meet N-body - I. A practical recipe for the evolution of massive black hole binaries in stellar environments". In: MNRAS 454, pp. L66–L70. DOI: 10.1093/mnrasl/slv131. arXiv: 1505.02062 (cit. on pp. xiii, 31, 33, 37, 39, 53, 62, 105).

Sesana, A., A. Vecchio, and M. Volonteri (Apr. 2009). "Gravitational waves from resolvable massive black hole binary systems and observations with Pulsar Timing Arrays". In: MNRAS 394, pp. 2255–2265. DOI: 10.1111/j.1365-2966.2009.14499.x. arXiv: 0809.3412 (cit. on p. 122).

Sesana, A. et al. (Aug. 2004). "Low-Frequency Gravitational Radiation from Coalescing Massive Black Hole Binaries in Hierarchical Cosmologies". In: ApJ 611, pp. 623–632. DOI: 10.1086/422185. eprint: astro-ph/0401543 (cit. on p. xi).

Sesana, A. et al. (Apr. 2005). "The Gravitational Wave Signal from Massive Black Hole Binaries and Its Contribution to the LISA Data Stream". In: ApJ 623, pp. 23–30. DOI: 10.1086/428492. eprint: astro-ph/0409255 (cit. on p. xi).

Sesana, A. et al. (Oct. 2014). "Linking the Spin Evolution of Massive Black Holes to Galaxy Kinematics". In: ApJ 794, 104, p. 104. DOI: 10.1088/0004-637X/794/2/104. arXiv: 1402.7088 (cit. on p. 102).

Sesana, A. et al. (Nov. 2016). "Selection bias in dynamically measured supermassive black hole samples: consequences for pulsar timing arrays". In: MNRAS 463, pp. L6–L11. DOI: 10.1093/mnrasl/slw139. arXiv: 1603.09348 (cit. on pp. 125, 128, 132).

Shankar, F. et al. (Aug. 2016). "Selection bias in dynamically measured supermassive black hole samples: its consequences and the quest for the most fundamental relation". In: MNRAS 460, pp. 3119–3142. DOI: 10.1093/mnras/stw678. arXiv: 1603.01276 (cit. on pp. 125, 129).

Shannon, R. M. et al. (Sept. 2015). "Gravitational waves from binary supermassive black holes missing in pulsar observations". In: *Science* 349, pp. 1522–1525. DOI: 10.1126/science.aab1910. arXiv: 1509.07320 (cit. on p. 128).

Siemens, X. et al. (Nov. 2013). "The stochastic background: scaling laws and time to detection for pulsar timing arrays". In: *Classical and Quantum Gravity* 30.22, 224015, p. 224015. DOI: 10.1088/0264-9381/30/22/224015. arXiv: 1305.3196 [astro-ph.IM] (cit. on pp. xvii, 125).

Sijacki, D., V. Springel, and M. G. Haehnelt (Nov. 2009). "Growing the first bright quasars in cosmological simulations of structure formation". In: MNRAS 400, pp. 100–122. DOI: 10.1111/j.1365-2966.2009.15452.x. arXiv: 0905.1689 (cit. on p. 101).

Sijacki, D., V. Springel, and M. G. Haehnelt (July 2011). "Gravitational recoils of supermassive black holes in hydrodynamical simulations of gas-rich galaxies". In: MNRAS 414, pp. 3656–3670. DOI: 10.1111/j.1365-2966.2011.18666.x. arXiv: 1008.3313 (cit. on pp. 90, 101).

Somerville, R. S. and J. R. Primack (Dec. 1999). "Semi-analytic modelling of galaxy formation: the local Universe". In: MNRAS 310, pp. 1087–1110. DOI: 10.1046/j.1365-8711.1999.03032.x. eprint: astro-ph/9802268 (cit. on p. 102).

Somerville, R. S. et al. (Dec. 2008). "A semi-analytic model for the co-evolution of galaxies, black holes and active galactic nuclei". In: MNRAS 391, pp. 481–506. DOI: 10.1111/j.1365-2966.2008.13805.x. arXiv: 0808.1227 (cit. on p. 102).

Springel, V. (Dec. 2005). "The cosmological simulation code GADGET-2". In: MNRAS 364, pp. 1105–1134. DOI: 10.1111/j.1365-2966.2005.09655.x. eprint: astro-ph/0505010 (cit. on p. 101).

Springel, V. and L. Hernquist (Feb. 2003). "The history of star formation in a Λ cold dark matter universe". In: MNRAS 339, pp. 312–334. DOI: 10.1046/j.1365-8711.2003.06207.x. eprint: astro-ph/0206395 (cit. on p. 101).

Taffoni, G. et al. (May 2003). "On the life and death of satellite haloes". In: MNRAS 341, pp. 434–448. DOI: 10.1046/j.1365-8711.2003.06395.x. eprint: astro-ph/0301271 (cit. on p. 104).

Tassis, K., A. V. Kravtsov, and N. Y. Gnedin (Jan. 2008). "Scaling Relations of Dwarf Galaxies without Supernova-driven Winds". In: ApJ 672, 888-903, pp. 888–903. DOI: 10.1086/523880. eprint: astro-ph/0609763 (cit. on p. 101).

Tassis, K. et al. (Apr. 2003). "Numerical Simulations of High-Redshift Star Formation in Dwarf Galaxies". In: ApJ 587, pp. 13–24. DOI: 10.1086/368148. eprint: astro-ph/0212457 (cit. on p. 101).

Taylor, S. R., J. Simon, and L. Sampson (May 2017). "Constraints on the Dynamical Environments of Supermassive Black-Hole Binaries Using Pulsar-Timing Arrays". In: *Physical Review Letters* 118.18, 181102, p. 181102. DOI: 10.1103/PhysRevLett.118.181102. arXiv: 1612.02817 (cit. on pp. 114, 120).

Taylor, S. R. et al. (Mar. 2016a). "Are We There Yet? Time to Detection of Nanohertz Gravitational Waves Based on Pulsar-timing Array Limits". In:

ApJ 819, L6, p. L6. DOI: 10.3847/2041-8205/819/1/L6. arXiv: 1511.05564 [astro-ph.IM] (cit. on p. 125).

Taylor, S. R. et al. (Jan. 2016b). "Detecting Eccentric Supermassive Black Hole Binaries with Pulsar Timing Arrays: Resolvable Source Strategies". In: ApJ 817, 70, p. 70. DOI: 10.3847/0004-637X/817/1/70. arXiv: 1505.06208 [gr-qc] (cit. on p. 122).

Teyssier, R. et al. (June 2011). "Mass distribution in galaxy clusters: the role of Active Galactic Nuclei feedback". In: MNRAS 414, pp. 195–208. DOI: 10.1111/j.1365-2966.2011.18399.x. arXiv: 1003.4744 (cit. on p. 101).

Thorne, K. S. (1980). "Multipole Expansions of Gravitational Radiation". In: *Rev. Mod. Phys.* 52, pp. 299–339. DOI: 10.1103/RevModPhys.52.299 (cit. on p. 6).

Vasiliev, E. (Dec. 2014). "Rates of capture of stars by supermassive black holes in non-spherical galactic nuclei". In: *Classical and Quantum Gravity* 31.24, 244002, p. 244002. DOI: 10.1088/0264-9381/31/24/244002. arXiv: 1411.1760 (cit. on p. xiii).

Vasiliev, E., F. Antonini, and D. Merritt (Sept. 2015). "The Final-parsec Problem in the Collisionless Limit". In: ApJ 810, 49, p. 49. DOI: 10.1088/0004-637X/810/1/49. arXiv: 1505.05480 (cit. on pp. xii, xiii, 62).

Vasiliev, Eugene, Fabio Antonini, and David Merritt (2014). "The final-parsec problem in nonspherical galaxies revisited". In: *Astrophys. J.* 785, p. 163. DOI: 10.1088/0004-637X/785/2/163. arXiv: 1311.1167 [astro-ph.GA] (cit. on pp. xii, xiii).

Vogelsberger, M. et al. (May 2014). "Properties of galaxies reproduced by a hydrodynamic simulation". In: Nature 509, pp. 177–182. DOI: 10.1038/nature13316. arXiv: 1405.1418 (cit. on p. 101).

Volonteri, M. (Aug. 2012). "The Formation and Evolution of Massive Black Holes". In: *Science* 337, p. 544. DOI: 10.1126/science.1220843. arXiv: 1208.1106 (cit. on p. xi).

Volonteri, M., G. Lodato, and P. Natarajan (Jan. 2008). "The evolution of massive black hole seeds". In: MNRAS 383, pp. 1079–1088. DOI: 10.1111/j.1365-2966.2007.12589.x. arXiv: 0709.0529 (cit. on pp. 103, 139).

Volonteri, M., P. Madau, and F. Haardt (Aug. 2003). "The Formation of Galaxy Stellar Cores by the Hierarchical Merging of Supermassive Black Holes". In: ApJ 593, pp. 661–666. DOI: 10.1086/376722. eprint: astro-ph/0304389 (cit. on pp. 39, 65).

Volonteri, M. et al. (Aug. 2016). "The cosmic evolution of massive black holes in the Horizon-AGN simulation". In: MNRAS 460, pp. 2979–2996. DOI: 10.1093/mnras/stw1123. arXiv: 1602.01941 (cit. on p. 101).

Weinberg, S. (July 1972). *Gravitation and Cosmology: Principles and Applications of the General Theory of Relativity*, p. 688 (cit. on p. 21).

Wen, L. (Nov. 2003). "On the Eccentricity Distribution of Coalescing Black Hole Binaries Driven by the Kozai Mechanism in Globular Clusters". In: ApJ 598, pp. 419–430. DOI: 10.1086/378794. eprint: astro-ph/0211492 (cit. on pp. 63, 80).

Will, C. M. (Oct. 1993). *Books-Received - Theory and Experiment in Gravitational Physics ED.2*. Vol. 262, p. 263 (cit. on p. 1).

Wyithe, J. S. B. and A. Loeb (June 2003). "Low-Frequency Gravitational Waves from Massive Black Hole Binaries: Predictions for LISA and Pulsar Timing Arrays". In: ApJ 590, pp. 691–706. DOI: 10.1086/375187. eprint: astro-ph/0211556 (cit. on p. xi).

Yu, Q. (Apr. 2002). "Evolution of massive binary black holes". In: MNRAS 331, pp. 935–958. DOI: 10.1046/j.1365-8711.2002.05242.x. eprint: astro-ph/0109530 (cit. on p. xiii).